

#### Numerical modelling of transient low-frequency sound propagation and vibration in buildings

Citation for published version (APA):

Sihar, I. (2022). Numerical modelling of transient low-frequency sound propagation and vibration in buildings. [Phd Thesis 1 (Research TU/e / Graduation TU/e), Built Environment]. Eindhoven University of Technology.

#### Document status and date:

Published: 01/07/2022

#### Document Version:

Publisher's PDF, also known as Version of Record (includes final page, issue and volume numbers)

#### Please check the document version of this publication:

- A submitted manuscript is the version of the article upon submission and before peer-review. There can be important differences between the submitted version and the official published version of record. People interested in the research are advised to contact the author for the final version of the publication, or visit the DOI to the publisher's website.
- The final author version and the galley proof are versions of the publication after peer review.
- The final published version features the final layout of the paper including the volume, issue and page numbers.

Link to publication

#### General rights

Copyright and moral rights for the publications made accessible in the public portal are retained by the authors and/or other copyright owners and it is a condition of accessing publications that users recognise and abide by the legal requirements associated with these rights.

- · Users may download and print one copy of any publication from the public portal for the purpose of private study or research.
- You may not further distribute the material or use it for any profit-making activity or commercial gain
  You may freely distribute the URL identifying the publication in the public portal.

If the publication is distributed under the terms of Article 25fa of the Dutch Copyright Act, indicated by the "Taverne" license above, please follow below link for the End User Agreement:

www.tue.nl/taverne

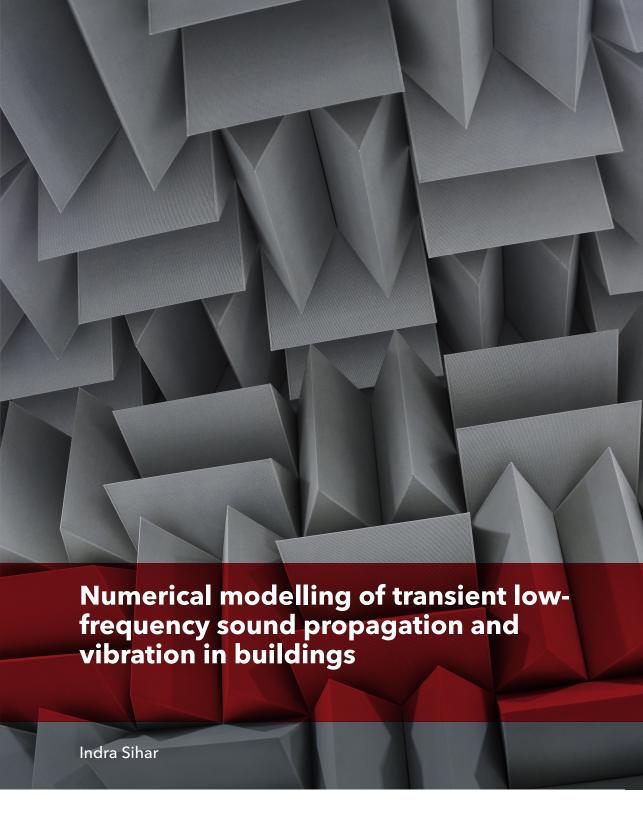
#### Take down policy

If you believe that this document breaches copyright please contact us at:

openaccess@tue.nl

providing details and we will investigate your claim.

Download date: 04. Oct. 2023



# Numerical modelling of transient low-frequency sound propagation and vibration in buildings

INDRA SIHAR

Department of the Built Environment Eindhoven University of Technology

The work in this dissertation was financially supported by Lembaga Pengelola Dana Pendidikan (Indonesia Endowment Fund for Education) - LPDP under the Ministry of Finance of the Republic of Indonesia.

© July 2022, Indra Sihar

A catalogue record is available from the Eindhoven University of Technology Library.

ISBN: 978-90-386-5540-6

NUR: 955

Keywords: discontinuous Galerkin, room acoustics, outdoor sound propagation, structural vibration, sound radiation, sound transmission.

# Numerical modelling of transient low-frequency sound propagation and vibration in buildings

#### **PROEFSCHRIFT**

ter verkrijging van de graad van doctor aan de Technische Universiteit Eindhoven, op gezag van de rector magnificus prof.dr.ir. F.P.T. Baaijens, voor een commissie aangewezen door het College voor Promoties, in het openbaar te verdedigen op vrijdag 1 July 2022 om 11.00 uur

door

Indra Sihar

geboren te Pematang Siantar, Indonesia

Dit proefschrift is goedgekeurd door de promotoren en de samenstelling van de promotiecommissie is als volgt:

voorzitter: prof.dr.ir. Pieter van Wesemael 1e promotor: prof.dr.ir. Maarten C.J. Hornikx

copromotor: dr. Jieun Yang

leden: prof.dr.ir Akke S.J. Suiker

prof.dr.ir Ines Lopez Arteaga

prof.dr. Carl Hopkins (University of Liverpool)

prof.dr.-ing. Steffen Marburg (Technical University of

Munich)

Het onderzoek dat in dit proefschrift wordt beschreven is uitgevoerd in overeenstemming met de TU/e Gedragscode Wetenschapsbeoefening.

#### Summary

The urban environment is increasingly exposed to excessive noise from the environmental noise sources and neighbours. To address this problem, an acoustically high-quality built environment is needed to ensure health and comfort. In designing such an environment, the prediction of sound propagation and vibrations in buildings have a vital role. This research aims to develop an efficient yet detailed numerical model of sound propagation and vibration in building applications, especially in the low-frequency range. It targets solving sound propagation, structural vibration, and vibroacoustic problems. This research employs a wave-based method to solve these problems.

The chosen wave-based method is the time-domain nodal discontinuous Galerkin (DG) method due to its favourable features such as computational efficiency, high-order accuracy, geometric flexibility, and the potential for massive parallel computing. This computational method has been used in many other branches of applied physics, but its use for vibration and vibroacoustic problems in buildings has not been investigated yet. This research is divided into three parts: the first part is concerned with the nodal DG method development for sound propagation in air; the second part is devoted to the development of the method for structural vibrations; the third part expands the method for sound and vibration interaction (vibroacoustic) problems.

The first part of this research is comprised of two sections. The first section demonstrates the implementation of the nodal DG method for applications in room acoustics. In this section, the numerical formulation of the method for the linear acoustic equations is presented, along with a strategy to realise the frequency-independent impedance boundary condition (BC). Several simulation configurations are analysed to determine the convergence, dispersion, and dissipation errors of this method. This analysis shows the great potential of the nodal DG method for room acoustics problems. Afterwards, sound propagation in a room under laboratory conditions is computed and compared with the experimental data, which showed satisfactory results. The second section demonstrates an application of the nodal DG method for outdoor sound propagation. The method is applied to investigate several noise intervention scenarios in an airport environment in the presence of wind flow. This investigation extends the room acoustics application by solving the same governing equations, while the wind conditions are incorporated by using an effective sound speed approach. This approach is validated with results from the finite element method (FEM). It is shown that the intervention scenarios effectively reduce the aircraft noise propagation from the airport to the residential area in the low-frequency range.

In the second part, the implementation of the nodal DG method for structural vibration is presented. This part is divided into two sections. The first section is devoted to the vibration of monolithic structures. These structures include rectangular plates and an L-shaped structure, whose vibrations are modelled by the linear elasticity equations in three-dimensional geometry. The numerical formulation of the nodal

DG method for the linear elasticity equations are presented, along with several aspects such as boundary conditions, point force excitation, and the upwind numerical flux. The numerical results are validated for rectangular concrete slabs with different BCs and thicknesses by comparing vibration mobilities derived from classical plate theory (CPT) and the first-order shear deformation theory (FSDT) via the modal expansion method. An excellent agreement is found between the numerical solution and the FSDT. In case of the L-shaped structure, the vibration mobility is compared with the mobilities obtained using the CPT, FSDT and linear elasticity equations (via FEM). It shows excellent agreement with the mobility obtained by the FEM over the entire frequency range of interest (up to 1 kHz). However, the numerical mobility agrees well with the CPT and FSDT only in the lower frequency range (below 700 Hz). In the second section of this part, the nodal DG method is presented for the vibrations of structures with piecewise constant material properties. The previous nodal DG application is extended by simulating vibration of assemblies of several monolithic components that differ in their mechanical properties. Two examples are simulated: a T-shaped structure and a scaled lightweight wooden floor. In the nodal DG method, the Rankine-Hugoniot jump conditions are used to obtain an accurate numerical flux, and the constant viscous damping forces were added to model vibration energy losses in the structure. To validate the method, the numerical results are compared with experimental data as obtained from actual structures. Good agreement is found between numerical and experimental results; however, there are discrepancies in the higher frequency region (>250 Hz). The main reason for this was that the chosen damping approach is insufficient to represent a wide frequency range.

In the last part of this thesis, the nodal DG method is applied to the vibroacoustic problems. Two vibroacoustic cases that typically occur in buildings were simulated. The first case concerned the impact sound radiation from a rectangular slab into a cuboid room, and the second was the sound transmission between two cuboid rooms with direct and flanking contributions. As a combination of the previous methodologies, the vibration was governed by the linear elasticity equations and the linearised acoustic equations governed the sound propagation. In this part, the upwind numerical flux for the linearised acoustic equations based on Rankine-Hugoniot jump conditions are presented, as well as the coupling conditions between acoustic and vibration variables. In the first case, the nodal DG results are compared with those obtained by the modal expansion method, and in the second case the nodal DG results are compared with those obtained by FEM. Good agreements are found between the solutions obtained with the nodal DG method and those obtained with the modal expansion method/FEM. These examples demonstrate the applicability of the nodal DG methodology for the vibroacoustic problems.

#### Table of contents

Sı	ımm	ary	i		
Ta	able	of contents	iii		
Li	ist of acronyms				
1	Gei	neral introduction	1		
	1.1	Motivation	1		
	1.2	Background	2		
	1.3	Modelling and prediction for room acoustics	8		
	1.4	Modelling and prediction for building acoustics	9		
	1.5	Wave-based numerical method for building acoustics	12		
	1.6	Motivation of selected modelling approaches	16		
	1.7	Research objectives and contributions	17		
	1.8	Thesis structure and related publications	18		
_	D.				
I of		${f e}$ velopments of time-domain DG method for simulation loor and outdoor sound propagation	21		
2	Dis	continuous Galerkin method for room acoustics applications	23		
	2.1	Introduction	23		
	2.2	Linear acoustic equations and nodal DG method	25		
	2.3	Impedance boundary conditions and numerical stability	30		
	2.4	Applications	34		
	2.5	Conclusions	43		
3	Dis	continuous Galerkin method for outdoor acoustics applications	47		
	3.1	Introduction	47		

	3.2	Noise intervention case	51			
	3.3	Methodology	55			
	3.4	Results and discussions	61			
	3.5	Conclusions	71			
H	D	Developments of time-domain DG method for simula-	_			
ti		of structural vibration	73			
4	Dis	continous Galerkin method for vibration of monolithic structure	75			
	4.1	Introduction	76			
	4.2	Methodology	77			
	4.3	Case studies				
	4.4	Results and discussions	90			
	4.5	Conclusions	103			
5	Discontinous Galerkin method for vibration of structures with piece-					
	wise	e constant material properties	105			
	5.1	Introduction				
	5.2	Methodology				
	5.3	Case studies				
	5.4	Computational settings				
	5.5	Experimental validation				
	5.6	Results and Discussions				
	5.7	Conclusion	132			
H	т 1	Developments of time-domain DG method for vibroa-	_			
		-	133			
6	Dis	continuous Galerkin method for predicting sound radiation and	ł			
	trai	nsmission of building components	135			
	6.1	Introduction	135			
	6.2	Methodology	138			
	6.3	Case studies	144			
	6.4	Results and discussions	148			
	6.5	Conclusions	153			
7	Cor	nclusions and future work	155			
	7.1	Conclusions	155			

	7.2 Future work	. 157
Li	st of Figures	177
Li	st of Tables	182
$\mathbf{A}_{ m l}$	ppendices	185
A	Derivations of the total discrete acoustic energy of the semi-discret system	ete 186
В	Validation case for outdoor sound propagation applications         B.1 Computational model	
C	Impedance of ground surface and resonator absorber rooftops C.1 Ground surface impedance	
D	Upwind numerical flux for the linear elasticity equations	198
E	Mechanical properties extraction of the wooden structure	201
$\mathbf{F}$	Additional result on the T-shaped structure	204
$\mathbf{G}$	Upwind numerical flux for linear acoustic equations	205
Н	Impact sound radiation solution         H.1 Sound field          H.2 Modal interaction	
A	cknowledgements	211
Cı	urriculum Vitae	213

vi List of acronyms

#### List of acronyms

ABL Atmospheric boundary layer

**ARD** Adaptive rectangular decomposition

BC Boundary condition

**BEM** Boundary element method

CA Computational acoustic

**CFD** Computational fluid dynamics

**CPT** Classical plate theory

**DG** Discontinuous Galerkin

**DoF** Degrees of freedom

**DPW** Degrees of freedom per wavelength

**ESM** Equivalent source method

**FDTD** Finite difference time-domain

**FEM** Finite element method

**FFP** Fast-field programme

**FSDT** First-order shear deformation theory

 ${f FVM}$  Finite volume method

**GA** Geometrical acoustics

IL Insertion loss

**ODE** Ordinary differential equation

PDE Partial differential equation

PE Parabolic equation

viii List of acronyms

PML	Perfectly matched layer
PSTD	Pseudo-spectral time-domain
RANS	Reynolds-averaged Navier-Stokes
RKF84	Fourth-order Runge-Kutta method with eight stages
SEA	Statistical energy analysis
S-S-S-C	Simply supported - simply supported - clamped
S-S-S-F	Simply supported - simply supported - free
S-S-S-S	Simply supported - simply supported - simply supported - simply supported
$\mathbf{TL}$	Transmission loss

#### 1 | General introduction

#### 1.1 Motivation

Noise is defined as unwanted sound generated primarily by various human activities, ranging from occupational, commuting, and domestic activities. Noise is present everywhere, including in the work place, urban areas, and dwellings. Within industry, some occupations are exposed to excessive noise, which can cause hearing loss (such as: miners, construction workers, carpenters) [1], [2]. In urban areas, people suffer from environmental noise generated by traffic, outdoor equipment, and leisure activities (such as: live music events, recreational noise, personal listening devices) [3]. In dwellings, people can also be affected by domestic noise caused by various sources, such as noisy neighbours, household appliances, and footsteps [4].

Noise can affect comfort and cause adverse health effects. The World Health Organization reported that road traffic and aircraft noise increase the risk of cardiovascular diseases such as ischaemic heart disease, heart attacks, and hypertension [5]. This environmental noise can also cause cognitive impairment in children, sleep disturbances, tinnitus, and annoyance (which leads to anger, distraction, stress, tiredness, etc.). Besides environmental noise, there is a growing awareness of neighbour noise (e.g., speech, music, footsteps) as one of the sources for domestic noise. This type of noise has the potential for task distraction since it draws human attention due to its informative sounds even if at low levels [6]. It also could affect health via long-lasting annoyance [4]. A recent review and study on neighbour noise can be found in Ref. [7], where it is shown that annoyance caused by neighbour noise results in physical and mental health symptoms.

Increased awareness of the noise hazards has led many countries to enact regulations to control noise levels. This has resulted in the introduction of policy and practical measures to reduce noise exposure in the workplace, such as the OSHA instruction PER 04-00-004 [8] and the EU directive 2003/10/EC [9], which requires employers to implement a hearing protection programme for workers. It also prompts the governments to issue regulations to control environmental noise, such as the EU directive 2002/49/EC (END) [5]. The END requires EU members to assess environmental noise exposure to their population and to create a noise management action plan related to the assessment. Related to the domestic noise, minimum values of airborne

and impact sound insulation for dwellings have been regulated in many countries [10], [11]. These regulations require the new dwellings to fulfil minimum standardised sound insulation descriptors, as presented in ISO 717:1996. These regulations have evolved in all European countries since the early 1960s [12], [13].

Although various policies have been undertaken to control noise levels, the number of people exposed to environmental noise is still high. The European Environmental Agency [14] reported that the number of people exposed to high levels of noise since 2012 has broadly remained stable following the END in 2002. The number of people exposed to road traffic noise inside urban areas is still expected to increase by approximately 8% by 2030. This outlook is projected as a result of future urban growth and increased mobility demand. This is in line with studies in Refs.[15], [16].

As shown in Refs. [4], [7], [17], the number of people annoyed by neighbourhood noise has remained high. Several factors caused this, for example, the trend in construction in moving from heavyweight (concrete, masonry, heavy-steel elements) to lightweight (timber, plasterboard, glass, light-steel elements) construction systems and elements, increased number of noise sources (e.g., wall- and floor-mounted household appliances, consumer electronics, etc.), and poor design/workmanship of the sound insulating properties of building construction. The trend towards the use of lightweight constructions is still ongoing. There are a number of advantages to lightweight construction over heavyweight construction. For example, timber-frame construction demonstrates several critical aspects of sustainability. For instance, it enables the storage of CO<sub>2</sub>, is a renewable raw material, and requires little energy to manufacture [18], [19]. Another advantage is that building components of a lightweight construction are easier to be prefabricated; therefore it lefts less waste on site and the assembly process is fast.

The adverse effects of noise and the outlook of environmental and domestic noise demand a built environment with a high acoustic quality. To achieve this, the acoustics of the building must be designed appropriately. For this reason, modelling and prediction of sound propagation and vibrations are essential. The main motivation of this thesis is to contribute to enabling the creation of such environments by further developing a numerical technique for the prediction of sound and vibration fields in room (and outdoor) acoustics and building acoustics applications, with more emphasis on the latter.

#### 1.2 Background

An illustration of a simple building construction and its environment is presented in Figure 1.1. This picture shows that sound can propagate into the lower right room in a building from various sources, such as vehicles outside the building, walking sound from the upper-floor, and entertainment equipment in the next room. To model the sound propagation and structural vibration, there are several governing equations that can be used, and they are described in this section.

1 | General introduction 3



Figure 1.1: Illustration of a simple building with its environment. The front façade is removed to see the building section.

Sound propagation in a room is governed by the linear acoustic equations. This set of equations models the small perturbation of pressure and velocities in air, and is derived from the conservation and state equations as:

$$\frac{\partial \mathbf{v}}{\partial t} + \frac{1}{\rho_0} \nabla p = 0, 
\frac{\partial p}{\partial t} + \rho_0 c_0^2 \nabla \cdot \mathbf{v} = 0,$$
(1.1)

where  $\mathbf{v} = [u, v, w]^T$  is the particle velocity, p is the sound pressure,  $\rho_0$  is the air density, and  $c_0$  is the adiabatic sound speed. Equations (1.1) also can be used to model the outdoor sound propagation, but with a limited accuracy [20]. This is conducted by setting the sound speed as a space-dependent variable to accommodate the atmospheric conditions (temperature and wind fields).

When sound impinges on the building structure (solid media), or a force excitation is given, vibrations occur in solid media. The linear elasticity equations, which govern the propagation of elastic waves, can be used to model this structural vibration. This set of equations is derived from momentum conservation and Hooke's constitutive equations [21]. For a Cartesian three-dimensional coordinate system, the equations for an isotropic medium can be written in a velocity-stress form, as shown in Equations (1.2). The  $v_x$ ,  $v_y$ ,  $v_z$  are the solid particle velocity. The  $\sigma_{xx}$ ,  $\sigma_{yy}$ ,  $\sigma_{zz}$ ,  $\sigma_{xz}$ ,  $\sigma_{yz}$ ,  $\sigma_{xy}$  are the normal and shear stress components,  $\rho$  is the solid mass density,  $\lambda$  is the first Lamé parameter, and  $\mu$  is the second Lamé parameter or the shear modulus.

$$\begin{split} \frac{\partial v_x}{\partial t} &- \frac{1}{\rho} \frac{\partial \sigma_{xx}}{\partial x} - \frac{1}{\rho} \frac{\partial \sigma_{xy}}{\partial y} - \frac{1}{\rho} \frac{\partial \sigma_{xz}}{\partial z} = 0, \\ \frac{\partial v_y}{\partial t} &- \frac{1}{\rho} \frac{\partial \sigma_{xy}}{\partial x} - \frac{1}{\rho} \frac{\partial \sigma_{yy}}{\partial y} - \frac{1}{\rho} \frac{\partial \sigma_{yz}}{\partial z} = 0, \\ \frac{\partial v_z}{\partial t} &- \frac{1}{\rho} \frac{\partial \sigma_{xz}}{\partial x} - \frac{1}{\rho} \frac{\partial \sigma_{yz}}{\partial y} - \frac{1}{\rho} \frac{\partial \sigma_{zz}}{\partial z} = 0, \\ \frac{\partial \sigma_{xx}}{\partial t} &- (\lambda + 2\mu) \frac{\partial v_x}{\partial x} - \lambda \frac{\partial v_y}{\partial y} - \lambda \frac{\partial v_z}{\partial z} = 0, \\ \frac{\partial \sigma_{yy}}{\partial t} &- \lambda \frac{\partial v_x}{\partial x} - (\lambda + 2\mu) \frac{\partial v_y}{\partial y} - \lambda \frac{\partial v_z}{\partial z} = 0, \\ \frac{\partial \sigma_{zz}}{\partial t} &- \lambda \frac{\partial v_x}{\partial x} - \lambda \frac{\partial v_y}{\partial y} - (\lambda + 2\mu) \frac{\partial v_z}{\partial z} = 0, \\ \frac{\partial \sigma_{xz}}{\partial t} &- \mu \frac{\partial v_x}{\partial z} - \mu \frac{\partial v_z}{\partial x} = 0, \\ \frac{\partial \sigma_{yz}}{\partial t} &- \mu \frac{\partial v_y}{\partial z} - \mu \frac{\partial v_z}{\partial y} = 0, \\ \frac{\partial \sigma_{xy}}{\partial t} &- \mu \frac{\partial v_y}{\partial z} - \mu \frac{\partial v_y}{\partial y} = 0, \\ \frac{\partial \sigma_{xy}}{\partial t} &- \mu \frac{\partial v_y}{\partial z} - \mu \frac{\partial v_y}{\partial y} = 0. \end{split}$$

Structural vibrations could also be modelled using different governing equations other than the linear elasticity equations. These equations are derived for a structure with a cross-sectional dimension that is much larger than its thickness. For this condition, the structure's bending deformation can be modelled by two-dimensional plate theories. These theories assume certain deformation at the thickness dimension of a structure, such as shown in Ref. [22].

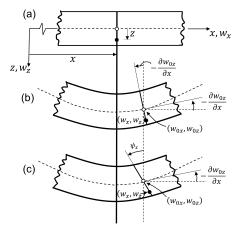


Figure 1.2: Deformation of the plate based on different plate theory adapted from Ref. [22]. (a) initial undeformed condition, (b) plate deformation based on the classical plate theory (CPT), (c) plate deformation based on the first-order shear deformation theory (FSDT).

| General introduction 5

There are two commonly used theories: the classical plate theory (CPT) or known as thin plate theory, and the first-order shear deformation theory (FSDT) or known as thick plate theory. The illustration of the plate deformation based on these theories is presented in Figure 1.2. The CPT is derived based on Kirchhoff-Love assumption [22], [23]. This theory has three assumptions: first, straight lines perpendicular to the mid-surface (i.e., transverse normals) before deformation remain straight after deformation; second, the transverse normals do not experience elongation; third, the transverse normals rotate such that they remain perpendicular to the middle surface after deformation. For an isotropic rectangular plate with thickness h, the CPT governing equation can be written as:

$$I_0 \frac{\partial^2 w_0}{\partial t^2} + D \left( \frac{\partial^4 w_0}{\partial x^4} + 2 \frac{\partial^4 w_0}{\partial x^2 \partial y^2} + \frac{\partial^4 w_0}{\partial y^4} \right) = 0, \tag{1.3}$$

where  $D = Eh^3/12 \left(1 - \nu^2\right)$ ,  $I_0 = \rho h$ ,  $w_0$  is the displacement normal to the plate surface, and  $E, \nu$  are the Young's modulus and Poisson's ratio of the solid media, respectively. The FSDT is derived based on the Mindlin-Reissner assumption. This assumption extends the CPT by relaxing the normality restriction and allowing for arbitrary but constant rotation of transverse normals [22], [24]. The governing equations can be written as:

$$I_{0}\frac{\partial^{2}w_{0}}{\partial t^{2}} + \kappa^{2}\mu h \left[\nabla^{2}w_{0} + \left(\frac{\partial\varphi_{x}}{\partial x} + \frac{\partial\varphi_{y}}{\partial y}\right)\right] = 0, \tag{1.4}$$

$$I_{2}\frac{\partial^{2}\varphi_{y}}{\partial t^{2}} + \frac{D\left(1-\nu\right)}{2}\nabla^{2}\varphi_{y} + \frac{D\left(1+\nu\right)}{2}\left(\frac{\partial^{2}\varphi_{x}}{\partial x\partial y} + \frac{\partial^{2}\varphi_{y}}{\partial y^{2}}\right) - \kappa^{2}\mu h \left(\varphi_{y} + \frac{\partial w_{0}}{\partial y}\right) = 0,$$

$$I_{2}\frac{\partial^{2}\varphi_{x}}{\partial t^{2}} + \frac{D\left(1-\nu\right)}{2}\nabla^{2}\varphi_{x} + \frac{D\left(1+\nu\right)}{2}\left(\frac{\partial^{2}\varphi_{y}}{\partial x\partial y} + \frac{\partial^{2}\varphi_{x}}{\partial x^{2}}\right) - \kappa^{2}\mu h \left(\varphi_{x} + \frac{\partial w_{0}}{\partial x}\right) = 0,$$

where  $\kappa$  is the shear correction factor, rotary inertia  $I_2 = \rho h^3/12$ ,  $\varphi_x$  and  $\varphi_y$  are the bending rotations of a transverse normal about the y- and x-axes, respectively. In this work, to model the structural vibration, the linear elasticity equations are used, and the vibration results based on CPT and FSDT are used as a comparison. Please note that all equations described above are without source terms. Moreover, when a structure has only one dimension which is much longer than the other two, its vibration can be modelled using beam theories. Details on these theories can be found in Ref. [25].

6 1 General introduction

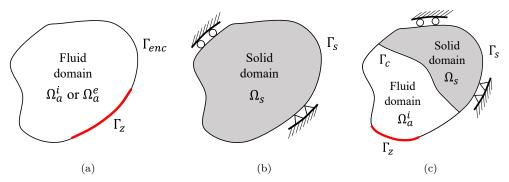


Figure 1.3: Problem domains and boundary conditions for the sound and vibration in the built environment: (a) pure acoustic problem, (b) solid vibration problem, (c) fluid-structure interaction problem.

There are three acoustic research fields concerning sound propagation in the built environment: sound waves in fluid, structural vibrations, and their interaction (fluid-structure interaction). Figures 1.3a - 1.3c show simplified illustration of wave-propagation domains of interest in this thesis. The domains of the figure can be categorized into two fluid (pure acoustic) domains ( $\Omega_a^i$  and  $\Omega_a^e$ ) and one solid domain ( $\Omega_s$ ).  $\Omega_a^i$  and  $\Omega_a^e$  represent the indoor and outdoor acoustic domains, respectively, and  $\Omega_s$  represents structural components of buildings.

In Figure 1.3, the  $\Omega_a^i$  or  $\Omega_a^e$  is bounded by boundaries  $\Gamma_z$ ,  $\Gamma_{enc}$ , and  $\Gamma_c$ ; they denote surface impedance boundary, encompassing boundary, and fluid-structure interaction boundary, respectively. The impedance boundary,  $\Gamma_z$ , is defined as the ratio between the sound pressure and the particle velocity component normal to the  $\Gamma_z$ . The encompassing boundary,  $\Gamma_{enc}$ , could be defined as a hardwall to represent indoor domain  $(\Omega_a^i)$  or an infinite boundary to represent the outdoor domain  $(\Omega_a^e)$ . On surface  $\Gamma_c$ , the sound and structural motion are coupled. The building structure is a solid domain denoted by  $\Omega_s$  and has surface boundary  $\Gamma_s$ . The  $\Gamma_s$  is generally assumed as a specified traction/velocities surface supported by fixed or rotating edges.

There are several types of acoustic problems that can be identified in Figure 1.3. First is the room acoustics problem where the source of sound and the listenere are located in the same room, which happens in  $\Omega_a^i$ . In  $\Omega_a^i$ , the structural motion of the encompassing boundary ( $\Gamma_c$ ) is assumed insignificant and the domain can be modelled by using the governing equation shown in Equation (1.1), while boundary conditions (BCs) are described using acoustic impedance values.  $\Omega_a^e$  is the outdoor acoustic domain.  $\Omega_a^e$  is similar to  $\Omega_a^i$  apart from that it is not fully enclosed and wind and temperature effects may play a significant role in sound propagation. An example of the outdoor acoustic domain is shown in Figure 1.4, where a sound wave is seen propagating over a sequence of building canyons.

1 General introduction 7

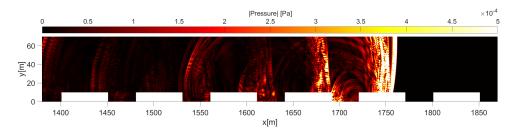


Figure 1.4: Spatial distribution of absolute sound pressure at certain time over building canyons taken from an example case in Chapter 3.

The second type of problem is that of the structural vibration system, where the solid media is excited by a force, and the vibration response of the solid media is of interest. This problem occurs in  $\Omega_s$  when the interaction with air is not of interest, and the effect of air on the vibration is considered negligible. The third type is the vibroacoustic problem in the form of sound radiation and transmission. The vibration occurs when force excites the solid domain  $\Omega_s$  and interacts with the air domain  $\Omega_a^i$  to radiate sound. An example of this problem is exhibited in Figure 1.5, where the absolute sound pressure distribution in a room due to impact excitation is shown. Moreover, another vibroacoustic problem is the sound transmission between two spaces (from  $\Omega_a^i$  to  $\Omega_a^i$  or  $\Omega_a^i$  to  $\Omega_a^e$ , or vice versa) through solid structures.

To solve all of these acoustical problems, methods for modelling and predicting the sound and vibration fields are needed. This thesis gives overviews of these methods in the following sections, with more emphasis on the building acoustics applications.

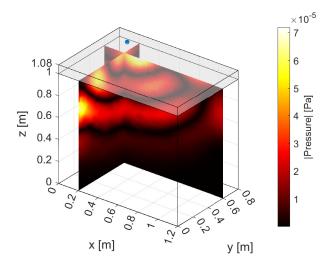


Figure 1.5: Spatial distribution of absolute sound pressure at certain time taken from impact sound radiation case in Chapter 6. Blue dot denotes the impact excitation position and grey cuboid denotes a concrete slab.

General introduction

#### 1.3 Modelling and prediction for room acoustics

This section discusses briefly the methods used to model sound propagation for room acoustics applications. Generally, the main objective of room acoustic simulations is to provide time-energy or impulse responses that can be used to calculate various field descriptors such as reverberation time and speech transmission index. With these descriptors, interior spaces can be designed to have good acoustic quality and support different activities (e.g. speech, rest, learning).

There are three methods commonly used to model interior sound propagation: geometrical acoustics (GA) method, energy-based method, and wave-based method. Each of these methods have been described in detail in the literature. Some basic concepts, implementations, and applications of these methods are reviewed in Refs. [26]-[28] for geometrical and wave-based methods, while energy-based methods are described, for example, in Refs. [29]-[31]. In the GA methods, a sound wave is assumed to propagate like a ray and various wave properties are neglected [27]. Two primary methods of the GA methods are the ray tracing and the image sources method. The ray tracing method describes sound energy propagation as a stochastic process of particle radiation and detection, while the image source method uses geometrically constructed sound sources that correspond to specular paths of sound rays |26|. This assumption is valid at high frequencies, where the wavelength of sound is short compared to surface dimensions and the overall dimensions of the interior space. However, the GA methods fail for small and medium-sized rooms and for studies with distinct wave effects, such as wave diffraction or interference. In practice, the GA techniques are widely used to calculate room acoustic parameters in the mid-and high-frequency ranges [32], [33].

Another approach to model sound propagation in the air is the energy-based method. One method example of this method is the diffusion equation method [29]–[31]. This method assumes the propagation of sound energy as air particle movement in gas with diffusive boundaries or objects. In this method, the flow of sound energy follows a diffusion gradient equation, which means that an energy gradient produces a mean motion of sound particles from high to lower density volume. The main advantage of this method is the accurate prediction of the late part of sound energy decay. The main limitation of this method is the inability to predict the specular reflections or sound diffraction. The diffusion equation is a generalisation of the famous classical diffuse sound-field theory such as the Sabine's or Eyring's equations [34]. In classical diffuse sound field theory, sound energy is assumed to be uniform throughout the space. This causes the gradient term in the diffusion equation to be zero. If applied to model the sound energy decay in a room under these conditions, the diffusion equation solution will be the same as the Sabine's or Eyring's equations.

In contrast with previous methods, wave-based methods solve the governing equations as shown in Section 1.2. Examples of wave-based methods are the finite element method (FEM), the boundary element method (BEM), and the finite difference time domain (FDTD) method. The main advantage of wave-based methods is that they can model sound propagation accurately because all wave properties are present in-

| General introduction 9

trinsically. This method can be accurate if all simulation aspects, such as source directivity, impedance BCs, and detailed geometry are also defined precisely. The main disadvantage of these methods is that the required computational effort increases rapidly with the simulated sound frequency. They are suitable for low frequencies as solving high frequencies requires high computational effort. Among these methods, time-domain approaches for modelling wave problems have attracted considerable attention in the last decades as they are preferred over frequency-domain methods for auralisation purposes. The main time-domain wave-based numerical methods used for room acoustic problems are FDTD [35] [36] [37] [38], FEM [39], finite volume method (FVM) [40], and Fourier spectral methods such as adaptive rectangular decomposition (ARD) [41] and pseudospectral time-domain (PSTD) method [42] [43] [44].

More detailed reviews of modelling and prediction methods for room acoustics applications can be found in Ph.D. dissertations by Wang [45] and Pagán Muñoz [46]. These references also focus on the wave-based methods developed in this work using the time-domain DG method. In the next section, a more detailed review on modelling and prediction methods for building acoustics applications is given.

## 1.4 Modelling and prediction for building acoustics

When sound is generated in a room, it can be transmitted to another room via different paths such as walls, floors, and façades. Likewise, if vibration is excited by sources (such as footsteps or household appliances), it can be radiated into rooms via these paths. The insulation of the transmitted or radiated sound energy in a room is termed as airborne or impact sound insulation. The noise generated from impact excitation on the floor or stairs in a building is characterised by the impact sound pressure level. This level is measured by using a standardised tapping machine according to measurement standards ISO 16283-2 in buildings [47] or ISO 10140-3 in the laboratory [48]. On the other hand, the sound transmission loss (TL) or sound reduction index is used to quantify the airborne sound insulation, as defined in Equation (1.5).

$$TL = -10 \log_{10}(\tau) = -10 \log_{10}\left(\frac{W_t}{W_s}\right).$$
 (1.5)

 $\tau$  is the sound transmission coefficient,  $W_t$  is the transmitted sound power to the receiver room, and  $W_s$  is the incident sound power on the room's partition in the source room. It should be noted that the total sound transmission between two rooms is divided into separate transmission paths (direct and flanking paths), with each path starting with an excited structure by sound pressure in the source room and ending with a radiating structure in the receiving room [49]. In this section, the modelling and prediction of airborne insulation is reviewed.

There are many different aspects that influence the airborne sound insulation of a

building element such as geometrical details (room sizes, wall dimensions, thickness of structure, position of the sound source/receiver), mechanical properties (densities, stiffnesses of materials, damping), or acoustic parameters (surface impedance, structural BC). To design a building component such as partition wall, façade, or floor, the sound transmission prediction models that can take into account the previously mentioned factors are needed. Many approaches of theoretical or semi-empirical models have been investigated to predict the sound transmission loss of a component [50], [51]. Some of these prediction models are described below.

There are several analytical models that can be used to predict the direct sound transmission loss of a single panel construction. These analytical models generally assumed that the bending wave is the considered wave type on the panel. One of the models is the mass law and it has been used under the assumption that the panel has infinite dimensions and is excited by a plane wave [51]. In the mass law model, the sound transmission loss increases by 6 dB per doubling the frequency or doubling the mass per unit area. This model depends only on the mass surface density of the plate and not on its stiffness. Cremer [52] extended the mass law by including the coincidence condition in the sound transmission loss prediction. The coincidence condition occurs when the projection of the wavelength in air onto the surface of the plate equals to the bending wavelength [50]. This condition leads to an almost undamped transmission of the sound energy. With grazing angle of incidence, this coincidence occurs at the critical frequency of the plate. Cremer studied the role of panel stiffness in estimating sound transmission loss using the coincidence condition. Furthermore, London [53] developed the prediction of the transmission loss for a random incidence excitation field. The average transmission loss for a diffuse incident sound field was discovered by integrating the transmission coefficient over the angles of incidence. In his work, London also included the panel dissipation/attenuation term for the prediction of sound transmission loss.

The previously mentioned models assume infinite dimensions for the panels. However, real constructions have components with finite dimensions. Sewell [54] developed a sound transmission loss model for the finite panel with the panel vibration following the thin plate theory. Sewell used a modal expansion to describe panel vibrations and travelling waves to describe sound propagation in semi-infinite air. Sewell showed that the resonance of the panels played an important role in the prediction of sound transmission loss. These developments provided a more accurate theory of the sound insulation of individual panels.

Multi-panel systems are commonly utilised to boost the sound insulation of a construction component. Sound insulation prediction models are needed for such systems. Some examples of predictions for infinite double panels without structural connections or studs were proposed by Beranek and Work [55], and by London [56], and double panel systems connected by points or line studs were proposed by Davy [57]. Since the 1960s, many prediction models have been proposed for different configurations of double panel systems. A survey of models of the double infinite panel systems (excluding numerical models) was made by Hongisto [58]. Hongisto tested seventeen different models using measurement results for different categories of double

1 General introduction 11

walls. The result was that the average prediction errors of each 1/3 octave frequency band were up to 20 dB for most models, while they were less than 10 dB for the best models. None of the models were sufficiently accurate to predict the sound insulation of double walls.

As the construction of walls or floors becomes more complex, it is difficult to formulate accurate analytical models to predict sound insulation. Ideally, a method that predicts sound insulation over a broad frequency range is preferred. For example the frequency range in sound insulation measurement is between 50 - 5000 Hz. However, the computing power might be too high for the high-frequency region or for an acoustically large domain (for example by using FEM). Some methods can predict sound insulation suitably depending on the frequency range of interest, i.e., high, mid, and low-frequency methods. In building acoustics applications, the low-frequency range is usually defined at: 50 - 200 1/3 octave band Hz, mid-frequency: 250 - 1000 1/3 octave band Hz, and high-frequency range: 1250 - 5000 1/3 octave band Hz [50].

In the high-frequency range, the characteristic length of the room or building component is much greater than the wavelength of the sound. In this condition, the modal density<sup>1</sup> and modal overlap<sup>2</sup> is high, and the system is very sensitive to small variations in material properties, geometrical details, and BCs [50]. Since the number of modal frequencies and the modal overlap are high, the analysis of the system can be conducted using a statistical approach. This approach is the statistical energy analysis (SEA) [60], [61]. SEA is a framework for calculating the flow and storage of dynamic energy in a complex system. Building components are defined as interconnected subsystems in this framework. Each subsystem is made up of a set of modal energies that are related to one another, such as bending vibration, torsional vibration, or acoustic energy. This energy can be dissipated via system dampening or redistributed across subsystems. The response of each subsystem to the energy input is determined in frequency bands. The SEA relies on power balance equations that can be solved by linear algebra. The energy in each subsystem is based on parameters such as modal density, damping, and coupling loss factor. The drawbacks of this method are the random excitation assumption (this is defined as unity magnitude, random phase, multi-point excitation over the entire subsystem), an equal spatial energy distribution in each subsystem, and also it holds for subsystems with homogenous material properties. Further details on this method can be found in the Refs. [50], [62].

In the low-frequency range, the characteristic length of the room is much smaller (or of the same order) than the sound wavelength. In this range, the sound field is determined by well-separated modes and can be predicted by wave-based numerical methods such as the FEM, the finite difference method, and the FVM. In these methods, the spatial domain is discretised. Afterwards, the solution of the PDE that govern the sound propagation and vibration are approximated. These methods are explored in more detail in Section 1.5.

<sup>&</sup>lt;sup>1</sup>average number of modal natural frequencies per unit frequency [59]

<sup>&</sup>lt;sup>2</sup>average number of modal resonance frequencies lying within the half-power bandwidth of the average mode [59].

In the mid-frequency range, no specific method is generally used to evaluate sound and vibration fields. However, several approaches are commonly utilised to cover this frequency range [63]. The first is to extend the frequency range of the wave-based numerical methods. In this range, the linear system equations are large, and the optimised iterative solver can be used instead of the direct method to solve the system of equations especially for frequency domain FEM/BEM [64]. Moreover, parallel computing can be adopted to accelerate the calculations. The second approach is to extend the SEA towards the lower frequency region. For example, application of SEA method for low modal density systems with low modal overlap (such as in concrete/masonry walls or floors the in low-frequency range) [65], or to relax the assumptions imposed by SEA so that the modal energies in subsystems need not be similar [66]. A recent review of the extension of the SEA method can be found in Ref. [67]. Another approach is a hybrid between a wave-based numerical method and the SEA method. In this approach, the wave-based numerical method is used for the deterministic subsystem in the mid-frequency range, and the SEA method is used for the subsystem that is very sensitive to the local variation of the system (such as material properties and geometrical details). A reciprocity relation gives the coupling between the two methods [68]-[70]. There are some other approaches on the mid-frequency region. More rigorous review on these approaches for general acoustic and vibration applications can be found in Ref. [71].

### 1.5 Wave-based numerical method for building acoustics

Using a wave-based numerical technique, this thesis offers a system for solving the propagation of sound and vibration in structures. Finally, the primary objective is to forecast sound transmission through building components. Since the target frequency is low to mid frequency, the wave-based numerical method is used. The wave-based numerical methods solve Equations (1.1)-(1.2) that determine the sound and vibration fields in buildings and their interaction. In the following subsections, an overview of different wave-based numerical methods is given, especially concerning their application in building acoustics problems if available.

#### 1.5.1 Finite element method

The finite element method (FEM) is one of the most versatile methods for solving PDEs. FEM discretizes the domain into smaller regions or finite elements. In each element, the unknown variables are approximated by known functions. These functions are usually polynomials, which may be linear or higher-order expansions of functions. Then the PDEs are integrated as in the weighted residuals method, and the residuals are summed over the entire problem domain, which is enforced to be zero. This technique yields a set of finite linear equations with regard to the unknown variables at the element nodes. Because the nodes are shared on the faces of neighbouring elements, the discretised system is linked between the elements, resulting in a substantial sparse linear system that may be solved using linear algebra techniques.

l General introduction 13

Several researchers applied FEM to room and building acoustics. For example, Panneton and Atalla [72] used FEM to solve the sound transmission problem of finite multilayer systems containing a combination of plates, air, and poroelastic materials in frequency domain. The approach was based on a three-dimensional geometry with a semi-infinite medium on the receiver and source sides. The FEM was coupled with BEM to account for fluid-structure coupling, where the BEM was used to model sound radiation in the fluid. In addition, Sgard et al. [73] used the same approach and extended the feature for a diffuse field excitation on the plate. Maluski and Gibbs [74] investigated sound transmission between two rooms at low frequencies using FEM for unequal rooms volume and asymmetric configurations. The walls consisted of brick and mortar layers and were modelled as a finite thin plate with various BCs. A good agreement was found between measured and predicted values in the 1:4 scale and full-size rooms. Another example comes from Davidsson et al. [75], who studied the sound transmission loss of double panels (with studs) in the low-frequency range using FEM. In the study, the structure of the double panels was modelled as thin plates. Furthermore, Arjunan et al. [76] solved the same problem using FEM, modelling the walls as a three-dimensional solid structure instead of thin plates. The coupling elements between fluid and solid were introduced, and the simulation results were validated using standard experiments in a broader frequency range (100 - 3150 Hz). The two-dimensional plane strain elasticity approach was also used to model the sound insulation of a multilayer lightweight concrete hollow block wall and a double wall with steel columns in a two-dimensional geometry. The model was solved using FEM [77]-[79] and the spectral element method (high order variant of FEM) [80]. The approach was used to reduce the computational cost and extend the frequency range up to 5 kHz. However, the two-dimensional approach was inaccurate compared to the measured results.

All of the previously mentioned FEM techniques are based on the frequency-domain formulation of the governing equations. To the author's knowledge, FEM in the time domain is rarely used for vibration or vibroacoustic applications. However, FEM in the time domain has been used for room-acoustic applications, such as presented in Refs. [81]–[84].

#### 1.5.2 Finite difference time-domain method

One of the most popular wave-based methods is the finite difference time domain (FDTD) method [85]. The term FDTD was coined by Taflove in the computational electromagnetics community for the solution of Maxwell's equations in the 1980s [86]. The FDTD method solves a PDE by discretising the spatial domain and the time interval into discrete points. At each point, the partial derivative is approximated by finite differences, for example, by Taylor expansion series from the values of the neighbouring points. With this technique, the differential equations are transformed into a linear system of equations that can be solved with matrix algebraic techniques. Due to its relative ease of implementation and robustness for a wide range of wave problems, FDTD is widely used in many engineering applications, including room acoustic, structural vibration and building acoustic applications.

For room acoustic applications, there are many examples, such as the work of Botteldooren [35], Sakamoto [87], Sakamoto et al. [88], and Sakamoto et al. [89]. The FDTD method has also been adapted to solve many structural vibration problems. For example, the vibration of framed structures using the beam theory [90], the vibration of plate structures [91], the vibration of beam-plate structures [92], and the vibration of heterogeneous solid orthotropic three-dimensional structures [93].

In addition, the FDTD method has also been used for vibroacoustic applications, especially for sound transmission problems. The method solves the coupling between linear acoustic equations and the various vibration models. The earliest work was conducted by Toyoda and Takahashi, who solved linear elasticity equations with two damping terms using the FDTD method for impact sound transmission in two-storey concrete buildings [94]. In their paper, sound propagation in air and vibration of concrete building were modelled using the same equations. These equations were used regardless of the medium so that no additional interface element is required for the sound and vibration interaction. However, this leads to high computational costs. To reduce this cost, the coupling between linear acoustic equations and the plates equations (based on CPT and FSDT) has been used in the FDTD method. The coupling with the thin plate equations was undertaken to solve the transmission problem of glass panels by Asakura et al. [95], and for transmission problem of plasterboard walls by Asakura and Sakamoto [96]. The coupling with the thick plate equations was carried out for several concrete elements in Ref. [97]. Moreover, Asakura developed the sound radiation of a double slab floor structure [98], impact sound auralisation of floor [99], and Asakura et al. developed FDTD for the building facade transmission problem [100]. Another work by Ferreira and Hopkins developed a scaling approach for the FDTD method to solve the linear elasticity equations with three damping terms to reduce computation times [101]. The scaling approach is conducted by modifying the geometry and physical properties of the structure that preserve the dynamic characteristics of the model, whilst allowing a much larger time step and it could reduce the computation times. Although the FDTD method is flexible enough to adapt to different PDEs, it lacks geometric flexibility due to its structured mesh. If the Cartesian grid is used, curved geometries have to be approximated with a staircase approximation, which would lead to artificial scattering on a smooth surface.

#### 1.5.3 Pseudospectral time-domain method

Another wave-based method used for wave propagation is the pseudospectral time-domain method (PSTD). The PSTD method approximates the solution of the PDE using trigonometric or Chebyshev polynomials [102]–[104]. In the PSTD method, the computational domain is discretised by grid points. In contrast to the FDTD method, where the spatial partial derivative is approximated using the neighbouring values, it is approximated by the derivatives of the expansion polynomials, which cover the entire spatial domain. Once the spatial derivatives have been obtained, various methods such as the Runge-Kutta method or the finite difference method can be used to perform the integration of the temporal derivative.

l | General introduction 15

The PSTD method has spectral accuracy, which means that the numerical dispersion error decreases exponentially with the grid density when applied to a single region with a smooth inner medium. Depending on the expansion polynomials, the PSTD method is mainly divided into the Fourier (trigonometric) or the Chebyshev PSTD method. In the Fourier PSTD method, the forward and inverse spatial discrete Fourier transform are used to evaluate the partial spatial derivatives. One advantage of the Fourier transform is that it has no dispersion error since the Fourier transforms used to describe the spatial derivatives or integrals are exact. In addition, the Fourier PSTD method requires only two cells per wavelength, which is given by the Nyquist sampling theorem [103]. For this reason, the PSTD method is one of the most computationally efficient methods for wave propagation. However, like the FDTD methods, it lacks geometric flexibility due to its structured point grid. Furthermore, due to the discrete Fourier transform, periodicity is assumed in the spatial dimensions. This periodicity is a disadvantage of the PSTD method, as it hardly occurs in reality.

In the field of room acoustics, the PSTD method has been used for many problems [43], [44], [105]–[107]. The PSTD method has been applied to outdoor sound propagation around screens and urban canyons with moving atmosphere by Hornikx et al. [108], and also to evaluate noise mitigation measures for road traffic noise propagation to the roadside yard by Hornikx and Forssén [109]. In addition, the latest improvement of the hybrid method of PSTD and discontinuous Galerkin method was carried out [110]. To the author's knowledge, PSTD has not been used for vibration or vibroacoustic modelling.

#### 1.5.4 Nodal discontinuous Galerkin method

Another wave-based numerical method is the discontinuous Galerkin (DG) method. This approach offers characteristics that make it a potential method for solving an acoustically large domain or for vibroacoustic prediction in the low and mid-frequency regions. Like the FEM, the DG method discretises the spatial domain into several elements. This method allows an unstructured discretisation for domains with complex geometry. In each element, the DG method approximates the unknown variables using interpolation polynomials that are discontinuous at the interface with the neighbouring elements. At this interface, the approximated solution is duplicated to ensure the locality of the scheme. Afterwards, the weighted residual formulation can be performed using Galerkin methods.

To ensure the global solution's uniqueness and connect each local solution to its neighbours, numerical fluxes are introduced as in the FVM. The calculation of numerical fluxes is the only operation that is not local in the DG method. This element-wise formulation allows for a relatively simple parallelisation computation that can accelerate the DG calculation [111]. The structure of the DG method is very similar to that of the FEM. It allows local refinement by increasing the polynomial order or the number of elements. However, unlike FEM, the mass or stiffness matrices are local and, thus, can be inverted at a minimal cost. However, this comes at a price, mainly by increasing the degrees of freedom (DoF) due to decoupling the elements. The details of the method can be found in the literature written by Hesthaven and

Warburton [112].

The DG method was originally published by Reed and Hill in 1973 [113]. The DG method has been applied in various fields of physics and engineering. For example, it was used by Hesthaven and Warburton for electromagnetic problems [114]–[116]. In the geophysics field, the DG method has been used in several papers by Käser and Dumbser [117], [118], Käser et al. [119], De La Puente [120], and Dumbser et al. [121]. In the field of room acoustics, the DG method has been used in several publications by Wang et al. [122], Wang and Hornikx [123] and Wang et al. [124].

#### 1.5.5 Other methods

Several other wave-based numerical methods have been applied to vibroacoustic applications, such as the FVM and the BEM. The FVM is derived based on the integral form of the conservation law [21]. In the FVM, the problem domain is discretised into several cells. The PDE is then integrated within each cell. The volume integrals in a PDE containing a divergence term are converted into surface integrals using the divergence theorem. The advantage of this method over the finite difference method is that it allows an unstructured discretisation of the problem domain. This method has been applied for room acoustics in Refs. [125], [126], and vibroacoustic application in Ref. [127]. The disadvantage of FVM is that it requires a large number of elements to achieve the same accuracy as FEM. The BEM is a wave-based numerical method that solves the PDE with a boundary discretisation, which is different from other methods that use spatial discretisation. The method uses the boundary integral formulation of the PDE and requires fewer elements and nodes, significantly reducing the number of DoFs of the problems. It is a powerful method for sound radiation and scattering in the free field. The BEM typically produces a linear system with a dense matrix that must be solved. This matrix causes a large number of operations and memory requirements, making it difficult to apply BEM to large problems [128]. However, the development of the fast multiple method has been employed to accelerate the solution of a BEM system of equations [129], [130]. The BEM also has been applied for the plate vibration problems and linear elasticity equations such as shown in Ref. [131]. The details of this method and its application to various acoustic and vibration problems can be found in the Refs. [128], [131], [132].

#### 1.6 Motivation of selected modelling approaches

According to the literature review above, there is a lack of a wave-based method to solve any building acoustic problem in the time domain for low and mid frequencies. In this research, the nodal DG method is proposed to solve vibroacoustic problems in the field of building acoustics, ranging from low-frequency to the mid-frequency range. To the authors' best knowledge, no reference is found in the scientific literature about the application of the nodal DG method to building acoustics problems. The aim of this work is to extend its application. There are several main reasons for the interest in the nodal DG method for solving the propagation of sound and structural vibrations:

1 General introduction 17

1. Nodal DG method discretises the problem domain by using structured/unstructured mesh elements of various element shapes. This feature allows geometric flexibility in representing a complex domain.

- 2. Nodal DG method uses simple linear algebra techniques to solve the system of linear equations.
- The element-wise formulation allows straightforward implementation of parallel computation, thereby, having a high potential to get accelerated on modern computer architectures.
- 4. The method offers flexible ways to achieve high accuracy by increasing the number of elements or applying for a higher polynomial order within the elements.
- 5. The method naturally handles impulsive wave behaviour. As a time-domain solver, the nodal DG method can directly calculate broadband temporal waveforms or the sinusoidal steady-state response at any frequency within the excitation spectrum.

#### 1.7 Research objectives and contributions

This research contributes to creating a built environment with high acoustic quality by developing an efficient computational method for sound propagation, structural vibration, and vibroacoustic applications. This work is divided into three main parts with the following objectives, and for all three objectives the time-domain solutions are targeted.

- 1. Development of the nodal DG method to solve the governing equations for room acoustics. This methodology is important because indoor sound propagation, as part of the sound insulation problem, has different governing equations than the vibration in the solid part. Additionally, the application of the method to outdoor sound propagation is given as a special application.
- 2. Development of the nodal DG method to solve structural vibration problems in building elements. This methodology is important because sound can be generated or transmitted by the vibration of the structure. In this part, the nodal DG method is targeted to the vibration of isotropic structures.
- 3. Development of the DG method to solve vibroacoustic problems in buildings. This method is required because the interaction of sound and vibration manifests through the sound radiation and sound transmission in buildings. This part should combine the previous two methodologies for solving various building acoustics applications.

The research contributions are listed below:

 An important feature that has not yet been developed with the nodal DG method is the vibration of structures. In this research, computational aspects of predicting vibration in isotropic structures has been developed, including force excitation, a constant viscous damping approach, and vibration with piece-constant material properties.

- Another important feature not yet developed in the nodal DG method is modelling sound transmission and impact sound radiation. In this research paper, the impact sound radiation of a single slab structure and the problem of sound transmission through a wall are addressed with direct and flanking contributions.
- A joint contribution to this work is the implementation of the nodal DG method
  for room acoustic application, which according to the authors' best knowledge
  was not shown before. This work deals with the error analysis and the implementation of the frequency independent impedance BCs.
- Another joint contribution to this work is the application of the nodal DG method for outdoor sound propagation. In this paper, the application of the nodal DG method for sound propagation in an airport environment is presented. The wind conditions are given by the effective sound velocity approach. This approach could also be applied to the insulation of building facades in the future.

#### 1.8 Thesis structure and related publications

This thesis consists of three main parts. The first part is devoted to the development of the nodal DG method for indoor and outdoor sound propagation. The second part develops the nodal DG method for structural vibrations, and the third part deals with the problems of sound-vibration interaction. In addition, this thesis contains two general chapters: Chapter 1 gives an introduction to the thesis, and Chapter 7 summarises the research results and gives suggestions for further work.

The first part is divided into two chapters. Chapter 2 demonstrates the application of DG to room acoustics in a static medium (no wind flow). An example of sound propagation in a room under laboratory conditions is simulated and compared with measurements. Chapter 3 applies the nodal DG method to outdoor sound propagation in a moving atmosphere (under wind flow conditions) under the effective sound speed approach. As an example, several scenarios of noise mitigation in the airport environment are simulated using the nodal DG method. These chapters are primarily based on work presented in the following journal articles:

- H. Wang, I. Sihar, R. Pagán Muñoz, and M. Hornikx. (2019). Room acoustics modelling in the time-domain with the nodal discontinuous Galerkin method. The Journal of the Acoustical Society of America, 145(4), 2650–2663.
  - H. Wang: conceptualization, methodology, software, validation, visualization, formal analysis, writing (whole paper except for Section I, IV.D and IV.C). **I. Sihar**: software, validation, writing (Section IV.C). R. Pagán Muñoz: software,

1 General introduction 19

validation, investigation, writing (Section I and IV.D). M. Hornikx: supervision, writing-reviewing and editing.

- I. Sihar, R. Pagán Muñoz, C.F. Fernandez, J. Yang, and M. Hornikx. Numerical modelling of noise intervention scenarios in an airport environment. *Manuscript in preparation for submission*.
  - I. Sihar: conceptualization, methodology, software, validation, visualisation, formal analysis, writing. R. Pagán Muñoz: conceptualization, software, investigation, visualisation, writing original draft. C.F. Fernandez: methodology, software, writing original draft. J. Yang: supervision, writing-reviewing, and editing. M. Hornikx: supervision, writing-reviewing and editing.

The second part consists of two chapters. Chapter 4 presents the application of the nodal DG method to the vibrations of monolithic structures. These structures include an L-shaped structure and plates with different BCs and thicknesses. Moreover, the results of the nodal DG method are compared with analytical solutions. Chapter 5 demonstrates the application of the nodal DG method to the vibrations of complex structures with piecewise constant material properties. A T-shaped structure and a scaled lightweight wooden floor are used as examples. In this chapter, the numerical results are compared with experimental results of the actual structures. These chapters are based on work contained in the following journals/conference papers:

- I. Sihar, M. Hornikx, and Pranowo. (2017). Time-domain structural vibration simulations by solving the linear elasticity equations with the discontinuous Galerkin method. Proceedings of the 24th International Congress on Sound & Vibration (ICSV-24), 23-27 July 2017, London, United Kingdom.
  - **I. Sihar**: conceptualization, methodology, software, validation, visualisation, formal analysis, writing. M. Hornikx: supervision, writing-reviewing and editing. Pranowo: methodology.
- I. Sihar and M. Hornikx. (2019). Implementation of the nodal discontinuous Galerkin method for the plate vibration problem using linear elasticity equations. Acta Acustica united with Acustica, 105(4), 668-681.
  - **I. Sihar**: conceptualization, methodology, software, validation, visualisation, formal analysis, writing. M. Hornikx: supervision, writing-reviewing and editing.
- I. Sihar, J. Yang, and M. Hornikx. (2021) Numerical modelling of structural vibration with piece-wise constant material properties using the nodal discontinuous Galerkin method. In Proceedings of Euronoise 2021.
  - I. Sihar: conceptualization, methodology, software, validation, visualisation, formal analysis, writing. J. Yang: supervision, writing-reviewing and editing. M. Hornikx: supervision, writing-reviewing and editing.
- I. Sihar, J. Yang, and M. Hornikx. Application of the time-domain nodal dis-

continuous Galerkin method for low-frequency structural vibrations with piecewise constant material properties. *Manuscript in preparation for submission*.

I. Sihar: conceptualization, methodology, software, validation, visualisation, formal analysis, writing. J. Yang: supervision, writing-reviewing and editing. M. Hornikx: supervision, writing-reviewing and editing.

The last part consists of a single chapter: Chapter 6 presents the nodal DG method for impact sound radiation and sound transmission through a wall with different shapes. The different shapes are intended to create direct and flanking transmission. This chapter presents the coupling between the equations of linear elasticity and linear acoustics via numerical fluxes. The numerical results are then compared with analytical and FEM solutions. This chapter is based on the work in the given journal/conference paper:

- I. Sihar, J. Yang, and M. Hornikx. Implementation of nodal discontinuous Galerkin method for vibro-acoustic problems to predict sound radiation and transmission in buildings. *Manuscript in preparation for submission*.
  - I. Sihar: conceptualization, methodology, software, validation, visualisation, formal analysis, writing. J. Yang: supervision, writing-reviewing and editing. M. Hornikx: supervision, writing-reviewing and editing.

#### Part I

# Developments of time-domain DG method for simulation of indoor and outdoor sound propagation

# 2 | Discontinuous Galerkin method for room acoustics applications

This chapter is based on the journal paper:

• H. Wang, I. Sihar, R. Pagán Muñoz, & M. Hornikx. (2019). Room acoustics modelling in the time-domain with the nodal discontinuous Galerkin method. The Journal of the Acoustical Society of America, 145(4), 2650–2663.

The contributions of the author of this thesis to this research are indicated in Section 1.7.

#### Abstract

In this chapter, the performance of the time-domain nodal discontinuous Galerkin (DG) method is evaluated when solving the linear acoustic equations for room acoustic purposes. A nodal DG method is used for the evaluation of the spatial derivatives, and for the time-integration an explicit multi-stage Runge-Kutta method is adopted. The scheme supports a high order approximation on unstructured meshes. To model frequency-independent real-valued impedance boundary conditions, a formulation based on the plane wave reflection coefficient is proposed. Semi-discrete stability of the scheme is analysed using an energy method. The performance of the DG method is evaluated for four three-dimensional configurations. The first two cases concern sound propagation in free field and over a flat impedance ground surface. Results show that the solution converges with increasing DG polynomial order and the accuracy of the impedance boundary condition is independent on the incidence angle. The third configuration is a cuboid room with rigid boundaries, for which an analytical solution serves as the reference solution. Finally, DG results for a real room scenario are compared with experimental results and the comparison is quite satisfactory.

#### 2.1 Introduction

Computer simulation of the sound field in indoor environments has been investigated during the period since the publication by Schroeder [133]. After all these years,

prediction methods for room acoustic applications are still under development in an effort to improve efficiency of the calculations and accuracy and realism of the results, hand in hand with the advances in computer power. In acoustics, the computational techniques are mainly separated between wave-based, geometrical and diffuse field methods. Each of these methodologies has been amply presented in literature. Concepts, implementations and applications of room simulation methods are reviewed by Vorländer [26], Savioja and Svensson [27], and Hamilton [28] for geometrical and wave-based methods, while diffuse field methods are described for instance by Valeau et al. [30] or Navarro et al. [31].

In contrast with the high-frequency simplifications assumed in the geometrical and diffuse field methods, wave-based methodologies solve the governing physical equations, implicitly including all wave effects such as diffraction and interference. Among these methods, time domain approaches to model wave problems have attracted significant attention in the last decades, since they are favoured for auralisation purposes over frequency domain methods. The main wave-based time domain numerical techniques employed in room acoustics problems are finite difference time-domain (FDTD) [35] [36] [37] [38], finite element method (FEM) [39] and finite volume method (FVM) [40], and Fourier spectral methods such as the adaptive rectangular decomposition method [41] and pseudospectral time domain methods (PSTD) [42] [43] [44].

In the last few years, the time-domain DG method [134] is another approach gaining importance, mainly in the aero-acoustic community [135] [136] [137]. The DG method discretises the spatial domain into non-overlapping mesh elements, in which the governing equations are solved elementwise, and uses the so-called numerical flux at adjacent elements interfaces to communicate the information between them. The DG method combines the favourable properties of existing wave-based time domain methods for room acoustics as it preserves high order accuracy, allows for local refinement by a variable polynomial order and element size, and therefore can deal with complex geometries. Also because equations are solved elementwise, it allows for easy parallelisation and massive calculation acceleration opportunities [111], like other methods as FDTD and FVM. DG method can be seen as an extension to FVM by using a polynomial basis for evaluating the spatial derivatives, leading to a higher order method. Also, DG method can be seen as an extended FEM version by decoupling the elements without imposing continuity of the variables, thereby creating local matrices. Therefore, DG method is a very suitable numerical method for acoustic propagation problems including, definitely, room acoustics. However, some developments towards room acoustic applications are still missing: although results for impedance boundary conditions (BCs) with the DG method have been presented [138], a proper formulation of these BCs in the framework of DG has not been published. In contrast, frequency-dependent impedance conditions have been extensively developed in other methodologies (FDTD, FVM) [40]. In the present work, a frequency-independent real-valued impedance BC formulation, based on the plane wave reflection coefficient is proposed, following the idea firstly presented by Fung and Ju [139].

To the authors' best knowledge, no reference is found in scientific literature about the application of DG method to room acoustics problems. The aim of this work is to address the positioning of DG method as a wave-based method for room acoustics. The accuracy of the method for this type of applications is quantified and the developments needed to arrive at a fully-fledged DG method for room acoustics are summarised as future work.

The chapter is organised as follows. In Section 2.2, the governing acoustic equations are introduced as well as the solution by the time-domain nodal DG method. The formulations of impedance BCs and its semi-discrete stability analysis are presented in Section 2.3, and are in this work restricted to locally reacting frequency independent conditions. Section 2.4 quantifies and discusses the accuracy of the implemented nodal DG method for sound propagation in several scenarios: 1) Free field propagation in a periodic domain; 2) A single reflective plane; 3) A cuboid room with acoustically rigid boundaries; 4) A real room. Finally, conclusions and outlook can be found in Section 2.5.

## 2.2 Linear acoustic equations and nodal DG method

#### 2.2.1 Linear acoustic equations

Acoustic wave propagation is governed by the linear acoustic equations, which are derived from the general conservation laws [140]. For room acoustics applications, it can be assumed that sound propagation in air that is completely at rest and constant in temperature. Under these assumptions, the homogeneous linear acoustic equations are:

$$\frac{\partial \mathbf{v}}{\partial t} + \frac{1}{\rho_0} \nabla p = \mathbf{0},$$

$$\frac{\partial p}{\partial t} + \rho_0 c_0^2 \nabla \cdot \mathbf{v} = 0,$$
(2.1)

where  $\mathbf{v} = [u, v, w]^T$  is the particle velocity vector, p is the sound pressure,  $\rho_0$  is the constant density of air and  $c_0$  is the constant adiabatic sound speed. The linear acoustic equations can be combined into one equation: the wave equation. Equations (2.1), completed with initial values or a force formulation at the right side, as well as a formulation of BCs at all room boundaries, complete the problem definition. In this study, the linear acoustic equations are solved instead of the wave equation because it is beneficial for implementing impedance BCs.

#### 2.2.2 Time-domain Nodal DG method

To numerically solve Equations (2.1), the nodal discontinuous Galerkin method is used to discretise the spatial derivative operators. First of all, Equations (2.1) are

rewritten into the following linear hyperbolic system:

$$\frac{\partial \mathbf{q}_a}{\partial t} + \nabla \cdot \mathbf{F}(\mathbf{q}_a) = \frac{\partial \mathbf{q}_a}{\partial t} + \mathbf{A}_j \frac{\partial \mathbf{q}_a}{\partial x_j} = 0, \tag{2.2}$$

where  $\mathbf{q}_a(\mathbf{x},t) = [u,v,w,p]^T$  is the acoustic variable vector and  $\mathbf{x} = [x,y,z]$  is the spatial coordinate vector with index  $j \in [x,y,z]$ . The flux is given as:

$$F = [f_x, f_y, f_z] = [A_x q_a, A_y q_a, A_z q_a], \qquad (2.3)$$

where the constant flux Jacobian matrix  $A_j$ :

$$\mathbf{A}_{j} = \begin{bmatrix} 0 & 0 & 0 & \frac{\delta_{xj}}{\rho_{0}} \\ 0 & 0 & 0 & \frac{\delta_{yj}}{\rho_{0}} \\ 0 & 0 & 0 & \frac{\delta_{zj}}{\rho_{0}} \\ \rho_{0}c_{0}^{2}\delta_{xj} & \rho_{0}c_{0}^{2}\delta_{yj} & \rho_{0}c_{0}^{2}\delta_{zj} & 0 \end{bmatrix}, \tag{2.4}$$

and  $\delta_{ij}$  denotes the Kronecker delta function.

Similar to the FEM, the physical domain  $\Omega$  is approximated by a computational domain  $\Omega_h$ , which is further divided into a set of K non-overlapping elements  $D^k$ , i.e.,  $\Omega_h = \bigcup_{k=1}^K D^k$ . This work adopts the quadrature-free approach [141] and follows the nodal DG algorithm presented in Ref. [112]. The global solution is approximated by a direct sum of local piecewise polynomial solutions as:

$$q_a(\mathbf{x},t) \approx q_{ah}(\mathbf{x},t) = \bigoplus_{k=1}^K q_{ah}^k(\mathbf{x},t).$$
 (2.5)

The local solution  $\boldsymbol{q}_{ah}^k(\boldsymbol{x},t)$  in element  $D^k$  is expressed by:

$$\mathbf{q}_{ah}^{k}(\mathbf{x},t) = \sum_{i=1}^{N_{p}} \mathbf{q}_{ah}^{k}(\mathbf{x}_{i}^{k},t) l_{i}^{k}(\mathbf{x}),$$
 (2.6)

where  $\mathbf{q}_{ah}^k(\mathbf{x}_i^k,t)$  are the unknown nodal values in element  $D^k$ ,  $l_i^k(\mathbf{x}_i^k)$  is the multidimensional Lagrange polynomial basis of order N based on the nodes  $\mathbf{x} \in D^k$ , which satisfies  $l_i^k(\mathbf{x}_j^k) = \delta_{ij}$ . The number of local basis functions (or nodes)  $N_p$  is determined by both the dimensionality of the problem d and the order of the polynomial basis N, which can be computed as  $N_p = (N+d)!/N!d!$ . In this work, the  $\alpha$ -optimized nodes distribution [142] for tetrahedron elements are used over a wide range of polynomial order N. The locally defined basis functions constitutes a function space as  $V_h^k = \text{span}\{l_i^k(\mathbf{x})\}_{i=1}^{N_p}$ . Then, the Galerkin projection is followed by choosing test functions equal to the basis functions. The solution is found by imposing an orthogonality condition: the local residual is orthogonal to all the test functions in  $V_h^k$ ,

$$\int_{D^k} \left( \frac{\partial \boldsymbol{q}_{ah}^k}{\partial t} + \nabla \cdot \boldsymbol{F}_h^k(\boldsymbol{q}_{ah}^k) \right) l_i^k d\boldsymbol{x} = 0.$$
 (2.7)

Integration by parts and applying the divergence theorem results in the local weak formulation:

$$\int_{D^k} \left( \frac{\partial \boldsymbol{q}_{ah}^k}{\partial t} l_i^k - \boldsymbol{F}_h^k(\boldsymbol{q}_{ah}^k) \cdot \nabla l_i^k \right) d\boldsymbol{x} = -\int_{\partial D^k} \boldsymbol{n} \cdot \boldsymbol{F}^* l_i^k d\boldsymbol{x}, \tag{2.8}$$

where  $\mathbf{n} = [n_x, n_y, n_z]$  is the outward normal vector of the element surface  $\partial D^k$  and  $\mathbf{F}^*(\mathbf{q}_{ah}^-, \mathbf{q}_{ah}^+)$  is the so-called numerical flux from element  $D^k$  to its neighboring elements through their intersection  $\partial D^k$ . In contrast to the classical continuous Galerkin method, the discontinuous Galerkin method uses local basis functions and test functions that are smooth within each element and discontinuous across the element intersections. As a result, the solutions are multiply defined on the intersections  $\partial D^k$ , where the numerical flux  $\mathbf{F}^*(\mathbf{q}_{ah}^-, \mathbf{q}_{ah}^+)$  should be defined properly as a function of both the interior and exterior (or neighboring) solution. In the remainder, the solution value from the interior side of the intersection is denoted by a superscript "-" and the exterior value by "+". Applying integration by parts once again to the spatial derivative term in Equation (2.8) yields the strong formulation:

$$\int_{D^k} \left( \frac{\partial \boldsymbol{q}_{ah}^k}{\partial t} + \nabla \cdot \boldsymbol{F}_h^k(\boldsymbol{q}_{ah}^k) \right) l_i^k \, d\boldsymbol{x} = \int_{\partial D^k} \boldsymbol{n} \cdot \left( \boldsymbol{F}_h^k(\boldsymbol{q}_{ah}^k) - \boldsymbol{F}^* \right) l_i^k \, d\boldsymbol{x}. \tag{2.9}$$

In this study, the flux-splitting approach in [21] is followed and the upwind numerical flux is presented in the following derivation. Let consider the case where the element  $D^k$  lies in the interior of the computational domain. As is shown in Equation (2.9), the formulation of the flux along the surface normal direction,  $\mathbf{n}$  i.e.,  $\mathbf{n} \cdot \mathbf{F} = (n_x \mathbf{f}_x + n_y \mathbf{f}_y + n_z \mathbf{f}_z)$  is of interest. To derive the upwind flux, the hyperbolic property of the system is used, decomposing the normal flux on the interface  $\partial D^k$  into outgoing and incoming waves. Mathematically, an eigen decomposition applied to the normally projected flux Jacobian  $\mathbf{A}_n = (n_x \mathbf{A}_x + n_y \mathbf{A}_y + n_z \mathbf{A}_z)$  yields:

$$\boldsymbol{A}_{n} = \begin{bmatrix} 0 & 0 & 0 & \frac{n_{x}}{\rho_{0}} \\ 0 & 0 & 0 & \frac{n_{y}}{\rho_{0}} \\ 0 & 0 & 0 & \frac{n_{z}}{\rho_{0}} \\ \rho_{0}c_{0}^{2}n_{x} & \rho_{0}c_{0}^{2}n_{y} & \rho_{0}c_{0}^{2}n_{z} & 0 \end{bmatrix} = \boldsymbol{L}\boldsymbol{\Lambda}\boldsymbol{L}^{-1}, \tag{2.10}$$

where

The upwind numerical flux is defined by considering the direction of the characteristic speed as:

$$(\boldsymbol{n} \cdot \boldsymbol{F})^* = \boldsymbol{L} (\boldsymbol{\Lambda}^+ \boldsymbol{L}^{-1} \boldsymbol{q}_{ah}^- + \boldsymbol{\Lambda}^- \boldsymbol{L}^{-1} \boldsymbol{q}_{ah}^+). \tag{2.12}$$

where  $\Lambda^+$  and  $\Lambda^-$  contain the positive and negative entries of  $\Lambda$  respectively. Physically,  $\Lambda^+$  ( $\Lambda^-$ , respectively) corresponds to the characteristic waves propagating along (opposite to, respectively) the normal direction n, which are referred to as outgoing waves out of  $D_k$  (incoming waves into  $D_k$ , respectively). Therefore, the outgoing waves are associated with the interior solution  $q_{ah}^-$  whereas the incoming waves are dependent on the exterior (neighbouring) solution  $q_{ah}^+$ . Finally, the semi-discrete formulation is obtained by substituting the nodal basis expansion Equation (2.6) and the upwind flux Equation (2.12) into the strong formulation Equation (2.9), which can be further recast into the following matrix form:

$$\boldsymbol{M}^{k} \frac{\partial \boldsymbol{u}_{h}^{k}}{\partial t} + \frac{1}{\rho_{0}} \boldsymbol{S}_{x}^{k} \boldsymbol{p}_{h}^{k} = \sum_{r=1}^{f} \boldsymbol{M}^{kr} \hat{\boldsymbol{F}}_{u}^{kr}, \qquad (2.13a)$$

$$\boldsymbol{M}^{k} \frac{\partial \boldsymbol{v}_{h}^{k}}{\partial t} + \frac{1}{\rho_{0}} \boldsymbol{S}_{y}^{k} \boldsymbol{p}_{h}^{k} = \sum_{r=1}^{f} \boldsymbol{M}^{kr} \hat{\boldsymbol{F}}_{v}^{kr}, \qquad (2.13b)$$

$$\boldsymbol{M}^{k} \frac{\partial \boldsymbol{w}_{h}^{k}}{\partial t} + \frac{1}{\rho_{0}} \boldsymbol{S}_{z}^{k} \boldsymbol{p}_{h}^{k} = \sum_{r=1}^{f} \boldsymbol{M}^{kr} \hat{\boldsymbol{F}}_{w}^{kr}, \qquad (2.13c)$$

$$\boldsymbol{M}^{k} \frac{\partial \boldsymbol{p}_{h}^{k}}{\partial t} + \rho_{0} c_{0}^{2} \boldsymbol{S}_{x}^{k} \boldsymbol{u}_{h}^{k} + \rho_{0} c_{0}^{2} \boldsymbol{S}_{y}^{k} \boldsymbol{v}_{h}^{k} + \rho_{0} c_{0}^{2} \boldsymbol{S}_{z}^{k} \boldsymbol{w}_{h}^{k} = \sum_{r=1}^{f} \boldsymbol{M}^{kr} \hat{\boldsymbol{F}}_{p}^{kr}, \qquad (2.13d)$$

where the second superscript r denotes the  $r^{th}$  faces  $\partial D^{kr}$  of the element  $D^k$  and f is the total number of faces of the element  $D^k$ , which is equal to four for tetrahedra elements.  $\boldsymbol{u}_h^k, \boldsymbol{v}_h^k, \boldsymbol{w}_h^k$ , and  $\boldsymbol{p}_h^k$  are vectors representing all the unknown nodal values  $u_h^k(\boldsymbol{x}_i^k,t), v_h^k(\boldsymbol{x}_i^k,t)$ , and  $p_h^k(\boldsymbol{x}_i^k,t)$ , respectively, e.g.,  $\boldsymbol{u}_h^k = [u_h^k(\boldsymbol{x}_1^k,t), u_h^k(\boldsymbol{x}_2^k,t), \dots, u_h^k(\boldsymbol{x}_{N_p}^k,t)]^T$ .  $\hat{\boldsymbol{F}}_u^{kr}, \hat{\boldsymbol{F}}_v^{kr}, \hat{\boldsymbol{F}}_w^{kr}$ , and  $\hat{\boldsymbol{F}}_p^{kr}$  are flux terms associated with the integrand  $\boldsymbol{n} \cdot (\boldsymbol{F}_h^k(\boldsymbol{q}_{ah}^k) - \boldsymbol{F}^*)$  over the element surface  $\partial D^{kr}$  in the strong formulation Equation (2.9). The element mass matrix  $\boldsymbol{M}^k$ , the element stiffness matrices  $\boldsymbol{S}_j^k$  and the element face matrices  $\boldsymbol{M}^{kr}$  are defined as:

$$\boldsymbol{M}_{mn}^{k} = \int_{D^{k}} l_{m}^{k}(\boldsymbol{x}) l_{n}^{k}(\boldsymbol{x}) d\boldsymbol{x} \in \mathbb{R}^{N_{p} \times N_{p}},$$
 (2.14a)

$$(\boldsymbol{S}_{j}^{k})_{mn} = \int_{D^{k}} l_{m}^{k}(\boldsymbol{x}) \frac{\partial l_{n}^{k}(\boldsymbol{x})}{\partial x_{j}} d\boldsymbol{x} \in \mathbb{R}^{N_{p} \times N_{p}},$$
(2.14b)

$$\boldsymbol{M}_{mn}^{kr} = \int_{\partial D^{kr}} l_m^{kr}(\boldsymbol{x}) l_n^{kr}(\boldsymbol{x}) d\boldsymbol{x} \in \mathbb{R}^{N_p \times N_{fp}},$$
 (2.14c)

where j is the  $j^{th}$  Cartesian coordinates and  $N_{fp}$  is the number of nodes along one element face. When the upwind flux is used, the flux terms for each acoustic variable

read as:

$$\hat{\boldsymbol{F}}_{u}^{kr} = -\frac{c_{0}n_{x}^{kr^{2}}}{2}[\boldsymbol{u}_{h}^{kr}] - \frac{c_{0}n_{x}^{kr}n_{y}^{kr}}{2}[\boldsymbol{v}_{h}^{kr}] - \frac{c_{0}n_{x}^{kr}n_{z}^{kr}}{2}[\boldsymbol{w}_{h}^{kr}] + \frac{n_{x}^{kr}}{2\rho_{0}}[\boldsymbol{p}_{h}^{kr}], (2.15a)$$

$$\hat{\boldsymbol{F}}_{v}^{kr} = -\frac{c_{0}n_{y}^{kr^{2}}}{2}[\boldsymbol{v}_{h}^{kr}] - \frac{c_{0}n_{x}^{kr}n_{y}^{kr}}{2}[\boldsymbol{u}_{h}^{kr}] - \frac{c_{0}n_{y}^{kr}n_{z}^{kr}}{2}[\boldsymbol{w}_{h}^{kr}] + \frac{n_{y}^{kr}}{2\rho_{0}}[\boldsymbol{p}_{h}^{kr}], (2.15b)$$

$$\hat{\boldsymbol{F}}_{w}^{kr} = -\frac{c_{0}n_{z}^{kr^{2}}}{2}[\boldsymbol{w}_{h}^{kr}] - \frac{c_{0}n_{x}^{kr}n_{z}^{kr}}{2}[\boldsymbol{u}_{h}^{kr}] - \frac{c_{0}n_{y}^{kr}n_{z}^{kr}}{2}[\boldsymbol{v}_{h}^{kr}] + \frac{n_{z}^{kr}}{2\rho_{0}}[\boldsymbol{p}_{h}^{kr}], (2.15c)$$

$$\hat{\boldsymbol{F}}_{p}^{kr} = \frac{c_{0}^{2}\rho_{0}n_{x}^{kr}}{2}[\boldsymbol{u}_{h}^{kr}] + \frac{c_{0}^{2}\rho_{0}n_{y}^{kr}}{2}[\boldsymbol{v}_{h}^{kr}] + \frac{c_{0}^{2}\rho_{0}n_{z}^{kr}}{2}[\boldsymbol{w}_{h}^{kr}] - \frac{c_{0}}{2}[\boldsymbol{p}_{h}^{kr}], (2.15d)$$

where  $[\boldsymbol{u}_h^{kr}] := \boldsymbol{u}_h^{kr} - \boldsymbol{u}^{ls}, [\boldsymbol{v}_h^{kr}] := \boldsymbol{v}_h^{kr} - \boldsymbol{v}_h^{ls}, [\boldsymbol{w}_h^{kr}] := \boldsymbol{w}_h^{kr} - \boldsymbol{w}_h^{ls}$  and  $[\boldsymbol{p}_h^{kr}] := \boldsymbol{p}_h^{kr} - \boldsymbol{p}_h^{ls}$  are the jump differences across the shared intersection face  $\partial D^{kr}$  or equivalently  $\partial D^{ls}$ , between neighboring elements  $D^k$  and  $D^l$ ,  $\boldsymbol{u}_h^{kr}$ , etc. are the nodal value vector, over the element surface  $\partial D^{kr}$ .

In this work, flat-faced tetrahedral elements are used so that each tetrahedron can be mapped into a reference tetrahedron by a linear transformation with a constant Jacobian matrix. As a consequence, the integrals in the above element matrices, i.e.,  $M^k$ ,  $S_j^k$  and  $M^{kr}$ , need to be evaluated only once. The reader is referred to Ref. [112] for more details on how to compute the matrices locally and efficiently.

#### 2.2.3 Numerical dissipation and dispersion properties

For a DG scheme that uses polynomial basis up to order N, it is well known that generally the rate of convergence in terms of the global  $L^2$  error is  $h^{N+1/2}$  (h being the element size) [143]. The dominant error comes from the representations of the initial conditions, while the additional dispersive and dissipative errors from the wave propagations are relatively small and only visible after a very long time integration [112]. The one-dimensional eigenvalue problem for the spatially propagating waves is studied in [144] and it is reported that the dispersion relation is accurate to  $(\kappa h)^{2N+2}$ locally, where  $\kappa$  is the wavenumber. When the upwind flux is used, the dissipation error has been proved to be of order  $(\kappa h)^{2N+2}$  while the dispersion error is of order  $(\kappa h)^{2N+3}$  [145]. When the centered numerical flux is used, the dissipation rate is exactly zero, but the discrete dispersion relation can only approximate the exact one for a smaller range of the wavenumber [146]. Extensions to the two-dimensional hyperbolic system on triangle and quadrilateral mesh are studied in [147] and the same numerical dispersion relation as the one-dimensional case are reported. In [145], a rigorous mathematical proof of the above numerical dispersion relation and error behavior is provided for a general multi-dimensional setting (including threedimensional).

### 2.2.4 Time integration with the optimal Runge-Kutta method

After the spatial discretisation by the nodal DG method, the semi-discrete system can be expressed in a general form of ordinary differential equations (ODE) as:

$$\frac{\mathrm{d}\boldsymbol{q}_{ah}}{\mathrm{d}t} = \mathcal{L}(\boldsymbol{q}_{ah}(t), t), \tag{2.16}$$

where  $q_{ah}$  is the vector of all discrete nodal solutions and  $\mathcal{L}$  the spatial discretization operator of DG. Here, a low-storage explicit Runge-Kutta method is used to integrate Equation (2.16), which reads as:

$$\mathbf{q}_{ah}^{(0)} = \mathbf{q}_{ah}^{n},$$

$$\begin{cases} \mathbf{k}^{(i)} = a_{i}\mathbf{k}^{(i-1)} + \Delta t \mathcal{L}(t^{n} + c_{i}\Delta t, \mathbf{q}_{ah}^{(i-1)}), \\ \mathbf{q}_{ah}^{(i)} = \mathbf{q}_{ah}^{(i-1)} + b_{i}\mathbf{k}^{(i)}, \end{cases}$$
 for  $i = 1, \dots, s$ 

$$\mathbf{q}_{ah}^{n+1} = \mathbf{q}_{ah}^{(s)},$$

where  $\Delta t = t^{n+1} - t^n$  is the time step,  $q_{ah}^{n+1}$  and  $q_{ah}^n$  are the solution vectors at time  $t^{n+1}$  and  $t^n$ , respectively, s is the number of stages of a particular scheme. In this work, the coefficients  $a_i, b_i$ , and  $c_i$  are chosen from the optimal Runge-Kutta scheme reported in [148].

# 2.3 Impedance boundary conditions and numerical stability

In this section, a new formulation of the impedance BCs based on the plane wave reflection coefficient is proposed to simulate the locally-reacting surfaces with frequency-independent real-valued impedances. Additionally, the stability properties of the DG scheme is discussed.

## 2.3.1 Numerical flux for frequency-independent impedance boundary conditions

The numerical flux  $F^*$  plays a key role in the DG scheme. Apart from linking neighboring interior elements, it serves to impose the BCs and to guarantee stability of the formulation. BCs can be enforced weakly through the numerical flux either by reformulating the flux subject to specific BCs or by providing the exterior solution  $q_{ah}^+$  [149]. In both cases, the solutions from the interior side of the element face (equivalent to boundary surface)  $q_{ah}^-$  are readily used, whereas, for the second case, the exterior solutions  $q_{ah}^+$  need to be suitably defined as a function of interior solution  $q_{ah}^-$  based on the imposed conditions. In the following, the impedance BC is prescribed by reformulating the numerical flux. It should be noted that throughout this study,

only plane-shaped reflecting boundary surfaces are considered. Furthermore, only locally-reacting surfaces are considered, whose surface impedance is independent of the incident angle. This assumption is in accordance with the nodal DG scheme, since the unknown acoustic particle velocities on the boundary surface nodes depend on the pressure at exactly the same positions.

To reformulate the numerical flux at an impedance boundary, we take advantage of the characteristics of the underlying hyperbolic system and utilize the reflection coefficient R for plane waves at normal incidence. Firstly, the same eigendecomposition procedure is performed for the projected flux Jacobian on the boundary as is shown in Equation (2.10). Secondly, by pre-multiplying the acoustic variables  $q_a$  with the left eigenmatrix  $L^{-1}$ , the characteristics corresponding to the acoustic waves [150], [151] read:

$$\begin{bmatrix} \omega_o \\ \omega_i \end{bmatrix} = \begin{bmatrix} p/\rho_0 c_0 + u n_x + v n_y + w n_z \\ p/\rho_0 c_0 - u n_x - v n_y - w n_z \end{bmatrix}, \tag{2.17}$$

where  $\omega_o$  corresponds to the outgoing characteristic variable that leaves the computational domain and  $\omega_i$  is the incoming characteristic variable.

The general principle for imposing BCs of hyperbolic systems is that the outgoing characteristic variable should be computed with the upwind scheme using the interior values, while the incoming characteristic variable are specified conforming with the prescribed behaviour across the boundary. The proposed real-valued impedance BC formulation is accomplished by setting the incoming characteristic variable as the product of the reflection coefficient and the outgoing characteristic variable, i.e.,  $\omega_i = R \cdot \omega_o$ . Finally, the numerical flux on the impedance boundary surface can be expressed in terms of the interior values  $\mathbf{q}_{ah}^-$  as follows:

$$(\boldsymbol{n} \cdot \boldsymbol{F}^*) = \boldsymbol{L} \boldsymbol{\Lambda} \begin{bmatrix} 0 \\ 0 \\ \boldsymbol{p}_h^- / \rho_0 c_0 + \boldsymbol{u}_h^- n_x + \boldsymbol{v}_h^- n_y + \boldsymbol{w}_h^- n_z \\ R \cdot (\boldsymbol{p}_h^- / \rho_0 c_0 + \boldsymbol{u}_h^- n_x + \boldsymbol{v}_h^- n_y + \boldsymbol{w}_h^- n_z) \end{bmatrix}.$$
(2.18)

For given constant values of the normalized surface impedance  $Z_s$ , the reflection coefficient can be calculated from  $R = (Z_s - 1)/(Z_s + 1)$ , which is consistent with the fact that the numerical flux from the nodal DG scheme is always normal to the boundary surface. When the reflection coefficient is set to zero it can be easily verified that the proposed formulation reduces to the characteristic non-reflective BC, which is equivalent to the first-order Engquist-Majda absorbing BC [152].

#### 2.3.2 Numerical stability of the DG scheme

In this section, the stability properties of the DG scheme are discussed. Firstly, the semi-boundedness of the spatial DG operator together with the proposed impedance BC is analysed using the energy method. Secondly, the fully discrete stability is discussed and the criterion for choosing the discrete time step is presented.

#### Stability of the semi-discrete formulation

Under a certain initial condition and impedance BC, the Equations (2.1) constitute a general initial-boundary value problem. For real-valued impedance BCs, the classical von Neumann (or Fourier) stability analysis can no longer be applied, because the necessary periodic BC for the Fourier components do not exist. To analyse the stability or boundedness of the semi-discrete system, the energy method [153] is adopted here. The principle is to construct a norm and to demonstrate it does not grow with increasing time. This technique has also been applied in other acoustic simulation methods [28], [154], even in the fully-discrete case.

For the numerical solution of the acoustic variables, e.g.,  $u_h(\boldsymbol{x},t)$ , the local inner product and its associated  $L^2$  norm in function space  $V_h^k$  are defined as:

$$(u_h^k, u_h^k)_{D^k} = \int_{D^k} u_h^k(\mathbf{x}, t) u_h^k(\mathbf{x}, t) d\mathbf{x} = \|u_h^k\|_{D^k}^2.$$
 (2.19)

Similarly, over the element surface  $\partial D^{kr}$ , define:

$$(u_h^{kr}, u_h^{kr})_{\partial D^{kr}} = \int_{\partial D^{kr}} u_h^{kr}(\boldsymbol{x}, t) u_h^{kr}(\boldsymbol{x}, t) d\boldsymbol{x} = \|u_h^{kr}\|_{\partial D^{kr}}^2,$$
 (2.20)

where  $u_h^{kr}$  is the numerical solution on the element surface  $\partial D^{kr}$ . Now, the discrete acoustic energy norm inside single element  $D^k$  can be defined as:

$$E_h^k = \frac{1}{2}\rho_0 \|u_h^k\|_{D^k}^2 + \frac{1}{2}\rho_0 \|v_h^k\|_{D^k}^2 + \frac{1}{2}\rho_0 \|w_h^k\|_{D^k}^2 + \frac{1}{2\rho_0 c_0^2} \|p_h^k\|_{D^k}^2.$$
 (2.21)

This definition is in complete analogy with the continuous acoustic energy, denoted as E, throughout the whole domain  $\Omega$ , i.e.,  $E = \int_{\Omega} (1/2\rho_0 c_0^2) p^2 + \rho_0/2 |v^2| dx$ .

By summing all the local discrete acoustic energies over the volume and the boundaries, it can be proved in Appendix A that the total discrete acoustic energy, which

is denoted as 
$$E_h = \sum_{k=1}^{K} E_h^k$$
, is governed by:

$$\frac{\mathrm{d}}{\mathrm{d}t}E_{h} = -\sum_{\partial D^{mt} \in \mathcal{F}_{B}} \left( \frac{1 - R^{mt}}{2\rho_{0}c_{0}} \|p_{h}^{mt}\|_{\partial D^{mt}}^{2} + \frac{\rho_{0}c_{0}}{2} (1 + R^{mt}) \|v_{hn}^{mt}\|_{\partial D^{mt}}^{2} \right) \dots 
- \sum_{\partial D^{kr} \in \mathcal{F}_{I}} \left( \frac{1}{2\rho_{0}c_{0}} \|[p_{h}^{kr}]\|_{\partial D^{kr}}^{2} + \frac{\rho c}{2} \|n_{x}^{kr}[u_{h}^{kr}] + n_{y}^{kr}[v_{h}^{kr}] + n_{z}^{kr}[w_{h}^{kr}]\|_{\partial D^{kr}}^{2} \right),$$
(2.22)

where  $\mathcal{F}_I$  and  $\mathcal{F}_B$  denote the union set of interior elements and elements with at least one surface collocated with a physical boundary.  $[\cdot]$  denotes the jump differences across the element surfaces.  $v_{hn}^{mt} = n_x^{mt} u_h^{mt} + n_y^{mt} v_h^{mt} + n_z^{mt} w_h^{mt}$  denotes the outward velocity component normal to the impedance boundary.  $R^{mt}$  is the normal incidence

plane-wave reflection coefficient along the  $t^{th}$  boundary surface of element  $\partial D^m$ .  $\partial D^{kr}$  and  $\partial D^{ls}$  refer to the same element intersection surface between neighbouring elements  $D^k$  and  $D^l$ . Since each norm is non-negative and  $R \in [-1,1]$  holds for a passive impedance BC [155], it is proved that the semi-discrete acoustic system resulting from the DG discretisation is unconditionally stable for passive BCs with a real-valued impedance.

It is worth mentioning that the second sum term of the above Equation (2.22) is related to the energy dissipation inside the computational domain due to the use of the upwind scheme. This dissipation will converge to zero when the jump differences across the shared element interfaces converge to zero at a rate corresponding to the approximation polynomial order. The first sum of the above Equation (2.22) is associated with the energy flow through the impedance boundary. One advantage of using the reflection coefficient to impose the impedance BC is that the following singular cases can be considered without the need for exceptional treatments.

- Hard wall case. As  $Z_s \to \infty$  or  $R \to 1$ ,  $v_{hn} \to 0$ , then the boundary energy term converges to 0, meaning that the energy is conserved.
- Pressure-release condition. As  $Z_s \to 0$  or  $R \to -1$ ,  $p_h \to 0$ , then the boundary energy term once again converges to 0, and the energy is conserved as well.

#### Stability of the fully discrete formulation and time step choices

The above analysis is devoted to the stability analysis of the semi-discrete formulation Equation (2.16), which in matrix form read as:

$$\frac{\mathrm{d}\boldsymbol{q}_{ah}}{\mathrm{d}t} = \boldsymbol{L}_h \boldsymbol{q}_{ah},\tag{2.23}$$

where  $L_h$  is the matrix representation of the spatial operator  $\mathcal{L}$ . Ideally, the fully discrete approximation should be stable, at least under a reasonable upper bound on the time step size. Unfortunately, the theoretical ground for stability of a discretized PDE system is not very complete [153], particularly for high order time integration methods. A commonly-used approach based on the von Neumann analysis is to choose the time step size  $\Delta t$  small enough so that the product of  $\Delta t$  with the full eigenvalue spectrum of  $L_h$  falls inside the stability region of the time integration scheme. It should be noted that this is only a necessary condition for a general initial-boundary value problem, with the sufficient condition being more restrictive and complex [156], [157]. However, for real world problems, this necessary condition serves as a useful guideline.

It is computationally infeasible to compute the eigenvalue of  $L_h$  before the simulation is started for various unstructured mesh, polynomial order and BCs. For the DG method, it is found that for the first order system Equation (2.16), the gradients of the normalized N-th order polynomial basis are of order  $\mathcal{O}(N^2/h)$  near the boundary part of the element [112], consequently the magnitude of the maximum eigenvalue  $\lambda_N$  scales with the polynomial order N as:  $\max(\lambda_N) \propto N^2$ , indicating that  $\Delta t \propto$ 

 $N^{-2}$ . This severe time step size restriction limits the computational efficiency of high polynomial order approximations. In all the numerical experiments presented in this work, the temporal time steps are determined in the following way [148]:

$$\Delta t = C_{CFL} \cdot \min(r_D) \cdot \frac{1}{c},\tag{2.24}$$

where  $r_D$  is the radius of the inscribed sphere of the tetrahedral elements. As a reference, the tabulated maximum allowable Courant number  $C_{CFL}$  of the fourth-order Runge-Kutta method with eight stages (RKF84) scheme for each polynomial order N can be found in [148]. In each of the following numerical tests, the exact value of  $C_{CFL}$  are explicitly stated for completeness.

#### 2.4 Applications

To investigate the applicability of the nodal DG time domain method as described in Sections 2.2 and 2.3 for room acoustics problems, various three-dimensional numerical tests are designed and compared in this section. The first test is a free field propagation of a single frequency plane wave under periodic BCs. In this case, the dissipation error in terms of the wave amplitude and the dispersion error are investigated. The second configuration is a sound source over an impedance plane. The accuracy of the proposed DG formulation to simulate frequency-independent impedance BCs is verified. The third configuration is a sound source in a cuboid room with rigid BCs, embodying an approximation to a real room including multiple reflections. The modal behaviour of the space is investigated for different polynomial order N of the basis functions when compared with the analytical solution, together with an analysis of the sound energy conservation inside the room to quantify the numerical dissipation. Finally, the fourth configuration is adopted to demonstrate the applicability of the method to a real room. The configuration is a room with complex geometry and a real-valued impedance BC. In this configuration, the pressure response functions in the frequency domain are compared with the measured results at several receiver locations. For the acoustic speed and the air density,  $c_0 = 343$  m/s and  $\rho_0 = 1.2$ kg/m<sup>3</sup> are used in all calculations. Due to the fact that there are duplicated nodes along the element interfaces, in this work, the number of degrees of freedom per wavelength  $\lambda$  (DPW) is used to give a practical indication of the computational cost. It is computed as:

$$DPW = \lambda \sqrt[3]{\frac{N_p \times K}{V}}, \qquad (2.25)$$

where  $N_p \times K$  is the number of degrees of freedom for a single physical variable in the computational domain, V is the volume of the whole domain.

#### 2.4.1 Free field propagation in periodic domain

To verify the accuracy of the free field propagation, a cubic computational domain of size  $[0,1]^3$  in meter is considered, which is discretized with 6 congruent tetrahedral elements.  $10 \times 10 \times 10$  receivers are evenly spaced in all directions throughout the

domain. The domain is initialized with a single frequency plane wave propagating in the x-direction only:

$$p(\boldsymbol{x}, t = 0) = \sin(-2\pi x), \tag{2.26a}$$

$$u(\boldsymbol{x}, t = 0) = \frac{1}{\rho c} \sin(-2\pi x), \qquad (2.26b)$$

$$v(x, t = 0) = 0, \quad w(x, t = 0) = 0.$$
 (2.26c)

The wavelength  $\lambda$  is chosen to be equal to 1 m such that periodic BCs can be applied in all directions. As mentioned in Section 2.2.3, when an initial value problem is simulated, the approximation error associated with the representations of the initial conditions is a dominant component. In order to rule out this approximation error and to assess the dissipation and dispersion error accumulated from the wave propagation alone, the solution values at receiver locations recorded during the first wave period T of propagation are taken as the reference values. The solutions sampled during later time period inverval t = [(n-1)T, nT] are compared with these reference values, where  $n = 10, 20, 30, \ldots, 100$ . The amplitude and phase values of the single frequency wave at each of the receiver locations are obtained from a Fourier transform of the recorded time signals without windowing. The dissipation error  $\epsilon_{amp}$  in dB and the phase error  $\epsilon_{\phi}$  in % are calculated as follows:

$$\epsilon_{amp} = \max \left( 20 \log_{10} \frac{|P_{ref}(\boldsymbol{x})|}{|P_{nT}(\boldsymbol{x})|} \right),$$
(2.27a)

$$\epsilon_{\phi} = \max\left(\frac{\left|\phi\left(P_{nT}(\boldsymbol{x})\right) - \phi\left(P_{ref}(\boldsymbol{x})\right)\right|}{\pi} \times 100\%\right),$$
(2.27b)

where  $P_{ref}(\boldsymbol{x})$  and  $P_{nT}(\boldsymbol{x})$  are the Fourier transform of the recorded pressure values at different locations, during the first time period and the  $n^{th}$  period respectively.  $\phi(\cdot)$  extracts the phase angle of a complex number.

Simulations for N=5,6,7 corresponding to DPW=6.9, 7.9, 8.9 have been carried out and a single time step size  $\Delta t = T/100 = 1/(100*343)$  is used for all simulations to make sure the time integration error is much smaller than the spatial error.

The dissipation and the phase error from the explicit Runge-Kutta time integration is calculated based on the descriptions presented in [158] and shown as dashed lines in Fig. 1. As can be seen, both the dissipation error and the phase error grow linearly with respect to the propagation distance. For  $5^{th}$  order polynomial basis (DPW=6.9), the averaged dissipation error is approximately 0.035 dB when the wave travels one wavelength distance while the phase error is 0.095%. Both error drop to 0.002 dB and 0.005% respectively when the DPW increases to 8. When the DPW is equal to 8.9, the dissipation error is  $1.1 \cdot 10^{-4}$  dB per wavelength of propagation and the phase error is less than  $3 \cdot 10^{-4}$ %.

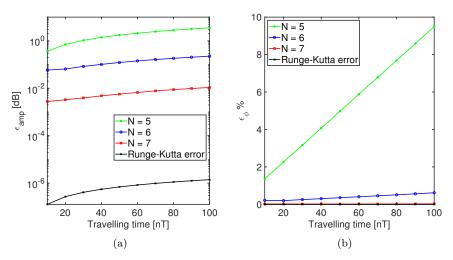


Figure 2.1: a) Amplitude error  $\epsilon_{amp}$  and b) phase error  $\epsilon_{\phi}$  for the periodic propagation of a single frequency plane wave Equation (2.26).

#### 2.4.2 Single reflective plane

To verify the performance of the proposed frequency-independent impedance BC, a single reflection scenario is considered and the reflection coefficient obtained from the numerical tests is compared with the analytical one based on a locally reacting impedance. The experiment consists of two simulations. In the first simulation, we consider a cubic domain of size  $[-8,8]^3$  in meter, where the source is located at the center [0,0,0] m, and two receivers are placed at  $x_{r1} = [0,0,-1]$  m and  $x_{r2} = [0,4,-1]$  m. In this case, the free field propagation of a sound source is simulated and sound pressure signals are recorded at both receiver locations. In the second simulation, a plane reflecting surface is placed 2 m away from the source at z = -2 m. The measured sound pressure signals not only contain the direct sound but also the sound reflected from the impedance surface. In both cases, initial pressure conditions are used to initiate the simulations:

$$p(\mathbf{x}, t = 0) = e^{\frac{-\ln(2)}{b^2} ((x - x_s)^2 + (y - y_s)^2 + (z - z_s)^2)},$$
 (2.28a)  
 $\mathbf{v}(\mathbf{x}, t = 0) = \mathbf{0},$  (2.28b)

which is a Gaussian pulse centered at the source coordinates  $[x_s,y_s,z_s]=[0,0,0]$ . The half-bandwith of this Gaussian pulse is chosen as b=0.25 m. Simulations are stopped at around 0.0321 s in order to avoid the waves reflected from the exterior boundaries of the whole domain. In order to eliminate the effects of the unstructured mesh quality on the accuracy, structured tetrahedra meshes are used for this study, which are generated with the meshing software Gmsh [159]. The whole cuboid domain is made up of structured cubes of the same size, then each cube is split into 6 tetrahedra elements. The length of each cube is 0.5 m.

Let  $p_d$  denote the direct sound signal measured from the first simulation, then the reflected sound signal  $p_r(t)$  is obtained by eliminating  $p_d(t)$  from the solution of the second simulation. Let  $R_1$  denote the distance between the source and the receiver and  $R_2$  is the distance between the receiver and the image source (located at [0,0,-4] m) mirrored by the reflecting impedance surface. The spectra of the direct sound and the reflected sound, denoted as  $P_d(f)$  and  $P_r(f)$  respectively, are obtained by Fourier transforming  $p_d$  and  $p_r$  without windowing. The numerical reflection coefficient  $Q_{num}$  is calculated as follows:

$$Q_{num}(f) = \frac{P_r(f) \cdot G(\kappa R_1)}{P_d(f) \cdot G(\kappa R_2)},\tag{2.29}$$

where

$$G(\kappa R) = e^{i\kappa R}/R, \tag{2.30}$$

is the Green function in three-dimensional free space.  $\kappa$  is the wavenumber. The analytical spherical wave reflection coefficient Q reads [160]:

$$Q = 1 - 2 \frac{\kappa R_2}{Z_s e^{i\kappa R_2}} \int_0^\infty e^{-\frac{q\kappa}{Z_s}} \frac{e^{i\kappa \sqrt{r_p^2 + (z + z_s + iq)^2}}}{\sqrt{r_p^2 + (z + z_s + iq)^2}} dq,$$
 (2.31)

where  $Z_s$  is the normalized surface impedance, z = 1 is the distance between the receiver and the reflecting surface,  $z_s = 2$  is the distance between the source and the surface,  $r_p$  is the distance between the source and the receiver projected on the reflecting surface.

Table 2.1:  $C_{CFL}$  number and time step  $\Delta t$  for single reflection case (h=0.5 m).

$\overline{N}$	$C_{CFL}$	$\Delta t$ [s]
5	0.185	$9.721 \cdot 10^{-5}$
6	0.144	$7.550 \cdot 10^{-5}$
7	0.114	$5.993 \cdot 10^{-5}$
8	0.094	$4.908 \cdot 10^{-5}$

Simulations with polynomial order N=5 up-to N=8 are carried out with the corresponding  $C_{CFL}$  and time step  $\Delta t$  presented in Table 2.1. The results of the numerical tests for  $Z_s=3$  are illustrated in Figure 2.2 The DPW is calculated based on the frequency of 500 Hz. The comparison of the magnitudes of the spherical wave reflection coefficient for both the normal incidence angle  $\theta=0^\circ$  and the oblique incidence  $(\theta=53^\circ)$  are shown in Figures 2.2a and 2.2b respectively. The phase angle comparison is presented in Figures 2.2c and 2.2d. It can be seen that with increasing polynomial order N (or DPW), the numerical reflection coefficient converges to the analytical one in terms of the magnitude and the phase angle. Also, the accuracy is rather independent on the two angles of incidence  $\theta$ . In order to achieve a satisfactory accuracy, at least 12 DPW are needed. Many tests are performed with different impedances  $(Z_s \in [1,\infty])$  and receiver locations  $(\theta \in [0^\circ, 90^\circ])$ , the same conclusion can be reached.

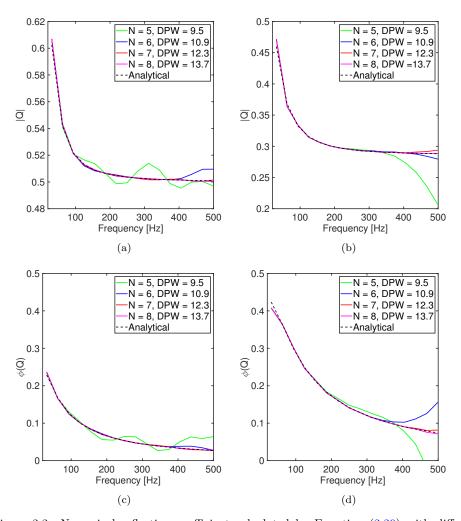


Figure 2.2: Numerical reflection coefficient calculated by Equation (2.29) with different polynomial orders, compared with the theoretical result according to Equation (2.31) (black dashed line): a) magnitude for receiver 1,  $\theta = 0^{\circ}$ , b) magnitude for receiver 2,  $\theta = 53^{\circ}$ , c) phase angle for receiver 1,  $\theta = 0^{\circ}$ , d) phase angle for receiver 2,  $\theta = 53^{\circ}$ .

#### 2.4.3 Cuboid room with rigid boundaries

In this section, the nodal DG method is applied to sound propagation in a three-dimensional room with rigid boundaries (R=1). In contrast to the previous applications, sound propagation inside the room is characterized by multiple reflections and sound energy is conserved. The domain of the room is  $[0, L_x] \times [0, L_y] \times [0, L_z]$  m, with  $L_x=1.8$ ,  $L_y=1.5$ ,  $L_z=2$ . Initial conditions are given as in Equations (2.28), with b=0.2 m. The source is positioned at [0.9, 0.75, 1] m, and a receiver is positioned at [1.7, 1.45, 1.9] m. Same as the previous test case, the room is discretized using structured tetrahedral elements of size 0.4 m. The analytical pressure response in a cuboid domain can be obtained by the modal summation method, and in the three-dimensional Cartesian coordinate can be written as [34]:

$$p(\boldsymbol{x},t) = \sum_{l=0}^{\infty} \sum_{m=0}^{\infty} \sum_{n=0}^{\infty} \hat{p}_{lmn}(t) \psi_{lmn}(\boldsymbol{x}) \cos(\omega_{lmn}t), \qquad (2.32a)$$

$$\psi_{lmn}\left(\boldsymbol{x}\right) = \cos\left(\frac{l\pi x}{L_x}\right)\cos\left(\frac{m\pi y}{L_y}\right)\cos\left(\frac{n\pi z}{L_z}\right),$$
(2.32b)

$$\omega_{lmn} = c_0 \sqrt{\left(\frac{l\pi}{L_x}\right)^2 + \left(\frac{m\pi}{L_y}\right)^2 + \left(\frac{n\pi}{L_z}\right)^2}, \qquad (2.32c)$$

with  $\psi_{lmn}$  the modal shape function,  $\hat{p}_{lmn}$  the modal participation factor,  $\omega_{lmn}$  the natural angular frequency, and l,m,n the mode indices. Since reflections from the room boundaries occur without energy loss, the modal participation factors are constant over time. To obtain  $\hat{p}_{lmn}(0)$ , the initial pressure distribution is projected onto each modal shape as:

$$\hat{p}_{lmn}(0) = \frac{1}{D_{lmn}} \int_{\Omega} p(\boldsymbol{x}, t = 0) \psi_{lmn}(\boldsymbol{x}) d\boldsymbol{x}, \qquad (2.33a)$$

$$D_{lmn} = \int_{\Omega} \psi_{lmn}^2(\boldsymbol{x}) d\boldsymbol{x}. \tag{2.33b}$$

The integration in Equation (2.33a) can be calculated separately for each coordinate. For example in x-coordinate, the indefinite integration can be expressed in terms of error function as:

$$\int e^{\left(-a_0(x-x_s)^2\right)} \cos(b_0 x) dx = \frac{\sqrt{\pi}}{4\sqrt{a_0}} e^{\left(-\frac{b_0^2}{4a_0} - ib_0 x_s\right)} \left[ \operatorname{erf}(B) + e^{(i2b_0 x_s)} \operatorname{erf}(B^*) \right] + C, \tag{2.34}$$

with  $B = \sqrt{a_0} (x - x_0) + ib_0/2\sqrt{a_0}$ ,  $a_0 = \ln(2)/b^2$ ,  $b_0 = l\pi/L_x$ , and C is a constant. The Equation (2.32a) is used as the reference solution with modal frequencies up to 8 kHz. Furthermore, to show the applicability of the nodal DG method for a long time simulation, 10 seconds are taken as the simulation duration. To solve for this

configuration, the  $C_{CFL}$  numbers and time steps for the approximating polynomial orders of N=3 up-to N=7 are presented in Table 2.2. To compare the nodal DG solution with the reference solution, the sound pressure level is computed as:

$$L_p = 20 \log_{10} \left| \frac{P(f)}{\sqrt{2}P_0} \right|,$$
 (2.35)

with  $P_0 = 2 \cdot 10^{-5}$  Pa, and P(f) as the spectrum of recorded pressure time signal p(t) at the receiver location. The end of the time signal is tapered using a Gaussian window with length of 3.5 s to avoid the Gibbs effect.

Table 2.2: Courant number  $C_{CFL}$  and time step  $\Delta t_{DG}$  for a rigid cuboid room (h=0.4 m).

$N_{DG}$	$C_{CFL}$	$\Delta t_{DG}$ [s]
3	0.355	$1.400\cdot10^{-4}$
4	0.248	$9.810 \cdot 10^{-5}$
5	0.185	$7.322 \cdot 10^{-5}$
6	0.144	$5.687 \cdot 10^{-5}$
7	0.114	$4.514 \cdot 10^{-5}$

Figure 2.3a shows the sound pressure level at the receiver location. The numerical solutions show an excellent agreement with the reference solution, with the accuracy of the numerical solution increasing as approximating polynomial order increases. Figure 2.3b displays the results in the frequency range from 950 to 1000 Hz. This figure shows that the resonance frequencies are not well represented for  $N \leq 5$ , for which DPW varies between 4.5 and 6.6 in this frequency range. On the other hand, the resonance frequencies are correctly represented for  $N \geq 6$ , where the minimum number of DPW is 7.2. The correct representation of the room resonance frequencies indicates that the numerical dispersion is low in the DG solution. The numerical dispersion aspect is essential with regards to the auralisation as shown by Saarelma et al. [161], where the audibility of the numerical dispersion error from the finite difference time domain simulation is investigated. Furthermore, Figure 2.3b shows that the amplitude of the resonances is smaller than for the reference solution for low order polynomials.

### 2.4.4 Real room with real-valued impedance boundary conditions

The final scenario presents a comparison between experimental and numerical results of a real room. The room was located in the Acoustics Laboratory building (ECHO building) at the campus of the Eindhoven University of Technology. Geometrical data of the room, including the dimensions and the location of the source and microphone positions are presented in Figure 2.4. The room has a volume of  $V = 89.54 \text{ m}^3$  and a boundary surface area of  $S = 125.08 \text{ m}^2$ .

The source is located at [1.7, 2.92, 1.77] m and microphones (M) are located at [3.8, 1.82, 1.66] m for M1 and [4.75, 3.87, 1.63] m for M2. The height (z-coordinate) of

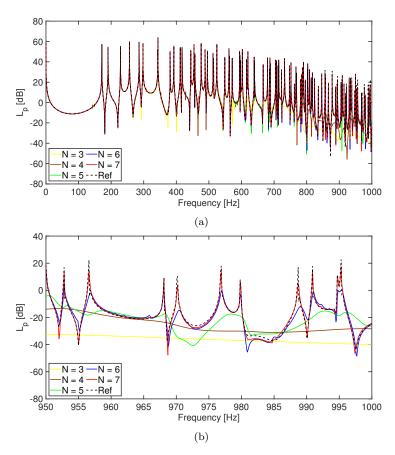


Figure 2.3: Sound pressure level at receiver position in the configuration of the three-dimensional rigid cuboid room for different polynomial orders presented for: a) complete evaluated frequency range and b) sound pressure level between 950 Hz and 1000 Hz.

the sound source location is measured at the opening (highest point) of the used sound source (B&K type 4295, OmniSource Sound Source). The measurements were performed using one free-field microphone B&K type 4189 connected to a Triton USB Audio Interface. The impulse responses were acquired with a sampling frequency of 48 KHz with a laptop using the room acoustics software DIRAC (B&K Type 7841). The input channel is calibrated before starting the measurements using a calibrator (B&K type 4230). The sound signal used for the excitation of the room is the DIRAC built-in e-Sweep signal with a duration of 87.4 seconds connected to an Amphion measurement amplifier. At each microphone position, three measurement repetitions were performed. The results presented in this section for M1 and M2 represent the average of the three repetitions.

The room was discretized in 9524 tetrahedral elements by using the mesh software Gmsh and the largest element size is 0.5 m. A detail of the mesh is shown in Figure 2.4b. The same initial pressure distribution as for the three-dimensional cuboid room of Section 2.4.3 was used. The polynomial order used in the calculations is N=4 with a CFL number of  $C_{CFL}=0.25$ . The computed impulse responses had a duration of 15 seconds. The model used a DPW of 13 for the frequency of 400 Hz. All the boundaries of the model were computed using a uniform real-valued reflection coefficient of R=0.991. The coefficient was calculated from the experimental results at M1 by computing the Q-value of the resonance at  $f_0=97.9$  Hz, using:

$$R = 1 - \frac{\delta_r 8V}{cS},\tag{2.36}$$

with  $\delta_r = 2\pi f_0/2Q$  the decay constant of the room's resonance [34]. Both impulse responses from the measurements and simulations were transformed to the frequency domain by using a forward Fourier transform. The end of the time signals was tapered by a single-sided Gaussian window with a length of 500 samples (approximately, 5.6 ms) to avoid the Gibbs effect. Furthermore, the time function of the numerical source was obtained from the following analytical expression:

$$p_{s,ana}(t) = \frac{r_{sr} - c_0 t}{2r_{sr}} e^{\frac{-\log(2)}{b^2} (r_{sr} - c_0 t)^2} + \frac{r_{sr} + c_0 t}{2r_{sr}} e^{\frac{-\log(2)}{b^2} (r_{sr} + c_0 t)^2},$$
(2.37)

with  $r_{sr}$  the source-receiver distance. This function was transformed to the frequency domain to normalise the calculated impulse responses in DG by the source power spectrum. Likewise, the experimental results were normalised by the B&K 4295 sound power spectra. The source spectra of an equivalent source B&K 4295 was obtained by measurements in the anechoic room of the Department of Medical Physics and Acoustics at Carl von Ossietzky Universität Oldenburg. The corrected results should be taken with care at frequencies below 50 Hz, due to limitations of the anechoic field in the determination of the power spectra of the source. The numerical and experimental results were normalised at 100 Hz, using the results of position M1.

The comparison of numerical and experimental solutions is shown in Figure 2.5 for narrow and 1/3 octave frequency bands. The results are satisfactory considering that

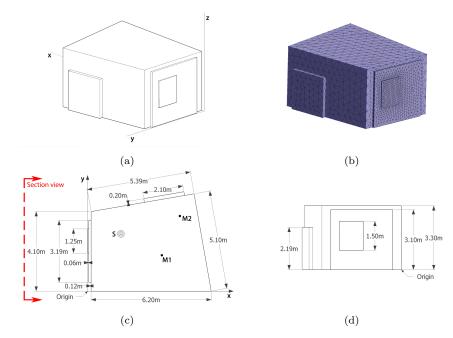


Figure 2.4: Graphical data of the room under investigation: (a) Isometric view; (b) Isometric view with surface elements; (c) Plan view; (d) Section view; (e) Picture during the measurements.

only one uniform real-valued impedance has been used for the whole frequency range of interest. The biggest deviation, 3.6 dB, is found at position M2 in the 63 Hz 1/3 octave band, while for position M1 the maximum deviation is 2.8 dB in the 250 Hz 1/3 octave band. The average deviation for the 1/3 octave band spectra is 1.2 dB for M1 and 2.3 dB for M2. Overall, the deviations shown in Figure 2.5 are within a reasonable range. Factors like the geometrical mismatches between the real room and the model or the uncertainty in the location of the source and microphone positions are influencing the deviations.

#### 2.5 Conclusions

In this chapter, the time-domain nodal discontinuous Galerkin method has been evaluated as a technique to solve the linear acoustic equations for room acoustic purposes. A nodal DG method was used for the evaluation of the spatial derivatives, and for time-integration a low-storage optimised 8-stage explicit Runge-Kutta method was adopted. A new formulation of the impedance BC, which is based on the plane wave reflection coefficient, is proposed to simulate the locally-reacting surfaces with frequency-independent real-valued impedances and its stability is analysed using the energy method.

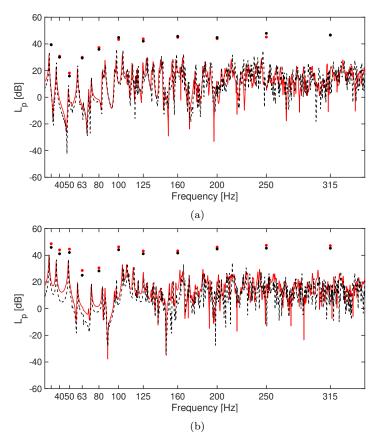


Figure 2.5: Sound pressure level  $L_p$  in the real room configuration for the experimental and the DG results in narrow frequency bands (black broken line and red solid line, respectively) and 1/3 octave bands (black dot and red dot, respectively) for the microphone positions a) M1 and b) M2.

The time-domain nodal discontinuous Galerkin method was implemented for four configurations. The first test case is a free field propagation, where the dissipation error and the dispersion error are investigated using different polynomial orders. Numerical dissipation exists due to the upwind numerical flux. The benefits of using high-order basis are demonstrated by the significant improvement in accuracy. When DPW is around 9, the dissipation error is  $1.1 \cdot 10^{-4}$  dB and the phase error is less than  $3\cdot 10^{-4}\%$  under propagation of one wavelength. In the second configuration, the validity and convergence of the proposed impedance boundary formulation is demonstrated by investigating the single reflection of a point source over a planar impedance surface. It is found that the accuracy is rather independent on the incidence angle. As a third scenario, a cuboid room with rigid boundaries is used, for which a long time (10 seconds) simulation is run. By comparing against the analytical solution, it can be concluded again that with a sufficiently high polynomial order, the dispersion and dissipation error become very small. Finally, the comparison between numerical and experimental solutions shows that DG is a suitable tool for acoustic predictions in rooms. Taking into account that only one uniform real-valued impedance has been used for the whole frequency range of interest, the results are quite satisfactory. In this case, the implementation of frequency dependent BCs will clearly improve the precision of the numerical results.

In this study, the performance of the time-domain nodal DG method is investigated by comparing with analytical solutions and experimental results, without comparing with other commonly-used room acoustics modelling techniques such as FDTD and FEM. The aim of this work is to demonstrate the viability of the DG method to room acoustics modelling, where high-order accuracy and geometrical flexibility are of key importance. With the opportunity to massively parallelise the DG method, it has a great potential as wave-based method for room acoustic purposes. Whereas the results show that high accuracy can be achieved with DG, some issues remain to be addressed. The improvements in accuracy using high-order schemes come at a cost of smaller time step size for the sake of stability. There is a trade-off between a high-order scheme with a small time step and fewer spatial points and a low-order methods, where a larger time step is allowed but a higher number of spatial points are needed to achieve the same accuracy.

# $\begin{array}{c|c} 3 & \text{Discontinuous Galerkin method for} \\ & \text{outdoor acoustics applications} \end{array}$

#### Abstract

Mitigating ground noise from aircrafts by rows of industrial buildlings is numerically studied in this chapter. The environment of interest includes an airport and a nearby residential area, affected by aircraft noise pollution. A sound source representing an aircraft is positioned 4 m above the ground on an airport runway, and the residential area is located approximately 2 km from the runway. Different numbers and shapes of industrial buildings have been modelled in an intervention area between the runway and the affected residential area. To estimate the effect of the noise intervention in the residential region, calculations are conducted for a non-refracting atmosphere and for conditions with downwind from runway to residential area, calculated using computational fluid dynamics (CFD), solving the Reynolds-averaged Navier-Stokes (RANS) equations. Using the effective sound speed approach, the sound field is calculated by solving the linearised acoustic equations using the time-domain nodal discontinuous Galerkin (DG) method. The locally-reacting impedance boundary conditions are used to simulate the boundary conditions at the ground and the building facades. It is found that the noise insertion loss (IL) values are more stable around 10 dB in the configuration without wind over the whole frequency range. However, the IL values fluctuate over frequency between 1.3 dB (at 250 Hz frequency band) to 24.7 dB (at 25 Hz frequency band) in the configuration without wind. Moreover, by implementing the intervention measure C1 under wind condition, the levels produced by a B747-400 aircraft during take-off can be reduced from 73 dB to 55.9 dB and from 55.2 dB to 47.8 dB for the octave bands of 31.5 Hz and 63 Hz, respectively.

#### 3.1 Introduction

The increase in air transportation has resulted in many airports operating at their maximum capacity [162]. One factor limiting the operational capacity of airports is aircraft noise pollution. To address this problem, the international civil aviation organization has proposed a balanced approach to manage noise at airports [163]. The approach consists of four elements: reduction at source, land-use planning and

management, operational procedures for noise abatement, and aircraft operational restrictions. The implementation of these elements has been enforced for European airports by Regulation (EU) No 598/2014 on rules and procedures concerning noise-related operating restrictions at airports [164]. In this study, the land-use planning and management element is studied around Amsterdam Schipol airport. A noise intervention study is conducted to discover a means of reducing the noise from the airport within the surrounding area.

As shown in Figure 3.1, the intervention area is part of Hoofddorp (coloured in blue) and lies between the N201 road (yellow line) and the noise contours of Amsterdam Airport Schiphol (LIB 4 and LIB 5, coloured in green and yellow, respectively). This area lies outside the noise contours of Amsterdam Airport Schiphol and could be used as a new building area. In this study, noise propagation from the airport runway (white line) to Hoofddorp via intervention area is simulated, where the general wind direction (black arrows) blows from the runway to the residential area (downwind condition). This study evaluates the benefits of including buildings such as industrial buildings that do not have strict noise regulations in the intervention area as an aircraft take-off noise mitigating measure. This acoustic evaluation will serve as an initial guideline that can be considered by urban planners designing the zone.

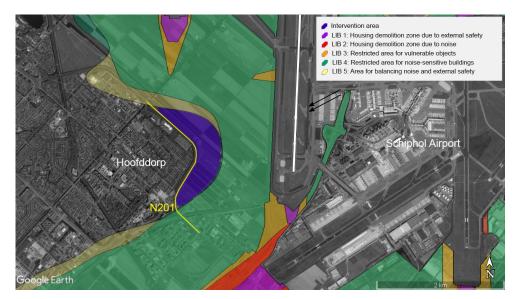


Figure 3.1: Top view of the area of interest.

In this study, two-dimensional sound propagation simulations are conducted in the intervention area, which extends over approximately 2 km. With such a distant propagation, the atmospheric conditions in the area are important. In a certain refractive atmospheric boundary layer (ABL), aircraft noise levels may be greater in the residential area than in an environment with no significant wind or temperature gradients. This is the case, for example, when there is a positive temperature gra-

dient or under downwind conditions. Under these conditions, the sound is refracted downwards, increasing the sound pressure level close to the ground surface [20]. To accurately predict such an environment, a sound propagation model that considers multiple reflections, diffraction, scattering, impedance boundary conditions, and the wind field around buildings is required. A two-step methodology is used to account for the factors mentioned above. First, the wind field on the intervention area is modelled using computational fluid dynamics (CFD). Second, the wind field is adopted in a wave-based computational acoustic (CA) method to calculate the sound field.

There are several wave-based CA methods that can account for sound propagation in an ABL. One example is the parabolic equation (PE) method [20]. In the PE method, the sound field is computed by solving a PE that follows the acoustic wave equation by neglecting the contributions of sound waves with large elevation angles to the field, as well as back propagation. This method was used by Salomons and Rasmussen [165], [166] to model the wind effect on the performance of a noise screen. They determined the wind field around the noise screen using a CFD simulation and wind-tunnel experiments. The wind field was then adopted using the effective sound speed approach. PE method was also used by Rosenbaum [167] to predict the sound propagation of aircraft noise, and by Bosschaart et al., [168] to predict the noise attenuation of sound scattering elements from ground taxiing aircraft in the vicinity of Amsterdam Airport Schiphol. The PE method is a computationally efficient CA method. However, it has a drawback for the present scenario of Figure 3.1 that the reflected waves are not taken into account.

Another wave-based CA method is the finite difference time domain (FDTD) method. Van Renterghem and Botteldooren used the FDTD method to predict the effects of wind on the performance of noise barriers [169]. The wind field was determined using the CFD approach and adapted to the sound propagation using linearised Euler equations. The method was extended into a more efficient wave-based CA method by combining the PE and FDTD approaches [170], [171]. Heimann applied the FDTD method to 3-D idealised urban situations to investigate the effects of different roof types, soil properties, wind flow, and turbulence on sound propagation [172]. Oshima et al. used the FDTD method to model the atmospheric sound propagation on actual urban terrain. They employed the digital geographical information to create a realistic urban geometry, and a CFD technique was applied to obtain the wind field [173]. The FDTD method has the advantage of being robust and straightforward in implementation. However, it is unable to model complex geometries, for example, all grid points in the simulation domain are structured, which can result in non-physical scattering from a tilted smooth surface.

A more recent CA method is the pseudo-spectral time-domain (PSTD) method. Hornikx et al. [108] used the PSTD method to compute atmospheric sound propagation for several applications such as noise barriers and urban canyons. Hornikx et al. [174] also modelled sound propagation in generic 2-D urban configurations with multiple building blocks under a downward refracting ABL. The wind field was computed using a CFD approach and values were adopted in the linearised acoustic equations using the effective sound speed approach. The PSTD method is a com-

putationally efficient method, and it requires only two grid points per wavelength to achieve good accuracy. However, similar to the FDTD method, there are limitations in the structured approximation of the geometries and the frequency-dependent impedance boundary conditions (BC) implementation.

Another numerical method is the finite element method (FEM). This method was rarely used for outdoor sound propagation due to special treatment in solving the acoustic wave equation for exterior problems [128], [175]. However, as commercial software has been developed, the FEM has become increasingly used in urban sound propagation. Pelat et al. [176] modelled sound propagation in a street canyon with buildings of different sizes using FEM and modal-FEM by solving acoustic wave equation. The same method was also used by Miguel et al.[177] to evaluate sound propagation in 3-D periodic urban canyons. The FEM was also used to investigate the effect of several façade configurations on the sound field in street canyons [178], and to calculate insertion loss from noise barriers [179]. There are also other CA methods that can be used to simulate sound propagation in urban environments, such as the boundary element method (BEM), fast-field programme (FFP), and equivalent source method (ESM). More details on other CA methods can be found in Ref. [180].

In this study, the time-domain nodal discontinuous Galerkin (DG) method [112] is used to investigate noise intervention cases in an airport environment. The nodal DG method has several advantages compared to other CA methods. For example, it can use an unstructured mesh to represent the simulation domain, unlike the FDTD and PSTD methods that use structured grids/staircase approximation. In addition, the spatially dependent atmospheric field variables, such as wind speed, can be represented, which is not possible in the BEM, ESM, and FFP methods. Another advantage is that the DG variational formulation results in an element-wise formulation unlike FEM. Therefore, it allows for relatively easy parallel computation, especially for large domains such as an airport environment. The accuracy of the nodal DG method can also be improved by reducing the element size or by increasing the polynomial order, the so-called hp refinement [181]. Moreover, the recent developments by Wang et al. [182] and Wang and Hornikx [183] have shown the ability of the nodal DG method to deal with both frequency-independent and -dependent impedance BCs.

The following sections of this chapter is organised as follows: Section 3.2 provides details of the calculation models for the noise intervention cases; In Section 3.3, methodologies for calculating the wind flow field and sound propagation are presented and the computational setting and the processing of the results are described as well; The simulation results of all configurations are discussed in Section 3.4; Finally, conclusions and suggestions for further work can be found in Section 3.5. In the appendices, the validation on the nodal DG methodology is given with the details of the impedance BCs used for the simulation.

#### 3.2 Noise intervention case

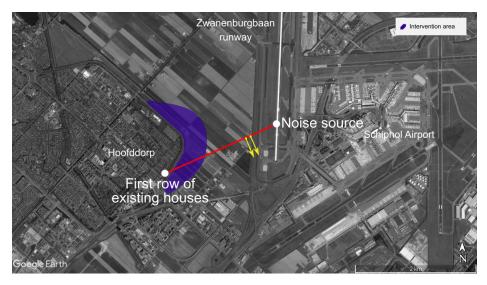


Figure 3.2: The top view of the simulated two-dimensional scenarios between the noise source and the first row of residential houses. Two arrows represent the viewing angle of the computational cases.

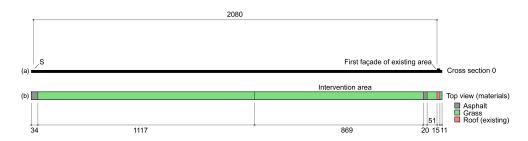


Figure 3.3: (a) Cross-sectional view of the case without noise intervention (case 0). (b) Colors in the top view specify materials (asphalt and grass) considered. Dimensions in meters.

The red line in Figure 3.2 represents the top view of the 2-D section of the noise intervention case. The line is drawn at an angle of about 45 degrees from the runway axis. This direction corresponds to the angle where the main lobe is located in the directivity pattern of aircraft noise, and it is assumed as the direction of high noise radiation. The computational domain was chosen to represent a simplified geometry between the source and the first row of existing houses in the residential area.

Figure 3.3 (a) shows the cross-sectional view of the computational domain without

the noise intervention (case 0). The origin of the coordinate system is at the leftmost side of the domain on the ground level, and the sound source (S) is placed at  $(x_s, z_s) = (11, 4)$  m. Figure 3.3 (b) shows the materials used in the configurations (excluding the surfaces of the buildings). The first row of residential houses is modelled on the rightmost side of the simulation domain. The height of the house is 8 m. The total dimensions of the simulation domain are  $(L_x, L_z) = (2117, 70)$  m.

The noise mitigation concept is to populate the intervention area of 869 m depth with industrial buildings to significantly reduce the noise level from the runway to Hoofddorp. In this study, we consider two geometrical shapes of buildings of width 50 m and height 10 m with flat (Case 1) and tilted roofs (Case 2) shown in Figure 3.4.

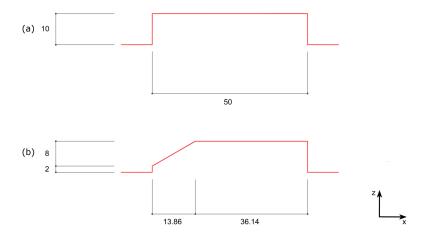


Figure 3.4: Cross-sectional view of building geometries in the intervention area representing (a) case 1: flat roof and (b) case 2: tilted roof. Dimensions in meters.

The tilted roof was considered to investigate the influence of upward sound reflection by the tilted roofs on the noise mitigation. The buildings are placed in the intervention area with certain distance in between, as listed below. Figures 3.5-3.6 show the cross-sectional and top views of the simulation cases.

- Case 1a: 10 buildings with a rectangular shape, and a separation of 30 m between the buildings (Figure 3.5 (a)).
- Case 2a: 10 buildings with tilted roofs (Figure 3.5 (b)).
- Case 1b: 14 buildings with a rectangular shape, and a separation of 5 m between the buildings (Figure 3.6 (a)).
- Case 2b: 14 buildings with tilted roofs (Figure 3.6 (b)).

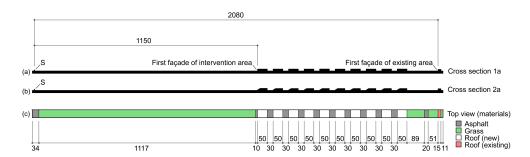


Figure 3.5: (a) Cross-sectional view of intervention case 1a, (b) Cross-sectional view of intervention case 2a, (c) top view of intervention case 1a and 2a. (dimensions in meters)

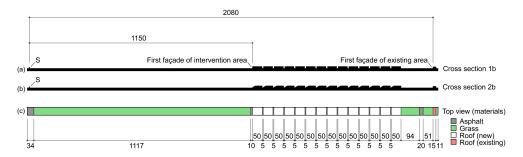


Figure 3.6: (a) Cross-sectional view of intervention case 1b, (b) Cross-sectional view of intervention case 2b, (c) top view of intervention case 1b and 2b. (dimensions in meters)

For each case, two atmospheric conditions have been studied: a static atmosphere (without wind), and a refractive atmosphere where the wind blowing from the NE direction (see Figure 3.1).

In addition, different sound absorption scenarios are considered in the impedance BCs of the rooftops to investigate the influence of different sound-absorbing mechanisms. Two types of acoustic absorption at the roofs of the new buildings are evaluated for all four intervention cases mentioned above (cases 1a, 1b, 2a, and 2b): roofs with a constant sound absorption coefficient, and a different resonant absorber for each roof. In total, there are 18 configurations of the simulation cases, including two configurations of case 0 (C0 and C0w, without wind and with wind, respectively). All the configurations are listed in Table 3.1 and the notations presented in the table will be used to present the results of the acoustic simulations.

Configuration #		Cases	Cases Reflection coefficients $R$ [-]				
Static atmosphere	Refractive atmosphere	· Casas	Asphalt	$\operatorname{Grass}^{\dagger}$	Roof	Roof <sup>2</sup>	Façades
C1	C1w	1a	0.95	A4	T.A.*	0.9	0.9
C2	C2w	1b	0.95	A4	T.A.*	0.9	0.9
C3	C3w	2a	0.95	A4	T.A.*	0.9	0.9
C4	C4w	2b	0.95	A4	T.A.*	0.9	0.9
C5	C5w	1a	0.95	A4	0.9	0.9	0.9
C6	C6w	1b	0.95	A4	0.9	0.9	0.9
C7	C7w	2a	0.95	A4	0.9	0.9	0.9
C8	C8w	2b	0.95	A4	0.9	0.9	0.9
C0	C0w	0	0.95	A4	-	0.9	0.9

A4 denotes the Attenborough's four parameters model (see Appendices B-C.1).

Table 3.1: Simulation configurations and reflection coefficients of the materials in each case.

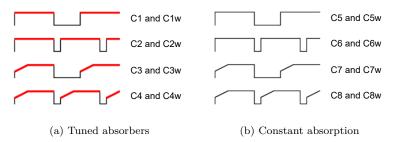


Figure 3.7: Notation to facilitate the reading of the results for the different configurations.

Additionally, Table 3.1 contains the normal-incidence reflection coefficients (R) of the different materials used in the model. For materials with a frequency-independent impedance, a constant value is given in the table. For the frequency-dependent absorption coefficient, i.e., the grass surfaces and resonant absorbers, the values are presented in Appendices C.1 and C.2, respectively. Each new building rooftop has a dedicated resonant absorber tuned to a different frequency in several configurations. Each resonant absorber is tuned at the centre frequencies of the one-third octave bands starting from 20 Hz. For cases 'a', 10 absorbers are used, while for cases 'b', 14 absorbers are used. Figure 3.7 is presented to facilitate the understanding of the differences between simulation cases. The red lines are where the frequency-dependent impedance BCs of tuned absorbers are applied, whereas the black lines are where the frequency-independent impedance BCs are applied.

Several receivers are placed in the domain as indicated in Table 3.2 and Table 3.3, for

<sup>&</sup>lt;sup>1</sup> Roofs of new industrial buildings

<sup>&</sup>lt;sup>2</sup> Roof of residential house

<sup>\*</sup> Tuned-resonant absorbers (see Appendix C.2)

Index	(x,z) [m]	x-distance [m]		
mach		Source-receiver	Previous receiver	
Source (S)	(11,4)	-	-	
$P1_a$	(1159,1.7)	1148	-	
$P2_a$	(1239,1.7)	1228	80	
$P3_a$	(1319,1.7)	1308	80	
$P4_a$	(1399, 1.7)	1388	80	
$P5_a$	(1479, 1.7)	1468	80	
$P6_a$	(1559, 1.7)	1548	80	
$P7_a$	(1639, 1.7)	1628	80	
$P8_a$	(1719,1.7)	1708	80	
$P9_a$	(1799, 1.7)	1788	80	
$P10_a$	(1879, 1.7)	1868	80	
PR	(2089, 1.7)	2078	210	

Table 3.2: Source and receiver positions for cases 0, 1a and 2a.

geometry cases a (Figure 3.5) and cases b (Figure 3.6), respectively. These tables are given in Section 3.4 to facilitate easier reading of the results. All receivers are located at 2 m before the building façades and 1.7 m above the ground. There are two main areas of interest related to the placement of receivers. The first one is close to the existing houses. The insertion loss is calculated at this receiver position to capture the impact of new buildings. The second area is the intervention area. By placing receivers in front of the façades of each new building, the sound pressure level can be compared with one another. Tables 3.2 and 3.3, additionally, show the horizontal distance between source and receiver and the distance to the previous receiver.

#### 3.3 Methodology

#### 3.3.1 Wind flow modelling

#### Computational model

Modelling wind flow over building canyons is important in regard to urban acoustics, as shown in Refs. [166], [174], [184]. In this study, the wind flow over the building canyons in the intervention area was obtained by a CFD model that assumes neutral atmospheric conditions where thermal effects (e.g., buoyancy) are neglected. The flow is assumed to be stationary, and the geometry is two dimensional.

The open-source finite-volume code OpenFOAM 2.4 [185], [186] was used to solve the incompressible Reynolds-averaged Navier-Stokes (RANS) equations. For the RANS equations, the standard  $k - \epsilon$  turbulence model [187] is used to complete the system of equations. The values of constants used in the  $k - \epsilon$  turbulence model are presented in Table 3.4, following Ref. [188]. Further numerical and modelling details of the turbulence model can be found in the literature, e.g., Ref. [189].

Index	(x,z) [m]	x-distance [m]		
mach	(w, ~) [III]	Source-receiver	Previous receiver	
Source (S)	(11,4)	-	-	
$P1_b$	(1159, 1.7)	1148	-	
$P2_b$	(1214,1.7)	1203	55	
$P3_b$	(1269, 1.7)	1258	55	
$P4_b$	(1324,1.7)	1313	55	
$P5_b$	(1379,1.7)	1368	55	
$P6_b$	(1434,1.7)	1423	55	
$P7_b$	(1489, 1.7)	1478	55	
$P8_b$	(1544, 1.7)	1533	55	
$P9_b$	(1599, 1.7)	1588	55	
$P10_b$	(1654, 1.7)	1643	55	
$P11_b$	(1709, 1.7)	1698	55	
$P12_b$	(1764, 1.7)	1753	55	
$P13_b$	(1819,1.7)	1808	55	
$P14_b$	(1874,1.7)	1863	55	
PR	(2089, 1.7)	2078	215	

Table 3.3: Source and receiver positions for cases 'b' and case 0.

Parameter	Value
$C_{\mu}$	0.09
$C_{\epsilon 1}$	1.44
$C_{\epsilon 2}$	1.92
$\sigma_k$	1.0
$\sigma_\epsilon$	1.3

Table 3.4: The  $k - \epsilon$  turbulence model constants.

#### Computational settings

In the noise intervention case, the atmospheric conditions are simulated by CFD techniques for all configurations with the wind (see Table 3.1). In the computational domain, a logarithmic horizontal velocity profile is imposed at the inlet as:

$$U(z) = \frac{u^*}{\kappa} \ln \left( \frac{z + z_0}{z_0} \right), \tag{3.1}$$

with friction velocity  $u^* = 0.888 \,\mathrm{m/s}$ , the aerodynamic roughness length  $z_0 = 0.1 \,\mathrm{m}$ , and the von Kármán constant  $\kappa = 0.41$ . The selected inlet condition is considered to be quite extreme, meaning that the wind velocity is high (10 m/s at 10 m height). Moreover, the grass and asphalt surfaces are modelled with a wall function suitable for the atmospheric boundary layer with a roughness constant  $C_S = 5$ , and the equivalent sand-grain roughness height  $k_S$  is calculated as proposed in Ref. [190].

The building roofs and façades are modelled with a wall-function without roughness (i.e., smooth), and the uppermost boundary is modelled with a slip wall. The detailed locations of these surfaces can be seen in Figures 3.3-3.6.

The computational grids of the configurations are generated using structured hexahedral cells. In total, the number of cells ranged from  $46 \cdot 10^3$  to  $93 \cdot 10^3$  depending on the configuration. The domain size is constructed taking the suggestions in Ref. [191]. The inlet is located at 25H in front of the first building façades, and the upper boundary is at 10H, where H is the height of the new buildings (10 m). In this case, the wind profile before the inlet is assumed following Equation (3.1) as the grass and asphalt surfaces are assumed to be flat. The outlet was placed at a sufficient distance downstream ( $\approx 100H$ ). Finally, the mean wind horizontal velocity field was interpolated onto the acoustic domain for the subsequent sound propagation modelling. Linear interpolation was done via a MATLAB function based on the Delaunay triangulation of the horizontal velocity field.

#### 3.3.2 Sound propagation modelling

#### Governing equations

The sound propagation is modelled by linearised acoustic equations for the acoustic pressure and velocity components:

$$\frac{\partial \mathbf{v}}{\partial t} + \frac{1}{\rho_0} \nabla p = 0, 
\frac{\partial p}{\partial t} + \rho_0 c_{eff}^2 \nabla \cdot \mathbf{v} = 0,$$
(3.2)

where  $\mathbf{v} = [u, v]^T$  is the particle velocity, p is the sound pressure, and  $\rho_0$  is the air density. The effect of the mean wind component is given by the effective sound speed  $c_{eff} = c_0 + U(x, z)$ , where U(x, z) is the horizontal mean wind component and  $c_0$  is the adiabatic sound speed in air. This approach is commonly adopted for atmospheric sound propagation modelling when the horizontal propagation distances are significantly larger than the vertical distances, or when horizontal wind speed components are dominant over the vertical ones [20]. Moreover, the effective sound speed approach is a reasonably accurate alternative to the linearised Euler equations for atmospheric sound propagation modelling for the low-frequency region as shown in Ref. [184], which is the frequency range of interest of this study. Also, because atmospheric acoustic absorption is more significant at higher frequencies and the influence in the low-frequency range is presumed minimal, it is omitted.

To solve Equations (3.2) numerically, the nodal DG method is used. This method discretises the computational domain using non-overlapping simplex elements. The particle velocity (v) and pressure (p) are approximated using 2-D Lagrange interpolation polynomial with order N in each local element to solve the spatial derivatives. Moreover, numerical fluxes between adjacent elements are used to satisfy the global connectivity. In this study, the triangular elements and the upwind numerical

flux is used throughout the whole domain [112]. Afterwards, the time-derivatives are integrated from the initial conditions using an eight-stage low-storage explicit Runge-Kutta method [148]. The results from the DG simulation was validated by the comparison with the results from FEM simulation. The details regarding this validation and its results are shown in Appendix B. Moreover, the detailed implementation of this method can be found in [112], [182], [192]. For this work, an in-house nodal DG algorithm implemented in MATLAB is used.

#### Impedance boundary conditions

The ground and the building envelopes are simulated by impedance BCs, following the locally reacting frequency-independent and dependent impedance BCs in the nodal DG method [182], [183]. In the nodal DG method, the impedance BC is implemented by decomposing the numerical flux along the boundary surfaces. This decomposition corresponds to the incoming and outgoing acoustic characteristics waves  $(\varpi_n^{in}(\omega), \varpi_n^{out}(\omega))$  that are oriented towards the outward-normal direction of the boundary surface [183]. By utilising these waves, the reflection coefficient is defined as:

$$R(\omega) = \frac{\varpi_n^{in}(\omega)}{\varpi_n^{out}(\omega)} = \frac{Z_s(\omega) - 1}{Z_s(\omega) + 1},$$
(3.3)

with  $Z_s(\omega)$  the surface impedance normalized to the characteristic impedance of air. Notice that  $Z_s(\omega)$  can be a complex number and the reflection coefficient  $R(\omega)$  is formulated in the frequency-domain.

Several steps should be taken to translate the quantity defined in the frequency domain into its time-domain counterpart. The first step is to transform the normalised surface impedance values  $(Z_s(\omega))$  into the corresponding normal reflection coefficients within the frequency range of interest  $(R(\omega))$ , as shown in Equation (3.3). The  $Z_s(\omega)$  values can be obtained from measurements or an acoustic model. Afterwards, the reflection coefficients should be approximated by a sum of rational functions

$$R(\omega) \approx R_{\infty} + \sum_{k=1}^{S} \frac{A_k}{\zeta_k + i\omega} + \sum_{l=1}^{T} \left( \frac{B_l i\omega + C_l \beta_l + \alpha_l B_l}{(\alpha_l + i\omega)^2 + \beta_l^2} \right), \tag{3.4}$$

with  $[R_{\infty}, A_k, B_l, C_l, \zeta_k, \alpha_l, \beta_l]$  all being real numbers. The approximation of the reflection coefficients  $R(\omega)$  in the form of Equation (3.4) is essential since this can be easily transformed into a function of time by an inverse Fourier transformation. The values of  $\zeta_k, \alpha_l, \beta_l$  should be positive to satisfy the causality and the reality conditions. An optimisation method has been employed to obtain all the coefficients in Equation (3.4) such as shown in Appendix B.

Each term in Equation (3.4) can be explained in terms of its absorption coefficient  $(\alpha = 1 - |R|^2)$ . The first term is the constant part of the reflection coefficient. It may be used to model relatively hard surfaces with a small sound absorption value at all frequencies. The second complex-valued term represents an acoustic low-pass filter. In practice, a surface with this term alone could mimic the behaviour of the sound

Parameter	Value
Medium density $\rho_0$ [kg/m <sup>3</sup> ]	1.2
Speed of sound $c_0$ [m/s]	344
Maximum frequency $f_{max}$ [Hz]	282
DG polynomial order $N$	6
Number of discrete mesh elements $K$	436k - 443k
Degrees of freedom per wavelength DPW	≈10
Gaussian source half-bandwidth $b$ [m]	0.5
Sound pressure recording duration $T[s]$	14
Time step $\Delta t$ [s]	$(8.4 - 9.1) \cdot 10^{-5}$

Table 3.5: Main parameters used in the nodal DG simulation for noise intervention case.

reflection by a porous material. The last complex-valued term corresponds with an acoustic band-pass filter. The last and the first terms can be combined to create an acoustic band-stop filter. This combination could mimic a resonant absorber, where the sound absorption is significant only around the resonance frequency.

After obtaining  $R(\omega)$ , the inverse Fourier transform is applied to obtain the time-domain reflection response function. The last step is to implement the time-domain reflection response function into the numerical flux on the boundaries. The details on this implementation can be observed in the work of Wang and Hornikx [183].

#### Computational settings

The intervention area was discretized in triangular elements using the meshing software Gmsh [159], and all configurations use the same Gaussian-shaped initial condition as follows:

$$p(x,z) = e^{-\frac{\ln(2)}{b^2}((x-x_s)^2 + (z-z_s)^2)},$$
  

$$v(x,z) = 0,$$
(3.5)

with  $(x_s, z_s) = (11, 4)$  m, and b = 0.5 is the width of the pulse. This width is taken to have the source power up to the 250 octave band Hz. The maximum frequency of interest  $(f_{max})$  in this octave band is 282 Hz. To indicate the cost and accuracy of the computation related to this maximum frequency, the number of degrees of freedom per wavelength DPW is used:

$$DPW = \frac{c_0}{f_{max}} \sqrt{\frac{N_p K}{S_a}}, \tag{3.6}$$

where  $N_p = (N+2)(N+1)/2$  is the number of nodes in each element with N is the DG model polynomial order, K is the number of triangular elements of the DG mesh, and  $S_a$  [m<sup>2</sup>] is the surface area of the computational domain. For all noise intervention configurations, the general parameters are summarised in Table 3.5.

Moreover, the left, right, and upper edges of the computational domain are terminated by a perfectly matched layer (PML) to get reflection-free terminations. In all

cases, the thickness of the PML is 20 m with a maximum element size of 1 m. The PML has previously been applied to the nodal DG method for acoustic application by, Pagán Muñoz [192], and it is adopted in this work.

According to Ref. [20], Sound propagation in a refractive atmosphere (such as the researched scenarios where downwind circumstances are included) has a so-called turning point of sound rays, which corresponds to the maximum height before the sound begins to refract towards the ground. In this study, the total height of the computational domain is 70 m. This dimension guarantees the highest turning point, which is about 64 m, lies inside the domain for the investigated scenarios.

#### 3.3.3 Acoustic quantifiers

Two quantities are calculated to evaluate the acoustic conditions of the studied cases. The first quantity is the sound pressure level:

$$L_p(f_n, \mathbf{x}_i) = 10 \log_{10} \left( \frac{1}{2} \frac{|P(f_n, \mathbf{x}_i)|^2}{P_{ref}^2} \right),$$
 (3.7)

where P is the complex sound pressure in frequency-domain, and  $P_{ref} = 2 \cdot 10^{-5} \,\text{Pa}$  is the sound pressure reference.  $f_n$  denotes the third-octave band center frequency, and  $x_i$  is the discrete receiver location in space. The second quantity is the insertion loss:

$$IL(f, \mathbf{x}_i) = L_{p,nai}(f, \mathbf{x}_i) - L_{p,ai}(f, \mathbf{x}_i), \tag{3.8}$$

where  $L_{p,nai}$  and  $L_{p,ai}$  are the sound pressure level without and with an acoustic intervention, respectively. This quantity is used to show the effectiveness of a noise intervention configuration where a positive IL value represents a noise reduction in a certain frequency and location. The IL is presented in 1/3 octave bands between 25 Hz and 250 Hz near the residential buildings at location PR according to Tables 3.2 or 3.3.

Additionally, in the noise intervention case, the sound pressure level  $(L_p)$  [dB] from a typical operating aircraft during ground operation is evaluated at different locations for the frequency bands of 31.5 Hz and 63 Hz. These bands are where the acoustic energy is primarily concentrated for the aircraft take-off operation [193]. The sound pressure  $p_{2D}(t)$  [Pa] has been recorded at the receiver locations (see Tables 3.2 and 3.3) to obtain the acoustic quantities of interest. The time recordings have been corrected for each location by changing the cylindrical spreading of sound as obtained from the 2-D simulation to spherical spreading of sound, which holds for 3-D simulations. This correction has been conducted to approximate the corresponding 3-D results  $p_{3D}(t)$  according to Equation (3.9) [180]. Finally,  $p_{3D}(t)$  were transformed into the frequency domain by using the Fourier transform. It needs to be emphasised that this correction does not return the 3-D solution, as the simulation was conducted where both the source and the domain were 2-D. This acts as an approximation where

the buildings are assumed to be invariant in the perpendicular direction.

$$p_{3D}(t) = p_{2D}(t) \frac{1}{\sqrt{c_0 t}}. (3.9)$$

#### 3.4 Results and discussions

#### 3.4.1 Noise intervention case results

#### Wind flow around new buildings

Figures 3.8-3.11 show the wind fields of the horizontal velocity in the range between  $x=1100\,\mathrm{m}$  to  $2127\,\mathrm{m}$  and  $z=0\,\mathrm{m}$  to  $50\,\mathrm{m}$ , around the intervention area. Prior to this region ( $x<1100\,\mathrm{m}$ ), the wind flow deviates only slightly from the inlet profile because there is no obstacle presented. The figures show that a negative wind speed is generated behind each building, indicating the formation of wind vortices, and the wind flows often to have a similar profile in each canyon.

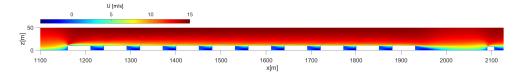


Figure 3.8: The horizontal wind velocity for Case 1a for  $x = 1100 \,\mathrm{m}$  to 2127 m.

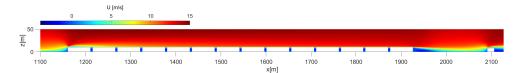


Figure 3.9: The horizontal wind velocity for Case 1b for  $x = 1100 \,\mathrm{m}$  to  $2127 \,\mathrm{m}$ .

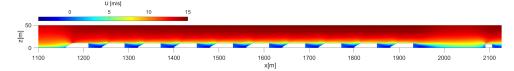


Figure 3.10: The horizontal wind velocity for Case 2a for  $x = 1100 \,\mathrm{m}$  to  $2127 \,\mathrm{m}$ .

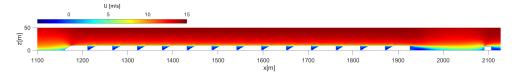


Figure 3.11: The horizontal wind velocity for Case 2b for  $x = 1100 \,\mathrm{m}$  to  $2127 \,\mathrm{m}$ .

#### Insertion loss at the residential building façade

To compute IL, intervention cases C1 to C8 are compared with configuration C0 for the static atmosphere; while scenarios C1w to C8w are compared with C0w for the refracting atmosphere (see Table 3.1). In this section, the IL results for the different configurations are presented in Figures 3.12 to 3.14. In each figure, one main feature of the configurations is compared:

- Figure 3.12 presents the comparison of the configurations with a different distribution of new buildings.
- Figure 3.13 presents the comparison of the configurations with a different roof type.
- Figure 3.14 presents the comparison of the configurations with a different type of roof absorption.

The investigated configurations, show that the noise intervention measures have positive impact to the residential building, with all IL values are positive, showing that there is noise shielding effect from the industrial buildings as shown in Figures 3.12 to 3.14. The IL values are more stable around 10 dB for the configurations with static atmosphere, while the IL values fluctuate over frequency between 1.3 dB (at 250 Hz frequency band) to 24.7 dB (at 25 Hz frequency band) in the refracting atmosphere configurations.

The downward refractive atmosphere reduces the shielding effect of the buildings as the IL values become smaller at all frequencies except at 25 Hz frequency band, when compared to the IL values of static atmosphere. This effect also decreases with increasing frequency as the IL values become smaller at high frequencies. These results are also consistent with the study by Hornikx et al. [174]. In addition, the IL values vary more with frequency compared to the static atmosphere as shown in Figures 3.12 to 3.14. This could be due to the fact that sound is refracted in the canyons and excites the canyon modes more. For all configurations, the IL maximum values for the static atmosphere are at the 1/3 frequency bands between 50 and 100 Hz, and when wind conditions are included, the IL maximum values are at the 1/3 frequency band of 25 Hz. The reason for the significantly higher IL values at the 25 Hz frequency band is not yet known and requires further investigation.

Considering the results for the configurations with a different distribution of buildings in Figure 3.12, a lower number of buildings in the intervention area is favoured. This analysis can be drawn at least for the static atmosphere, where the average IL value

is 1 dB higher for a lower number of buildings. Schiff et al. [194] have shown that the sound attenuation of building canyons depends on the alley width (relative to the total distance between receiver and source points) and also on the number of building canyons. Increasing these two factors has a positive effect on the IL value. Thus, there is no preference between these two factors. In this study, the attenuation of 10 buildings with wider alleys is greater than that of 14 buildings with smaller alleys for a constant field length between source and receiver. However, this feature is very limited with only a 1 dB higher IL average value.

Figure 3.13 shows the comparison of the configurations with a different building geometry. The influence of this feature is very limited in this case, as the average IL for the tilted-roof is only 0.4 dB higher than the flat-roof. This means that buildings with tilted roofs offer small advantages over flat roofs in the current configurations.

Moreover, the analysis of the different types of roof absorption is presented in Figure 3.14. For a static atmosphere, tuned absorbers are more beneficial than the constant absorption for all frequency bands, with the average IL is 0.9 dB higher. The minimal gain compared to the constant absorber may be due to the limited interaction between the sound waves and the roof of the building. As shown in the Appendix C.2, each roof is tuned to a different resonant absorber, and the interaction only occurs when sound waves pass through each roof of the building. For the refracting atmosphere, the conclusion is more difficult to reach.

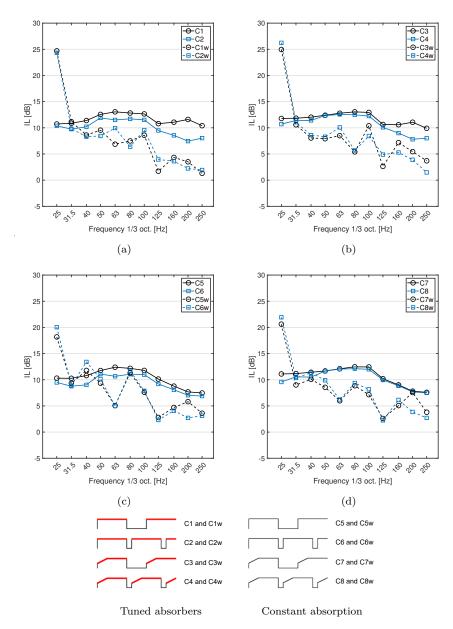


Figure 3.12: Comparison of results between configurations with a different distribution of buildings.

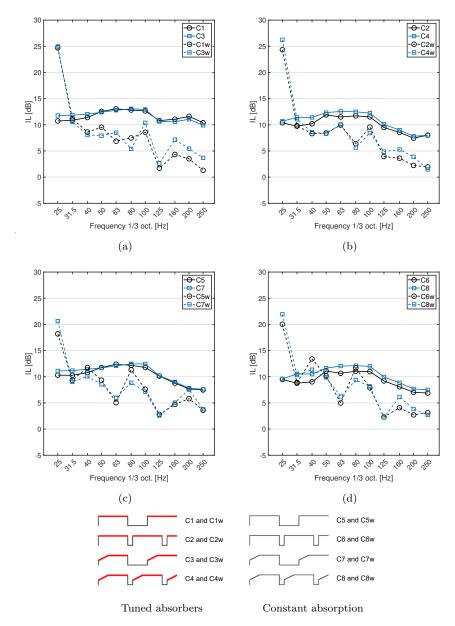


Figure 3.13: Comparison of results between configurations with a different building geometry.

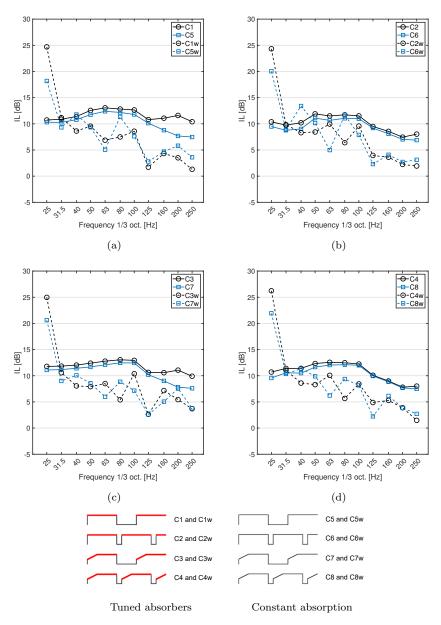


Figure 3.14: Comparison of results between configurations with a different type of roof absorption.

#### Sound pressure level due to the aircraft noise emission

The sound pressure level  $(L_p)$  has been evaluated at all the receiver locations indicated in Tables 3.2 and 3.3. The computed values of  $L_p$  results are presented for the full

octave frequency bands of 31.5 Hz and 63 Hz. The calculations are performed using the sound power levels  $L_W$  emitted by a sound source corresponding to an aircraft type B747-400, as included in the technical report [195] (no source directivity is included in the calculations). Type B747-400 is one of the most common aircraft currently operating at Amsterdam Airport Schiphol [195]. The results of the sound pressure level  $L_p$  are presented in Figures 3.15 and 3.16 for the static atmosphere and the refractive atmosphere, respectively.

Figures 3.15 and 3.16 show the benefits of including the proposed noise control measures in the intervention area, as already seen in Section 3.4.1. In general, noise reduction is quite significant for all cases and locations. The maximum noise reduction between buildings in the intervention area reaches 22.7 and 31.9 dB for the octave band of 31.5 Hz for cases 'a' and 'b', respectively. While for the 63 Hz octave band, the maximum noise reduction for the same cases equals to 26.8 and 35.5 dB. It is important to remind that the recording positions  $P1_a$  to  $P10_a$  and  $P1_b$  to  $P14_b$  are equally spaced, respectively, however, PR is placed at a further distance (see Tables 3.2 and 3.3). With the exception of several some results of the recording positions  $P1_a$  and  $P1_b$  (right before the first row of buildings of the intervention area), the sound pressure levels are lower than those obtained under the current situation, i.e., no intervention. The intervention is less effective at the recording position PR (right before the first row of residential buildings) than for some locations situated in between the new buildings.

The overall levels at the residential buildings (PR) without any acoustic intervention produced by an aircraft type B747-400 during take-off roll operation (not including source directivity in the calculations) can reach 73 dB when including wind for the 31.5 Hz octave band and 55.3 dB for the 63 Hz band. When including the evaluated acoustic interventions, the levels can be lowered down to 55.7 dB (octave band 31.5 Hz) for intervention C4w, and 46.3 dB (octave band 63 Hz) for intervention C6w.

Additionally, Figures 3.15 and 3.16 show that the first building of the intervention area reduces quite significantly the sound pressure levels due to the shielding from the direct sound. It can be observed that for the configurations with tuned absorbers on the roofs, the first buildings have a higher impact on reducing the noise levels. This effect is clearer for the results of the 31.5 Hz octave band. This is due to the way the tuned absorbers are spatially distributed. The absorbers of the first buildings are tuned to the lowest frequency bands (see Appendix C.2). However, the results of each graph in Figures 3.15 and 3.16 converge approximately to the same levels at positions R.

The results show that the cases 'b', i.e., the configurations with more buildings in the intervention area (Figures 3.15b, 3.15d, 3.16b, and 3.16d), present a higher noise reduction in the canyons between buildings. For these configurations, the canyons are narrower (5 m) than the ones of cases 'a' (30 m). In general, for the positions between buildings, configurations with a tilted roof present a better performance than the cases with flat roofs. For static atmosphere, the average noise reduction for each receiver at 31.5 Hz and 62 Hz for the tilted roof is 1.5 dB and 2.6 dB

higher, respectively, and for refractive atmosphere, the average noise reduction for each receiver at  $31.5~{\rm Hz}$  and  $62~{\rm Hz}$  for the pitched roof is  $0.7~{\rm dB}$  and  $1.2~{\rm dB}$  higher, respectively.

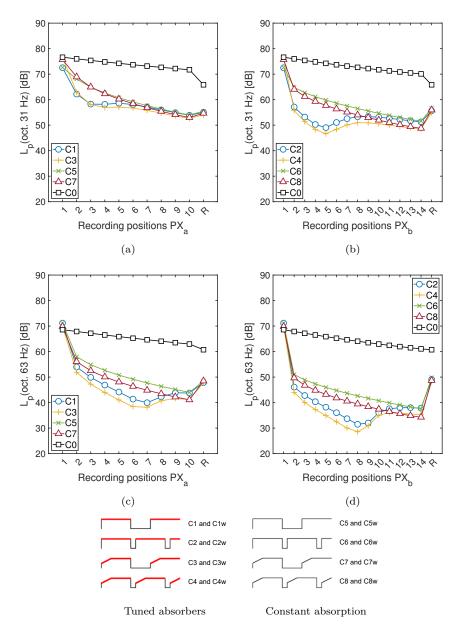


Figure 3.15: Comparison of sound pressure level results for ground operations of aircraft type B747-400 under a static atmosphere. Graphs (a) and (b) present the results for the octave frequency band of 31.5 Hz, and (c) and (d) for the band of 63 Hz. Graphs (a) and (c) show the results for configuration cases 'a' (10 new buildings), while (b) and (d) present the results for cases 'b' (14 new buildings). C0 represents the no intervention configuration under a static atmosphere.

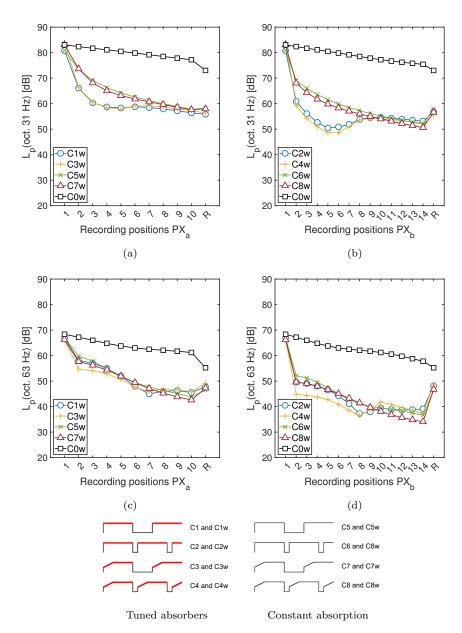


Figure 3.16: Comparison of sound pressure level results for ground operations of aircraft type B747-400 under a refractive atmosphere (wind). Graphs (a) and (b) present the results for the octave frequency band of 31.5 Hz, and (c) and (d) for the band of 63 Hz. Graphs (a) and (c) show the results for configuration cases 'a' (10 new buildings), while (b) and (d) present the results for cases 'b' (14 new buildings). C0w represents the no intervention configuration under a refractive atmosphere.

## 3.5 Conclusions

In this chapter, the nodal DG method has been evaluated as a technique to solve the linear acoustic equations for outdoor sound propagation. This study simulates distant sound propagation over the atmospheric boundary layer with an effective sound speed approach. This method is validated by comparing the results to those obtained using the finite element method. The comparison between the two results shows close agreement at various impedance boundary conditions.

Moreover, this method evaluates the acoustic effects of using industrial buildings around Amsterdam Airport Schiphol as noise mitigation measures. The atmospheric condition around the buildings is simulated using CFD-RANS, and it significantly influences the sound field in the residential area. It can be concluded that the building topology studied is quite effective for the atmospheric sound propagation problem at hand. Noise reduction is significant for all configurations at the residential building site and in the intervention area. Some results of this study are:

- The IL values are more stable around 10 dB for the configurations with static atmosphere, while the IL values fluctuate over frequency between 1.3 dB (at 250 Hz frequency band) to 24.7 dB (at 25 Hz frequency band) in the refracting atmosphere configurations.
- In general, the studied building configurations give almost similar noise reduction results at the residential buildings.
- For the receiver locations in between the canyons, the configurations with more buildings (cases 'b') present a higher noise reduction, and the cases with tilted roofs have a better performance in general.
- For the residential buildings, the maximum reduction is achieved for the 1/3 octave bands between 50 and 100 Hz for the static atmosphere and at the 25 Hz 1/3 octave band for the refractive atmosphere.
- By implementing the evaluated acoustic interventions C1 under the refractive atmosphere, the levels generated by an aircraft type B747-400 during take-off can be reduced from 73 dB to 55.9 dB and from 55.2 dB to 47.8 dB for the octave bands of 31.5 Hz and 63 Hz, respectively. In addition, the levels under the static atmosphere can be reduced from 65.8 dB to 55.0 dB and from 60.7 dB to 47.8 dB for the octave bands of 31.5 Hz and 63 Hz, respectively. This configuration has higher average noise reduction values for the two octave bands.

For future work, the study on the optimal number and location of buildings in the intervention area to achieve maximum IL values is needed. Moreover, investigation of the 3-D configuration could be important, since it is assumed that the industrial buildings in the intervention area are invariant in the third dimension. However, the number of buildings is limited and their sizes may vary in reality. Finally, it might be possible to extend this method to a higher frequency range by including the atmospheric absorption, which means that acoustic equations with internal damping

would be required to model the sound propagation, and the application of these equations to the nodal DG method could be a topic for further research.

# Part II

# Developments of time-domain DG method for simulation of structural vibration

# 4 | Discontinous Galerkin method for vibration of monolithic structure

This chapter is based on the journal paper:

• I. Sihar & M. Hornikx, (2019). Implementation of the nodal discontinuous Galerkin method for the plate vibration problem using linear elasticity equations. Acta Acustica united with Acustica, 105 (4), 668-681.

The contributions of the author of this thesis to this research are indicated in Section 1.7.

#### Abstract

This work presents a numerical solution of the plate vibration problem using the nodal discontinuous Galerkin (DG) method. The plate is modelled as a three-dimensional domain, and its vibration is governed by the linear elasticity equations. The nodal DG method discretises the spatial domain and computes the spatial derivatives of the equations element-wise, while the time integration is conducted using the Runge-Kutta method. This method is of particular interest as it is very favourable to carry out the computation by a parallel implementation. Several aspects regarding the numerical implementation, such as the plate boundary conditions, the point force excitation, and the upwind numerical flux, are presented. The numerical results are validated for rectangular concrete plates with different sets of boundary conditions and thicknesses, by a comparison with the exact mobilities that are derived from the classical plate theory (CPT) and the first-order shear deformation theory (FSDT) via the modal expansion method. The plate thickness is varied to understand its effect regarding the comparison with the CPT. An excellent agreement between the numerical solution and the FSDT was found. The agreement with the CPT occurs only at the first couple of resonance frequencies and as the plate is getting thinner. Furthermore, the numerical example is extended to an L-shaped concrete plate. The mobility is then compared with the mobilities obtained by the CPT, FSDT, and linear elasticity equations.

#### 4.1 Introduction

To obtain a good building acoustic performance, an accurate prediction of the vibroacoustic characteristics of the building components is essential. Building components, such as floors and walls, can be modelled as monolithic structures to obtain their vibroacoustic characteristics. However, when a building component involves multiple structures such as beams, plates, and cavities, the wave dynamics are complex, and the monolithic models are not sufficient to represent the structures. Moreover, when waves propagate across junctions or complex structures (i.e., non-homogeneous walls), a more general model is needed to predict the vibroacoustic characteristics. To solve this problem, one may use the energy flow model such as presented in the European standard EN 12354 or a more general statistical energy analysis [196]. However, these methods are based on the assumption that the sound and vibration fields are diffuse and have sufficient modal counts in each sub-system, while this assumption is no longer appropriate in the low-frequency range. In that case, a wave-based method capable of couple the dynamics of the air and the structure is of interest to predict the vibroacoustic characteristics.

One approach is by modelling both the structural vibration and the wave propagation in the air using the linear elasticity equations [197], [198]. The linear elasticity equations are often used in solid mechanics studies, yet its implementation in the vibroacoustic problem is also feasible. There are advantages of using the linear elasticity equations to solve vibroacoustic problems in a building. One advantage is when the thin structure assumption does not hold, as thick structures can be solved in the linear elasticity equations. Another advantage is when there are changes in the cross-section area due to stiffeners, junctions, or any discontinuities, as they could be treated directly in the model.

The linear elasticity equations have frequently been used to model seismic wave propagation in the geophysics field. For instance, Vireux used the 2-D linear elasticity equations to model the Rayleigh surface waves and solved it using FDTD method [199]. Dumbser and Käser modelled three-dimensional seismic wave propagation using linear elasticity equations and solved it using the arbitrary high-order derivatives discontinuous Galerkin (ADER-DG) method [118]. Another example is by Wilcox et al., who used DG to simulate seismic waves propagation through coupled acoustic-elastic media [200].

In the field of sound and vibration, Toyoda and Takahashi [94] have used the linear elasticity equations to model impact sound in a two-story building and solved it using the FDTD method. Another example is by Xuan et al. who applied the linear elasticity equations to the structural-acoustic problem and solved it using FVM [127]. Additionally, Bermúdez at al. have modelled the vibroacoustic problem of a three-dimensional vessel filled with fluid using linear elasticity equations and used the FEM to calculate its eigenvalues [201].

In solving a real-life building acoustics problem, there is a need for a more efficient method to solve the linear elasticity equations than FDTD, FVM, and FEM. This

efficiency can be provided by the discontinuous Galerkin (DG) method. This method is of particular interest as it is very favourable to carry out DG calculations by a parallel implementation, opening opportunities to solve real-world problems in a reasonable computation time.

In this chapter, as a first step to solve the vibroacoustic problem in a complex building structure, the impact vibrations of plates are modelled. The vibration is modelled using the linear elasticity equations and then solved numerically using the nodal DG method. The nodal DG method satisfies the strong form of linear elasticity equations by utilising the Lagrange interpolation polynomials as the basis functions, and the Runge-Kutta method as the time integration solver. It has been used widely to solve electromagnetic and fluid mechanics problems [112]. Furthermore, the hybrid approach of the nodal DG method and Fourier pseudo-spectral time-domain has been developed by Pagán Muñoz and Hornikx to solve the acoustic propagation problem in air [202], which can be coupled with the current vibration problem.

The remainder of this chaper is organised as follows. Section 4.2 introduces the linear elasticity equations and the numerical aspects such as the nodal DG formulation, the upwind numerical flux, and the point force excitation. Section 4.3 introduces rectangular plates and L-shaped plate configurations. In this section, the problem domains, boundary conditions (BCs), and numerical settings are given. Section 4.4 discuss the comparison between transfer mobilities obtained by the nodal DG method and other solutions. Finally, conclusions are given in Section 4.5

# 4.2 Methodology

# 4.2.1 Linear elasticity equations

In solid media, the structural vibration can be modelled using the conservation equations and constitutive equations. This set of equations is known as the linear elasticity equations [21]. The linear elasticity equations for isotropic structures can be written in the stress-velocity form using three-dimensional rectangular Cartesian coordinates as:

$$\frac{\partial \mathbf{q}_{s}}{\partial t} + \nabla \cdot \mathbf{H}(\mathbf{q}_{s}) = \frac{\partial \mathbf{q}_{s}}{\partial t} + \mathbf{B}_{j} \frac{\partial \mathbf{q}_{s}}{\partial x_{j}} = \mathbf{g},$$

$$\mathbf{q}_{s}(\mathbf{x}, t) = \begin{bmatrix} v_{x} & v_{y} & v_{z} & \sigma_{xx} & \sigma_{yy} & \sigma_{zz} & \sigma_{xz} & \sigma_{yz} & \sigma_{xy} \end{bmatrix}^{T},$$

$$\mathbf{g}(\mathbf{x}, t) = \begin{bmatrix} g_{x} & g_{y} & g_{z} & 0 & 0 & 0 & 0 & 0 \end{bmatrix}^{T}.$$
(4.1)

where  $\sigma_{xx}, \sigma_{yy}, \sigma_{zz}, \sigma_{xz}, \sigma_{yz}, \sigma_{xy}$  are the stress components;  $v_x, v_y, v_z$  are the velocity components; and  $g_x, g_y, g_z$  are the body force components. The flux matrix reads  $H(q_s) = [h_x, h_y, h_z] = [B_x q_s, B_y q_s, B_z q_s]$ . The constant flux Jacobian matrix  $B_j$ 

is given as:

$$\begin{split} \boldsymbol{B}_{j} &= \left[ \begin{array}{c|ccc} \mathbf{0}_{3\times3} & \boldsymbol{B}_{1,j} \\ \hline \boldsymbol{B}_{2,j} & \mathbf{0}_{6\times6} \end{array} \right], \boldsymbol{B}_{1,j} = -\frac{1}{\rho} \left[ \begin{array}{cccc} \delta_{xj} & 0 & 0 & \delta_{zj} & 0 & \delta_{yj} \\ 0 & \delta_{yj} & 0 & 0 & \delta_{zj} & \delta_{xj} \\ 0 & 0 & \delta_{zj} & \delta_{xj} & \delta_{yj} & 0 \end{array} \right], \\ \boldsymbol{B}_{2,j} &= - \left[ \begin{array}{cccc} (\lambda + 2\mu)\delta_{xj} & \lambda\delta_{yj} & \lambda\delta_{zj} \\ \lambda\delta_{xj} & (\lambda + 2\mu)\delta_{yj} & \lambda\delta_{zj} \\ \lambda\delta_{xj} & \lambda\delta_{yj} & (\lambda + 2\mu)\delta_{zj} \\ \lambda\delta_{xj} & \lambda\delta_{yj} & (\lambda + 2\mu)\delta_{zj} \\ \mu\delta_{zj} & 0 & \mu\delta_{xj} \\ 0 & \mu\delta_{zj} & \mu\delta_{yj} \\ \mu\delta_{yj} & \mu\delta_{xj} & 0 \end{array} \right], \end{split}$$

where  $\lambda$  and  $\mu$  are the Lamé parameters,  $\rho$  is the mass density and index j has components [x,y,z]. The  $\delta_{ij}$  denotes the Kronecker delta function. The solution of Equations (4.1) consists of a linear combination of elastic waves propagating with longitudinal wave speed  $(c_p = \sqrt{(\lambda + 2\mu)/\rho})$  and transverse wave speed  $(c_s = \sqrt{\mu/\rho})$  [21]. The Lame parameters are represented by using Young's modulus (E) and Poisson's ratio  $(\nu)$  as  $\lambda = E\nu/(1+\nu)(1-2\nu)$  and  $\mu = E/2(1+\nu)$ . The complete description of the domain and the BCs are written in Section 4.3.1.

#### 4.2.2 Nodal discontinuous Galerkin method

In this section, the nodal DG method as presented by Hesthaven and Warburton [112] is applied to solve Equation (4.1). Initially, the problem domain is approximated by the computational domain  $\Omega_h$  with K number of non-overlapping rectilinear tetrahedral elements  $D^k$  as  $\Omega_h = \bigcup_{k=1}^K D^k$ . The solution on each  $D_k$  is defined as the local solution  $\mathbf{q}_{sh}^k(\boldsymbol{x},t)$ , and the global solutions are approximated as the direct sum of the local solutions as:

$$\mathbf{q}_s(\mathbf{x},t) \approx \mathbf{q}_{sh}(\mathbf{x},t) = \bigoplus_{k=1}^K \mathbf{q}_{sh}^k(\mathbf{x},t).$$
 (4.2)

Each local solution is expanded by a combination of basis functions as:

$$\mathbf{q}_{sh}^{k}(\mathbf{x},t) = \sum_{i=1}^{N_p} \mathbf{q}_{sh}^{k}(\mathbf{x}_i,t)l_i(\mathbf{x}) = \sum_{j=1}^{N_p} \hat{\mathbf{q}}_{shj}^{k}(t)\Psi_j(\mathbf{x}), \tag{4.3}$$

where  $l_i(\boldsymbol{x})$  are the three-dimensional Lagrange interpolation polynomials based on nodal points  $\boldsymbol{x}_i$ ,  $N_p$  is the number of the nodal points,  $\Psi_j(\boldsymbol{x})$  are three-dimensional modal basis functions, and  $\hat{\boldsymbol{q}}_{shj}^k$  are the coefficients of the modal basis functions. The expression of  $\Psi_j(\boldsymbol{x})$  is given in Section 5.2.3.

The first term of Equation (4.3) is known as the nodal form, and the second term is known as the modal form. In the nodal DG method, the nodal form is used to approximate the solution. However, the closed-form expression of the Lagrange interpolation polynomials in tetrahedral elements does not exist; therefore it is constructed by utilising the modal form. The relationship between nodal and modal

form is established by the Vandermonde matrix (V) as:

$$\mathbf{q}_{sh} = \mathbf{V}\hat{\mathbf{q}}_{sh}, \ \mathbf{V}_{ij} = \Psi_j(\mathbf{x}_i), \ \mathbf{l}(\mathbf{x}) = \left(\mathbf{V}^T\right)^{-1} \mathbf{\Psi}(\mathbf{x}).$$
 (4.4)

In each element, we need to have a minimum number of nodal points  $N_p$  to establish Lagrange interpolation polynomials of order N.  $N_p$  is defined as  $N_p = (N+1)(N+2)(N+3)/6$ . Moreover, to have a well-conditioned Vandermonde matrix, the nodal points are distributed following the optimised Legendre Gauss Lobato (LGL) points over a tetrahedral element [112].

Afterwards, the nodal basis functions are used to approximate the unknown variables and the body forces in Equation (4.1). The residuals of the approximations are then multiplied by the test functions in accordance with the Galerkin method. The strong formulation of Equation (4.1) takes the following form after performing spatial integration by parts twice:

$$\int_{D^k} \left[ \frac{\partial \boldsymbol{q}_{sh}^k}{\partial t} + \nabla \cdot \boldsymbol{H}(\boldsymbol{q}_{sh}^k) \right] l_i^k d\boldsymbol{x} = \int_{D^k} \boldsymbol{g}_h^k l_i^k d\boldsymbol{x} - \int_{\partial D^k} \boldsymbol{n} \cdot \left[ \boldsymbol{H}^* - \boldsymbol{H}(\boldsymbol{q}_{sh}^k) \right] l_i d\boldsymbol{x}, \tag{4.5}$$

where  $\partial D^k$  is the element surface,  $\boldsymbol{g}_h^k$  is the approximated body force vector, and  $\mathbf{n} = [n_x, n_y, n_z]$  is the outward normal vector of the element surface  $\partial D^k$ . The flux along the normal direction of the element surface is defined as  $\boldsymbol{n} \cdot \boldsymbol{H} = (n_x \boldsymbol{h}_x + n_y \boldsymbol{h}_y + n_z \boldsymbol{h}_z)$ , and the  $\boldsymbol{H}^*$  is the numerical flux. Equation (4.5) can be solved element-wise, and the numerical flux has a role in ensuring continuity of the global solution. This role makes the selection of numerical flux vital in the DG method. In this work, we select the upwind numerical flux as the numerical flux. The details on this flux are elaborated in Section 4.2.3.

After defining the numerical flux, we substitute the nodal basis and the numerical flux into Equation (4.5) to obtain the semi-discrete form for each element as:

$$M^{k} \frac{\partial \boldsymbol{v}_{xh}^{k}}{\partial t} - \frac{1}{\rho} \left( \boldsymbol{S}_{x}^{k} \boldsymbol{\sigma}_{xxh}^{k} + \boldsymbol{S}_{y}^{k} \boldsymbol{\sigma}_{xyh}^{k} + \boldsymbol{S}_{z}^{k} \boldsymbol{\sigma}_{xzh}^{k} \right) = M^{k} \boldsymbol{g}_{xh}^{k} - \sum_{r=1}^{4} M^{kr} \hat{\boldsymbol{H}}_{v_{x}}^{kr},$$

$$M^{k} \frac{\partial \boldsymbol{v}_{yh}^{k}}{\partial t} - \frac{1}{\rho} \left( \boldsymbol{S}_{x}^{k} \boldsymbol{\sigma}_{xyh}^{k} + \boldsymbol{S}_{y}^{k} \boldsymbol{\sigma}_{yyh}^{k} + \boldsymbol{S}_{z}^{k} \boldsymbol{\sigma}_{yzh}^{k} \right) = M^{k} \boldsymbol{g}_{yh}^{k} - \sum_{r=1}^{4} M^{kr} \hat{\boldsymbol{H}}_{v_{y}}^{kr},$$

$$M^{k} \frac{\partial \boldsymbol{v}_{zh}^{k}}{\partial t} - \frac{1}{\rho} \left( \boldsymbol{S}_{x}^{k} \boldsymbol{\sigma}_{xzh}^{k} + \boldsymbol{S}_{y}^{k} \boldsymbol{\sigma}_{yzh}^{k} + \boldsymbol{S}_{z}^{k} \boldsymbol{\sigma}_{zzh}^{k} \right) = M^{k} \boldsymbol{g}_{zh}^{k} - \sum_{r=1}^{4} M^{kr} \hat{\boldsymbol{H}}_{v_{z}}^{kr},$$

$$M^{k} \frac{\partial \boldsymbol{\sigma}_{xxh}^{k}}{\partial t} - (\lambda + 2\mu) \boldsymbol{S}_{x}^{k} \boldsymbol{v}_{xh}^{k} - \lambda \boldsymbol{S}_{y}^{k} \boldsymbol{v}_{yh}^{k} - \lambda \boldsymbol{S}_{z}^{k} \boldsymbol{v}_{zh}^{k} = -\sum_{r=1}^{4} M^{kr} \hat{\boldsymbol{H}}_{\sigma_{xx}}^{kr},$$

$$M^{k} \frac{\partial \boldsymbol{\sigma}_{yyh}^{k}}{\partial t} - \lambda \boldsymbol{S}_{x}^{k} \boldsymbol{v}_{xh}^{k} - (\lambda + 2\mu) \boldsymbol{S}_{y}^{k} \boldsymbol{v}_{yh}^{k} - \lambda \boldsymbol{S}_{z}^{k} \boldsymbol{v}_{zh}^{k} = -\sum_{r=1}^{4} M^{kr} \hat{\boldsymbol{H}}_{\sigma_{yy}}^{kr},$$

$$M^{k} \frac{\partial \boldsymbol{\sigma}_{yyh}^{k}}{\partial t} - \lambda \boldsymbol{S}_{x}^{k} \boldsymbol{v}_{xh}^{k} - (\lambda + 2\mu) \boldsymbol{S}_{y}^{k} \boldsymbol{v}_{yh}^{k} - \lambda \boldsymbol{S}_{z}^{k} \boldsymbol{v}_{zh}^{k} = -\sum_{r=1}^{4} M^{kr} \hat{\boldsymbol{H}}_{\sigma_{yy}}^{kr},$$

$$(4.6)$$

$$\begin{split} \boldsymbol{M}^{k} \frac{\partial \boldsymbol{\sigma}_{\boldsymbol{z} \boldsymbol{z}_{h}^{k}}}{\partial t} - \lambda \boldsymbol{S}_{x}^{k} \boldsymbol{v}_{xh}^{k} - \lambda \boldsymbol{S}_{y}^{k} \boldsymbol{v}_{yh}^{k} - (\lambda + 2\mu) \boldsymbol{S}_{z}^{k} \boldsymbol{v}_{zh}^{k} = -\sum_{r=1}^{4} \boldsymbol{M}^{kr} \hat{\boldsymbol{H}}_{\sigma_{zz}}^{kr}, \\ \boldsymbol{M}^{k} \frac{\partial \boldsymbol{\sigma}_{\boldsymbol{x} \boldsymbol{z}_{h}^{k}}}{\partial t} - \mu \boldsymbol{S}_{z}^{k} \boldsymbol{v}_{xh}^{k} - \mu \boldsymbol{S}_{x}^{k} \boldsymbol{v}_{zh}^{k} = -\sum_{r=1}^{4} \boldsymbol{M}^{kr} \hat{\boldsymbol{H}}_{\sigma_{xz}}^{kr}, \\ \boldsymbol{M}^{k} \frac{\partial \boldsymbol{\sigma}_{\boldsymbol{y} \boldsymbol{z}_{h}^{k}}}{\partial t} - \mu \boldsymbol{S}_{z}^{k} \boldsymbol{v}_{yh}^{k} - \mu \boldsymbol{S}_{y}^{k} \boldsymbol{v}_{zh}^{k} = -\sum_{r=1}^{4} \boldsymbol{M}^{kr} \hat{\boldsymbol{H}}_{\sigma_{yz}}^{kr}, \\ \boldsymbol{M}^{k} \frac{\partial \boldsymbol{\sigma}_{\boldsymbol{x} \boldsymbol{y}_{h}^{k}}}{\partial t} - \mu \boldsymbol{S}_{y}^{k} \boldsymbol{v}_{xh}^{k} - \mu \boldsymbol{S}_{x}^{k} \boldsymbol{v}_{yh}^{k} = -\sum_{r=1}^{4} \boldsymbol{M}^{kr} \hat{\boldsymbol{H}}_{\sigma_{xy}}^{kr}. \end{split}$$

The  $\boldsymbol{v}_{xh}^k$ ,  $\boldsymbol{v}_{yh}^k$ ,  $\boldsymbol{v}_{zh}^k$ ,  $\boldsymbol{\sigma}_{xxh}^k$ ,  $\boldsymbol{\sigma}_{yyh}^k$ ,  $\boldsymbol{\sigma}_{zzh}^k$ ,  $\boldsymbol{\sigma}_{xzh}^k$ ,  $\boldsymbol{\sigma}_{yzh}^k$ , and  $\boldsymbol{\sigma}_{xyh}^k$  are vectors representing all unknown variables at the nodal points  $\boldsymbol{x}_i$ , with i=1 to  $N_p$ . Note that all the mechanical properties in Equation (4.6) are defined in the interior element, with the exception of the numerical flux terms. The second superscript r denotes the rth faces of  $\partial D^{kr}$  of the element  $D^k$ . The terms  $\hat{\boldsymbol{H}}_u^{kr}$ ,  $\hat{\boldsymbol{H}}_v^{kr}$ ,  $\hat{\boldsymbol{H}}_w^{kr}$ ,  $\hat{\boldsymbol{H}}_{\sigma_{xx}}^{kr}$ ,  $\hat{\boldsymbol{H}}_{\sigma_{xy}}^{kr}$ ,  $\hat{\boldsymbol{H}}_{\sigma_{xy}}^{kr}$ , and  $\hat{\boldsymbol{H}}_{\sigma_{xy}}^{kr}$  are associated with the flux terms  $\boldsymbol{n} \cdot [\boldsymbol{H}^* - \boldsymbol{H}(\boldsymbol{q}_{sh}^k)]$  over the element surface in Equation (4.5).  $\boldsymbol{M}^k$  is the element mass matrix,  $\boldsymbol{S}_j^k$  are the element stiffness matrices in the j-directions, and  $\boldsymbol{M}^{kr}$  are the element face matrices. Details on these matrices are provided in Refs. [112], [203].

Having the semi-discrete form at hand, Equation (4.6) for the whole computational domain can be expressed in the form of ordinary differential equations as:

$$\frac{\mathrm{d}\boldsymbol{q}_{sh}}{\mathrm{d}t} = \mathcal{L}\left(\boldsymbol{q}_{sh}(t), t\right),\tag{4.7}$$

where  $q_{sh}$  is the vector of all nodal solutions, and  $\mathcal{L}$  is the semi-discrete operator conducted over all elements. Finally, various methods can be employed to integrate the time derivative in Equation 4.7. The fourth-order Runge-Kutta method with eight stages (RKF84) is used in this work, as described in Ref. [148]. For the time integration, the time-step ( $\Delta t$ ) is defined as:

$$\Delta t = \frac{C_{CFL} \cdot \min(r_{D^k})}{N^2 \cdot c_p},\tag{4.8}$$

where  $\mathcal{L}$  is the semi-discrete operator,  $C_{CFL}$  is the Courant number,  $c_p$  is the longitudinal wave speed, and  $\min(r_{D^k})$  is the shortest element edge in the computational domain. In the implementation of nodal DG method, the mapping between the standard tetrahedral element and the general tetrahedral element (I) is introduced to generalise the computation. The mapping between  $D^k$  and I will be discussed more in Section 4.2.4.

#### 4.2.3 Upwind numerical flux

In this section, the upwind numerical flux is derived. For more details on the numerical flux, we refer to the work of LeVeque [21], Wilcox et al. [200], or Dumbser et al. [118]. To formulate the upwind numerical flux, the Riemann problem of Equation (4.1) at the interfaces of each element should be solved. The Riemann problem is a discontinuous initial value problem, where the initial value ( $\mathbf{q}_s$ ) is defined as:

$$\mathbf{\mathring{q}}_s(x) = \begin{cases} \mathbf{q}_s^- & \text{for } x < 0, \\ \mathbf{q}_s^+ & \text{for } x > 0, \end{cases}$$

where  $q_s^-$  represents the variable at the local element, and  $q_s^+$  represents the variable at the neighbor elements. Since Equations (4.1) are hyperbolic equations,  $\boldsymbol{B}$  can be decomposed as  $\boldsymbol{B} = \boldsymbol{R} \boldsymbol{\Lambda} \boldsymbol{R}^{-1}$ , with  $\boldsymbol{\Lambda}$  the eigen-values, and  $\boldsymbol{R}$  the eigen-vectors.  $\boldsymbol{\Lambda}$  can be written as:

$$\begin{split} \mathbf{\Lambda} &= diag\left(-c_p, -c_s, -c_s, 0, 0, 0, c_s, c_s, c_p\right), \\ c_p &= \sqrt{\left(\lambda + 2\mu\right)/\rho}, c_s = \sqrt{\mu/\rho}, \end{split}$$

where  $c_p$  is the longitudinal wave speed, and  $c_s$  is the shear wave speed. Further, introducing  $\boldsymbol{w}_c = \boldsymbol{R}^{-1}\boldsymbol{q}_s$  as the characteristic variables, the homogeneous form of Equation (4.1) can be diagonalized by the multiplication with  $\boldsymbol{R}^{-1}$  to obtain the following form:

$$\frac{\partial \boldsymbol{w}_c}{\partial t} + \boldsymbol{\Lambda} \nabla \cdot \boldsymbol{w}_c = 0. \tag{4.9}$$

The initial characteristic variable is defined as:

$$\dot{\boldsymbol{w}}_c(x) = \begin{cases} \boldsymbol{R}^{-1} \boldsymbol{q}_s^- & \text{for } x < 0, \\ \boldsymbol{R}^{-1} \boldsymbol{q}_s^+ & \text{for } x > 0. \end{cases}$$

Equation (4.9) shows that each characteristic variable  $(w_{ci}(x,t))$  is decoupled and can be treated as an advection equation. The general solution of  $w_{ci}(x,t)$  is:

$$w_{ci}(x,t) = \begin{cases} w_{ci}^{-} & \text{for } (x - \lambda_i t) < 0, \\ w_{ci}^{+} & \text{for } (x - \lambda_i t) > 0, \end{cases}$$

where  $\lambda_i$  is the wave velocity in the eigen-values matrix. This solution shows that the discontinuity emanating from x=0 is propagating along the characteristic curves  $x=\lambda_i t$ . Now, if p is defined as the maximum value of i for which  $x-\lambda_i t>0$  at (x,t), and transform it back to the original unknown variables by multiplying it with  $\mathbf{R}$ , the Riemann solution at the interface of the elements may be written as:

$$\mathbf{q}_s(x,t) = \sum_{i=1}^p w_{ci}^+ \mathbf{r}_i + \sum_{i=p+1}^6 w_{ci}^- \mathbf{r}_i.$$
 (4.10)

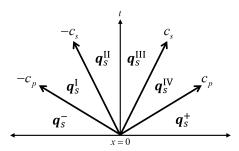


Figure 4.1: Illustration of the Ranking–Hugoniot jump conditions to construct the solution of the Riemann problem.

Equation (4.10) shows that the Riemann solution is a combination of eigen-vectors  $r_i$  with  $w_i$  as the magnitude. To get better insight, the Riemann solution is illustrated in Figure 4.1, where six characteristic curves emanating from x = 0 are drawn. The characteristic curves are related to the eigen-values  $-c_p, -c_s, c_s, c_p$ . Notice that there are two coincident characteristic curves at  $-c_s$  and  $c_s$ . The zero eigen-values are omitted since there is no contribution related to these eigen-vectors.

Based on Figure 4.1, the Riemann solution can be divided into six regions:  $q_s^-, q_s^{\rm I}, q_s^{\rm II}, q_s^{\rm II}, q_s^{\rm IV}, q_s^+$ . Each region represents the region of (x,t) with the same solution.  $q_s^-$  is the solution of the first region where  $(x+c_pt<0)$ ;  $q_s^{\rm I}$  is the solution of the second region where  $(x+c_pt>0)$  and  $(x+c_st<0)$ ;  $q_s^{\rm II}$  is the solution of the third region where  $(x+c_st)>0$  and  $(x-c_st<0)$ ; and so on. The  $q_s^{\rm I}, q_s^{\rm II}, q_s^{\rm II}, q_s^{\rm IV}$  are known as the intermediate states [21]. In these regions, the solution and should be determined from the known initial values  $q_s^+$  and  $q_s^-$ . From Equation (4.10), it is known that across each *i*-th characteristic curve, the jump of the solution  $q_s$  can be defined as  $(w_{ci}^+ - w_{ci}^-) r_i$ . Hence, the total jump between  $q_s^+$  and  $q_s^-$  is:

$$q_{s}^{+} - q_{s}^{-} = (w_{c1}^{+} - w_{c1}^{-}) \mathbf{r}_{1} + (w_{c2}^{+} - w_{c2}^{-}) \mathbf{r}_{2}$$

$$+ (w_{c3}^{+} - w_{c3}^{-}) \mathbf{r}_{3} + (w_{c4}^{+} - w_{c4}^{-}) \mathbf{r}_{4}$$

$$+ (w_{c5}^{+} - w_{c5}^{-}) \mathbf{r}_{5} + (w_{c6}^{+} - w_{c6}^{-}) \mathbf{r}_{6}.$$

$$(4.11)$$

This jump between regions is called the Rankine-Hugoniot jump condition. This condition is essential to derive the solution for the intermediate states. Further,  $\alpha_i = \left(w_{ci}^+ - w_{ci}^-\right)$  is defined to have a more compact notation. Thus, Equation (4.11) can be written as:

$$\boldsymbol{q}_s^+ - \boldsymbol{q}_s^- = \alpha_1 \boldsymbol{r}_1 + \alpha_2 \boldsymbol{r}_2 + \alpha_3 \boldsymbol{r}_3 \tag{4.12}$$

$$+\alpha_4 \boldsymbol{r}_4 + \alpha_5 \boldsymbol{r}_5 + \alpha_6 \boldsymbol{r}_6. \tag{4.13}$$

Moreover,  $\alpha$  can be defined from the jump condition as:

$$\alpha = \mathbf{R}^{-1} \left( \mathbf{q}_s^+ - \mathbf{q}_s^- \right). \tag{4.14}$$

Having  $\alpha$  at hand, now the intermediate states at any position and time can be obtained. In the DG method, the location of discontinuity is at the interface between elements. To calculate the numerical fluxes, the intermediate states located at the discontinuity is needed, which in this case is the state at  $q_s^{\text{II}}$  or  $q_s^{\text{III}}$  regions, both expressions are equal. Based on Equations (4.10) and 4.14, these regions can be written as:

$$\boldsymbol{q}_{s}^{\mathrm{II}} = \boldsymbol{q}_{s}^{-} + \alpha_{1} \boldsymbol{r}_{1} + \alpha_{2} \boldsymbol{r}_{2} + \alpha_{3} \boldsymbol{r}_{3},$$

or

$$\boldsymbol{q}_{s}^{\text{III}} = \boldsymbol{q}_{s}^{+} - \alpha_{6} \boldsymbol{r}_{6} - \alpha_{5} \boldsymbol{r}_{5} + \alpha_{4} \boldsymbol{r}_{4}.$$

The region  $q_s^{\text{II}}$  is taken as the region of interest, and the upwind numerical flux is expressed as  $H^* = Bq_s^{\text{II}}$ . The details of  $H^*$  is given in the Appendix D.

#### 4.2.4 Point force excitation

In order to insert force into a plate domain, an external source can be introduced by having the body force vector  $\mathbf{g}$  [N/kg] at the right-hand side of the linear elasticity equations. The point body force is approximated using the Lagrange interpolation polynomials to excite the point body force solely at z-direction  $g_z(\mathbf{x},t)$  as:

$$g_z(\mathbf{x},t) = A(t) \cdot \delta(\mathbf{x} - \mathbf{x}_0), \tag{4.15}$$

where A(t) is an excitation function in time,  $\delta(\mathbf{x})$  is the spatial Dirac delta function, and  $\mathbf{x}_0$  is the excitation location. The point body force can be approximated by exciting one nodal basis in an element. However, it could create forces with certain directivity where the support of the body force only depend on one element such as shown by Etienne [204]. To overcome this problem, the same  $g_z(\mathbf{x},t)$  are distributed on several elements that have vertex located at the same  $\mathbf{x}_0$ . After applying the same body force in each element, the total force F(t) [N] in the computational domain can be computed as:

$$F(t) = \rho \sum_{k=1}^{K_p} G^k(t) = \rho \sum_{k=1}^{K_p} \int_{D_k} g_z^k(\mathbf{x}, t) d\mathbf{x},$$
 (4.16)

where  $K_p$  is the total number of elements around the excitation location, and  $g_z^k(\boldsymbol{x},t)$  is the body force function in each element k. The integration in Equation (4.16) can be conducted in each element by transform it into a standard tetrahedral element (I) as:

$$G^{k}(t) = A(t)J^{k} \int_{\mathbf{I}} \sum_{i=1}^{N_{p}} g_{z}^{k}(\boldsymbol{\xi}_{i}, t)\varphi_{i}(\boldsymbol{\xi})d\boldsymbol{\xi}, \tag{4.17}$$

where  $J^k$  is the transformation Jacobian of element  $D_k$ ,  $\boldsymbol{\xi}_i$  are the optimised LGL points at  $\mathbf{I}$ , and  $\boldsymbol{\xi}$  is the reference coordinate  $(\xi_1, \xi_2, \xi_3)$ . The  $\mathbf{I}$  is defined as:

$$\mathbf{I} = \{ (\xi_1, \xi_2, \xi_3) \mid \xi_1, \xi_2, \xi_3 \geqslant -1; \, \xi_1 + \xi + \xi_3 \leqslant 1 \} \,. \tag{4.18}$$

Since only one nodal basis in each element is excited, the sum over index i on Equation (4.17) only have a value at one nodal point. However, this nodal point might be different for each element, so the index i is kept. To have the integration of Equation (4.17), the closed-form of  $\varphi_i(\boldsymbol{\xi})$  is needed, and it can be expressed by the three-dimensional orthogonal basis function  $\Psi_j(\boldsymbol{\xi})$  such as defined in Equation (4.4). By this relation, Equation (4.17) could be re-written as:

$$F^{k}(t) = \rho A(t) J^{k} \sum_{i=1}^{N_{p}} \sum_{j=1}^{N_{p}} g_{z}^{k}(\boldsymbol{\xi}_{i}, t) (\mathbf{V}^{T})_{ij}^{-1} \int_{\mathbf{I}} \Psi_{j}(\boldsymbol{\xi}) d\boldsymbol{\xi}.$$
 (4.19)

The modal basis  $\Psi_i(\boldsymbol{\xi})$  is defined following Hesthaven [112] as:

$$\Psi_j(\xi_1, \xi_2, \xi_3) = \sqrt{8} P_a^{(0,0)}(\eta_1) P_b^{(2a+1,0)}(\eta_2)$$

$$P_c^{(2a+2b+2,0)}(\eta_3) (1 - \eta_2)^a (1 - \eta_3)^{a+b}, \tag{4.20}$$

$$\eta_1 = \frac{-2(1+\xi_1)}{\xi_2 + \xi_3}, \eta_2 = \frac{2(1+\xi_1)}{1-\xi_3} - 1, \eta_3 = \xi_3,$$
(4.21)

where  $P_a^{(\alpha,\beta)}$  is the Jacobi polynomials with weight  $\alpha$  and  $\beta$ , and  $a+b+c \leq N$ . The  $(\eta_1,\eta_2,\eta_3)$  are the collapsed coordinates and they varies between [-1,1]. By expressing the  $\Psi_j(\boldsymbol{\xi})$  using the collapsed coordinates, the integration in Equation (4.19) is separable and can be presented as:

$$\int_{\mathbf{I}} \Psi_{j}(\boldsymbol{\xi}) d\boldsymbol{\xi} = \frac{1}{\sqrt{8}} \int_{-1}^{1} P_{a}^{(0,0)}(\eta_{1}) d\eta_{1}.$$

$$\int_{-1}^{1} (1 - \eta_{2})^{a+1} P_{b}^{(2a+1,0)}(\eta_{2}) d\eta_{2}.$$

$$\int_{-1}^{1} (1 - \eta_{3})^{a+b+2} P_{c}^{(2a+2b+2,0)}(\eta_{2}) d\eta_{3}.$$
(4.22)

It should be noted that the transformation Jacobian between reference coordinate and the collapsed coordinate is included in Equation (4.22). Finally, the Equation (4.22) can be integrated using the Gauss-Jacobi quadrature to have the total force that is inserted into the computational domain. To summarise, the time-domain body force is given at a specific vertex in several elements around the point force excitation; afterwards, the Gauss-Jacobi quadrature formula is applied to compute the total force. The total force is used to calculate the plate mobility of the nodal DG solution such as configured in the next sections.

## 4.3 Case studies

#### 4.3.1 Rectangular plate configuration

The first case study in this chapter is the vibration of a rectangular plate. A rectangular plate represented by a cuboid computational domain of sizes  $[0, 1.8] \times [0, 1.2] \times [0, h]$  m, with h is the plate thickness is taken an example. The plate is made of concrete with Young's modulus (E) 33.7 GPa, density  $(\rho)$  2300  $^{\text{kg}}$ /m³, and Poisson's ratio (v) 0.3. The corresponding Lame parameters are  $\lambda = Ev/(1+v)(1-2v)$  and  $\mu = E/2(1+v)$ .

The first objective of this case configuration is to compute the transfer mobilities of the rectangular plates with the mechanical properties as mentioned above with different BCs and thicknesses. The transfer mobility is computed between the force located at F = [0.3, 0.9, h] m and the velocity located at R = [1.6, 0.3, h] m. The plate thickness are vary of h = [0.12, 0.08, 0.04] m, and each thickness has three sets of BCs: S-S-S-S, S-S-S-C, and S-S-S-F BCs. Each set of the plate BCs is described in Section 4.3.1.

The second objective is to analyse the accuracy of transfer mobility around the point force excitation location. The plate with S-S-S-F BCs and h=0.12 m is taken as an example to investigate the accuracy. The transfer mobilities are taken between the force located at F and several velocities located at R1 = [0.3, 0.85, h] m, R2 = [0.25, 0.85, h] m, R3 = [0.35, 0.95, h] m, and R4 = [0.4, 0.9, h] m, which are located close to the excitation point. To excite the vibration, the body force  $g_z(\mathbf{x}, t)$  is given with A(t) in the form of Ricker wavelet:

$$A(t) = (0.5 - (\pi f_c(t - t_d))^2)e^{(\pi f_c(t - t_d))^2},$$

with the center frequency  $f_c = 500\,\mathrm{Hz}$  and the center time  $t_d = 5\,\mathrm{ms}$ . This center frequency is taken to have the force excitation up to 1 kHz. The plate is discretised using unstructured tetrahedral elements generated by Gambit mesh generator [205]. The mesh of plate with  $h = 0.12\,\mathrm{m}$  is shown at Figure 4.2. The locations of the force (F) and receiver (R) are marked in Figure 4.2, and the elements that are associated with the point force are highlighted with red colour. Afterwards, the BCs are ascribed to each computational face such as presented in Section 4.3.1. Moreover, the nodal basis of N = 3 is used for all cases on rectangular plate configuration. Finally, the details of the mesh, degrees of freedom (DoF), and time steps are given in the Table 4.1.

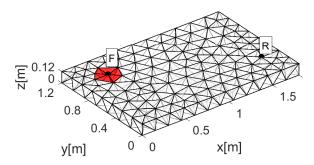


Figure 4.2: Rectangular plate computational domain with thickness of h = 0.12 m. The excitation force (F) and receiver (R) locations are marked, and the elements that are associated with the point force are highlighted with red colour.

Table 4.1: Numerical settings of the nodal DG method for the computation of the rectangular plate configuration.

h	K	DoF	$C_{CFL}$	$\Delta t$
$0.12\mathrm{m}$	641	12820	1	$2.86\cdot10^{-6}$
$0.08\mathrm{m}$	630	12600	1	$2.02 \cdot 10^{-6}$
$0.04\mathrm{m}$	616	12320	0.7	$7.09 \cdot 10^{-7}$

#### **Boundary conditions**

To complete the problem definition, the BCs are ascribed to each plate face. There are six sets of rectangular plate BCs that have exact mode shapes and eigenvalues based on plate theories [206], [207]. In this work, three sets of BCs are considered which is the S-S-S-S plate, the S-S-S-C plate, and the S-S-S-F plate. The labels refer to the plate faces at  $x=0,y=0,x=1.8\,\mathrm{m}$ , and at  $y=1.2\,\mathrm{m}$ , respectively. The indexes S, C, and F indicates the simply supported BC, the clamped BC, and the free BC, respectively. For all different BCs, the top and bottom faces at z=h and z=0 are considered as the free BCs which implies:

$$\sigma_{xz} = \sigma_{yz} = \sigma_{zz} = 0. \tag{4.23}$$

In the nodal DG method, this translates to the following conditions:

$$\sigma_{xz}^{+} = -\sigma_{xz}^{-}, \quad \sigma_{xx}^{+} = \sigma_{xx}^{-}, \quad v_{x}^{+} = v_{x}^{-}, 
\sigma_{yz}^{+} = -\sigma_{yz}^{-}, \quad \sigma_{yy}^{+} = \sigma_{yy}^{-}, \quad v_{y}^{+} = v_{y}^{-}, 
\sigma_{zz}^{+} = -\sigma_{zz}^{-}, \quad \sigma_{xy}^{+} = \sigma_{xy}^{-}, \quad v_{z}^{+} = v_{z}^{-}.$$

$$(4.24)$$

These settings set the stress components at the top and the bottom faces as in Equation (4.23).

#### S-S-S plate

The details considering the S-S-S-S plate on the three-dimensional domain can be found in the work of Srinivas et.al. [208]. According to them, to satisfy the simply supported BC, the plate face at x=0 and  $x=1.8\,\mathrm{m}$  should have the following conditions:

$$v_y = 0, \quad \sigma_{xx} = 0, \quad \sigma_{zz} = 0, v_z = 0, \quad \sigma_{yy} = 0, \quad \sigma_{yz} = 0.$$
 (4.25)

In the nodal DG method, this BC is implemented as:

$$\begin{aligned}
 v_y^+ &= -v_y^-, & \sigma_{xx}^+ &= -\sigma_{xx}^-, & \sigma_{zz}^+ &= -\sigma_{zz}^-, \\
 v_z^+ &= -v_z^-, & \sigma_{yy}^+ &= -\sigma_{yy}^-, & \sigma_{yz}^+ &= -\sigma_{yz}^-, \\
 v_x^+ &= v_x^-, & \sigma_{xy}^+ &= \sigma_{xy}^-, & \sigma_{xz}^+ &= \sigma_{zz}^-. 
 \end{aligned}$$

$$(4.26)$$

For the plate face at y = 0 and y = 1.2 m, it should have the following conditions:

$$v_x = 0, \quad \sigma_{xx} = 0, \quad \sigma_{zz} = 0, v_z = 0, \quad \sigma_{yy} = 0, \quad \sigma_{xz} = 0.$$
 (4.27)

In the nodal DG method, this BC is implemented as:

$$v_x^+ = -v_x^-, \quad \sigma_{xx}^+ = -\sigma_{xx}^-, \quad \sigma_{zz}^+ = -\sigma_{zz}^-, 
 v_z^+ = -v_z^-, \quad \sigma_{yy}^+ = -\sigma_{yy}^-, \quad \sigma_{xz}^+ = -\sigma_{xz}^-, 
 v_y^+ = v_y^-, \quad \sigma_{xy}^+ = \sigma_{xy}^-, \quad \sigma_{yz}^+ = \sigma_{yz}^-.$$

$$(4.28)$$

#### S-S-S-C plate

To obtain the S-S-S-C plate, the plate faces at x=0 and  $x=1.8\,\mathrm{m}$  should satisfy Equation (4.25) and follow the nodal DG settings at Equation (4.26). Afterwards, the face at y=0 should satisfy Equation (4.27) and follow the implementation at Equation (4.28). For the face at  $y=1.2\,\mathrm{m}$ , the plate should satisfy the following conditions:

$$v_x = v_y = v_z = 0.$$

In the nodal DG method, this BC is implemented as:

$$\begin{array}{llll} \sigma_{xx}^{+} = & \sigma_{xx}^{-}, & \sigma_{xz}^{+} = & \sigma_{xz}^{-}, & v_{x}^{+} = & -v_{x}^{-}, \\ \sigma_{yy}^{+} = & \sigma_{yy}^{-}, & \sigma_{yz}^{+} = & \sigma_{yz}^{-}, & v_{y}^{+} = & -v_{y}^{-}, \\ \sigma_{zz}^{+} = & \sigma_{zz}^{-}, & \sigma_{xy}^{+} = & \sigma_{xy}^{-}, & v_{z}^{+} = & -v_{z}^{-}. \end{array}$$

#### S-S-S-F plate

The S-S-S-F plate has the same settings as the S-S-S-C plate at the faces of x = 0,  $x = 1.8 \, m$ , and y = 0. For the face at  $y = 1.2 \, m$ , the plate should satisfy the following condition:

$$\sigma_{xy} = \sigma_{yy} = \sigma_{yz} = 0. \tag{4.29}$$

In the nodal DG method, this BC is implemented as:

$$\sigma_{xy}^{+} = -\sigma_{xy}^{-}, \quad \sigma_{xx}^{+} = \sigma_{xx}^{-}, \quad v_{x}^{+} = v_{x}^{-}, 
\sigma_{yy}^{+} = -\sigma_{yy}^{-}, \quad \sigma_{zz}^{+} = \sigma_{zz}^{-}, \quad v_{y}^{+} = v_{y}^{-}, 
\sigma_{yz}^{+} = -\sigma_{yz}^{-}, \quad \sigma_{xz}^{+} = \sigma_{xz}^{-}, \quad v_{z}^{+} = v_{z}^{-}.$$
(4.30)

#### 4.3.2 Rectangular plate analytical mobility

To validate the numerical results from the nodal DG method, the plate mobility obtained by the nodal DG method is compared with exact mobility obtained from plate theories: classical plate theory (CPT) and first-order shear deformation plate theory (FSDT). The CPT is selected since it has been used extensively in building acoustics applications, and the FSDT is selected since it is more accurate than the CPT. The mode shape and the natural frequency from each plate theories are obtained and the mobility is calculated by applying the modal expansion method. The details of the CPT and the FSDT can be found in literature [22]. The mobility (Y) between the force located at  $(x_0, y_0)$  and the velocity  $(v_z)$  located at  $(x_r, y_r)$  can be written as:

$$Y(\omega) = i\omega \sum_{m_1=1}^{\infty} \sum_{m_2=1}^{\infty} \frac{F_{m_1 m_2}(x_0, y_0) \Xi_{m_1 m_2}(x_r, y_r)}{M(\omega_{m_1 m_2}^2 (1 + j\zeta) - \omega^2)},$$
(4.31)

where  $F_{m_1m_2}$  is the mode force,  $\Xi_{m_1m_2}$  is the mode shape, M is the inertia component,  $\omega_{m_1m_2}$  is the angular frequency of the natural mode  $m_1, m_2$ ,  $\zeta$  is the structural damping, and  $\omega$  is the angular frequency. The indexes  $m_1$  and  $m_2$  represent the mode shape in x-direction and y-direction, respectively.  $F_{m_1m_2}$  is the projection of the force to the  $m_1m_2$  natural mode shape. For the point force excitation, mobility can be written as:

$$F_{m_1 m_2} = \frac{\Xi_{m_1 m_2}(x_0, y_0)}{\int_0^{L_x} \int_0^{L_y} \Xi_{m_1 m_2}^2(x, y) dxdy},$$

where  $L_x$  and  $L_y$  are the plate length and width. According to the CPT, the S-S-S-S plate mode shape and natural angular frequency can be written as:

$$\Xi_{m_1 m_2}(x, y) = \sin(\alpha_{m_1} x) \sin(\beta_{m_2} y), \tag{4.32}$$

$$\omega_{m_1 m_2}^2 = D(\alpha_{m_1}^2 + \beta_{m_2}^2)^2 / M, \tag{4.33}$$

where  $\alpha_{m_1} = m_1 \pi/a$ ,  $\beta_{m_2} = m_2 \pi/b$ , the bending stiffness  $D = (Eh^3)/(12(1-v^2))$ , and the inertia component  $M = \rho h$ . In practical applications, often plate rotary inertia is omitted in CPT. However, it could over-estimate the plate natural frequencies. For the S-S-S-S plate, the effect of rotary inertia is included to calculate the mobility by defining the inertia component in Equation (4.33) as:

$$M = \rho h + \frac{\rho h^3}{12} \left( \alpha_{m_1}^2 + \beta_{m_2}^2 \right).$$

For the mobility according to FSDT, Wang has presented an exact relationship between the natural angular frequency obtained by the CPT and the FSDT [207]. This

relation has the mode shape as in Equation (4.33) and the natural angular frequency  $\omega_{m_1m_2}^{FSDT}$  is as follows:

$$\left(\omega_{m_1 m_2}^{FSDT}\right)^2 = \frac{6K_sG}{\rho h^2} \left(C_{m_1 m_2} - \sqrt{C_{m_1 m_2}^2 - \frac{\rho h^2 \left(\omega_{m_1 m_2}^2\right)}{3K_sG}}\right),$$

$$C_{m_1 m_2} = 1 + \frac{\omega_{m_1 m_2} h^2}{12} \sqrt{\frac{\rho h}{D}} \left(1 + \frac{2}{K_s^2 (1 - v)}\right),$$

where  $K_s$  is the shear correction factor. By this relation, the FSDT mobility is obtained by replacing  $\omega_{m_1m_2}^2$  with  $\left(\omega_{m_1m_2}^{FSDT}\right)^2$  in Equation (4.31). Concerning the S-S-S-C and S-S-S-F plates, the mobility based on the CPT are calculated by adopting the work of Gorman [209], and for the mobility based on the FSDT is calculated by adopting the work of Wang and Wang [207]. These authors provide the exact natural frequency and the mode shape of the plates. The interested reader is referred to the Refs. [206], [207], [209] for further information.

#### 4.3.3 L-shaped plate configuration

To have more complex plate vibration problem, the mobility of a three-dimensional L-shaped plate is calculated. The problem domain is a merge between two cuboid of h=0.12 m. The first cuboid is of size  $[-h/2,1.8]\times[0,1.2]\times[-h/2,h/2]$  m, and the second cuboid is of size  $[-h/2,h/2]\times[0,1.2]\times[-h/2,1.8]$  m. The cuboids have domain overlap at  $[-h/2,h/2]\times[0,1.2]\times[-h/2,h/2]$  m. The computational domain for this configuration can be seen in Figure 4.3.

The objective of this configuration is to compute the transfer mobilities between the point force located at F = [1.52, 0.21, h/2], and the velocity  $(v_z)$  at R1 = [0.4, 0.2, h/2] m, R2 = [h/2, 0.6, 0.4] m, and R3 = [h/2, 1, 0.8] m. Figure 4.3 shows the computational domain, the point force location, and the velocity locations. To complete the formulation, the BC is defined at each plate face. The faces at x = 1.8 m, x = -h/2 m, and x = h/2 m are the free BCs, this implies:

$$\sigma_{xx} = \sigma_{xy} = \sigma_{xz} = 0.$$

In the nodal DG method, this BC is implemented as:

$$\begin{array}{llll} \sigma_{xx}^{+} = & -\sigma_{xx}^{-}, & \sigma_{yy}^{+} = & \sigma_{yy}^{-}, & v_{x}^{+} = & v_{x}^{-}, \\ \sigma_{xy}^{+} = & -\sigma_{xy}^{-}, & \sigma_{zz}^{+} = & \sigma_{zz}^{-}, & v_{y}^{+} = & v_{y}^{-}, \\ \sigma_{xz}^{+} = & -\sigma_{xz}^{-}, & \sigma_{yz}^{+} = & \sigma_{yz}^{-}, & v_{z}^{+} = & v_{z}^{-}. \end{array}$$

The faces at z=-h/2 m, z=h/2 m, and z=1.8 m are also the free BCs. The conditions are following Equation (4.23), and implemented in the nodal DG method following Equation (4.24). Finally, the faces at y=0 and y=1.2 are simply supported BC which follow Equation (4.27), and implemented in the nodal DG method following the Equation (4.28) In this work, the L-shaped plate is discretized with K=3289 which equals to DoF = 65780.

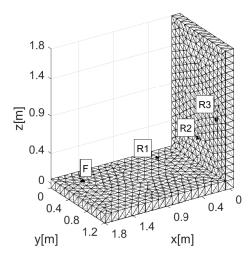


Figure 4.3: L-shaped plate computational domain with thickness h=0.12 m. The force excitation location (F) and receiver (R1,R2,R3) locations are marked by dots on the surface of the structure.

#### 4.4 Results and discussions

In this section, the plate mobilities from the various configurations are displayed. The spectra of the force and the velocity from the nodal DG solution are obtained to compute the plates mobilities. The spectra are obtained from a one-second time-domain signal, windowed in the last 0.5 seconds using a Hann window to reduce the Gibbs effect. Moreover, each spectrum is processed to have a 1 Hz resolution. Afterwards, the nodal DG mobility are compared with the CPT and the FSDT mobilities. It should be noted that a very weak constant damping (0.1%) is given into the CPT and the FSDT to bound the amplitude of the mobility. Moreover, the value of 0.86667 is used as the shear correction factor for the FSDT model following Hashemi [206]. Section 4.4.1 - 4.4.3 show the rectangular plate mobilities for various thickness and BCs, section 4.4.4 shows the mobilities of S-S-S-F plate for the locations near to the excitation point, and section 4.4.5 shows the L-shaped plate mobilities.

# 4.4.1 S-S-S-S plate

Figures 4.4-4.6 show the mobilities of the S-S-S-S plate with different thicknesses. The red lines are the mobilities obtained by the nodal DG method; the black solid lines are the mobilities obtained by the CPT; the black dashed lines are the mobilities obtained by the CPT with the including the rotary inertia (CPT-RI), and the blue lines are the mobilities obtained by FSDT. The rotary inertia inclusion is shown only for the S-S-S-S plate to show its significance to the results. From Figures 4.4-4.6, it can be observed that the plate bending stiffness is lowered as the thickness is reduced. This is shown by the reduction of the first natural frequency. At the natural frequencies, the nodal DG mobility has a higher quality factor (Q factor) compared to the other

mobilities. The high Q factor shows that the energy is conserved well throughout the simulation. Overall, the comparison shows that the nodal DG mobility has an excellent agreement with FSDT mobility.

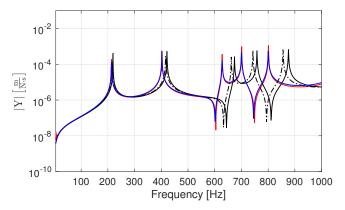


Figure 4.4: Rectangular plate mobility with thickness of h = 0.12 m and S-S-S-S BCs. The red, black, dashed black, and blue lines represent the mobility obtained by the nodal DG method, CPT, CPT with including rotary inertia, and FSDT, respectively.

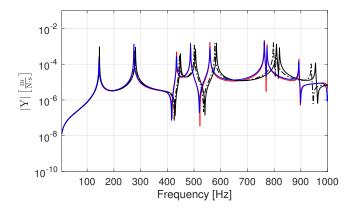


Figure 4.5: Rectangular plate mobility with thickness of h = 0.08 m and S-S-S-S BCs. The red, black, dashed black, and blue lines represent the mobility obtained by the nodal DG method, CPT, CPT with including rotary inertia, and FSDT, respectively.

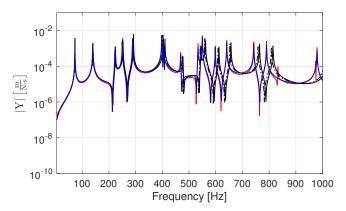


Figure 4.6: Rectangular plate mobility with thickness of h = 0.04 m and S-S-S-S BCs. The red, black, dashed black, and blue lines represent the mobility obtained by the nodal DG method, CPT, CPT with including rotary inertia, and FSDT, respectively.

The natural frequencies of the plate are tabulated in Tables 4.2-4.4. Compared to the FSDT, the natural frequency differences are between 0 to 1 Hz for every thickness. On the other hand, the nodal DG mobility shows significant natural frequency differences in comparison with the CPT. The differences are varying between 5 to 75 Hz for the plate with h=0.12 m; 2 to 62 Hz for the plate with h=0.08 m; and 0 to 24 Hz for the plate with h=0.04 m. Furthermore, the differences are reduced if the effect of rotary inertia is included in the CPT model, where the differences are varying between 4 to 55 Hz for the plate with h=0.12 m; 2 to 46 Hz for the plate with h=0.08 m; and 0 to 18 Hz for the plate with h=0.04 m. It is important to notice that the bending wavelength for the S-S-S-S plate with h=0.12m at 1 kHz is 0.934 m. It indicates that the thickness is well below 1/6 of the wavelength for every thickness taken. This principle has been a rule of thumb to use CPT in building acoustics application; however, considerable errors especially for high frequency are present even for the thinner plate.

Table 4.2: Natural frequencies of the rectangular plate with thickness of h=0.12 m and S-S-S-B BCs for the frequency up to 1 kHz.

DG	CPT	CPT-RI	FSDT
214	219	218	214
402	421	416	402
628	674	662	628
701	758	743	700
801	876	856	800

Table 4.3: Natural frequencies of the rectangular plate with thickness of h=0.08 m and S-S-S-S BCs for the frequency up to 1 kHz.

DG	CPT	CPT-RI	FSDT
144	146	146	144
275	281	279	275
435	449	446	435
487	505	501	487
560	584	578	560
763	809	797	763
774	820	808	773
893	955	939	892

Table 4.4: Natural frequencies of the rectangular plate with thickness of h=0.04 m and S-S-S-S BCs for the frequency up to 1 kHz.

DG	CPT	CPT-RI	FSDT
73	73	73	73
140	140	140	140
223	225	224	223
250	253	252	250
289	292	291	289
398	404	403	398
404	410	409	404
469	477	475	469
534	545	542	534
550	562	559	550
598	612	609	598
641	657	653	641
742	764	759	742
790	814	808	790

#### 4.4.2 S-S-S-C Plate

Figures 4.7-4.9 show the mobilities of the S-S-S-C plate with different thicknesses. It can be seen that the bending stiffness of S-S-S-C plate is higher than the S-S-S-S plate. The increment is shown by the natural frequencies shift to higher frequencies. This shift occurs as a result of one plate face is clamped instead of simply supported.

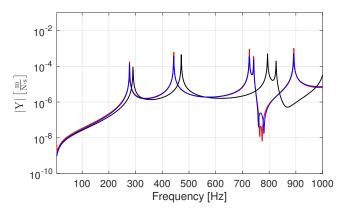


Figure 4.7: Rectangular plate mobility with thickness of h=0.12 m and S-S-S-C BCs. The red, black, and blue lines represent the mobility obtained by the nodal DG method, CPT, and FSDT, respectively.

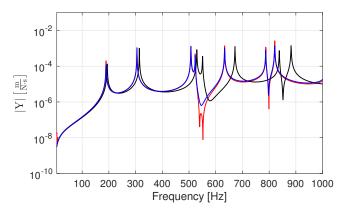


Figure 4.8: Rectangular plate mobility with thickness of h=0.08 m and S-S-S-C BCs. The red, black, and blue lines represent the mobility obtained by the nodal DG method, CPT, and FSDT, respectively.

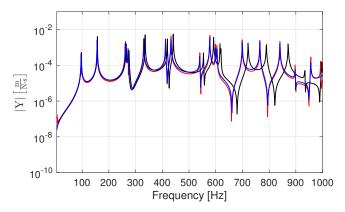


Figure 4.9: Rectangular plate mobility with thickness of h=0.12 m and S-S-S-C BCs. The red, black, and blue lines represent the mobility obtained by the nodal DG method, CPT, and FSDT, respectively.

Tables 4.5-4.7 show the natural frequencies of each plate thickness. Moreover, similar to the results obtained by the S-S-S-S plate, the comparison shows that the nodal DG mobility has an excellent agreement with FSDT mobility. The natural frequency differences are between 0 to 1 Hz for every thickness. On the other hand, the comparison with the CPT shows that differences are varying between 13 to 84 Hz for the plate with h=0.12 m; 5 to 61 Hz for the plate with h=0.08 m; and 1 to 41 Hz for the plate with h=0.04 m.

Table 4.5: Natural frequencies of the rectangular plate with thickness of h=0.12 m and S-S-S-C BCs for the frequency up to 1 kHz.

$\overline{\mathrm{DG}}$	CPT	FSDT
277	290	277
443	471	443
726	794	726
742	826	742

Table 4.6: Natural frequencies of the rectangular plate with thickness of  $h=0.08~\mathrm{m}$  and S-S-S-C BCs for the frequency up to 1 kHz.

DG	CPT	FSDT
189	194	190
305	314	305
507	529	507
523	551	523
633	672	633
787	838	787
821	882	821

Table 4.7: Natural frequencies of the rectangular plate with thickness of h=0.04 m and S-S-S-C BCs for the frequency up to 1 kHz.

DG	CPT	FSDT
96	97	96
156	157	156
262	265	262
272	275	272
331	336	331
412	419	412
433	441	433
540	554	540
578	592	578
600	616	599
605	619	605
699	721	699
765	790	765
840	871	840
897	934	897
956	997	956

# 4.4.3 S-S-S-F Plate

Figures 4.10-4.12 show the mobilities of the S-S-S-F plate with different thicknesses. It can seen that the bending stiffness of the S-S-S-F plate is lower than the S-S-S-S plate, and the natural frequencies are shifted towards lower frequencies. This shift occurs as a result of one plate face is free instead of suspending the transverse displacement.

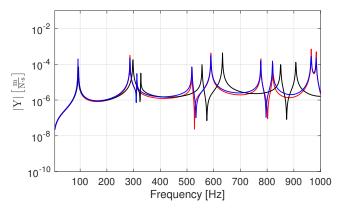


Figure 4.10: Rectangular plate mobility with thickness of h=0.12 m and S-S-S-F BCs. The red, black, and blue lines represent the mobility obtained by the nodal DG method, CPT, and FSDT, respectively.

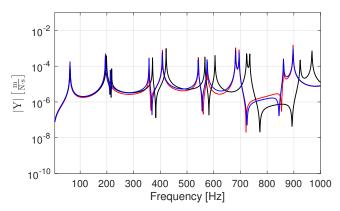


Figure 4.11: Rectangular plate mobility with thickness of h=0.08 m and S-S-S-F BCs. The red, black, and blue lines represent the mobility obtained by the nodal DG method, CPT, and FSDT, respectively.

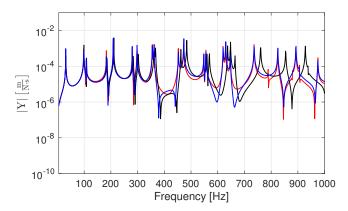


Figure 4.12: Rectangular plate mobility with thickness of h=0.04 m and S-S-S-F BCs. The red, black, and blue lines represent the mobility obtained by the nodal DG method, CPT, and FSDT, respectively.

Tables 4.8 4.10 show the natural frequencies of each plate thickness. Moreover, similar to the results obtained by the S-S-S-S plate, the comparison shows that the nodal DG mobility has an excellent agreement with FSDT mobility. The resonance frequency differences are between 0 to 1 Hz for every thickness. On the other hand, the comparison with CPT mobility shows the differences are varying between 2 to 88 Hz for the plate with  $h=0.12~\mathrm{m}$ ; 0 to 71 Hz for the plate with  $h=0.08~\mathrm{m}$ ; and 0 to 36 Hz for the plate with  $h=0.04~\mathrm{m}$ .

Table 4.8: Natural frequencies of the rectangular plate with thickness of h=0.12 m and S-S-S-F BCs for the frequency up to 1 kHz.

DG	CPT	FSDT
92	94	92
286	298	286
312	327	312
518	556	518
589	633	589
777	851	776
820	908	820

Table 4.9: Natural frequencies of the rectangular plate with thickness of  $h=0.08~\mathrm{m}$  and S-S-S-F BCs for the frequency up to 1 kHz.

DG	CPT	FSDT
62	62	62
195	198	195
213	218	213
358	371	358
408	422	408
542	567	542
575	605	575
682	723	682
695	735	695
861	924	861
897	968	897

Table 4.10: Natural frequencies of the rectangular plate with thickness of  $h=0.04~\mathrm{m}$  and S-S-S-F BCs for the frequency up to 1 kHz.

DG	CPT	FSDT
31	31	31
99	99	99
108	109	108
183	185	183
209	211	209
280	283	280
298	302	298
355	362	355
362	367	362
453	462	453
473	484	473
548	560	548
556	569	556
620	637	620
630	648	630
647	665	647
736	761	736
825	854	825
892	928	893

# 4.4.4 Mobility near to excitation point

In this section, the mobilities of the S-S-S-F plate with h=0.12 m around the excitation point are presented. It should be noticed that the R1-R4 positions are

located at the highlighted elements near to the point F such as shown in Figure 4.2, hence the velocity responses are taken at the same element where the force is excited. Figure 4.13 shows the mobilities at R1 and R2, and Figure 4.14 shows the mobilities at R3 and R4. Both figures show that the nodal DG mobilities are in an excellent agreement with the FSDT mobilities. The maximum difference of the natural frequency is 1 Hz for all velocity positions. However, some discrepancies happen at the anti-resonance frequencies. The anti-resonance frequencies have a lower Q factor compared to the FSDT anti-resonance frequencies. At R1, R2, R3, and R4, the anti-resonance frequency differences vary between 0-10 Hz, 1-7 Hz, 1-11 Hz, and 1-11 Hz, respectively. Moreover, it can be observed that at the R4 location, the maximum discrepancy happens at 451 Hz instead of at the highest anti-resonance frequency of 977 Hz. Although the discrepancy at the anti-resonance frequency is not a significant issue to the vibration problems, the agreement could be improved by refining the mesh near the excitation point.

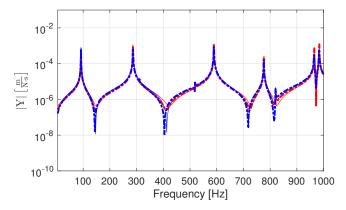


Figure 4.13: Rectangular plate mobility with thickness of h = 0.12 m and S-S-S-F BCs at position R1 (solid lines) and R2 (dashed lines). The red and blue lines represent the mobility obtained by the nodal DG method and FSDT, respectively.

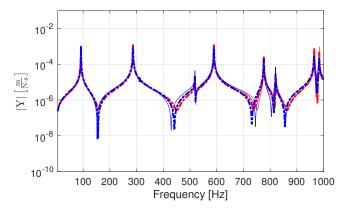


Figure 4.14: Rectangular plate mobility with thickness of h = 0.12 m and S-S-S-F BCs at position R3 (solid lines) and R4 (dashed lines). The red and blue lines represent the mobility obtained by the nodal DG method and FSDT, respectively.

# 4.4.5 L-Plate

In this section, the L-shaped plate mobilities between position F and R1-R3 are presented following the configuration of section 4.3.3. The mobilities based on the CPT, the FSDT and the linear elasticity equation model are calculated to be compared with the mobility obtained by the nodal DG method. Kessissoglou presented the exact CPT mobility for this configuration, where the transverse and in-plane plate displacements are described in terms of a modal and travelling wave solution [210]. This solution is used for comparison. Moreover, the finite element method (FEM) in the frequency-domain is used to obtain the mobilities based on the FSDT and the three-dimensional linear elasticity equations. The FEM model is implemented using COMSOL Multiphysics [211], where the FSDT is solved with a DoF up-to  $98 \cdot 10^3$ , and the three-dimensional linear elasticity equations are solved with a DoF number up-to  $264 \cdot 10^3$ . These numbers are taken to have the resonance frequencies converged within a 1 Hz uncertainty. All mobilities are presented in Figures 4.15-4.17.

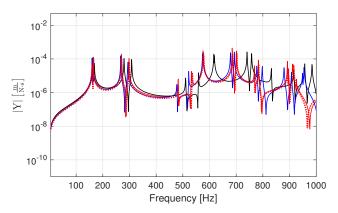


Figure 4.15: L-shaped plate mobilities at position R1. The red, black, and blue solid lines represent the mobility obtained by the nodal DG method, CPT, and FSDT, respectively. The red dashed line represent mobility obtained by FEM.

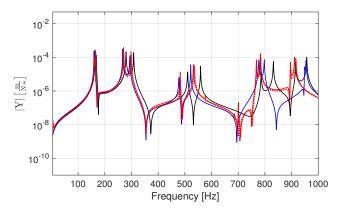


Figure 4.16: L-shaped plate mobilities at position R2. The red, black, and blue solid lines represent the mobility obtained by the nodal DG method, CPT, and FSDT, respectively. The red dashed line represent mobility obtained by FEM.

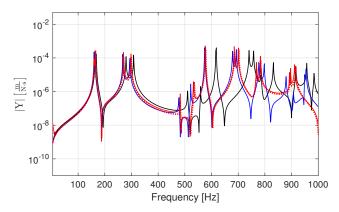


Figure 4.17: L-shaped plate mobilities at position R3. The red, black, and blue solid lines represent the mobility obtained by the nodal DG method, CPT, and FSDT, respectively. The red dashed line represent mobility obtained by FEM.

At all locations (R1-R3), Figure 4.15-Figure 4.17 show that the mobilities obtained by CPT, FSDT and nodal DG method are in a good agreement at frequency range below 700 Hz. It can be observed that each natural frequency of nodal DG mobility has its counterpart with the CPT or the FSDT mobility at all frequency range. However, the CPT mobility has higher natural frequencies than nodal DG mobility. These discrepancies are found as well in the rectangular plate case. The differences vary between 4 Hz and 58 Hz at R1, 3 and 73 Hz at R2, and 3 and 49 Hz at R3. Compared to the FSDT mobility, nodal DG natural frequencies have more difference in the L-shaped plate case than in the rectangular plate case. The natural frequencies differences are up to 38 Hz at R1, up to 53 Hz at R2, and up to 42 Hz at R3. At R2 location, one also could notice that the anti-resonance trend is not similar between the nodal DG and the CPT/FSDT mobilities at around 700 Hz. Above 700 Hz, the similarities between the nodal DG mobility and the CPT/FSDT mobilities are lessening due to the resonance or the anti-resonance location.

For further validation on the nodal DG solution, the mobilities that are calculated by FEM in Figures 4.15-4.17. The mobilities from nodal DG method and the FEM show an excellent agreement with a maximum discrepancy of the natural frequency less than 4 Hz.

# 4.5 Conclusions

The nodal DG method has been presented to solve the forced plate vibration problem. The upwind numerical flux of the three-dimensional linear elasticity equations has been presented in detail using the Rankine-Hugoniot condition for the stress-velocity variables. Furthermore, numerical aspects such as the point force excitation and the boundary conditions for the plates with S-S-S-S, S-S-S-F and S-S-C boundary conditions have been implemented in the nodal DG methodology.

For the rectangular plate case, the nodal DG mobility shows an excellent agreement with the exact mobility of the first order shear deformation theory (FSDT). The agreement could be observed even at the location near to the point force excitation. On the other hand, a good agreement with the classical plate theory (CPT) happens solely at the first couple of resonance frequencies, with increased accuracy as the plate thickness is reduced.

For the L-shaped plate case, the nodal DG mobility shows a good agreement with the CPT and FSDT in the lower frequency range. However, in the higher frequency range, there are some disagreements due to significant frequency differences of the resonance and the anti-resonance frequencies. However, the nodal DG mobility has an excellent agreement with the mobility obtained by the finite element method of the three-dimensional linear elasticity equations. An acceleration of the nodal DG method by a parallel implementation will make this method highly useful for industrial applications.

# 5 | Discontinous Galerkin method for vibration of structures with piece-wise constant material properties

# **Abstract**

In this work, vibrations of complex structures excited by an impact source are modelled using the time domain nodal discontinuous Galerkin (DG) method, which solves linear elasticity equations. Two structures of interest, a T-shaped structure and a scaled lightweight wooden floor, are taken as example cases. Both structures consist of components that differ in their mechanical properties. Rankine-Hugoniot jump conditions for piece-wise constant material properties are used to obtain accurate numerical fluxes in the DG method. Free or fixed boundary conditions are imposed on the surfaces in the structures, and constant viscous damping forces are added to the model to create vibrational energy losses of the structures. To validate the numerical results, the mobility of the structures is calculated and compared with experimental data. The agreement is good regarding the natural frequencies, with a maximum absolute difference of less than 20 Hz for the T-shaped structure in the frequency range below 500 Hz, and less than 11 Hz for the scaled LWF in the frequency range below 200 Hz. The adopted damping approach is shown to be insufficient to represent a broad frequency range.

# 5.1 Introduction

Due to the increasing focus on the sustainability issues with conventional concrete-based construction methods, wood-based building methods have steadily gained traction. However, due to the low weight of building components, these wooden building methods suffer from poor sound insulation in the low-frequency range [212], [213]. Structural motions caused by human activity or mechanical systems can induce vibrations in structures. These vibrations transmit through the building's elements and then radiate low-frequency noise, causing noise-related disturbance to the building's occupants.

T-shaped structures and lightweight wooden floors (LWF) are two types of structures

that are commonly found in wooden-based buildings. To minimalise the noise and vibration levels, it is necessary to accurately predict the level of vibration within the structures. Several vibration models of the T-shaped structure were developed using the beam and the plate theories in Refs. [214]–[216]. These models consider both out-of-plane and in-plane vibrations. Some models have been developed to predict the LWF vibration field by utilising thin plate and Euler beam vibration theories [22], [25]. The modal expansion method was used to solve these models, as shown in Refs. [217]–[219]. Reviews on the LWF vibration prediction methods can be found in Refs. [220], [221]. According to a recent review [221], the LWF vibration model could be refined using more general plate and beam vibration models, such as the Mindlin plate and Timoshenko beam vibrations theories. However, analytical solutions for these methods are only possible for specific geometries, boundary conditions, and homogeneous materials.

To determine the transmission of vibrations through complex systems, energy-based or wave-based methods are commonly used [63], [220]. Statistical energy analysis (SEA) is one such energy-based method, which is primarily used at high frequencies where the modal density is high. This method has been utilised to analyse vibration transmission in coupled masonry and concrete walls [222]. Energy-based methods are frequently preferred because they provide a quick solution, or when detailed information on the structure is not required, such as octave band analysis. On the other hand, energy-based methods fail in the low-frequency region, which is critical for vibration problems in building acoustics applications [212].

Wave-based methods are numerical approaches for resolving the structural vibration governing equations commonly used in the low-frequency region. Numerous wave-based numerical methods are employed to predict the vibration field of structural elements, including the finite element method (FEM) [223], the finite difference time domain (FDTD) method [128], the spectral finite element method (SFEM) [224], and the discontinuous Galerkin (DG) method [225]. Among these methods, the nodal DG method is a comparatively recent methodology for modelling with vibration. This method has a number of advantages over other wave-based methods. For example, it can readily cope with a complex domain by representing it with an unstructured mesh, and it allows refinement of the solution by increasing the polynomial order or element number. Additionally, the nodal DG method solves the governing equations using an element-wise formulation. As a result, it provides a framework that is well suited for parallel computation. This allows for significantly accelerated calculations [111]. This method has been extensively studied for application seismology [200]. Its application to structural vibration, however, is still in its infancy.

The purpose of this study is to present the nodal DG method to the vibration problem of solid structures with piece-wise constant material properties. The proposed model is based on a three-dimensional solid domain, whereas the majority of other methods propose vibration models in reduced dimensions such as beams and plates [221]. Mobilities of the structures are determined using the nodal DG method and are compared with experimental results. This chapter is organised as follows: Section 5.2 describes the governing equations and the methodology of the nodal DG method; Section 5.3 shows the details of the case studies; Section 5.4 displays the experimental setup for validating the nodal DG results. The computational settings used to solve each case are shown in Section 5.5; Section 5.6 discusses the numerical and experimental results, and Section 5.7 concludes the chapter.

#### 5.2Methodology

#### 5.2.1Linear elasticity equations

The linear elasticity equations which govern the propagation of elastic waves in a solid medium can be used to model the linear vibration of a structure. This set of equations consists of the momentum conservation and Hooke's constitutive equations [21]. For a Cartesian three-dimensional coordinate system, the equations for an isotropic medium can be written in a velocity-stress form as follows:

$$\frac{\partial \boldsymbol{q}_{s}}{\partial t} + \nabla \cdot \boldsymbol{H}(\boldsymbol{q}_{s}) = \frac{\partial \boldsymbol{q}_{s}}{\partial t} + \boldsymbol{B}_{j} \frac{\partial \boldsymbol{q}_{s}}{\partial x_{j}} = \boldsymbol{g} - \zeta \boldsymbol{q}_{s}, \tag{5.1}$$

$$\boldsymbol{q}_{s}(\boldsymbol{x}, t) = \begin{bmatrix} v_{x} & v_{y} & v_{z} & \sigma_{xx} & \sigma_{yy} & \sigma_{zz} & \sigma_{xz} & \sigma_{yz} & \sigma_{xy} \end{bmatrix}^{T},$$

$$\boldsymbol{g}(\boldsymbol{x}, t) = \begin{bmatrix} g_{x} & g_{y} & g_{z} & 0 & 0 & 0 & 0 & 0 \end{bmatrix}^{T},$$

$$\zeta = \operatorname{diag} \begin{pmatrix} \zeta_{x} & \zeta_{y} & \zeta_{z} & 0 & 0 & 0 & 0 & 0 \end{pmatrix},$$

where  $v_x, v_y, v_z$  are the velocities in the x-, y-, and z- directions, respectively.  $\sigma_{xx}$ ,  $\sigma_{yy}, \ \sigma_{zz}, \ \sigma_{xz}, \ \sigma_{yz}, \ \sigma_{xy}$  are the normal and shear stress components,  $g_x, g_y, g_z$  are the body forces, and  $\zeta_x, \zeta_y, \zeta_z$  are the viscous damping forces. The flux matrix reads  $m{H}(m{q}_s) = [m{h}_x, m{h}_y, m{h}_z] = [m{B}_x m{q}_s, m{B}_y m{q}_s, m{B}_z m{q}_s]$ . The constant flux Jacobian matrix  $m{B}_j$ is given as:

$$\begin{split} \boldsymbol{B}_{j} &= \left[ \begin{array}{c|ccc} \mathbf{0}_{3\times3} & \boldsymbol{B}_{1,j} \\ \hline \boldsymbol{B}_{2,j} & \mathbf{0}_{6\times6} \end{array} \right], \boldsymbol{B}_{1,j} = -\frac{1}{\rho} \left[ \begin{array}{cccc} \delta_{xj} & 0 & 0 & \delta_{zj} & 0 & \delta_{yj} \\ 0 & \delta_{yj} & 0 & 0 & \delta_{zj} & \delta_{xj} \\ 0 & 0 & \delta_{zj} & \delta_{xj} & \delta_{xj} \end{array} \right], \\ \boldsymbol{B}_{2,j} &= - \left[ \begin{array}{cccc} (\lambda + 2\mu)\delta_{xj} & \lambda\delta_{yj} & \lambda\delta_{zj} \\ \lambda\delta_{xj} & (\lambda + 2\mu)\delta_{yj} & \lambda\delta_{zj} \\ \lambda\delta_{xj} & \lambda\delta_{yj} & (\lambda + 2\mu)\delta_{zj} \\ \mu\delta_{zj} & 0 & \mu\delta_{xj} \\ 0 & \mu\delta_{zj} & \mu\delta_{yj} \end{array} \right], \end{split}$$

where  $\lambda$  and  $\mu$  are the Lamé parameters,  $\rho$  is the mass density and index j has components [x, y, z]. The  $\delta_{ij}$  denotes the Kronecker delta function. The solution of Equations (5.1) consists of a linear combination of elastic waves propagating with longitudinal wave speed  $(c_p = \sqrt{(\lambda + 2\mu)/\rho})$  and transverse wave speed  $(c_s = \sqrt{\mu/\rho})$ . The Lame parameters are represented by using Young's modulus (E) and Poisson's ratio  $(\nu)$  as  $\lambda = E\nu/(1+\nu)(1-2\nu)$  and  $\mu = E/2(1+\nu)$ .

### 5.2.2 Nodal discontinuous Galerkin method

The nodal discontinuous Galerkin (DG) method is used to solve the Equation (5.1). The algorithm of the method is developed by Hesthaven and Warburton [112] and is adopted in this thesis. The problem domain is approximated by the computational domain  $\Omega_h$  with K number of non-overlapping rectilinear tetrahedral elements  $D^k$  as  $\Omega_h = \bigcup_{k=1}^K D^k$ . On each  $D^k$ , the local solution is expanded by nodal basis functions as:

$$\mathbf{q}_{sh}^{k}(\mathbf{x},t) = \sum_{i=1}^{N_p} \mathbf{q}_{sh}^{k}(\mathbf{x}_{i}^{k},t) l_{i}^{k}(\mathbf{x}),$$
 (5.2)

where  $q_{sh}^k(\boldsymbol{x}_i^k,t)$  are the unknown nodal values of the elastic wave variables.  $l_i^k(\boldsymbol{x})$  are the three-dimensional Lagrange interpolation polynomials based on the nodal points  $\boldsymbol{x}_i$ , and  $N_p$  is the number of nodal points. The global solutions are approximated as the direct sum of the local solutions as:

$$\boldsymbol{q}_s(\boldsymbol{x},t) \approx \boldsymbol{q}_{sh}(\boldsymbol{x},t) = \bigoplus_{k=1}^K \boldsymbol{q}_{sh}^k(\boldsymbol{x},t). \tag{5.3}$$

The closed expression of the Lagrangian interpolation polynomials in tetrahedral element is constructed by the products of the Jacobi polynomials of order N, with the number of nodal points per element is  $N_p = (N+1)(N+2)(N+3)/6$ . The distribution of these points follows the optimised Legendre-Gauss-Lobato (LGL) points over a tetrahedral element as described in Ref. [112].

In each element, the nodal basis functions are used to approximate the unknown variables and the body forces in Equation (5.1). The residuals of the approximations are then multiplied by the test functions in accordance with the Galerkin method. The strong formulation of Equation (5.1) takes the following form after performing spatial integration by parts twice:

$$\int_{D^k} \left[ \frac{\partial \boldsymbol{q}_{sh}^k}{\partial t} + \nabla \cdot \boldsymbol{H}(\boldsymbol{q}_{sh}^k) \right] l_i^k d\boldsymbol{x} = \int_{D^k} (\boldsymbol{g}_h^k - \zeta \boldsymbol{q}_{sh}^k) l_i^k d\boldsymbol{x} \\
- \int_{\partial D^k} \boldsymbol{n} \cdot \left[ \boldsymbol{H}^* - \boldsymbol{H}(\boldsymbol{q}_{sh}^k) \right] l_i d\boldsymbol{x}, \tag{5.4}$$

where  $\partial D^k$  is the element surface,  $\boldsymbol{g}_h^k$  is the approximated body force vector, and  $\boldsymbol{n} = [n_x, n_y, n_z]$  is the outward normal vector of the element surface  $\partial D^k$ . The flux along the normal direction of the element surface is defined as  $\boldsymbol{n} \cdot \boldsymbol{H} = (n_x \boldsymbol{h}_x + n_y \boldsymbol{h}_y + n_z \boldsymbol{h}_z)$ , and the  $\boldsymbol{H}^*$  is the numerical flux.

In the DG method, the numerical flux ensures continuity of the global solution. It is a function of the interior solution  $(q_{sh}^-)$ , which is the solution within the element  $D^k$ , and the exterior solution  $(q_{sh}^+)$ , which is the solution of the adjacent elements around  $D^k$ . The numerical flux used in this work is the upwind numerical flux. The upwind numerical flux can be derived by solving the Riemann problem at the interface of two

homogeneous media. This interface represents the faces of two adjacent elements that are located in the same position. Consider that the interface is located at x = 0. The properties of the medium  $(\lambda^-, \mu^-, \rho^-)$  are those of the internal medium at x < 0, and  $(\lambda^+, \mu^+, \rho^+)$  are those of the adjacent medium at x > 0. The Riemann problem is a discontinuous initial value problem that occurs at this interface as:

$$\boldsymbol{q}_{sh}(\boldsymbol{x},0) = \begin{cases} \boldsymbol{q}_{sh}^{-} & \text{if } \boldsymbol{x} < 0, \\ \boldsymbol{q}_{sh}^{+} & \text{if } \boldsymbol{x} > 0. \end{cases}$$
 (5.5)

The solution to this problem is the intermediate solution  $(q_{sh}^*(\mathbf{0},t))$ . It is derived using the Rankine-Hugoniot jump condition as described in Refs. [225],[200],[21],[226]. The term  $n \cdot |H^* - H(q_{sh}^k)|$ , which appears on the right-hand side of Equation (5.4), is described in detail in Appendix D. The numerical fluxes  $n \cdot H^* = n \cdot H(q_{sh}^*)$  are a function of the intermediate solution.

Following the definition of the numerical flux, the nodal basis and numerical flux are substituted into Equation (5.4) to obtain the semi-discrete form for each element as:

$$M^{k} \frac{\partial \boldsymbol{v}_{xh}^{k}}{\partial t} - \frac{1}{\rho} \left( \boldsymbol{S}_{x}^{k} \boldsymbol{\sigma}_{xxh}^{k} + \boldsymbol{S}_{y}^{k} \boldsymbol{\sigma}_{xyh}^{k} + \boldsymbol{S}_{z}^{k} \boldsymbol{\sigma}_{xzh}^{k} \right) = M^{k} \left( \boldsymbol{g}_{xh}^{k} - \zeta_{x} \boldsymbol{v}_{xh}^{k} \right) - \sum_{r=1}^{4} \boldsymbol{M}^{kr} \hat{\boldsymbol{H}}_{v_{x}}^{kr},$$

$$M^{k} \frac{\partial \boldsymbol{v}_{yh}^{k}}{\partial t} - \frac{1}{\rho} \left( \boldsymbol{S}_{x}^{k} \boldsymbol{\sigma}_{xyh}^{k} + \boldsymbol{S}_{y}^{k} \boldsymbol{\sigma}_{yyh}^{k} + \boldsymbol{S}_{z}^{k} \boldsymbol{\sigma}_{yzh}^{k} \right) = M^{k} \left( \boldsymbol{g}_{yh}^{k} - \zeta_{y} \boldsymbol{v}_{yh}^{k} \right) - \sum_{r=1}^{4} \boldsymbol{M}^{kr} \hat{\boldsymbol{H}}_{v_{y}}^{kr},$$

$$M^{k} \frac{\partial \boldsymbol{v}_{zh}^{k}}{\partial t} - \frac{1}{\rho} \left( \boldsymbol{S}_{x}^{k} \boldsymbol{\sigma}_{xzh}^{k} + \boldsymbol{S}_{y}^{k} \boldsymbol{\sigma}_{yzh}^{k} + \boldsymbol{S}_{z}^{k} \boldsymbol{\sigma}_{zzh}^{k} \right) = M^{k} \left( \boldsymbol{g}_{zh}^{k} - \zeta_{z} \boldsymbol{v}_{zh}^{k} \right) - \sum_{r=1}^{4} \boldsymbol{M}^{kr} \hat{\boldsymbol{H}}_{v_{y}}^{kr},$$

$$M^{k} \frac{\partial \boldsymbol{\sigma}_{xxh}^{k}}{\partial t} - \left( \boldsymbol{\lambda} + 2\mu \right) \boldsymbol{S}_{x}^{k} \boldsymbol{v}_{xh}^{k} - \lambda \boldsymbol{S}_{y}^{k} \boldsymbol{v}_{yh}^{k} - \lambda \boldsymbol{S}_{z}^{k} \boldsymbol{v}_{zh}^{k} = - \sum_{r=1}^{4} \boldsymbol{M}^{kr} \hat{\boldsymbol{H}}_{\sigma_{xx}}^{kr},$$

$$M^{k} \frac{\partial \boldsymbol{\sigma}_{yyh}^{k}}{\partial t} - \lambda \boldsymbol{S}_{x}^{k} \boldsymbol{v}_{xh}^{k} - (\boldsymbol{\lambda} + 2\mu) \boldsymbol{S}_{y}^{k} \boldsymbol{v}_{yh}^{k} - \lambda \boldsymbol{S}_{z}^{k} \boldsymbol{v}_{zh}^{k} = - \sum_{r=1}^{4} \boldsymbol{M}^{kr} \hat{\boldsymbol{H}}_{\sigma_{yy}}^{kr},$$

$$M^{k} \frac{\partial \boldsymbol{\sigma}_{zzh}^{k}}{\partial t} - \lambda \boldsymbol{S}_{x}^{k} \boldsymbol{v}_{xh}^{k} - \lambda \boldsymbol{S}_{y}^{k} \boldsymbol{v}_{yh}^{k} - (\boldsymbol{\lambda} + 2\mu) \boldsymbol{S}_{z}^{k} \boldsymbol{v}_{zh}^{k} = - \sum_{r=1}^{4} \boldsymbol{M}^{kr} \hat{\boldsymbol{H}}_{\sigma_{xz}}^{kr},$$

$$M^{k} \frac{\partial \boldsymbol{\sigma}_{zzh}^{k}}{\partial t} - \mu \boldsymbol{S}_{x}^{k} \boldsymbol{v}_{xh}^{k} - \mu \boldsymbol{S}_{x}^{k} \boldsymbol{v}_{zh}^{k} = - \sum_{r=1}^{4} \boldsymbol{M}^{kr} \hat{\boldsymbol{H}}_{\sigma_{xz}}^{kr},$$

$$M^{k} \frac{\partial \boldsymbol{\sigma}_{yzh}^{k}}{\partial t} - \mu \boldsymbol{S}_{z}^{k} \boldsymbol{v}_{yh}^{k} - \mu \boldsymbol{S}_{x}^{k} \boldsymbol{v}_{zh}^{k} = - \sum_{r=1}^{4} \boldsymbol{M}^{kr} \hat{\boldsymbol{H}}_{\sigma_{xz}}^{kr},$$

$$M^{k} \frac{\partial \boldsymbol{\sigma}_{xyh}^{k}}{\partial t} - \mu \boldsymbol{S}_{z}^{k} \boldsymbol{v}_{yh}^{k} - \mu \boldsymbol{S}_{x}^{k} \boldsymbol{v}_{zh}^{k} = - \sum_{r=1}^{4} \boldsymbol{M}^{kr} \hat{\boldsymbol{H}}_{\sigma_{xz}}^{kr},$$

$$M^{k} \frac{\partial \boldsymbol{\sigma}_{xyh}^{k}}{\partial t} - \mu \boldsymbol{S}_{z}^{k} \boldsymbol{v}_{xh}^{k} - \mu \boldsymbol{S}_{x}^{k} \boldsymbol{v}_{zh}^{k} = - \sum_{r=1}^{4} \boldsymbol{M}^{kr} \hat{\boldsymbol{H}}_{\sigma_{xz}}^{kr},$$

 $\boldsymbol{v}_{xh}^k, \, \boldsymbol{v}_{yh}^k, \, \boldsymbol{v}_{zh}^k, \, \boldsymbol{\sigma}_{\boldsymbol{x}\boldsymbol{x}_h}^k, \, \boldsymbol{\sigma}_{\boldsymbol{y}\boldsymbol{y}_h}^k, \, \boldsymbol{\sigma}_{\boldsymbol{z}\boldsymbol{z}_h}^k, \, \boldsymbol{\sigma}_{\boldsymbol{x}\boldsymbol{z}_h}^k, \boldsymbol{\sigma}_{\boldsymbol{y}\boldsymbol{z}_h}^k, \, \text{and} \, \boldsymbol{\sigma}_{\boldsymbol{x}\boldsymbol{y}_h}^k \, \text{are vectors representing all elastic wave variables at the nodal points <math>\boldsymbol{x}_i$ , with i=1 to  $N_p$ . Note that all the mechanical properties in Equations (5.6) are defined in the interior element, except for the numerical flux terms. The second superscript r denotes the rth faces of  $\partial D^{kr}$  of the element  $D^k$ , where the number of faces of the tetrahedral element is four.  $\hat{\boldsymbol{H}}_{v_x}^{kr}, \, \hat{\boldsymbol{H}}_{v_y}^{kr}, \, \hat{\boldsymbol{H}}_{\sigma_{xx}}^{kr}, \, \hat{\boldsymbol{H}}_{\sigma_{xx}}^{kr},$ 

Having the semi-discrete form at hand, Equation (5.6) for the whole computational domain can be expressed in the form of ordinary differential equations as:

$$\frac{\mathrm{d}\boldsymbol{q}_{sh}}{\mathrm{d}t} = \mathcal{L}\left(\boldsymbol{q}_{sh}(t), t\right),\tag{5.7}$$

where  $q_{sh}$  is the vector of all nodal solutions, and  $\mathcal{L}$  is the semi-discrete operator conducted over all elements. Finally, various methods can be employed to integrate the time derivative in Equation (5.7). The fourth-order Runge-Kutta method with eight stages (RKF84) is used in this work, as described in Ref. [148]. For the time integration, the time-step ( $\Delta t$ ) is defined as:

$$\Delta t = \frac{C_{CFL} \cdot \min(r_{D^k})}{N^2 \cdot \max(c_p)},\tag{5.8}$$

where  $C_{CFL}$  is the Courant number,  $\max(c_p)$  is the maximum longitudinal wave speed, and  $\min(r_{D^k})$  is the shortest element edge in the computational domain.

# 5.2.3 Force excitation

The external excitation can be given by the body force components,  $[g_x, g_y, g_z, \mathbf{0}]$ , on the right-hand side of Equation (6.1). A point force excitation, similar to that presented in Ref.[225], is used in this work. The body force along the z-direction  $g_z(x,t)$  is approximated using the Lagrange interpolation polynomials as:

$$g_z(\mathbf{x},t) = A(t) \cdot \delta(\mathbf{x} - \mathbf{x}_0), \tag{5.9}$$

where A(t) is a time domain function,  $\delta(\mathbf{x})$  is the spatial Dirac delta function, and  $\mathbf{x}_0$  is the excitation position. To obtain a uniform directivity, A(t) is distributed over several elements, with one vertex located at  $\mathbf{x}_0$ . Following the application of the same body force to each element, the total force F(t)[N] can be computed as follows:

$$F(t) = \rho \sum_{k=1}^{K_p} G^k(t) = \rho \sum_{k=1}^{K_p} \int_{D_k} g_z^k(\mathbf{x}, t) d\mathbf{x},$$
 (5.10)

where  $K_p$  is the number of elements in the vicinity of the excitation point, and  $g_z^k(\boldsymbol{x},t)$  is the body force function in each element k. Please note that the body force is normalised to the mass density in Equation (5.1), and that multiplication by the density is required to obtain the total force. The details of the integration of Equation (5.10) can be found in Chapter 4.

#### 5.2.4Boundary conditions

The nodal DG method enables the numerical flux to enforce the boundary conditions (BCs) by providing the exterior solution  $(q_{sh}^+)$  at the boundary. The exterior solution must be suitably defined as a function of the interior solution  $(q_{sh}^-)$  based on the imposed BCs. This concept is analogous to how the ghost-cell values are determined in the finite volume method, as described in Ref. [21]. The elastic motions at the boundaries can be defined by imposing specific velocities or traction values. For given velocities (U, V, W), the exterior solution at the boundary's nodal points should satisfy the following conditions:

$$\begin{split} &\sigma_{xx_h}^{\ +} = \sigma_{xx_h}^{\ -}, \quad \sigma_{yy_h}^{\ +} = \sigma_{yy_h}^{\ -}, \quad \sigma_{zz_h}^{\ +} = \sigma_{zz_h}^{\ -}, \\ &\sigma_{xz_h}^{\ +} = \sigma_{xz_h}^{\ -}, \quad \sigma_{yz_h}^{\ +} = \sigma_{yz_h}^{\ -}, \quad \sigma_{xy_h}^{\ +} = \sigma_{xy_h}^{\ -}, \\ &v_{xh}^{+} = 2U - v_{xh}^{\ -}, \quad v_{yh}^{+} = 2V - v_{yh}^{\ -}, \quad v_{zh}^{+} = 2W - v_{zh}^{\ -}. \end{split}$$

In case of a traction boundary condition, the values of  $(\sigma_{xx}, \sigma_{xy}, \sigma_{xz})$  at the boundary are given as  $(\tau_{xx}, \tau_{xy}, \tau_{xz})$ . To meet this condition, the correct exterior solution on this boundary can be set as follows:

$$\begin{split} &\sigma_{xx_h}^{+} = 2\tau_{xx} - \sigma_{xx_h}^{-}, \quad \sigma_{yy_h}^{+} = \sigma_{yy_h}^{-}, \quad \sigma_{zz_h}^{+} = \sigma_{zz_h}^{-}, \\ &\sigma_{xz_h}^{+} = 2\tau_{xz} - \sigma_{xz_h}^{-}, \quad \sigma_{yz_h}^{+} = \sigma_{yz_h}^{-}, \quad \sigma_{xy_h}^{+} = 2\tau_{xy} - \sigma_{xy_h}^{-}, \\ &v_{xh}^{+} = v_{xh}^{-}, \quad v_{yh}^{+} = v_{yh}^{-}, \quad v_{zh}^{+} = v_{zh}^{-}. \end{split}$$

In this work, fixed boundary conditions (U = V = W = 0), and traction free boundary conditions, for example, ( $\sigma_{jx} = \sigma_{jy} = \sigma_{jz} = 0$ ), are used. These values ensure that the Riemann solutions at the boundary are equal to the specified values. This methodology was applied in the nodal DG method, as described in Refs. [225], [200]. Note that  $(\lambda^+, \mu^+, \rho^+)$  at the boundary are set equal to  $(\lambda^-, \mu^-, \rho^-)$  to satisfy the specified BCs above.

#### 5.3Case studies

The nodal DG method is utilised to simulate two cases of structural vibrations excited by an impact source. A T-shaped structure and a scaled lightweight wooden floor (LWF) are used as examples. Each structure is comprised of multiple medium density fibreboard components, each with its own set of mechanical properties. Appendix E details the procedure for obtaining these properties.

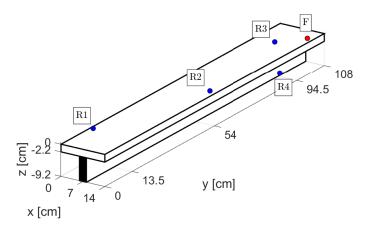


Figure 5.1: The case of the T-shaped structure in which a different boundary condition (fixed or free) is applied to the black coloured area. The red and blue dots indicate the excitation and receiver locations, respectively.

# 5.3.1 T-shaped structure

As illustrated in Figure 5.1, the T-shaped structure is a simple structure composed of two components: a vertical beam, and a horizontal beam with dimensions of [14 cm  $\times$  108 cm  $\times$  2.2 cm] and [2.2 cm  $\times$  108 cm  $\times$  7 cm], respectively. The origin of the coordinate system is on the left-hand corner. The two components are glued together to form a fixed connection at the interface z=-2.2 [cm]. The mechanical properties of the components are given in Table 5.1. Please note that the damping forces are assumed the same for both components and equal in all directions ( $\zeta_x = \zeta_y = \zeta_z = \zeta$ ).

Two types of boundary conditions are considered for this structure, namely fixed BCs and free BCs. Either boundary condition is applied to the black-coloured area (or the clamped area), while the rest of the structure's surfaces have free BCs. To excite the vibration, a point force (F) is applied at the coordinates (13, 101.25, 0) cm, marked with a red dot in Figure 5.1. To obtain the response of the structure, four receivers (R1-R4) are selected to record the structure's velocities, as shown with blue dots. The receivers are selected in this manner because they are distributed at varying distances from the force location. The coordinates of the receivers are R1 = (1, 13.5, 0) cm, R2 = (13, 54, 0) cm, R3 = (7, 94.5, 0) cm, and R4 = (8.1, 94.5, -8.2) cm.

Table 5.1: The mechanical properties of the constituting components of the T-shaped structure.

Component	Density $[kg/m^3]$	Young's Modulus [GPa]	Poisson's Ratio [-]	Damping force( $\zeta$ ) [N · m <sup>3</sup> /kg]
Vertical beam	616.1	2.39	$0.3 \\ 0.3$	10
Horizontal beam	720.8	3.57		10

#### 5.3.2Scaled lightweight wooden floor

The scaled LWF is composed of a single panel as the top plate and seven joists to reinforce the plate, as shown in Figure 5.2. This case represents a more complex structure than the T-shaped structure, with more components and different mechanical properties, as shown in Table 5.2. Each joist measures  $[108 \text{ cm} \times 2.2 \text{ cm} \times 7 \text{ cm}]$ and the top plate measures [112 cm  $\times$  112 cm  $\times$  0.9 cm]. The origin of the coordinate system is at the top corner of the plate. The joists are spaced evenly apart by 13.75 cm, with Joist 1 being the closest to the origin. All surfaces of the structure have free BCs. The connections between the top floor and joists are fixed, realised by nine screw connections spaced evenly along each joist in the experiment.

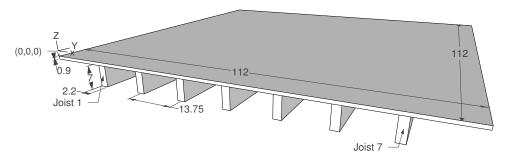


Figure 5.2: The scaled LWF structure, all dimensions are in cm.

Table 5.2: Mechanical properties of the individual	components of the scaled LWF structure.
--	---

Component	Density $[kg/m^3]$	Young's Modulus [GPa]	Poisson's Ratio [-]	Damping force( $\zeta$ ) [N · m <sup>3</sup> /kg]
Plate	670	3.70	0.3	20
Joist 1	583	1.89	0.3	20
Joist 2	565	2.06	0.3	20
Joist 3	559	2.07	0.3	20
Joist 4	571	2.14	0.3	20
Joist 5	577	2.16	0.3	20
Joist 6	589	2.39	0.3	20
Joist 7	577	2.10	0.3	20

Table 5.3: The excitation and receiver positions of the centre excitation configuration on the scaled LWF case.

Index	(x, y) [cm]
F	(56, 56)
C1	(62.875, 42.25)
C2	(76.625, 28.5)
C3	(83.5, 28.5)
C4	(97.25, 14.75)

Two configurations are chosen to investigate the vibration of this structure under an impact excitation. The first configuration is the centre excitation. As displayed in Figure 5.3a, the excitation point (F) of this configuration is located in the centre of the top plate. Four receivers, C1-C4, were selected to observe the vibration responses. Their coordinates are listed in Table 5.3 (C denotes the centre excitation). The second configuration is the corner excitation, as shown in Figure 5.3b. The excitation point is this configuration is located towards a left-hand corner of the structure. To examine the vibration response, several receiver points were distributed along the x-direction (H1-H13) and y-direction (V1-V6). These points were chosen to observe the floor mode shapes along the axial directions of the scaled LWF structure. The locations of the receivers and the excitations points are listed in Tables 5.4-5.5, all with z=0.

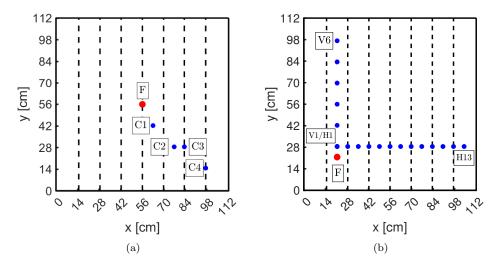


Figure 5.3: Top view of the scaled LWF structure. The red dots represent the impact source position and the blue dots represent the receiver positions of (a) the centre excitation configuration and (b) the corner excitation configuration.

Table 5.4: Coordinates of the excitation and receiver positions for the corner excitation configuration of the scaled LWF. All points are located between joists 1 and 2.

Index	(x, y) [cm]
F	(21.625, 21.625)
V1	(21.625, 28.5)
V2	(21.625, 42.25)
V3	(21.625, 56)
V4	(21.625, 69.75)
V5	(21.625, 83.5)
V6	(21.625, 97.25)

Table 5.5: Coordinates of the receiver positions for the corner excitation configuration on the scaled LWF. The receivers are located along the transversal direction of the joists.

Index	(x, y) [cm]
H1	(21.625, 28.5)
H2	(28.5, 28.5)
H3	(35.375, 28.5)
H4	(42.25, 28.5)
H5	(49.125, 28.5)
H6	(56, 28.5)
H7	(62.875, 28.5)
H8	(69.75, 28.5)
H9	(76.625, 28.5)
H10	(83.5, 28.5)
H11	(90.375, 28.5)
H12	(97.25, 28.5)
H13	(104.125, 28.5)

#### 5.4 Computational settings

#### 5.4.1T-shaped structure

To simulate the vibrations of the case studies using the nodal DG method, an in-house Matlab implementation is used to solve Equations (5.7). To assess the convergence of nodal DG results, the computational domain is represented by multiple numbers of elements. The T-shaped structure is discretised by unstructured tetrahedral elements using the COMSOL Multiphysics 5.4 mesh generator [211]. The same meshes are used for the two configurations of the T-shaped structure (different boundary condition). The initial number of elements, K = 1063, is used to obtain an average mesh skewness of 0.3. The vibration signals are captured for a duration of 1 second, and the maximum frequency of interest is 500 Hz. The remaining numerical settings are shown in Table 5.6.

Danamatan	Number of elements				
Parameter	K=1063	K=2126	K = 4089		
Maximum polynomial order, $N$	3	3	3		
Degrees of freedom	21260	42520	81780		
Minimum edge length, $h_{min}$ [m]	0.0103	0.0100	0.0099		
Maximum edge length, $h_{max}$ [m]	0.0522	0.0397	0.0343		
$\Delta t$ [s]	4.4283e-07	4.3983e-07	4.3883e-07		

Table 5.6: Elements and time discretization used in the nodal DG simulation for the Tshaped structure case.

The impact excitation on the T-shaped structure is given by external body force A(t)at z-direction in the form of Ricker wavelet as:

$$A(t) = (0.5 - (\pi f_c(t - t_d))^2) e^{(\pi f_c(t - t_d))^2},$$
(5.11)

with the centre-frequency of  $f_c = 250$  Hz and the centre-time of  $t_d = 7$  ms. These values are taken to impose a force excitation up to 500 Hz and to ensure a smooth wavelet excitation. With the exception of the face representing the clamped area, all faces of the T-shaped structure are set to free BCs (see Figure 5.1). The BC on the clamped area is set to a fixed or free BC, depending on the configuration. As mentioned in Section 5.2.4, the free BCs can be realised by setting the traction to 0 for the stress variable normal to the boundary, whereas fixed BCs is realised by setting the velocity to 0. The reader is referred to Chapter 4 for more specific details.

In the convergence evaluation, the nodal DG solution is also compared with the FEM solution via COMSOL Multiphysics 5.4 [211]. The three-dimensional solid mechanics solver is selected with a frequency-domain study. The Rayleigh damping is used in COMSOL Multiphysics to add the damping force, which is proportional to the velocity as modelled by the nodal DG method. To obtain an accurate solution, 125k elements are used to discretise the T-shaped structure.

#### 5.4.2Scaled lightweight wooden floor

 $\Delta t$  [s]

The scaled LWF is discretised by unstructured tetrahedral elements, as in the Tshaped structure. To evaluate the convergence of the numerical results, several number of elements are used to represent the computational domain. The simulation duration is 1 second with a maximum frequency of 500 Hz. The impact excitation is given by external body force, as presented in Equation (5.11). All faces of the scaled LWF are set to free BCs by using the traction free condition, as mentioned in Section 5.2.4. The remaining numerical settings are presented in Table 5.7.

Number of elements Parameter K = 6918K = 13685K = 210943 Maximum polynomial order, N3 3 Degrees of freedom 138.4k237.7k421.9kMinimum edge length,  $h_{min}$  [m] 0.0090.0090.014Maximum edge length,  $h_{max}$  [m] 0.0610.0540.0413.6677e-073.6677e-075.6895e-07 $\Delta t$  [s]

Table 5.7: Elements and time discretization used in the nodal DG simulation for the scaled LWF case.

#### Experimental validation 5.5

#### 5.5.1Experimental setup

This section describes the vibration experiments of the case studies as presented in Section 5.3. The T-shaped structure is comprised of vertical and horizontal beams. These beams were glued together to create a fixed connection. The vertical beam was fastened by a steel clamp set on a concrete slab to generate the fixed BCs configuration, as illustrated in Figure 5.4a. For the free BCs configuration, the structure was suspended from a steel structure via two rubber ropes as shown in Figure 5.4b. The T-shaped structure was assumed to have free BCs on all of its surfaces because of this configuration.

In case of the scaled LWF structure, the structure was made of a top plate with seven joists. In the experiment, each joist was attached to the bottom of the plate using nine screws spaced equally along the joists axial direction. By having closely adjacent screws, the joists were assumed to have a fixed connection to the top plate. In this study, the scaled-LWF structure is designed to have free BCs. To realise these BCs, several metal hooks were installed on the edge of the first and the last joists. Afterward, four rubber ropes connected these hooks to a crane machine to elevate the structure as shown in Figure 5.5. Upon elevation of the structure, it was assumed the free BCs could be obtained.

In both experiments, the acceleration was picked up by nine single-axis accelerometers (PCB 333B30). The signals were captured using National Instruments acquisition systems (NI 9234 and cDAQ-9178) for the duration of seven seconds with a sampling frequency of 51.2 kHz. The excitation was given using an impact hammer (BK 8202) with a plastic tip. As mentioned in Section 5.3, each case study has a different receiver and excitation positions; the accelerometers and impact position are given at those specified coordinates.

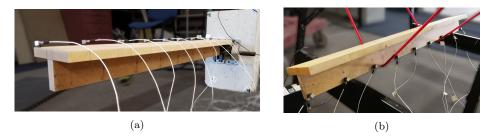


Figure 5.4: Experimental setup of the T-shaped structure for different configurations. (a) The fixed BCs configuration, (b) The free BCs configuration.

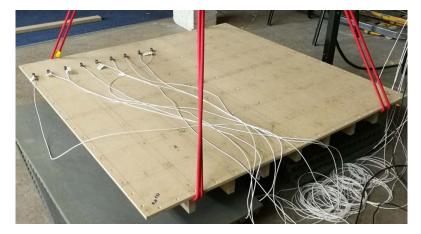


Figure 5.5: Experimental setup for the scaled LWF structure. The structure was elevated to have the free BCs.

# 5.5.2 Vibration data processing

The time-domain vibration signals were obtained from the experiments and the numerical computations in each case. The recorded signals were converted into frequency-domain data using the fast Fourier transform. In the frequency domain, the transfer function between velocity and force, i.e., mobility  $(Y_{ij})$ , was calculated to represent vibration responses of the individual case studies. It reads as:

$$Y_{ij}(f) = \frac{v_i(f)}{F_j(f)},\tag{5.12}$$

where i, j denote the velocity in the *i*-direction due to the force in the *j*-direction. In this study, two transfer mobilities are considered,  $Y_{zz}(f)$  and  $Y_{xz}(f)$ . To obtain the transfer mobilities from the experiment, the H1 estimator, according to Equation 5.13 was used, as shown in Ref.[227]. This estimator is used to reduce the influence

of the noise during the experiment.

$$Y_{ij}(f) = \frac{S_{v_i, F_j}(f)}{S_{F_i, F_i}(f)}. (5.13)$$

 $S_{v_i,F_i}(f)$  is the cross-spectral density function between the velocity in the *i*-direction and the force in the j-direction. The  $S_{F_i,F_i}(f)$  is the auto-spectral density function of the force in the j-direction. The velocity in the i-direction  $(v_i(f))$  can be calculated from the acceleration signals  $(a_i(f))$  using the relation  $v_i(f) = a_i(f)/j2\pi f$ . The experiment was conducted three times to obtain average values of the mobilities. The vertical mobility  $(Y_{zz})$  is evaluated at all receiver points on all computational cases, with the sole exception is the receiver R4 for the T-shaped structure case (see Figure 5.1). This point is located on the side of the vertical beam, and the horizontal mobility  $(Y_{xz})$  is evaluated.

#### Results and Discussions 5.6

#### 5.6.1T-shaped structure

### Fixed BCs configuration

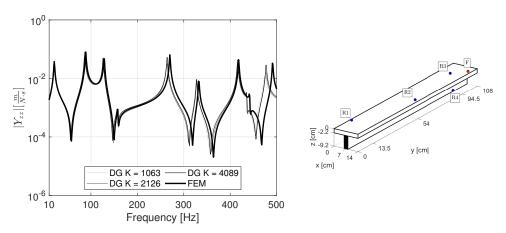


Figure 5.6: The mobilities at R2 position of the fixed BC configuration for different element numbers.

Figure 5.6 depicts the nodal DG solution for the current configuration. In this figure, three mobility curves  $Y_{zz}$  are shown at location R2. Each curve was obtained from the nodal DG solution with a different number of elements, K = 1063, 2126, and 4089. Table 5.8 lists all natural frequencies for each number of elements.

It should be noted that the slowest wave in the T-shaped structure, the transverse wave, has a velocity of 1221.5 m/s. This means that the minimum wavelength at 500 Hz is approximately 2.4 m, and the discretisation appears to have oversampled the structure. However, since the structure has a thickness of 2.2 cm, the discretisation should limit the skewness of the tetrahedral elements to achieve a good numerical result. Moreover, the changes in natural frequencies between all different element numbers are less than 2 Hz, assuming that the results have converged.

Table 5.8:	Natural	frequencies	at th	e T-shaped	structure	obtained	${\rm from}$	the	nodal	$\overline{\mathrm{DG}}$
method and	d the exp	eriment at p	ositio	n R2.						

Index	Natural frequency [Hz]					$ \Delta f_n $	
11101011	K = 1063	K=2126	K = 4089	Experiment	[Hz]	[%]	
1	21.0	20.0	20.0	19.3	0.7	3.6	
2	86.0	87.0	87.0	89.0	2.0	2.2	
3	127.0	126.0	126.0	128.6	2.6	2.0	
4	263.0	264.0	264.0	269.9	5.9	2.2	
5	328.0	327.0	328.0	330.6	2.6	< 1.0	
6	415.0	416.0	416.0	432.3	16.3	3.8	
7	475.0	476.0	477.0	475.7	2.7	< 1.0	

In addition, the same case is simulated with FEM using COMSOL Multiphysics 5.4 [211] in frequency domain by solving the linear elasticity equations. The comparison with the FEM solution shows that the nodal DG approach has a maximum difference of 15 Hz at the highest natural frequency. This is caused by the discontinuity of BCs at y=0 cm and z=-2.2 cm. Owing to its discontinuous elements, the nodal DG solution can have two solutions at the same point, whereas the solution in the FEM is continuous at the BCs discontinuity. This is supported by results from free BC configuration and also by additional calculations in Appendix F, where all boundaries at y=0 m are fixed), showing the natural frequency difference  $(|\Delta f_n|)$  is at most 1 Hz.

Moreover, the DG results of K=4089 are compared with the experimental results. The mobilities at receivers R1-R4 are shown in Figure 5.7. It can be seen that the mobilities obtained from the nodal DG method closely match those obtained from the experiment. Figures 5.8 and 5.9 show structural mode shapes obtained from the nodal DG method and the experiment. The comparison reveals that both mode shapes are almost identical.

Despite these similarities, there are discrepancies in the resonant frequencies and magnitudes of mobility. Table 5.8 lists all the discrepancies of the natural frequencies, with the sixth natural frequency having a maximum absolute frequency difference  $|\Delta f_n| = 16.3$  Hz from the measured value, which is 3.8% deviation. The other natural frequencies have smaller absolute differences. It is assumed that, because the MDF material has a slight orthotropic property [228], these differences are attributable to the isotropic assumption of the vertical and horizontal beams in the nodal DG model.

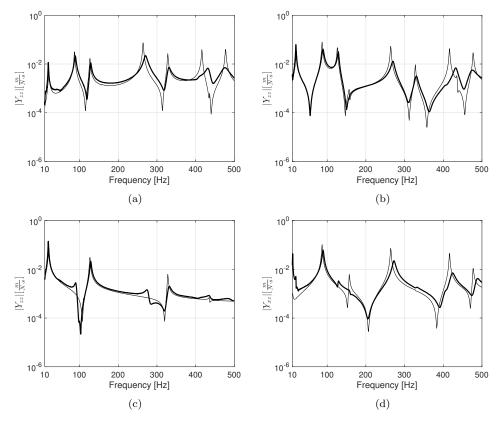


Figure 5.7: Mobilities of the T-shaped structure with the fixed BCs configuration obtained by the nodal DG method and the experiment at the positions: (a) R1, (b) R2, (c) R3, and (d) R4. (Thin lines represent nodal DG results and thick lines represent experimental results)

The magnitude discrepancies are caused by inadequacy of internal damping properties. The given constant viscous damping cannot capture the frequency-dependent damping properties of the structure. Figure 5.7 shows that the magnitude of mobilities obtained by the nodal DG method and the experiment are of the same order for the frequencies below 150 Hz. In the experimental data, however, the attenuation increases more rapidly with frequency than in the computational results. In Figure 5.7d, the mobility in the x-direction at position R4 is shown. This mobility has the same magnitude as the mobility in the z-direction at the other positions (R1-R3) due to the body force in the z-direction. Figures 5.8 and 5.9 show a similar magnitude of mobility. This indicates that the adhesive used to connect the two beams creates a strong coupling and allows good vibrational energy transmission between them.

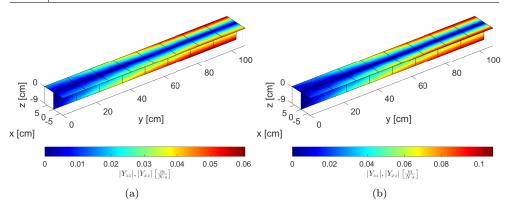


Figure 5.8: Second mode shape of the T-shaped structure with fixed BCs configuration obtained by (a) experiment (89 Hz) and (b) nodal DG method (87 Hz).

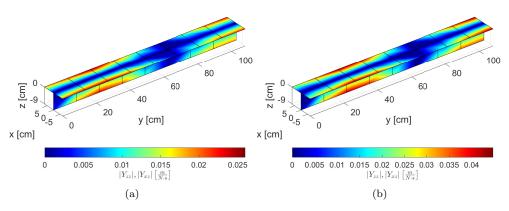


Figure 5.9: Fourth mode shape of the T-shaped structure with fixed BCs configuration obtained by (a) experiment (270.4 Hz) and (b) nodal DG method (266 Hz).

### Free BC configuration

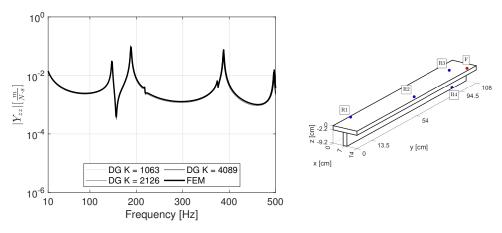


Figure 5.10: The mobilities at R1 position of the free BC configuration for different element numbers.

Figure 5.10 depicts the convergence of the nodal DG solution for the free BCs configuration. In this figure, three mobility curves  $Y_{zz}$  are shown at the R1 position. As in the previous configuration, each result is obtained from the nodal DG solution with K = 1063, 2026, 4089 elements. Convergence occurs when the number of elements is K = 4089, with natural frequency differences of no greater than 1 Hz when compared to the solution with K = 1063. Furthermore, the nodal DG solution has a maximum difference of 1 Hz at the highest natural frequency when compared to the FEM solution. All natural frequencies are listed in Table 5.9.

Table 5.9: Natural frequencies at the T-shaped structure obtained from the nodal DG method and the experiment at position R1.

Index	Natural frequency [Hz]					$ \Delta f_n $	
1114011	K = 1063	K=2126	K = 4089	Experiment	[Hz]	[%]	
1	147.0	147.0	147.0	150.3	3.3	2.2	
2	188.0	188.0	188.0	199.7	11.7	5.9	
3	386.0	387.0	387.0	406.4	19.4	4.8	

The mobility curves of receiver points R1-R4 are shown in Figure 5.11. The mobility calculated using the nodal DG approach matches well with the mobility determined from the experiment. Furthermore, as seen in Figures 5.12 and 5.13, these findings have nearly identical mode-shapes. The discrepancies between the natural frequencies are tabulated in Table 5.9, where the maximum absolute difference is 19.4 Hz, which corresponds to a textless 5% deviation from the experimental results. Similar to the fixed BCs configuration, the damping of the T-shaped structure is frequency-dependent and the current constant viscous damping cannot represent the mobility magnitude well at frequencies above 150 Hz.

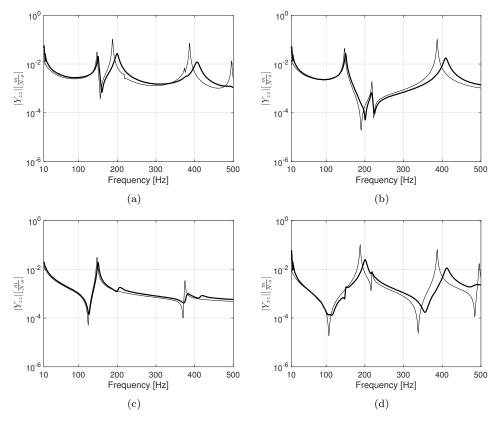


Figure 5.11: Mobilities of the T-shaped structure with free BC configuration obtained by the nodal DG method and the experiment at the positions: (a) R1, (b) R2, (c) R3, and (d) R4. (Thin lines represent nodal DG results and thick lines represent experimental results)

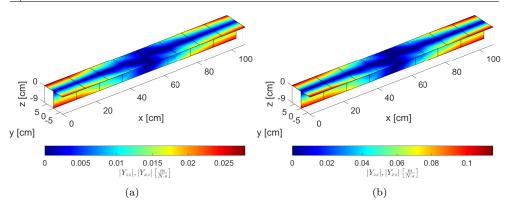


Figure 5.12: Second mode shape of the T-shaped structure with free BCs configuration obtained by (a) experiment (199.7 Hz) and (b) nodal DG method (188 Hz).

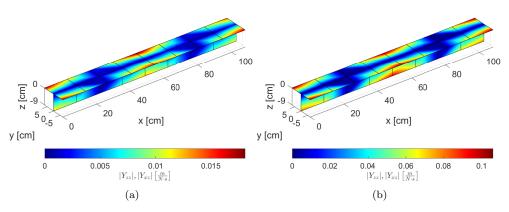


Figure 5.13: Fourth mode shape of the T-shaped structure with free BCs configuration obtained by (a) experiment (406.6 Hz) and (b) nodal DG method (387 Hz).

# 5.6.2 Scaled lightweight wooden floor

### Centre force excitation

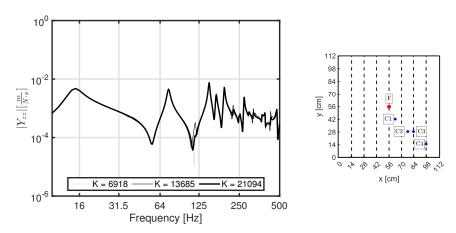


Figure 5.14: Numerical solutions of the scaled LWF at position C1 for different element numbers with center excitation.

Table 5.10: Natural frequencies at the scaled LWF structure obtained from the nodal DG method and experiment at position C1.

Index	Natural Frequency [Hz]					$ \Delta f_n $	
1110011	K = 6918	K = 13685	K = 21094	Experiment	[Hz]	[%]	
1	15.0	15.0	15.0	14.1	0.9	6.4	
2	73.0	74.0	74.0	70.1	3.9	5.6	
3	149.0	149.0	149.0	148.9	0.1	< 1.0	
4	167.0	168.0	168.0	159.6	8.4	5.3	
5	193.0	193.0	193.0	190.9	2.1	1.1	
6	270.0	271.0	272.0	260.9	10.1	3.9	

Figure 5.14 presents the nodal DG solution for the scaled LWF excited by the force at the centre position. In this figure, three mobility curves  $Y_{zz}$  are shown at location C1. Each curve was obtained from the nodal DG solution with a different number of elements, K = 6918, 13685, and 21094. It should be noted that the thickness of the plate structure is 0.9 cm, and a sufficient number of elements are required to maintain a good skewness of the element (average skewness for K = 6918 is 0.33). The average skewness of the element is expected to be more than 0.3 to have a good tetrahedral element. Table 5.10 lists all natural frequencies for each number of elements below 300 Hz. The changes in natural frequencies between the different element numbers are less than 2 Hz, and it could be assumed that the results have converged. In the subsequent comparison with the experimental results, the results from the DG

method with K = 13685 are used to save computational effort, since the difference to K = 13685 is at most 1 Hz.

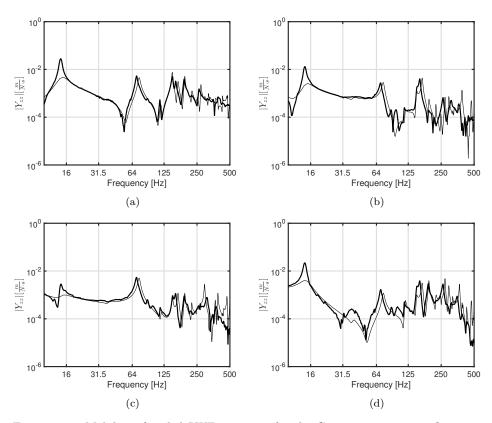


Figure 5.15: Mobility of scaled LWF structure for the Centre excitation configuration at position (a) C1, (b) C2, (c) C3, and (d) C4. (Thin lines represent nodal DG results and thick lines represent experimental results)

Figure 5.15 shows the mobilities at positions C1-C4. As mentioned in Section 5.3.2, these points are gradually further away from the excitation point. All mobilities obtained by the nodal DG method agree well with the experimental results, particularly in the frequency range 20-250 Hz. The disparity between experimental and simulation results widens beyond this range. Similar to the previous case, the constant damping is one reason for this, as the model does not capture the frequency-dependent damping of the structure. It can be seen that the first natural frequency at 15 Hz is heavily damped in nodal DG solution, and the constant damping applied to this mode is excessive. In contrast, above 250 Hz, the damping from the experimental results increases and the location of the natural frequencies becomes indistinct. The connection between the plate and the joists is another source of inconsistency. Modelling these connections as fixed connections along the contact interface may generate flaws since these components are fastened together with nails rather than glue.

### Corner force excitation

This configuration is used to show several vibrational mode-shapes along the scaled LWF structure axial directions. Receiver points H1-H13 are aligned in the x-direction to capture the mode shapes along y=28.5 cm, and receiver points V1-V6 are arranged to capture the mode shapes at x=21.6 cm in the y-direction.

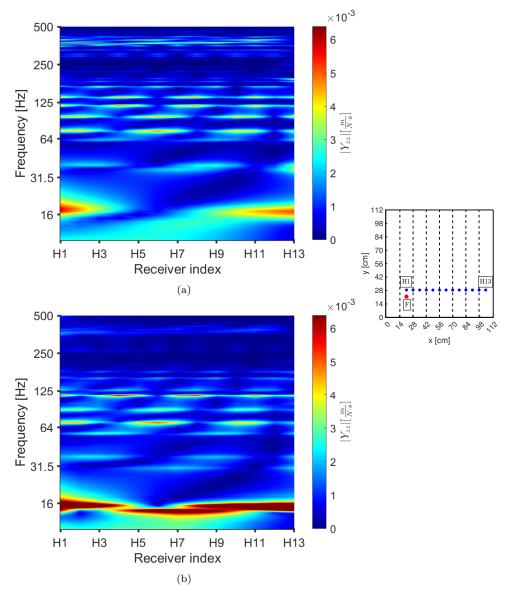


Figure 5.16: Mobility of the scaled LWF structure at the receiver positions H1-H13 obtained with (a) the nodal DG method, and (b) the experiment.

Figures 5.16a and 5.16b show the mobilities at receivers H1-H13 obtained from the nodal DG method and the experiment. The figures clearly display the nodes and anti-nodes of the mode shapes in the x-direction. At the lowest natural frequency, 17 Hz, there are two anti-nodes of the vibrational mode shape appearing at locations H1 and H13 as seen in Figure 5.16a. The node of this natural frequency occurs at position H6 according to the nodal DG approach. However, this node is not clearly visible from the experiment. Below 200 Hz, the mode shape determined from the nodal DG approach and the experiment have a significant correlation. The structural responses are heavily damped above this frequency, however, and the constant viscous damping in the nodal DG approach is insufficient to adequately model the real damping.

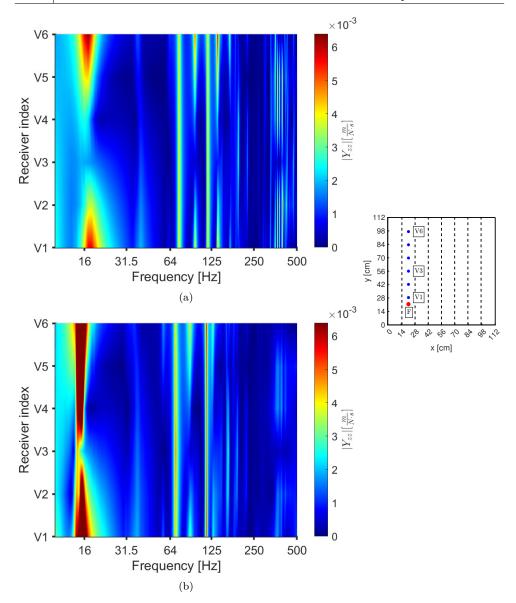


Figure 5.17: Mobility of the scaled LWF structure based on the receiver position V1-V6 obtained with the (a) nodal DG method, and (b) experiment.

The mode shapes in the y-direction are shown in Figures 5.17a and 5.17b. Compared to the previously observed mode shapes along the x-direction, this direction exhibits lower-order mode shapes. In the y-direction, there are at most two anti-nodes below 500 Hz, whereas five anti-nodes are observed along the x-direction in the frequency range up to 125 Hz. This is because the joists significantly increase the stiffness of the

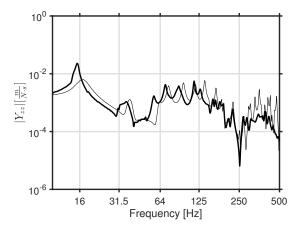


Figure 5.18: Mobility of scaled LWF structure for the Corner excitation configuration at position V6. (Thin lines represent nodal DG results and thick lines represent experimental results)

floor in the y-direction. Figures 5.17a and 5.17b show that the mode shapes obtained both from the experiment and the nodal DG method have a good correlation. For a clearer comparison, the mobilities at the receiver V6 are shown in Figure 5.18. The natural frequencies and mode shapes indices below 200 Hz are tabulated in Table 5.11 along with their discrepancies ( $|\Delta f_n|$ ). This table shows that the maximum discrepancy happens at the (5,2) mode, which is 10.4 Hz or about 8.2% difference from the experimental result. Moreover, it can be seen that these differences are larger compared for the excitation position more central on the floor (see Table 5.10).

Table 5.11: List of natural frequencies of the scaled LWF structure based on the corner excitation obtained by the nodal DG method and experiment at position V6. The mode index in the x- and y- directions is defined by the number of anti-nodes found at each resonant frequency.

Mode index	Natura DG	l frequency [Hz] Experiment	$ \Delta $ [Hz]	$f_n $ [%]
(2,2)	17.0	15.3	1.7	11.1
(3,1)	38.0	35.7	2.3	6.4
(4,1)	74.0	70.0	4.0	5.7
(4,2)	96.0	88.0	8.0	9.1
(5,1)	117.0	114.7	2.3	2.0
(5,2)	138.0	127.6	10.4	8.2
(6,1)	167.0	165.9	1.1	< 1.0
n.a.	184.0	178.6	5.4	3.0

For the scaled LWF structure, these discrepancies could be due to various factors.

For example, the MDF materials used in each component are rarely homogeneous or isotropic. Additionally, this structure includes several connections between the plate and joists, and incorrect modelling may result in discrepancies in natural frequencies. These connections are considered to be fixed in the nodal DG approach; nevertheless, in practical experiments, the nails connection may introduce further damping and stiffness. Furthermore, to depict the component's frequency-dependent internal damping, the constant viscous damping technique is insufficient. Moreover, the structure's boundary conditions, which are never completely free, may carry additional inconsistencies into the modelling.

#### 5.7 Conclusion

The nodal DG method has been presented and applied successfully to model the vibration of structures with piece-wise constant properties. The structures consist of a T-shaped structure and a scaled lightweight wooden floor comprised of several components with different material properties. The numerical fluxes are derived by the Rankine-Hugoniot jump condition, and are presented in detail in the Appendix. The numerical model is validated by comparing its results with the experimental results. The agreement on the natural frequencies is good, with a maximum absolute difference of 19.4 Hz or less than 5 % for the T-shaped structure in the frequency range below 500 Hz, and 10.4 Hz difference or less than 9% for the scaled LWF structure in the range below 200 Hz. Many factors contribute to these discrepancies. The selected damping strategy is insufficient to effectively depict a wide frequency range, which is one modelling factor. Incorporating frequency-dependent dampening into the nodal DG approach will be critical in the future. Furthermore, expanding the system to include materials with anisotropic mechanical characteristics, especially for wooden constructions, may be necessary.

## Part III

# Developments of time-domain DG method for vibroacoustic applications

# 6 Discontinuous Galerkin method for predicting sound radiation and transmission of building components

#### Abstract

This study presents numerical solutions for two vibroacoustic problems using the time-domain nodal discontinuous Galerkin (DG) method. The first problem is the impact sound radiation from a rectangular slab into a cuboid room, and the second is the sound transmission between two cuboid rooms with direct and flanking contributions. The structures are modelled as three-dimensional solid structure governed by the linear elasticity equations, and sound propagation in the rooms is governed by the linear acoustic equations. In the impact sound radiation case, the normalised sound pressure is evaluated and compared to the one obtained by the modal expansion method. In the sound transmission case, pressure transfer functions between different positions are calculated and compared to those obtained by the finite element method (FEM). The upwind numerical fluxes for both governing equations, as well as the coupling conditions, are presented in this thesis. There is excellent agreement between the solutions obtained by the nodal DG and those obtained by the modal expansion method/FEM. Although minor discrepancies exist in the resonance frequencies and magnitude, the overall trend shows good agreement.

#### 6.1 Introduction

Health effects of noise can manifest as the disturbance of well-being and adverse effects in the long term, including sleep disturbance, annoyance, interference with intended activities, and loss of task performance [5]. In dwellings, noise from neighbours can be annoying, and can imply a lack of privacy due to the poor sound (impact) insulation. This is apparent from several studies [229]–[231] that show the correlation between sound insulation performance and the occupant's perception of various constructions. Therefore, adequate sound insulation between dwellings is essential to create a healthy environment, privacy, and possibilities for activities without causing annoyance.

Many countries have regulations in buildings to address noise issues [11]. These

regulations include airborne and impact sound insulation. In order to comply with the regulations, prediction methods are needed to predict the sound insulation of building elements (e.g., walls, floors, windows, etc.). There are several models that can be used to predict airborne or impact sound insulation. Some of the simplest models assume an infinite structure or a locally reacting panel, coupled with semi-infinite or diffuse source and receiver rooms [51]. These models have been developed into engineering software equipped with material libraries and empirical modifications, such as those investigated in Ref. [232]. However, these models are limited to the assumption they use such diffuse field assumption or infinite structure. The finiteness of the structures and the rooms lead to different sound insulation properties, especially for sound insulation in the low-frequency region. In this region, the sound and vibration fields in buildings show modal behaviour, and many factors influence the sound insulation of a building element, such as mechanical properties, construction details, boundary conditions (BCs), excitation conditions, and receiver/room conditions [233], [234]. A prediction model that can take account of all these parameters is necessary.

Several analytical models can be used to predict sound insulation, such as the modal expansion methods described in Refs.[60], [235]–[237]. Sousa and Gibbs [233], [238] adapted the method to calculate the impact sound radiation in a room under a floor. A parametric survey was conducted on the factors affecting the low-frequency impact sound radiation, and experimentally validated the analytical model. However, these models are restricted to simple geometries and configurations for both structures and rooms (see Ref.[239] for limitations). To predict the sound insulation where all the details of the structures and the room are included, wave-based methods are required. Wave-based methods solve the equations that govern the structural vibrations and sound propagation in the rooms, including their interaction through sound radiation and transmission (vibroacoustic problems).

Several wave-based methods have been used to model sound radiation and transmission in buildings. The finite element method (FEM) is one of the wave-based methods often used to solve the partial differential equations that govern vibroacoustic problems. Maluski and Gibbs [74] used FEM to investigate sound transmission between dwellings, solving the acoustic wave and thin plate equation in the frequency domain to model sound and structural vibrations, respectively. To validate the approach, the results were compared with actual measurements, and several parametric studies were carried out on the effect of room size and the position of the source and receiver. Brunskog and Davidsson [239] and Davidsson et al. [75] conducted studies on the sound transmission of double-leaf walls using the FEM. In their studies, the sound transmission of two plasterboard panels connected with study and filled with porous material was determined in the frequency-domain. The structure was modelled using thin plate equations, and the sound propagation was modelled with modal basis functions. Another study on a similar structure was undertaken by Arjunan et al. [76]. They modelled the double-leaf walls using the three-dimensional solid structure instead of using a plate equation, and the acoustic wave equation used to model the sound propagation. The study was conducted using finite element software ANSYS.

Another wave-based method often used to model the building acoustic problem is the

finite-difference time-domain (FDTD) method. For example, Toyoda and Takahashi [94] used FDTD method to simulate impact sound radiation in a real-scale two-storey concrete building. The study modelled the building by the three-dimensional linear elasticity equations that solved elastic wave variables for both solid and air domains. In their study, the Lamé's second parameter was set as zero in the air domain to model sound propagation. Fereira [240] implemented the same FDTD methodology for several building acoustic applications but proposed a scaling approach to reduce the computational effort.

Another wave-based method that can be applied for the vibroacoustic problem is the time-domain discontinuous Galerkin (DG) method. The DG method is a relatively new method applied to vibroacoustic problems [225], [241]. To the authors' knowledge, the DG method has never been applied to sound transmission and radiation problems. This method has certain advantages compared to the other wave-based methods. For example, it can represent the problem domain using unstructured mesh to deal with a complex domain accurately, and it allows for refinement of the solution by increasing the polynomial order or element number. Another advantage is that the DG method uses an element-wise formulation to solve the governing equations. Therefore, it provides a framework well suited for parallel computation, as well as for local time-stepping [45]. This allows for significantly accelerated calculations [111]. This method has been extensively studied for application in another area of applied physics as seismology [117]–[120].

In the case of fluid-structure interaction problems in seismology, several studies have been carried out. Käser and Dumbser [242] applied the ADER-DG method to simulate seismic wave propagation in heterogeneous media containing fluid and solid. In their work, unified linear hyperbolic equations combining the linear elasticity equations and the linearised Euler equations are used to model the seismic waves in the velocity-stress formulation. This approach allows moving fluids in the problem, and similar to Toyoda and Takahashi [94], the fluid was treated by setting the Lamé's second parameter to zero in the fluid region. However, the computational cost of solving the wave propagation in fluids is the same as in solids using this approach, and it is not beneficial for a problem with a large fluid domain. The same method was also used by Shukla et al. [243] to make a comparison between explicit and implicit time integration in the DG method for seismic wave propagation. Moreover, Wilcox et al. [200] introduced the DG method for three-dimensional wave propagation problems in coupled elastic-acoustic media. This formulation is more efficient than that of Ref. [242] where the fluids are represented by elastic wave variables; however, the problem is restricted to non-moving fluids. Wilcox et al. used a velocity-strain formulation for the elastic wave propagation, and the upwind numerical flux was explained in detail, including the coupling between elastic-acoustic media. Furthermore, Zhang et al. [244] extended the DG methodology to the coupled elastic-acoustic anisotropic media.

This chapter uses the nodal DG method to solve two vibroacoustic problems. The first problem is the impact sound radiation from a rectangular slab into a cuboid room, and the second problem is the sound transmission between two cuboid rooms

with direct and flanking contributions. This work contributes to the application and validation of the DG method for building acoustic problems. The remainder of this chapter is organised as follows. In Section 6.2, the linear elasticity equations and the linear acoustic equations are presented. The nodal DG formulation to solve these equations is given, as well as the methodology to couple the two media using the numerical fluxes. Section 6.3 describes the example cases in detail. In Section 6.4, the simulation results for the first problem is compared with the results obtained by the modal expansion method, and the solution for the second problem is compared to the FEM solution. Finally, conclusions of the paper are given in Section 6.5. Moreover, the appendices present the details of the upwind fluxes for both equations and the modal expansion method used to obtain the analytical solution of the impact sound radiation.

### 6.2 Methodology

The nodal DG method is employed to solve vibroacoustic problems in this study. The vibrations of the structure are modelled by the linear elasticity equations, and sound propagation in air is modelled by the linear acoustic equations. In this section, each set of equations is presented along with the methodology to solve them using the nodal DG method. To couple the two governing equations, the continuity conditions between two subdomains are treated with the numerical flux presented in Section 6.2.4.

#### 6.2.1 Linear elasticity equations

The linear vibration of a structure can be modelled using the linear elasticity equations, which governs the propagation of elastic waves in a solid medium. This set of equations follows from the momentum conservation and constitutive equations [21]. For a Cartesian three-dimensional coordinate system, the equations for an isotropic medium can be written as a set of linear first-order hyperbolic equations in a velocity-stress form as:

$$\frac{\partial \boldsymbol{q}_{s}}{\partial t} + \nabla \cdot \boldsymbol{H}(\boldsymbol{q}_{s}) = \frac{\partial \boldsymbol{q}_{s}}{\partial t} + \boldsymbol{B}_{j} \frac{\partial \boldsymbol{q}_{s}}{\partial x_{j}} = \boldsymbol{g} - \zeta \boldsymbol{q}_{s}, \tag{6.1}$$

$$\boldsymbol{q}_{s}(\boldsymbol{x}, t) = \begin{bmatrix} v_{x} & v_{y} & v_{z} & \sigma_{xx} & \sigma_{yy} & \sigma_{zz} & \sigma_{xz} & \sigma_{yz} & \sigma_{xy} \end{bmatrix}^{T},$$

$$\boldsymbol{g}(\boldsymbol{x}, t) = \begin{bmatrix} g_{x} & g_{y} & g_{z} & 0 & 0 & 0 & 0 & 0 \end{bmatrix}^{T},$$

$$\zeta = \operatorname{diag} \begin{pmatrix} \zeta_{x} & \zeta_{y} & \zeta_{z} & 0 & 0 & 0 & 0 & 0 \end{pmatrix},$$

where  $v_x, v_y, v_z$  are the velocities in the x-, y-, and z- directions, respectively.  $\sigma_{xx}$ ,  $\sigma_{yy}$ ,  $\sigma_{zz}$ ,  $\sigma_{xz}$ ,  $\sigma_{yz}$ ,  $\sigma_{xy}$  are the normal and shear stress components,  $g_x, g_y, g_z$  are the body forces, and  $\zeta_x, \zeta_y, \zeta_z$  are the viscous damping forces. The linear elasticity used in this chapter is slightly different with the one used in Chapter 4 by the damping forces. The flux matrix reads  $H(q_s) = [h_x, h_y, h_z] = [B_x q_s, B_y q_s, B_z q_s]$ . The constant flux

Jacobian matrix  $B_j$  is given as:

$$\begin{split} \boldsymbol{B}_{j} &= \left[ \begin{array}{c|ccc} \mathbf{0}_{3\times3} & \boldsymbol{B}_{1,j} \\ \overline{\boldsymbol{B}_{2,j}} & \mathbf{0}_{6\times6} \end{array} \right], \boldsymbol{B}_{1,j} = -\frac{1}{\rho} \left[ \begin{array}{cccc} \delta_{xj} & 0 & 0 & \delta_{zj} & 0 & \delta_{yj} \\ 0 & \delta_{yj} & 0 & 0 & \delta_{zj} & \delta_{xj} \\ 0 & 0 & \delta_{zj} & \delta_{xj} & \delta_{xj} \end{array} \right], \\ \boldsymbol{B}_{2,j} &= - \left[ \begin{array}{cccc} (\lambda + 2\mu)\delta_{xj} & \lambda\delta_{yj} & \lambda\delta_{zj} \\ \lambda\delta_{xj} & (\lambda + 2\mu)\delta_{yj} & \lambda\delta_{zj} \\ \lambda\delta_{xj} & \lambda\delta_{yj} & (\lambda + 2\mu)\delta_{zj} \\ \lambda\delta_{xj} & \lambda\delta_{yj} & (\lambda + 2\mu)\delta_{zj} \\ \mu\delta_{zj} & 0 & \mu\delta_{xj} \\ 0 & \mu\delta_{zj} & \mu\delta_{yj} \\ \mu\delta_{yj} & \mu\delta_{xj} & 0 \end{array} \right], \end{split}$$

where  $\lambda$  and  $\mu$  are the Lamé parameters,  $\rho$  is the mass density, and index j has components [x,y,z]. The  $\delta_{ij}$  denotes the Kronecker delta function. The solution of Equation (6.1) consists of a linear combination of elastic waves propagating with longitudinal wave speed  $(c_p = \sqrt{(\lambda + 2\mu)/\rho})$  and transverse wave speed  $(c_s = \sqrt{\mu/\rho})$ . The Lamé parameters are represented by using Young's modulus (E) and Poisson's ratio  $(\nu)$  as  $\lambda = E\nu/(1+\nu)(1-2\nu)$  and  $\mu = E/2(1+\nu)$ .

#### 6.2.2 Linear acoustic equations

The propagation of sound in a room that is absent of wind and is at a constant temperature is governed by the linear acoustic equations. They are derived from the general conservation laws and the adiabatic process of the ideal gas. For Cartesian three-dimensional coordinates, these equations can be written as:

$$\frac{\partial \mathbf{q}_{a}}{\partial t} + \nabla \cdot \mathbf{F}(\mathbf{q}_{a}) = \frac{\partial \mathbf{q}_{a}}{\partial t} + \mathbf{A}_{j} \frac{\partial \mathbf{q}_{a}}{\partial x_{j}} = \mathbf{0}, 
\mathbf{q}_{a}(\mathbf{x}, t) = \begin{bmatrix} u & v & w & p \end{bmatrix}^{T}.$$
(6.2)

where p is the sound pressure, and u, v, w are the velocities in the x-, y-, and z- directions, respectively. The flux matrix reads  $F(q_s) = [f_x, f_y, f_z] = [A_x q_a, A_y q_a, A_z q_a]$ . The constant flux Jacobian matrix  $A_j$  is given as:

$$m{B}_j = \left[ egin{array}{cccc} 0 & 0 & 0 & rac{\delta_{xj}}{
ho_0} \ 0 & 0 & 0 & rac{\delta_{yj}}{
ho_0} \ 0 & 0 & 0 & rac{\delta_{zj}}{
ho_0} \ 
ho_0 c_0^2 \delta_{xj} & 
ho_0 c_0^2 \delta_{yj} & 
ho_0 c_0^2 \delta_{zj} & 0 \end{array} 
ight].$$

where  $\rho_0$  is the density of air, and  $c_0$  is the adiabatic sound speed. Equations (6.1)-(6.2) supplemented with initial values and BCs complete the problem definition.

#### 6.2.3 Nodal discontinuous Galerkin method

The nodal discontinuous Galerkin (DG) method is used to solve Equations (6.1)-(6.2). The algorithm of the method is developed by Hesthaven and Warburton [112] and is

adopted in this study. The problem domain is approximated by the computational domain  $\Omega_h$  with K number of non-overlapping rectilinear tetrahedral elements  $D^k$  as  $\Omega_h = \bigcup_{k=1}^K D^k$ . The problem domain consists of the structural subdomain  $(\Omega_h^s)$  and the air subdomain  $(\Omega_h^a)$  where  $\Omega_h = \Omega_h^s \cup \Omega_h^a$ . On each  $D^k$ , the local solution is expanded by a combination of nodal basis functions as:

$$\mathbf{q}_{sh}^{k}(\mathbf{x},t) = \sum_{i=1}^{N_p} \mathbf{q}_{sh}^{k}(\mathbf{x}_{i}^{k},t) l_{i}^{k}(\mathbf{x}), \tag{6.3}$$

$$\mathbf{q}_{ah}^{k}(\mathbf{x},t) = \sum_{i=1}^{N_{p}} \mathbf{q}_{ah}^{k}(\mathbf{x}_{i}^{k},t) l_{i}^{k}(\mathbf{x}), \tag{6.4}$$

where  $q_{sh}^k(\boldsymbol{x}_i^k,t)$ ,  $q_{ah}^k(\boldsymbol{x}_i^k,t)$  are the unknown nodal values of the elastic and acoustic wave variables, respectively.  $l_i^k(\boldsymbol{x})$  are the three-dimensional Lagrange interpolation polynomials based on the nodal points  $\boldsymbol{x}_i$ , and  $N_p$  is the number of nodal points. The global solutions are approximated as the direct sum of the local solutions as:

$$\boldsymbol{q}_s(\boldsymbol{x},t) \approx \boldsymbol{q}_{sh}(\boldsymbol{x},t) = \bigoplus_{k=1}^K \boldsymbol{q}_{sh}^k(\boldsymbol{x},t),$$
 (6.5)

$$\boldsymbol{q}_{a}(\boldsymbol{x},t) \approx \boldsymbol{q}_{ah}(\boldsymbol{x},t) = \bigoplus_{k=1}^{K} \boldsymbol{q}_{ah}^{k}(\boldsymbol{x},t). \tag{6.6}$$

The closed expression of the Lagrange interpolation polynomials in tetrahedral elements is constructed by the products of the Jacobi polynomials of order N, and the distribution of nodal points follows the optimised Legendre-Gauss-Lobato (LGL) points over a tetrahedral element as presented in Ref.[112]. The number of nodal points per element is  $N_p = (N+1)(N+2)(N+3)/6$ .

For each element in  $\Omega_h^s$ , the nodal basis functions are used to approximate the elastic wave variables and the body forces in Equation (6.1). Then the residuals of the approximations are multiplied by the test functions following the Galerkin method. By performing spatial integration by parts twice, the strong formulation of Equation (6.1) is as follows:

$$\int_{D^{k}} \left[ \frac{\partial \boldsymbol{q}_{sh}^{k}}{\partial t} + \nabla \cdot \boldsymbol{H}(\boldsymbol{q}_{sh}^{k}) \right] l_{i}^{k} d\boldsymbol{x} = \int_{D^{k}} (\boldsymbol{g}_{h}^{k} - \zeta \boldsymbol{q}_{sh}^{k}) l_{i}^{k} d\boldsymbol{x} 
- \int_{\partial D^{k}} \boldsymbol{n} \cdot \left[ \boldsymbol{H}^{*} - \boldsymbol{H}(\boldsymbol{q}_{sh}^{k}) \right] l_{i} d\boldsymbol{x},$$
(6.7)

where  $\partial D^k$  is the element surface,  $\boldsymbol{g}_h^k$  is the approximated body force vector, and  $\boldsymbol{n} = [n_x, n_y, n_z]$  is the outward normal vector of the element surface  $\partial D^k$ . The flux along the normal direction of the element surface is defined as  $\boldsymbol{n} \cdot \boldsymbol{H} = (n_x \boldsymbol{h}_x + n_y \boldsymbol{h}_y + n_z \boldsymbol{h}_z)$ , and the  $\boldsymbol{H}^*$  is the numerical flux.

The numerical flux ensures continuity of the global solution. It is a function of the interior solution  $(q_{sh}^-)$ , which is the solution within the element  $D^k$ , and the exterior solution  $(q_{sh}^+)$ , which is the solution of the neighbouring elements around  $D^k$ . In this work, the upwind numerical flux is chosen as the numerical flux. The upwind numerical

merical flux can be derived by solving the Riemann problem at the interface between two homogeneous media. This interface represents the faces of two neighbouring elements located at the same position. Consider that the interface lies at  $\mathbf{x} = 0$ . The properties of the medium  $(\lambda^-, \mu^-, \rho^-)$  are those of the internal medium at  $\mathbf{x} < 0$ , and  $(\lambda^+, \mu^+, \rho^+)$  are those of the adjacent one at  $\mathbf{x} > 0$ . The Riemann problem is a discontinuous initial value problem that happens at this interface as:

$$\label{eq:qsh} \boldsymbol{q}_{sh}(\boldsymbol{x},0) = \begin{cases} \boldsymbol{q}_{sh}^- & \text{if } \boldsymbol{x} < 0, \\ \boldsymbol{q}_{sh}^+ & \text{if } \boldsymbol{x} > 0. \end{cases}$$

The solution to this problem, the intermediate solution  $(q_{sh}^*(0,t))$ , is derived using the Rankine-Hugoniot jump condition as described in Refs. [225],[200],[21]. The numerical fluxes  $\mathbf{n} \cdot \mathbf{H}^* = \mathbf{n} \cdot \mathbf{H}(q_{sh}^*)$  are a function of the intermediate solution. After defining the numerical flux, the nodal basis and numerical flux are substituted into Equation (6.7) to obtain the semi-discrete form for each element as:

$$M^{k} \frac{\partial v_{xh}^{k}}{\partial t} - \frac{1}{\rho} \left( S_{x}^{k} \sigma_{xxh}^{k} + S_{y}^{k} \sigma_{xyh}^{k} + S_{z}^{k} \sigma_{xzh}^{k} \right) = M^{k} \left( g_{xh}^{k} - \zeta_{x} v_{xh}^{k} \right) - \sum_{r=1}^{4} M^{kr} \hat{H}_{v_{x}}^{kr},$$

$$M^{k} \frac{\partial v_{yh}^{k}}{\partial t} - \frac{1}{\rho} \left( S_{x}^{k} \sigma_{xyh}^{k} + S_{y}^{k} \sigma_{yyh}^{k} + S_{z}^{k} \sigma_{yzh}^{k} \right) = M^{k} \left( g_{yh}^{k} - \zeta_{y} v_{yh}^{k} \right) - \sum_{r=1}^{4} M^{kr} \hat{H}_{v_{y}}^{kr},$$

$$M^{k} \frac{\partial v_{zh}^{k}}{\partial t} - \frac{1}{\rho} \left( S_{x}^{k} \sigma_{xzh}^{k} + S_{y}^{k} \sigma_{yzh}^{k} + S_{z}^{k} \sigma_{zzh}^{k} \right) = M^{k} \left( g_{zh}^{k} - \zeta_{z} v_{zh}^{k} \right) - \sum_{r=1}^{4} M^{kr} \hat{H}_{v_{y}}^{kr},$$

$$M^{k} \frac{\partial \sigma_{xzh}^{k}}{\partial t} - \left( \lambda + 2\mu \right) S_{x}^{k} v_{xh}^{k} - \lambda S_{y}^{k} v_{yh}^{k} - \lambda S_{z}^{k} v_{zh}^{k} = - \sum_{r=1}^{4} M^{kr} \hat{H}_{\sigma_{xx}}^{kr},$$

$$M^{k} \frac{\partial \sigma_{yyh}^{k}}{\partial t} - \lambda S_{x}^{k} v_{xh}^{k} - \left( \lambda + 2\mu \right) S_{y}^{k} v_{yh}^{k} - \lambda S_{z}^{k} v_{zh}^{k} = - \sum_{r=1}^{4} M^{kr} \hat{H}_{\sigma_{yy}}^{kr},$$

$$M^{k} \frac{\partial \sigma_{zzh}^{k}}{\partial t} - \lambda S_{x}^{k} v_{xh}^{k} - \lambda S_{y}^{k} v_{yh}^{k} - \left( \lambda + 2\mu \right) S_{z}^{k} v_{zh}^{k} = - \sum_{r=1}^{4} M^{kr} \hat{H}_{\sigma_{xz}}^{kr},$$

$$M^{k} \frac{\partial \sigma_{zzh}^{k}}{\partial t} - \mu S_{z}^{k} v_{xh}^{k} - \mu S_{x}^{k} v_{zh}^{k} = - \sum_{r=1}^{4} M^{kr} \hat{H}_{\sigma_{xz}}^{kr},$$

$$M^{k} \frac{\partial \sigma_{yzh}^{k}}{\partial t} - \mu S_{z}^{k} v_{yh}^{k} - \mu S_{x}^{k} v_{zh}^{k} = - \sum_{r=1}^{4} M^{kr} \hat{H}_{\sigma_{xz}}^{kr},$$

$$M^{k} \frac{\partial \sigma_{xyh}^{k}}{\partial t} - \mu S_{z}^{k} v_{yh}^{k} - \mu S_{x}^{k} v_{zh}^{k} = - \sum_{r=1}^{4} M^{kr} \hat{H}_{\sigma_{xz}}^{kr},$$

$$M^{k} \frac{\partial \sigma_{xyh}^{k}}{\partial t} - \mu S_{y}^{k} v_{xh}^{k} - \mu S_{x}^{k} v_{yh}^{k} = - \sum_{r=1}^{4} M^{kr} \hat{H}_{\sigma_{xy}}^{kr}.$$

 $\boldsymbol{v}_{xh}^k, \, \boldsymbol{v}_{yh}^k, \, \boldsymbol{v}_{zh}^k, \, \boldsymbol{\sigma}_{\boldsymbol{x}\boldsymbol{x}_h}^k, \, \boldsymbol{\sigma}_{\boldsymbol{y}\boldsymbol{y}_h}^k, \, \boldsymbol{\sigma}_{\boldsymbol{z}\boldsymbol{z}_h}^k, \, \boldsymbol{\sigma}_{\boldsymbol{x}\boldsymbol{z}_h}^k, \boldsymbol{\sigma}_{\boldsymbol{y}\boldsymbol{z}_h}^k, \, \text{and} \, \boldsymbol{\sigma}_{\boldsymbol{x}\boldsymbol{y}_h}^k \, \text{are vectors representing all elastic wave variables at the nodal points <math>\boldsymbol{x}_i$ , with i=1 to  $N_p$ . Note that all the mechanical properties in Equations (6.8) are defined in the interior element, except for the numerical flux terms. The second superscript r denotes the rth faces of  $\partial D^{kr}$  of the element  $D^k$ , where the number of faces of the tetrahedral element is four.  $\hat{\boldsymbol{H}}_u^{kr}, \, \hat{\boldsymbol{H}}_v^{kr}, \, \hat{\boldsymbol{H}}_{\sigma_{xx}}^{kr}, \, \hat{\boldsymbol{H}}_{\sigma_{yy}}^{kr}, \, \hat{\boldsymbol{H}}_{\sigma_{zz}}^{kr}, \, \hat{\boldsymbol{H}}_{\sigma_{xz}}^{kr}, \, \hat{\boldsymbol{H}}_{\sigma_{yz}}^{kr}, \, \text{and} \, \hat{\boldsymbol{H}}_{\sigma_{xy}}^{kr} \, \text{are the flux terms associated with the term } \boldsymbol{n} \cdot \left[ \boldsymbol{H}^* - \boldsymbol{H}(\boldsymbol{q}_{sh}^k) \right]$  over the element surface in the strong form (Equation (6.7)).  $\boldsymbol{M}^k$  is the element mass matrix,  $\boldsymbol{S}_j^k$  are the element stiffness matrices in the j-directions, and  $\boldsymbol{M}^{kr}$  are the element face matrices. More details on these matrices are given in Refs. [112], [182].

For each element in the air subdomain  $\Omega_h^a$ , the same methodology as above are used. The nodal basis functions are used to approximate the sound wave variables in Equation (6.2). This leads to its strong formulation as:

$$\int_{D^k} \left[ \frac{\partial \boldsymbol{q}_{ah}^k}{\partial t} + \nabla \cdot \boldsymbol{F}(\boldsymbol{q}_{ah}^k) \right] l_i^k d\boldsymbol{x} = \int_{\partial D^k} \boldsymbol{n} \cdot \left[ \boldsymbol{F}^* - \boldsymbol{F}(\boldsymbol{q}_{ah}^k) \right] l_i d\boldsymbol{x}.$$
 (6.9)

The flux along the normal direction of the element surface is defined as  $\mathbf{n} \cdot \mathbf{F} = (n_x \mathbf{F}_x + n_y \mathbf{F}_y + n_z \mathbf{F}_z)$ , and the  $\mathbf{F}^*$  is the numerical flux for the sound wave variables. The upwind numerical flux is also used for the linear acoustics equations. Different from the elastic medium, air has interior medium properties that consist of  $(\rho_0^-, c_0^-)$  and  $(\rho_0^+, c_0^+)$  for the exterior one. It needs to be noted, that for this present study, the same polynomial orders are used for both structure and air subdomains. This is required to simplify the interface condition between air and structure, which is presented in the Section 6.2.4. The details on the numerical flux for wave propagation in air is given in Appendix G. After defining the numerical flux, the nodal basis and the numerical flux are substituted into Equation (6.9) to obtain the semi-discrete form for each element as:

$$M^{k} \frac{\partial \boldsymbol{u}_{h}^{k}}{\partial t} + \frac{1}{\rho_{0}} \boldsymbol{S}_{x}^{k} \boldsymbol{p}_{h}^{k} = \sum_{r=1}^{4} \boldsymbol{M}^{kr} \hat{\boldsymbol{F}}_{u}^{kr},$$

$$M^{k} \frac{\partial \boldsymbol{v}_{h}^{k}}{\partial t} + \frac{1}{\rho_{0}} \boldsymbol{S}_{y}^{k} \boldsymbol{p}_{h}^{k} = \sum_{r=1}^{4} \boldsymbol{M}^{kr} \hat{\boldsymbol{F}}_{v}^{kr},$$

$$M^{k} \frac{\partial \boldsymbol{w}_{h}^{k}}{\partial t} + \frac{1}{\rho_{0}} \boldsymbol{S}_{z}^{k} \boldsymbol{p}_{h}^{k} = \sum_{r=1}^{4} \boldsymbol{M}^{kr} \hat{\boldsymbol{F}}_{w}^{kr},$$

$$M^{k} \frac{\partial \boldsymbol{p}_{h}^{k}}{\partial t} + \rho_{0} c_{0}^{2} \boldsymbol{S}_{x}^{k} \boldsymbol{u}_{h}^{k} + \rho_{0} c_{0}^{2} \boldsymbol{S}_{y}^{k} \boldsymbol{v}_{h}^{k} + \rho_{0} c_{0}^{2} \boldsymbol{S}_{z}^{k} \boldsymbol{w}_{h}^{k} = \sum_{r=1}^{4} \boldsymbol{M}^{kr} \hat{\boldsymbol{F}}_{w}^{kr},$$

$$M^{k} \frac{\partial \boldsymbol{p}_{h}^{k}}{\partial t} + \rho_{0} c_{0}^{2} \boldsymbol{S}_{x}^{k} \boldsymbol{u}_{h}^{k} + \rho_{0} c_{0}^{2} \boldsymbol{S}_{y}^{k} \boldsymbol{v}_{h}^{k} + \rho_{0} c_{0}^{2} \boldsymbol{S}_{z}^{k} \boldsymbol{w}_{h}^{k} = \sum_{r=1}^{4} \boldsymbol{M}^{kr} \hat{\boldsymbol{F}}_{p}^{kr},$$

$$(6.10)$$

 $\boldsymbol{u}_h^k, \, \boldsymbol{v}_h^k, \, \boldsymbol{w}_h^k$ , and  $\boldsymbol{p}_h^k$  are vectors representing all sound wave variables at the nodal points  $\boldsymbol{x}_i$ , with i=1 to  $N_p$ . The terms  $\hat{\boldsymbol{F}}_u^{kr}, \, \hat{\boldsymbol{F}}_v^{kr}, \, \hat{\boldsymbol{F}}_w^{kr}$ , and  $\hat{\boldsymbol{F}}_p^{kr}$  are the flux terms associated with the term  $\boldsymbol{n} \cdot \left[ \boldsymbol{F}^* - \boldsymbol{F}(\boldsymbol{q}_{ah}^k) \right]$  over the element surface in Equation

(6.9). The element mass matrix  $(\boldsymbol{M}^k)$ , the element stiffness matrices  $(\boldsymbol{S}_x^k, \boldsymbol{S}_y^k, \boldsymbol{S}_z^k)$ , and the element face matrices  $(\boldsymbol{M}^{kr})$  are the same as mentioned before.

Having the semi-discrete form at hand, Equations (6.8) and (6.10) for the computational domain  $(\Omega_h)$  can be expressed in the form of ordinary differential equations as:

$$\frac{\mathrm{d}\boldsymbol{q}_{sh}}{\mathrm{d}t} = \boldsymbol{\mathcal{L}_s} \left( \boldsymbol{q}_{sh}(t), t \right), \tag{6.11}$$

$$\frac{\mathrm{d}\boldsymbol{q}_{sh}}{\mathrm{d}t} = \mathcal{L}_{s} \left( \boldsymbol{q}_{sh}(t), t \right),$$

$$\frac{\mathrm{d}\boldsymbol{q}_{ah}}{\mathrm{d}t} = \mathcal{L}_{a} \left( \boldsymbol{q}_{ah}(t), t \right).$$
(6.11)

where  $q_{sh}$ ,  $q_{ah}$  are the vector of all nodal solutions, and  $\mathcal{L}_s$ ,  $\mathcal{L}_a$  are the semi-discrete operator conducted over all elements in the solid and in air, respectively. Finally, various methods can be used to integrate the time derivative in Equations (6.11)-(6.12). In this work, the fourth-order Runge-Kutta method with eight stages (RKF84) is used, which is described in Ref. [148]. The time-step  $(\Delta t)$  for the time integration is defined as:

$$\Delta t = \frac{C_{CFL} \cdot \min(r_{D^k})}{N^2 \cdot \max(c_p)} \tag{6.13}$$

where  $C_{CFL}$  is the Courant number,  $\max(c_p)$  is the maximum longitudinal wave speed, and  $\min(r_{D^k})$  is the shortest element edge in the computational domain. It should be pointed out that  $\Delta t$  is determined by the fastest wave on the whole domain, which in this case is the elastic longitudinal wave. To complete the numerical formulation, the BCs, force excitation, and initial values should be given. The methodology to apply the force excitation and the BCs for the structure subdomain can be found in Ref. [225], while the BCs treatment for air subdomain can be found in Ref. [182].

#### 6.2.4Interface between solid and air

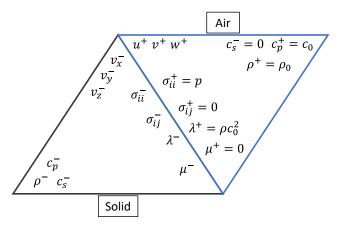


Figure 6.1: The jump conditions on the interface between solid and air

The interaction between solid and air is represented by the perfect slip boundary condition. In this condition, the shear stress has to vanish, while the continuity of the normal stresses and velocities has to be guaranteed [242]. In the nodal DG method, this can be constructed through the numerical fluxes. To realise this, the mesh must conform to the discontinuity between solid and air. It means that the element interfaces must be aligned with the material interface.

In the structural elements interfaces, the numerical fluxes are computed following Appendix G, with the exterior values of each variable set as illustrated in Figure 6.1. The air (exterior element) is assumed to be an inviscid fluid, where the fluid cannot sustain any shear stress. Thus, the transversal wave speed in the air  $c_s^+$  is zero, and the shear stresses are set as  $\sigma_{ij}^+ = 0$ . Moreover, the exterior values of density and longitudinal wave speed are  $\rho^+ = \rho_0$  and  $c_p^+ = c_0$  following medium properties of air. The exterior value of the first Lamé parameter is set as the bulk modulus of air,  $\lambda^+ = \rho_0 c_0^2$ , and the exterior second Lamé parameter (shear modulus) is set to zero,  $\mu^+ = 0$ .

To maintain the continuity of the velocities, the coupling can be set directly since the same variables exist both in air and solid material. The exterior velocity of the solid element,  $(v_x^+, v_y^+, v_z^+)$ , equals the velocity in the air, (u, v, w), element and vice versa. Moreover, the normal stresses are set by the condition  $\sigma_{ij}n_j = -pn_j$  such as presented in Ref.[245], and since shear stresses in air are zero, the normal stresses in the solid are equal to sound pressure in air as  $\sigma_{xx}^+ = \sigma_{yy}^+ = \sigma_{zz}^+ = -p$ . This methodology is also found in Refs. [21], [242].

#### 6.3 Case studies

In this study, three vibro-acoustic cases are simulated using the nodal DG method. The three cases are the sound radiation of a concrete slab into a room, sound transmission between two rooms through a single separating wall, and sound transmission between two rooms with flanking contributions. The first and second cases are compared with the analytical solution and the finite element method solution for the acoustic-solid interaction problem. These cases are selected to show the validity of the nodal DG methodology for vibro-acoustic problems. The third case is given to demonstrate the difference between sound transmission values of a wall with and without flanking paths.

#### 6.3.1 Impact sound radiation

The first case concerns impact sound radiation from a concrete slab into a room, as shown in Figure 6.2a. The slab only radiates the sound towards the room, where the upper surface does not radiate the sound. The room and the slab have dimensions  $[1.2 \text{ m} \times 0.8 \text{ m} \times 1 \text{ m}]$  and  $[1.2 \text{ m} \times 0.8 \text{ m} \times 0.08 \text{ m}]$ , respectively. The slab has simply supported BCs on the edges and free BCs on the top. The room has rigid BCs on all surfaces.

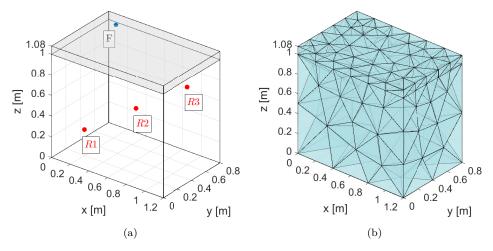


Figure 6.2: (a) The impact sound radiation case with the force and receiver positions, and (b) its mesh for the DG method computation.

The mechanical properties of the concrete slab are as follows: Young's modulus E=13.6 GPa, density  $\rho=2300\,\mathrm{kg/m^3}$ , and Poisson's ratio  $\nu=0.3$ . Air has a density of 1.2 kg/m<sup>3</sup> and a wave speed of 344 m/s. An impact force on the slab at position  $F=[0.2,0.64,1.08]\,\mathrm{m}$  (marked with blue dot) is given as:

$$A(t) = -\left(a_2 + a_1(t - t_d)^2\right) e^{a_1(t - t_d)^2},\tag{6.14}$$

with centre time  $t_d = 7$  ms, centre frequency  $f_c = 500$  Hz,  $a_1 = -(\pi f_c)^2$ , and  $a_2 = 0.5$ . The methodology to excite the point force can be seen in Chapter 4 and is adopted for this work. The impact point force is positioned close to a corner of the plate to reduce the possibility of hitting at multiple nodal lines of the slab at lower order modes. The simulation duration is 4 seconds, and three receivers are distributed along the room diagonal at R1 = [0.2, 0.2, 0.25] m, R2 = [0.6, 0.4, 0.5] m, R3 = [1, 0.6, 0.75] m to obtain the sound radiation from slab as shown in Figure 6.2a (marked by red dots).

To discretise the problem domain for the nodal DG method, the mesh generator of COMSOL Multiphysics is used [211]. The mesh is shown in Figure 6.2b. It consists of 241 and 452 tetrahedral elements to represent the concrete slab and the room, respectively. For the computation with the DG method, the Lagrange interpolation polynomials with an order of N=4 are applied. With this polynomial order, the room has 10 degrees of freedom per wavelength (DPW) at 850 Hz, which becomes the upper-frequency limit. Moreover, the material properties of the concrete slab determines the time step since the solid medium has a much faster longitudinal wave speed than air  $(c_p=2821.3 \text{ m/s})$ . The Courant number  $C_{CFL}=1$  is selected, resulting in  $\Delta t=1.5588\cdot 10^{-6}$  s. The elastic longitudinal wavelength at 850 Hz is 3.32 m, which means that the slab has a DPW number of 158.9. Note that the slab's length is much shorter than the wavelength, and the thickness of the slab controls the discretisation to have a good element skewness.

The nodal DG solution is then compared with the analytical solution based on the modal expansion method to validate the current computation. The time-domain sound pressure in each receiver and the force are converted into the frequency-domain data using the fast Fourier transform. The time-domain data is windowed using Hann window [227] with the length of 2 seconds to reduce the Gibbs effect. Having the frequency-domain data, the normalised sound pressure is calculated as:

$$P_n(\boldsymbol{x}, f) = \frac{P(\boldsymbol{x}, f)}{G(F, f)},\tag{6.15}$$

where P(x, f) is the frequency-domain pressure at each receiver location, and G(F, f) is the frequency-domain force. The modal expansion solution is obtained in frequency-domain, and the vibration of the slab is modelled by using the first shear deformation theory (FSDT) (see Appendix H for more details).

#### 6.3.2 Sound transmission

#### Direct sound transmission

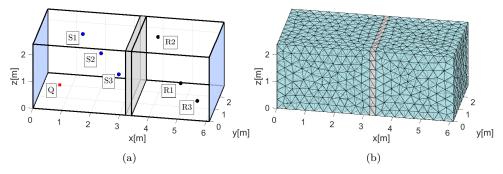


Figure 6.3: (a) The sound transmission through a single concrete panel case, and (b) its mesh for the DG method computation.

The second case is sound transmission between two rooms through a single concrete panel where flanking transmission is not included. The case geometry can be seen in Figure 6.3a, where the source room is the one closest to the coordinate origin. The source and receiver rooms have dimensions of  $[3.2~\text{m}\times2.9~\text{m}\times2.4~\text{m}]$  and  $[2.7~\text{m}\times2.9~\text{m}\times2.4~\text{m}]$ , respectively. The panel (marked by grey surfaces) has a thickness of 0.2 m, with all edges having fixed BCs. The red rectangle indicates the location of the sound source (Q), the blue dots mark the receivers in the source room (S1-S3), and the black dots mark the receivers in the receiver room (R1-R3). The locations of these points are shown in Table 6.1.

The properties of the concrete slab and air are the same as in the case of impact sound radiation (see Section 6.3.1). In addition, viscous damping forces  $\zeta_x = \zeta_y = \zeta_z = 20 \left[ N \cdot kg/m^3 \right]$  are added to the concrete to dissipate the vibration energy during transmission. Frequency-independent impedance BCs are applied to the surfaces of

the rooms indicated by blue surface in Figure 6.3a, and each surface has a real-valued reflection coefficient of R=0.95. Other surface in the room is set as rigid BCs. The simulation duration is 2 seconds, and to excite the sound on the location Q, initial values are given as:

$$p(\mathbf{x}, t = 0) = Q_0 \cdot e^{\frac{-\ln(2)}{b^2} ((x - x_q)^2 + (y - y_q)^2 + (z - z_q)^2)},$$
  

$$\mathbf{v}(\mathbf{x}, t = 0) = \mathbf{0}.$$

This is a pressure Gaussian pulse centered at the source coordinates  $(x_q, y_q, z_q)$ , with pulse half-bandwidth b = 0.15 and amplitude of  $Q_0 = 10$  Pa.

The mesh for the nodal DG method is shown in Figure 6.3b, where the concrete panel has 531 elements, and both rooms have a total of 16516 elements. The Lagrange interpolation polynomial order is N=3. With these values, the solution has approximately 10 DPW at 650 Hz, which is the upper frequency limit for the current configuration. The Courant number  $C_{CFL}=1$  is selected, resulting in  $\Delta t=6.4403\cdot 10^{-6}$  s. The methodology of applying the frequency-independent impedance BCs for the nodal DG method can be found in Ref.[182].

To evaluate the numerical accuracy of the nodal DG method solution, the difference between the sound pressure level  $(\Delta L_p)$  obtained in the source room  $(L_p^S(\boldsymbol{x}))$  and the one obtained in the receiver room  $(L_p^R(\boldsymbol{x}))$  is calculated as:

$$\Delta L_p = L_p^S(\mathbf{x}) - L_p^R(\mathbf{x}). \tag{6.16}$$

Three values of  $\Delta L_p$  are calculated, i.e., the  $\Delta L_p$  between S1 and R1, S2 and R2, and between S3 and R3. These  $\Delta L_p$  values are then compared with the values obtained by the FEM.

The FEM solutions are obtained by COMSOL Multiphysics 5.4 [211]. In COMSOL, the acoustic-solid interaction solver in the frequency-domain is used. In this solver, the acoustic wave equations and the elastic wave equations are solved for the three-dimensional geometry. The two-way coupling includes the acoustic pressure load on the structure and the structural acceleration as experienced by the air. The room is discretised using tetrahedral elements, and quadratic basis functions are used. The size of elements is at maximum 10 cm, which is approximately the length of minimum acoustic wavelength  $\lambda_{min}/5$ . In FEM, a point source is used to represent the sound excitation in the source room, and surface impedance BC is applied to the walls coloured in blue in Fig. 6.3a as  $Z_{wall} = Z_{air} \cdot (1 + R)/(1 - R)$ .

#### Sound transmission with flanking contribution

The third case is an extension of the single panel case from Section 6.3.2, where the top and bottom slabs of the building are included. These inclusions add flanking transmission contributions as shown in Figure 6.4. The first configuration is via the ceiling, and the second is via ceiling and floor. These configurations are simulated with the nodal DG method to show the differences in transfer functions compared

-1	- 1	വ
- 1	4	ŀ

Index	(x, y, z) [m]
Q	(0.8, 0.725, 0.6)
S1	(1.3, 2.4, 1.8)
S2	(2, 2, 1.3)
S3	(2.7, 1.5, 0.8)
R1	(4.8, 1.8, 0.5)
R2	(3.9, 2.4, 1.9)
R3	(5.6, 0.5, 0.5)

Table 6.1: Locations of the source and receivers for the single panel transmission case.

to the single panel configuration. The cases are given to demonstrate the ability of the nodal DG method to simulate building acoustic problems. The computational settings and material properties of these two configurations are the same as for the case with a single panel, as in Section 6.3.2. The number of elements in the rooms are slightly changed due to the inclusion of the ceiling and floor. The flanking configuration via ceiling has 1845 elements for the solid structure and 16724 elements for the air, while the one via ceiling and floor has 3210 elements for the solid structure and 16578 for the air.

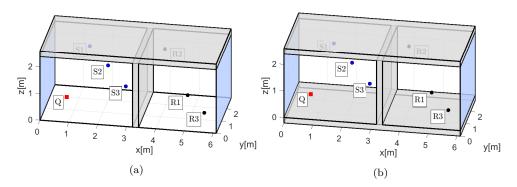


Figure 6.4: Sound transmission in rooms with flanking contribution, for case (a) via ceiling and (b) via ceiling and floor.

#### 6.4 Results and discussions

#### 6.4.1Impact sound radiation

Figures 6.5a-6.5c show the magnitudes of the normalised sound pressure at different receivers obtained by the nodal DG and modal expansion methods. As can be seen, both results are in excellent agreement. According to FSDT, there are five natural frequencies below 850 Hz. These frequencies are indicated by vertical lines in the figures and listed in Table 6.2. The natural frequencies of the slab are well separated within the frequency range of interest. While for the room, 90 natural frequencies exist below 850 Hz, assuming that the room has rigid BCs. Their distribution along the 1/3 octave bands is shown in Table 6.3.

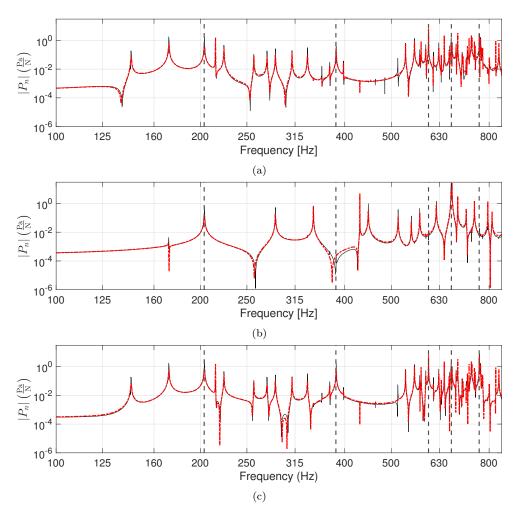


Figure 6.5: The normalised sound pressure for the impact sound radiation case at position (a) R1, (b) R2, and (c) R3. Black lines represent the nodal DG results, red dashed lines represent the modal expansion results, and the black dashed vertical lines represent the locations of the slab's natural frequencies based on FSDT.

The natural frequencies of the room primarily characterise the spectrum of the impact sound in the room since the room has more natural frequencies. There are minor discrepancies between the nodal DG and modal expansion solutions, especially in the magnitude and location of the peaks (local maxima) and throughs (local minima) of the normalised pressure. For instance, at receiver R2 (which is located exactly in the middle of the room) at 383 Hz and receiver R3 at around 300 Hz. Both

Table 6.2: Natural frequencies of the concrete slab obtained from FSDT. The  $m_1, m_2$  indicates the number of the anti-node in the x-, and y- directions. (see Appendix H)

Modal index $(m_1, m_2)$	Natural Frequency [Hz]
1,1	203.6
2,1	383.3
1,2	598.0
3,1	667.3
$^{2,2}$	762.7

Table 6.3: Number of room modes with rigid BCs for each 1/3 octave band.

1/3 octave band centre frequency [Hz]	Number of modes [-]
160	2
200	2
250	2
315	4
400	7
500	15
630	26
800	48

methods lack damping in the configuration, which may result in different magnitudes at these places. The modal expansion method is a frequency-domain method that assumes a steady-state solution, whereas the nodal DG method is a time-domain method that calculates the frequency-domain solution using windowing and signal truncation. This processing causes the sound wave interference that are not as strong as the frequency domain methods, and can result in minor deviations especially from the steady-state solution without damping. In addition, the modal expansion solution is based on the FSDT instead of the linear elasticity equation, which could account for some discrepancies.

#### 6.4.2 Sound transmission

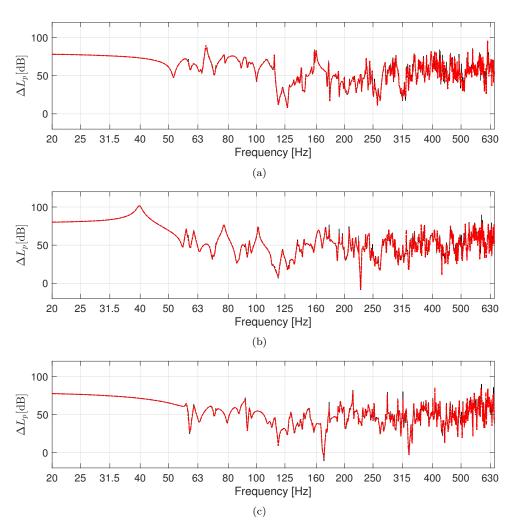


Figure 6.6: The  $\Delta L_p$  between position (a) S1 and R1, (b) S2 and R2, and (c) S3 and R3 for the direct transmission case. Black lines represent  $\Delta L_p$  obtained by the nodal DG and red dashed lines represent  $\Delta L_p$  obtained by the FEM.

The sound pressure level difference  $(\Delta L_p)$  values between two rooms divided by a single panel are presented in Figures 6.6a-6.6c. It can be seen that the results obtained by the nodal DG method and FEM are in a very good agreement. Minor discrepancies occur in the peak of  $\Delta L_p$  values, but the overall trends of the three  $\Delta L_p$  agree very well with the FEM solution. It can be seen that above 250 Hz the room acoustic modal density is high, with the peaks of the  $\Delta L_p$  close to each other. The number of acoustic modes in each frequency band is given in Table 6.4 assuming

that all surfaces are rigid. Due to this high number of modes, it is clearer to present the results in 1/3 octave frequency bands.

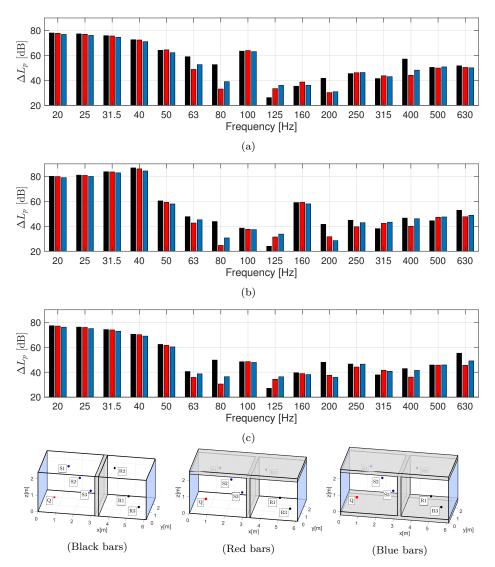


Figure 6.7: One-third octave band sound pressure level difference between position (a) S1 and R1, (b) S2 and R2, and (c) S3 and R3. Black bars refer to the single panel with only direct transmission path, red bars refer to the panel with flanking transmission via the ceiling, and blue bars refer to the panel with flanking transmission via ceiling and floor.

Now, the  $\Delta L_p$  values between the single panel to the panels with flanking transmission contribution (via ceiling and ceiling and floor) are presented. The  $\Delta L_p$  of different

1/3 octave band center	Number of modes [-]	
frequency [Hz]	Source room	Receiver room
50	1	0
63	2	2
80	1	2
100	4	2
125	5	6
160	13	9
200	19	15
250	33	32
315	66	57
400	126	110
500	154	156
630	314	224

Table 6.4: Number of the acoustic modes of the source and receiver rooms with all room surfaces are assumed rigid.

locations are shown in Figures 6.7a-6.7c. The single panel has a higher  $\Delta L_p$  at almost all frequency bands compared to the two scenarios that include flanking transmission. This means that the addition of ceiling and floor increases the overall transmitted sound energy from the source room to the receiver room.

The critical frequency of the concrete panel can be obtained as  $f_c = c_0/(1.8 \cdot c_p h) = 116.5$  Hz, where  $c_0, c_p$  and h are the sound wave velocity in air, the longitudinal elastic wave velocity and the panel thickness, respectively. Due to this frequency, the  $\Delta L_p$  values at 125 Hz are relatively low for all panel configurations, especially for the single panel configuration. The figures also show that for the configuration of flanking transmission via celing, the  $\Delta L_p$  values at 80 Hz are lower compare to other configurations. These might caused by the strong coupling between the ceiling vibration to the sound in the rooms. From these results, it is demonstrated that there are variations of the transfer functions (or sound transmission) due to the flanking paths. To have a good sound insulation design, analysis of panel configurations are needed to predict these variations. This analysis could be conducted by numerical models more efficiently compared to the experimental method.

#### 6.5 Conclusions

This chapter presented a methodology to solve vibroacoustic problems (represented by linear acoustic and elasticity equations) using the nodal DG method. The coupling conditions between acoustic and elastic wave variables provided by upwind fluxes are described. The methodology is used to solve problems involving impact sound radiation and sound transmission. The comparison of the impact sound radiation of a concrete slab into a room calculated using the nodal DG method and the analytical method shows a good agreement. There are slight discrepancies in the locations

154

and magnitudes of natural frequencies. For the transmission case, comparing the transfer functions between receiver locations in two rooms divided by a single wall as computed with the DG method and a reference solution using the FEM shows almost identical results. This illustrates that the methodology's results are correct and that it can potentially be applied to more advanced vibroacoustic applications. One drawback of the current methodology is the small time step  $(\Delta t)$ , which is determined by the elastic wave-speed in the structure. In further work, utilising a multi-time or a local time-stepping methodology could improve the computational performance of the nodal DG method for vibroacoustic applications. Once this is achieved, this technology will be a powerful tool for addressing engineering building acoustics challenges at low frequencies when full governing equation solutions are necessary.

# $oldsymbol{7}$ | Conclusions and future work

This PhD research contributes to creating a built environment with high acoustic quality. This contribution is made by developing an efficient, accurate, and geometrically flexible wave-based modelling method for building acoustics applications. The time-domain nodal discontinuous Galerkin (DG) method is a wave-based method with several ideal features to meet this aim. The spatial discretisation of this method creates a set of ordinary differential equations (ODE) with a block diagonal mass matrix, and this matrix can be inverted at very little cost. This feature makes the nodal DG method computationally efficient. This method can also achieve high-order accuracy, since it can refine the solution by increasing the polynomial order or the number of elements. Another feature of this method is its flexibility to handle complex geometries by using unstructured mesh elements. Moreover, various time-integration techniques can be used to solve the ODEs.

In this research, three objectives are defined related to the utilisation of the nodal DG method as a building acoustics simulation method: the first objective is to develop the nodal DG methodology to solve the governing equations for room acoustics; the second objective is to develop the nodal DG methodology to solve structural vibration problems in building elements; the final objective is to develop the nodal DG methodology to solve vibroacoustic problems in buildings. The conclusions of this research in regard fulfilling these three objectives are presented here. The first objective is addressed in Chapters 2 and 3, objective two is treated in Chapters 4 and 5, and the work related to objective three is presented in Chapter 6.

#### 7.1 Conclusions

The conclusions of this research are organised according to the chapters of this thesis as follows:

• In Chapter 2, the time-domain nodal DG method has been used to solve the linear acoustic equations for room acoustics applications. In free-field, the method showed that the dissipation error is  $1.1 \times 10^{-4}$  dB and the phase error is less than  $3 \times 10^{-4}\%$  under propagation of one wavelength when the degree of freedom per wavelength (DPW) is around 9. The frequency-independent impedance boundary formulation has been proposed using the plane-wave reflection coefficient via nu-

merical fluxes. The proposed formulation has been validated, and its convergence has been demonstrated. Additionally, a long-time simulation (10 s) was run for cuboid space with rigid boundary conditions. This case showed that the dispersion and dissipation error becomes very small compared to the solution of the modal expansion method DPW = 7.2 (at 1 kHz) was used. A simulation of a laboratory room with a more complex geometry was also carried out, and the obtained sound pressure level showed satisfactory agreement with the experimental results over the frequency range of interest. The average deviations of the 1/3 octave band sound pressure level at two receiver locations are 1.2 dB and 2.3 dB for frequencies below 500 Hz.

- In Chapter 3, the time-domain nodal DG method has been used to simulate noise propagation through the atmospheric boundary layer from aircraft take-offs. The environment of interest includes an airport and a residential area nearby, affected by aircraft noise pollution. The DG formulation of Chapter 2 is used, where the governing equations are the same but with a spatially varying effective sound speed to take into account the atmospheric conditions. The comparison of the results of this method with those of the finite element method (FEM) shows a good agreement for different impedance boundary conditions. Afterwards, the noise reducing benefits of using non-noise sensitive buildings were studied. The atmospheric conditions around the buildings were simulated using computational fluid dynamics by solving Reynolds averaged Navier-Stokes equations (CFD-RANS). It can be concluded that the building topology studied is quite effective to reduce the noise. For every building configuration, the insertion loss values are stable at around 10 dB for the configurations with a static atmosphere in the frequency up to 250 Hz 1/3 octave band frequency, while the IL values fluctuate over frequency between 1.3 dB (at 250 Hz frequency band) to 24.7 dB (at 25 Hz frequency band) in the refracting atmosphere conditions.
- In Chapter 4, the time-domain nodal DG method has been presented to solve the linear elasticity equations for the isotropic plate vibration problem. The methodology has been presented in detail for several aspects, such as the upwind numerical fluxes, point force excitation, and the implementation of various boundary conditions. This method has been applied for the vibration of several rectangular plates and an L-shaped plate. For the rectangular plate cases, the nodal DG mobility shows an excellent agreement with the mobility obtained by the first-order shear deformation theory (FSDT), where the maximum natural frequency difference is 1 Hz for every plate thickness and boundary condition. On the other hand, a good agreement with the classical plate theory (CPT) occurs solely at the first couple of natural frequencies, with increased accuracy as the plate thickness is reduced. For a more complex case, the L-shaped plate, the numerically calculated mobility agrees well with the CPT and FSDT results in the lower frequency range (<500Hz). However, at a higher frequency range (>700 Hz), the discrepancy of the natural frequency is up to 73 Hz, which is due to the difference in the used governing equations. When compared with the mobility obtained by the FEM using the linear elasticity equations, the nodal DG solution has a very good agreement with

a maximum natural frequency difference of 4 Hz at the frequency range up to 1 kHz.

- In Chapter 5, the time-domain nodal DG method has been presented to model the vibration of structures with piece-wise constant material properties. It extends the study of the previous chapter, where the structures are geometrically more complex and consist of several components with different material properties. Moreover, structural damping was introduced into the methodology by using constant viscous damping. The structures consist of a T-shaped structure and a scaled lightweight wooden floor, for which experiments have been conducted. The presented model has been validated by comparing its results with the experimental results. The agreement on the natural frequencies is good, with a maximum absolute difference of 19.4 Hz or less than 5% for the T-shaped structure in the frequency range below 500 Hz, and a 10.4 Hz difference or less than 9% for the scaled LWF structure in the range below 200 Hz. It is also found that the given constant viscous damping is not sufficient to model the actual damping of the structures accurately, especially in higher frequency regions.
- Finally, Chapter 6 presented the time-domain nodal DG method to solve vibroacoustic problems. The methodology for applying the coupling between the acoustic wave variables and the elastic wave variables using upwind numerical fluxes have been described in detail. The method was applied for impact sound radiation and airborne sound transmission problems. For the case of impact sound radiation, the numerical results were compared with the results obtained by the modal interaction method, and it shows good agreement. In the case of sound transmission, the comparison of sound pressure level difference between receiver locations calculated by the DG method and a reference solution calculated by the FEM shows almost identical results. This chapter also demonstrates the use of the nodal DG method for calculating sound transmission through a homogeneous wall and includes flanking transmission paths. This shows that the proposed methodology has the potential to be extended to more complex vibroacoustic applications.

#### 7.2 Future work

This PhD project presents several developments in applying the time-domain nodal DG method to simulate building acoustic problems. However, there are some issues that can be resolved to apply the method for more comprehensive problems. Several future topics that can be further investigated include:

• In this work, sound sources are given as initial pressure value distributions and have omnidirectional directivity. In general, sound sources have a specific directivity. To obtain more accurate sound field prediction, a method for applying source directivity must be included in the sound propagation modelling. Furthermore, with the spatially dependent effective sound speed as presented in Chapter 3, the initial pressure values can be a source of error in the simulation of distant sound propagation. The inhomogeneous linear acoustic equations with the source

term on the right-hand side of the equations can be further investigated. This development is also more beneficial when the source is close to the boundary or to the receiver point.

- The use of wooden structures in buildings, such as plywood or fibreboard, implies
  that the materials are anisotropic. Further development of this methodology for
  anisotropic media is necessary to improve the accuracy of modelling structural
  vibrations.
- Further development of the current method for vibration in a more general viscoelastic media is required. In this work, the vibration attenuation is modelled using the frequency-independent constant viscous damping. However, this may not be adequate to model varied materials in building structures across a wide frequency range. There are several models of elastic wave propagation in viscoelastic media, e.g., Maxwell, Kelvin-Voigt, and Zener models, as described in Ref. [246]. However, the general formulation of these models in the nodal DG methodology could be challenging due to the inclusion of in-elastic variables creates additional variables to be solved, increasing the degree of freedom rapidly. Moreover, formulating an accurate numerical flux for this case is not easy, especially when anisotropic viscoelastic media are required. This issue is essential to apply the nodal DG method for more extensive building acoustics problems.
- One of the limitations in using the proposed method for the vibroacoustic problem is that the allowed time-step in the solid media is significantly smaller than in air. To reduce the computational costs, the current methodology can be modified to use hexahedral elements. Using hexahedral elements, adjustments of the polynomial order in each direction that accounts for the solid structure with thinner dimensions could make the computation more efficient. Additionally, the local time-stepping methods or the implicit-explicit time-stepping methods could be used for more advanced time integration methods.
- In this work, the linear elasticity equations are used to model the structural vibrations. Further development by using other governing equations to model the vibration, such as the CPT or the FSDT, could be worth investigating. It is expected that this development will reduce the time-step constraints on time integration caused by the thin structure. This is because the spatial discretisation in the thickness dimension is not needed. However, further research is needed to determine the limitations and benefits of the nodal DG methodology for those governing equations, especially those related to building acoustic applications.
- Accuracy analysis of the time-domain DG method, especially for practical vibration problems, is still missing. The time-domain approach, as demonstrated in the literature, contains dissipation and dispersion errors that increase with simulation duration. However, comprehensive error analysis was not performed in this work, particularly to offer a more specific guidance on meshing quality (especially linked to element skewness), polynomial order, and time step sizes, which can ensure the accuracy of the simulation results.

• In this study, an in-house nodal DG method implementation using MATLAB was used. Developing this implementation with a lower programming language might be necessary to increase the efficiency of the computation. Furthermore, computation acceleration using parallel programming will increase the performance of the proposed methodology.

# **Bibliography**

- [1] J. D. Miller, "Effects of noise on people," Journal of the Acoustical Society of America, vol. 56, no. 3, 1974.
- [2] M. Concha-Barrientos, D. Campbell-Lendrum, and K. Steenland, Occupational noise: assessing the burden of disease from work-related hearing impairment at national and local levels. World Health Organization, 2004.
- [3] World Health Organization (WHO), Noise guidelines for the European region. WHO Regional Office for Europe, 2018.
- [4] H. Niemann, X. Bonnefoy, M. Braubach, K. Hecht, C. Maschke, C. Rodrigues, and N. Röbbel, "Noise-induced annoyance and morbidity results from the pan-European LARES study," *Noise & health*, vol. 8, Apr. 2006.
- [5] World Health Organization (WHO), Burden of disease from environmental noise: quantification of healthy life years lost in Europe. WHO Regional Office for Europe, 2011.
- [6] C. Maschke and H. Niemann, "Health effects of annoyance induced by neighbour noise," *Noise Control Engineering Journal*, vol. 55, May 2007.
- [7] H. Jensen, B. Rasmussen, and O. Ekholm, "Neighbour noise annoyance is associated with various mental and physical health symptoms: Results from a nationwide study among individuals living in multi-storey housing," *BMC Public Health*, vol. 19, Nov. 2019.
- [8] OSHA-United States Department of Labor, Per 04-00-004: Hearing conservation program, https://www.osha.gov/enforcement/directives/04-00-004, Accessed: 2022-03-30, 2008.
- [9] European Parliament and Council of the European Union, Directive 2003/10/ec: Minimum health and safety requirements regarding the exposure of workers to the risks arising from physical agents (noise), https://eur-lex.europa.eu/legal-content/EN/TXT/PDF/?uri=CELEX: 32003L0010&from=EN, Accessed: 2022-03-30, 2003.
- [10] B. H. Rasmussen and M. Machimbarrena, Building acoustics throughout Europe Volume 2: Housing and construction types country by country. Discript Preimpresion, 2014.
- [11] B. Rasmussen, "Sound insulation between dwellings requirements in building regulations in Europe," *Applied Acoustics*, vol. 71, 4 2010.

- [12] B. Rasmussen and J. H. Rindel, "Sound insulation between dwellings descriptors applied in building regulations in Europe," *Applied Acoustics*, vol. 71, 3 2010.
- [13] B. H. Rasmussen and M. Machimbarrena, Building acoustics throughout Europe Volume 1: Towards a common framework in building acoustics throughout Europe. DiScript Preimpresion, 2014.
- [14] E. Peris and others, "Environmental noise in Europe-2020," European Environment Agency, Denmark, Tech. Rep. 22/2019, 2020.
- [15] E. M. Salomons and M. Berghauser Pont, "Urban traffic noise and the relation to urban density, form, and traffic elasticity," *Landscape and Urban Planning*, vol. 108, no. 1, 2012.
- [16] H. Tong and J. Kang, "Relationship between urban development patterns and noise complaints in england," *Environment and Planning B: Urban Analytics and City Science*, vol. 48, no. 6, 2021.
- [17] S. L. Benz, J. Kuhlmann, D. Schreckenberg, and J. Wothge, "Contributors to neighbour noise annoyance," *International Journal of Environmental Research and Public Health*, vol. 18, no. 15, 2021.
- [18] L. de Geetere and B. Ingelaere, "A new building acoustical concept for lightweight timber frame constructions," in *Proceedings of the 43rd Interna*tional Congress on Noise Control Engineering (INTERNOISE), Melbourne, Nov. 2014.
- [19] F. Ljunggren and A. Ågren, "Potential solutions to improved sound performance of volume based lightweight multi-storey timber buildings," *Applied Acoustics*, vol. 72, no. 4, 2011.
- [20] E. M. Salomons, *Computational atmospheric acoustics*. Dordrecht: Kluwer Academic Publishers, 2001.
- [21] R. J. LeVeque, Finite volume methods for hyperbolic problems. Cambridge University Press, 2004.
- [22] J. N. Reddy, Theory and Analysis of Elastic Plates and Shells, 2nd ed. 2007.
- [23] G. B. Warburton, "The vibration of rectangular plates," *Proceedings of the Institution of Mechanical Engineers*, vol. 168, no. 1, 1954.
- [24] R. D. Mindlin, A. Schacknow, and H. Deresiewicz, "Flexural vibrations of rectangular plates," *Journal of Applied Mechanics*, vol. 23, no. 3, Sep. 1956.
- [25] C. Wang, J. Reddy, and K. Lee, Shear Deformable Beams and Plates. Oxford: Elsevier Science Ltd, 2000, ISBN: 978-0-08-043784-2.
- [26] M. Vorländer, "Computer simulations in room acoustics: Concepts and uncertainties," *The Journal of the Acoustical Society of America*, vol. 133, no. 3, 2013.
- [27] L. Savioja and U. P. Svensson, "Overview of geometrical room acoustic modeling techniques," The Journal of the Acoustical Society of America, vol. 138, no. 2, 2015.
- [28] B. Hamilton, "Finite difference and finite volume methods for wave-based modelling of room acoustics," Ph.D. dissertation, The University of Edinburgh, 2016.
- [29] J. Picaut, L. Simon, and J.-D. Polack, "Sound field in long rooms with diffusely reflecting boundaries," Applied Acoustics, vol. 56, no. 4, 1999.

7 BIBLIOGRAPHY 163

[30] V. Valeau, J. Picaut, and M. Hodgson, "On the use of a diffusion equation for room-acoustic prediction," *The Journal of the Acoustical Society of America*, vol. 119, no. 3, 2006.

- [31] J. M. Navarro, J. Escolano, and J. J. López, "Implementation and evaluation of a diffusion equation model based on finite difference schemes for sound field prediction in rooms," *Applied Acoustics*, vol. 73, no. 6-7, 2012.
- [32] CATT, Catt-acoustic, version 9, Mar. 31, 2022. [Online]. Available: https://www.catt.se.
- [33] Odeon A/S, Odeon, version 17, Mar. 31, 2022. [Online]. Available: https://odeon.dk.
- [34] H. Kuttruff, Acoustics: An Introduction. New York: CRC Press, 2006.
- [35] D. Botteldooren, "Finite-difference time-domain simulation of low-frequency room acoustic problems," *The Journal of the Acoustical Society of America*, vol. 98, no. 6, Dec. 1995.
- [36] J. Sheaffer, M. van Walstijn, and B. Fazenda, "Physical and numerical constraints in source modeling for finite difference simulation of room acoustics," The Journal of the Acoustical Society of America, vol. 135, no. 1, 2014.
- [37] C. Spa, A. Rey, and E. Hernandez, "A GPU implementation of an explicit compact FDTD algorithm with a digital impedance filter for room acoustics applications," *IEEE/ACM Transactions on Audio, Speech, and Language Processing*, vol. 23, no. 8, 2015.
- [38] B. Hamilton and S. Bilbao, "FDTD methods for 3-D room acoustics simulation with high-order accuracy in space and time," *IEEE/ACM Transactions on Audio, Speech, and Language Processing*, vol. 25, no. 11, 2017.
- [39] T. Okuzono, T. Yoshida, K. Sakagami, and T. Otsuru, "An explicit time-domain finite element method for room acoustics simulations: Comparison of the performance with implicit methods," *Applied Acoustics*, 2016.
- [40] S. Bilbao, "Modeling of complex geometries and boundary conditions in finite difference/finite volume time domain room acoustics simulation," *IEEE Transactions on Audio, Speech, and Language Processing*, vol. 21, no. 7, 2013.
- [41] R. Mehra, N. Raghuvanshi, L. Savioja, M. C. Lin, and D. Manocha, "An efficient GPU-based time domain solver for the acoustic wave equation," Applied Acoustics, vol. 73, no. 2, 2012.
- [42] C. Spa, A. Garriga, and J. Escolano, "Impedance boundary conditions for pseudo-spectral time-domain methods in room acoustics," *Applied Acoustics*, vol. 71, no. 5, 2010.
- [43] M. Hornikx, W. De Roeck, and W. Desmet, "A multi-domain Fourier pseudospectral time-domain method for the linearized Euler equations," *Journal of Computational Physics*, vol. 231, no. 14, May 2012.
- [44] M. Hornikx, C. Hak, and R. Wenmaekers, "Acoustic modelling of sports halls, two case studies," *Journal of Building Performance Simulation*, vol. 8, no. 1, 2015.
- [45] H. Wang, "Room acoustic modeling with the time-domain discontinuous Galerkin method," Ph.D. dissertation, Built Environment, 2021, ISBN: 978-90-386-5357-0.

- [46] R. Pagán Muñoz, "Numerical modeling for urban sound propagation: Developments in wave-based and energy-based methods," Ph.D. dissertation, Built Environment, 2019, ISBN: 978-90-386-4814-9.
- [47] International Organization for Standardization, ISO 16283-2: Acoustics Field measurement of sound insulation in buildings and of building elements Part 2: Impact sound insulation, Standard, 2020.
- [48] —, ISO 16283-2: Acoustics Laboratory measurement of sound insulation of building elements Part 3: Measurement of impact sound insulation, Standard, 2021.
- [49] E. Gerretsen, "Calculation of airborne and impact sound insulation between dwellings," *Applied Acoustics*, vol. 19, no. 4, 1986.
- [50] C. Hopkins, *Sound insulation*. Amsterdam: Elsevier / Butterworth-Heinemann, 2007.
- [51] J. H. Rindel, Sound Insulation in Buildings. CRC Press, 2018.
- [52] B. P. L. Cremer M. Heckl, Structure-Borne Sound. Springer, 2005.
- [53] A. London, "Transmission of reverberant sound through single walls," *Journal of Research of the National Bureau of Standards*, vol. 42, 1949.
- [54] E. Sewell, "Transmission of reverberant sound through a single-leaf partition surrounded by an infinite rigid baffle," *Journal of Sound and Vibration*, vol. 12, no. 1, 1970.
- [55] L. L. Beranek and G. A. Work, "Sound transmission through multiple structures containing flexible blankets," The Journal of the Acoustical Society of America, vol. 21, no. 4, 1949.
- [56] A. London, "Transmission of reverberant sound through double walls," *The Journal of the Acoustical Society of America*, vol. 22, no. 2, 1950.
- [57] J. L. Davy, "Sound transmission of cavity walls due to structure borne transmission via point and line connections," *The Journal of the Acoustical Society of America*, vol. 132, no. 2, 2012.
- [58] V. Hongisto, "Sound insulation of double panels comparison of existing prediction models," *Acta Acustica united with Acustica*, vol. 92, 2006.
- [59] F. Fahy, "Foundations of engineering acoustics," in London: Academic Press, 2001.
- [60] M. Crocker and A. Price, "Sound transmission using statistical energy analysis," *Journal of Sound and Vibration*, vol. 9, no. 3, 1969.
- [61] R. Craik, "The prediction of sound transmission through buildings using statistical energy analysis," *Journal of Sound and Vibration*, vol. 82, no. 4, 1982.
- [62] R. H. Lyon and R. G. DeJong, *Theory and Application of Statistical Energy Analysis*, Second Edition. Boston: Newnes, 1995.
- [63] E. Deckers, O. Atak, L. Coox, R. D'Amico, H. Devriendt, S. Jonckheere, K. Koo, B. Pluymers, D. Vandepitte, and W. Desmet, "The wave based method: An overview of 15 years of research," Wave Motion, vol. 51, no. 4, 2014.
- [64] Y. A. Erlangga, "Advances in iterative methods and preconditioners for the helmholtz equation," Archives of Computational Methods in Engineering, vol. 15, 2008.

7 BIBLIOGRAPHY 165

[65] C. Hopkins, "Statistical energy analysis of coupled plate systems with low modal density and low modal overlap," *Journal of Sound and Vibration*, vol. 251, no. 2, 2002.

- [66] L. Maxit and J.-L. Guyader, "Extension of SEA model to subsystems with non-uniform modal energy distribution," *Journal of Sound and Vibration*, vol. 265, no. 2, 2003.
- [67] J. Su, L. Zheng, Z. Deng, and Y. Jiang, "Research progress on highintermediate frequency extension methods of SEA," Shock and Vibration, vol. 2019, 2019.
- [68] R. S. Langley and J. A. Cordioli, "Hybrid deterministic-statistical analysis of vibro-acoustic systems with domain couplings on statistical components," *Journal of Sound and Vibration*, vol. 321, no. 3, 2009.
- [69] E. Reynders, R. S. Langley, A. Dijckmans, and G. Vermeir, "A hybrid finite element statistical energy analysis approach to robust sound transmission modeling," *Journal of Sound and Vibration*, vol. 333, no. 19, 2014.
- [70] C. Fang and Y. Zhang, "An improved hybrid FE-SEA model using modal analysis for the mid-frequency vibro-acoustic problems," *Mechanical Systems and Signal Processing*, vol. 161, 2021.
- [71] W. Desmet, B. Pluymers, and O. Atak, CAE Methodologies for Mid-Frequency Analysis in Vibration and Acoustics. Katholieke Universiteit Leuven - Faculty of Engineering, 2012.
- [72] R. Panneton and N. Atalla, "Numerical prediction of sound transmission through finite multilayer systems with poroelastic materials," *The Journal of the Acoustical Society of America*, vol. 100, no. 1, 1996.
- [73] F. C. Sgard, N. Atalla, and J. Nicolas, "A numerical model for the low frequency diffuse field sound transmission loss of double-wall sound barriers with elastic porous linings," The Journal of the Acoustical Society of America, vol. 108, no. 6, 2000.
- [74] S. P. S. Maluski and B. M. Gibbs, "Application of a finite-element model to low-frequency sound insulation in dwellings," The Journal of the Acoustical Society of America, vol. 108, no. 4, 2000.
- [75] P. Davidsson, J. Brunskog, P.-A. Wernberg, G. Sandberg, and P. Hammer, "Analysis of sound transmission loss of double-leaf walls in the low-frequency range using the finite element method," *Building Acoustics*, vol. 11, no. 4, 2004.
- [76] A. Arjunan, C. Wang, K. Yahiaoui, D. Mynors, T. Morgan, V. Nguyen, and M. English, "Development of a 3-D finite element acoustic model to predict the sound reduction index of stud based double-leaf walls," *Journal of Sound* and Vibration, vol. 333, no. 23, 2014.
- [77] J. del Coz Díaz, F. Álvarez Rabanal, P. García Nieto, and M. Serrano López, "Sound transmission loss analysis through a multilayer lightweight concrete hollow brick wall by fem and experimental validation," *Building and Environ*ment, vol. 45, no. 11, 2010.
- [78] A. Arjunan, C. Wang, K. Yahiaoui, D. Mynors, T. Morgan, and M. English, "Finite element acoustic analysis of a steel stud based double-leaf wall," *Building and Environment*, vol. 67, 2013.

- [79] B. Nguyen, T. Morgan, M. English, and M. Castellucci, "Vibro-acoustic performance of different steel studs in double-leaf walls by finite element analysis," *Building Acoustics*, vol. 22, no. 2, 2015.
- [80] E. Perras, C. Zhang, J. Chen, and Z. Ji, "Determination and optimization of sound insulation capabilities of geometrically complex walls," in *Proceedings* of the 23rd International Congress on Acoustics, Sep. 2019.
- [81] T. Okuzono, T. Otsuru, R. Tomiku, and N. Okamoto, "Fundamental accuracy of time domain finite element method for sound-field analysis of rooms," Applied Acoustics, vol. 71, no. 10, 2010.
- [82] —, "Application of modified integration rule to time-domain finite-element acoustic simulation of rooms," *The Journal of the Acoustical Society of America*, vol. 132, no. 2, 2012.
- [83] —, "A finite-element method using dispersion reduced spline elements for room acoustics simulation," *Applied Acoustics*, vol. 79, 2014.
- [84] T. Okuzono, T. Otsuru, and K. Sakagami, "Applicability of an explicit time-domain finite-element method on room acoustics simulation," Acoustical Science and Technology, vol. 36, no. 4, 2015.
- [85] K. Yee, "Numerical solution of initial boundary value problems involving maxwell's equations in isotropic media," *IEEE Transactions on Antennas and Propagation*, vol. 14, no. 3, 1966.
- [86] A. Taflove and S. C. Hagness, Computational electrodynamics: the finite-difference time-domain method. Artech House, 2005.
- [87] S. Sakamoto, "Phase-error analysis of high-order finite difference time domain scheme and its influence on calculation results of impulse response in closed sound field," Acoustical Science and Technology, vol. 28, no. 5, 2007.
- [88] S. Sakamoto, T. Seimiya, and H. Tachibana, "Visualization of sound reflection and diffraction using finite difference time domain method," *Acoustical Science and Technology*, vol. 23, no. 1, 2002.
- [89] S. Sakamoto, H. Nagatomo, A. Ushiyama, and H. Tachibana, "Calculation of impulse responses and acoustic parameters in a hall by the finite-difference time-domain method," Acoustical Science and Technology, vol. 29, no. 4, 2008.
- [90] T. Asakura, T. Ishizuka, T. Miyajima, M. Toyoda, and S. Sakamoto, "Vibration analysis for framed structures using the finite-difference time-domain method based on the Bernoulli-Euler beam theory," Acoustical Science and Technology, vol. 35, no. 3, 2014.
- [91] C. Lambourg, A. Chaigne, and D. Matignon, "Time-domain simulation of damped impacted plates. ii. numerical model and results," The Journal of the Acoustical Society of America, vol. 109, no. 4, 2001.
- [92] T. Asakura, T. Ishizuka, T. Miyajima, and M. Toyoda, "Finite-difference time-domain analysis of the vibration characteristics of a beam-plate structure using a dimension-reduced model," Applied Acoustics, vol. 92, 2015.
- [93] M. Toyoda, H. Miyazaki, Y. Shiba, A. Tanaka, and D. Takahashi, "Finite-difference time-domain method for heterogeneous orthotropic media with damping," Acoustical Science and Technology, vol. 33, no. 2, 2012.

7 BIBLIOGRAPHY 167

[94] M. Toyoda and D. Takahashi, "Prediction for architectural structure-borne sound by the finite-difference time-domain method," *Acoustical Science and Technology*, vol. 30, no. 4, 2009.

- [95] T. Asakura, T. Ishizuka, T. Miyajima, M. Toyoda, and S. Sakamoto, "Finite-difference time-domain analysis of structure-borne sound using a plate model based on the kirchhoff-love plate theory," Acoustical Science and Technology, vol. 35, no. 3, 2014.
- [96] T. Asakura and S. Sakamoto, "Finite-difference time-domain analysis of sound insulation performance of wall systems," *Building Acoustics*, vol. 16, no. 3, 2009.
- [97] T. Asakura, T. Ishizuka, T. Miyajima, M. Toyoda, and S. Sakamoto, "Prediction of low-frequency structure-borne sound in concrete structures using the finite-difference time-domain method," The Journal of the Acoustical Society of America, vol. 136, no. 3, 2014.
- [98] T. Asakura, "Prediction of vibroacoustic transmission characteristics through double-plate floor structures by using finite-difference time-domain analysis," Acoustical Science and Technology, vol. 40, no. 5, 2019.
- [99] —, "Finite-difference time-domain simulation of floor-impact sound excited by one-dimensional contact model and its application to auralization of floor-impact sound," *Acoustical Science and Technology*, vol. 42, no. 1, 2021.
- [100] T. Asakura, T. Miyajima, and S. Sakamoto, "Prediction method for sound from passing vehicle transmitted through building façade," *Applied Acoustics*, vol. 74, no. 5, 2013.
- [101] N. Ferreira and C. Hopkins, "Finite difference time domain modelling of a point-excited elastic plate radiating into an acoustic cavity," *The Journal of the Acoustical Society of America*, vol. 142, no. 5, 2017.
- [102] B. Fornberg, A Practical Guide to Pseudospectral Methods. Cambridge University Press, 1996.
- [103] Q. H. Liu, "The PSTD algorithm: A time-domain method requiring only two cells per wavelength," *Microwave and Optical Technology Letters*, vol. 15, no. 3, 1997.
- [104] J. S. Hesthaven, S. Gottlieb, and D. Gottlieb, Spectral methods for timedependent problems. Cambridge University Press, 2007.
- [105] N. Morales, R. Mehra, and D. Manocha, "A parallel time-domain wave simulator based on rectangular decomposition for distributed memory architectures," Applied Acoustics, vol. 97, 2015.
- [106] M. Hornikx and T. V. Renterghem, "Numerical investigation of the effect of crosswind on sound propagation outdoors," Acta Acustica united with Acustica, vol. 102, 2016.
- [107] F. Georgiou and M. Hornikx, "Incorporating directivity in the Fourier pseudospectral time-domain method using spherical harmonics," *The Journal of the Acoustical Society of America*, vol. 140, no. 2, 2016.
- [108] M. Hornikx, R. Waxler, and J. Forssén, "The extended Fourier pseudospectral time-domain method for atmospheric sound propagation," The Journal of the Acoustical Society of America, vol. 128, no. 4, 2010.

- [109] M. Hornikx and J. Forssén, "Modelling of sound propagation to threedimensional urban courtyards using the extended Fourier PSTD method," Applied Acoustics, vol. 72, 9 2011.
- [110] R. Pagán Muñoz and M. Hornikx, "Hybrid Fourier pseudospectral/discontinuous Galerkin time-domain method for wave propagation," *Journal of Computational Physics*, vol. 348, 2017.
- [111] A. Modave, A. St-Cyr, and T. Warburton, "GPU performance analysis of a nodal discontinuous Galerkin method for acoustic and elastic models," *Computers & Geosciences*, vol. 91, 2016.
- [112] J. S. Hesthaven and T. Warburton, Nodal Discontinuous Galerkin Methods: Algorithms, Analysis, and Applications. New York: Springer, 2008.
- [113] W. H. Reed and T. R. Hill, "Triangular mesh methods for the neutron transport equation," Los Alamos Scientific Laboratory, New Mexico, Tech. Rep., 1973.
- [114] J. S. Hesthaven and T. Warburton, "Nodal high-order methods on unstructured grids: I. time-domain solution of maxwell's equations," *Journal of Computational Physics*, vol. 181, no. 1, 2002.
- [115] —, "High-order nodal discontinuous Galerkin methods for the maxwell eigenvalue problem," *Philosophical Transactions of the Royal Society of London. Series A: Mathematical, Physical and Engineering Sciences*, vol. 362, no. 1816, 2004.
- [116] J. S. Hesthaven and T. Warburton, "High-order accurate methods for time-domain electromagnetics," *Computer Modeling in Engineering and Sciences*, vol. 5, no. 5, 2004.
- [117] M. Käser and M. Dumbser, "An arbitrary high-order discontinuous Galerkin method for elastic waves on unstructured meshes—i. the two-dimensional isotropic case with external source terms," Geophysical Journal International, vol. 166, no. 2, 2006.
- [118] M. Dumbser and M. Käser, "An arbitrary high-order discontinuous Galerkin method for elastic waves on unstructured meshes—ii. the three-dimensional isotropic case," *Geophysical Journal International*, vol. 167, no. 1, 2006.
- [119] M. Käser, M. Dumbser, J. De La Puente, and H. Igel, "An arbitrary high-order discontinuous Galerkin method for elastic waves on unstructured meshes—iii. viscoelastic attenuation," *Geophysical Journal International*, vol. 168, no. 1, 2007.
- [120] J. de la Puente, M. Käser, M. Dumbser, and H. Igel, "An arbitrary high-order discontinuous Galerkin method for elastic waves on unstructured meshes-iv. anisotropy," *Geophysical Journal International*, vol. 169, no. 3, 2007.
- [121] M. Dumbser, M. Käser, and E. F. Toro, "An arbitrary high-order discontinuous Galerkin method for elastic waves on unstructured meshes-v. local time stepping and p-adaptivity," *Geophysical Journal International*, vol. 171, no. 2, 2007.
- [122] H. Wang, J. Yang, and M. Hornikx, "Frequency-dependent transmission boundary condition in the acoustic time-domain nodal discontinuous Galerkin model," *Applied Acoustics*, vol. 164, 2020.

7 | BIBLIOGRAPHY 169

[123] H. Wang and M. Hornikx, "Time-domain impedance boundary condition modeling with the discontinuous Galerkin method for room acoustics simulations," The Journal of the Acoustical Society of America, vol. 147, no. 4, 2020.

- [124] H. Wang, M. Cosnefroy, and M. Hornikx, "An arbitrary high-order discontinuous Galerkin method with local time-stepping for linear acoustic wave propagation," *The Journal of the Acoustical Society of America*, vol. 149, no. 1, 2021.
- [125] S. Bilbao, B. Hamilton, J. Botts, and L. Savioja, "Finite volume time domain room acoustics simulation under general impedance boundary conditions," *IEEE/ACM Transactions on Audio, Speech, and Language Processing*, vol. 24, no. 1, 2015.
- [126] B. Hamilton, "Finite difference and finite volume methods for wave-based modelling of room acoustics," Ph.D. dissertation, 2016.
- [127] L. Xuan, G. Jin, J. Gong, W. Zhang, and P. Ming, "Time domain finite volume method for three-dimensional structural-acoustic coupling analysis," *Applied Acoustics*, vol. 76, pp. 138–149, 2014.
- [128] T. Sakuma, S. Sakamoto, and T. Otsuru, Computational Simulation in Architectural and Environmental Acoustics. Springer Japan, 2014.
- [129] T. Sakuma and Y. Yasuda, "Fast multipole boundary element method for large-scale steady-state sound field analysis. Part I: Setup and validation," Acta Acustica united with Acustica, vol. 88, Jul. 2002.
- [130] Y. Yasuda and T. Sakuma, "Fast multipole boundary element method for large-scale steady-state sound field analysis. Part II: Examination of numerical items," Acta Acustica united with Acustica, vol. 89, Jan. 2003.
- [131] A. Ali and C. Rajakumar, *The Boundary Element Method, applications in sound and vibration*. Boca Raton: Taylor and Francis, 2004.
- [132] S. Marburg and B. Nolte, Computational acoustics of noise propagation in fluids: finite and boundary element methods. Springer, 2008, vol. 578.
- [133] M. R. Schroeder, "Novel uses of digital computers in room acoustics," *The Journal of the Acoustical Society of America*, vol. 33, no. 11, 1961.
- [134] B. Cockburn and C.-W. Shu, "TVB Runge-Kutta local projection discontinuous Galerkin finite element method for conservation laws II: General framework," *Mathematics of Computation*, vol. 52, no. 186, p. 411, Apr. 1989.
- [135] Y. Reymen, W. De Roeck, G. Rubio, M. Baelmans, and W. Desmet, "A 3D discontinuous Galerkin method for aeroacoustic propagation," in 12th International Congress on Sound and Vibration, Lisbon, Portugal, 2005.
- [136] R. Della Ratta Rinaldi, A. Iob, and R. Arina, "An efficient discontinuous Galerkin method for aeroacoustic propagation," *International Journal for Nu*merical Methods in Fluids, vol. 69, no. 9, Jul. 2012.
- [137] J. Nytra, L. Čermák, and M. Jícha, "Applications of the discontinuous Galerkin method to propagating acoustic wave problems," Advances in Mechanical Engineering, vol. 9, no. 6, 2017.
- [138] Y. Reymen, M. Baelmans, and W. Desmet, "Efficient implementation of Tam and Auriault's time-domain impedance boundary condition," AIAA journal, vol. 46, no. 9, 2008.

- [139] K.-Y. Fung and H. Ju, "Broadband time-domain impedance models," *AIAA journal*, vol. 39, no. 8, 2001.
- [140] A. Pierce, Acoustics: An introduction to its physical principles and applications. Springer, 2019.
- [141] H. L. Atkins and C.-W. Shu, "Quadrature-free implementation of discontinuous Galerkin method for hyperbolic equations," AIAA journal, vol. 36, no. 5, 1998.
- [142] J. S. Hesthaven and C.-H. Teng, "Stable spectral methods on tetrahedral elements," SIAM Journal on Scientific Computing, vol. 21, no. 6, 2000.
- [143] P. Lasaint and P.-A. Raviart, "On a finite element method for solving the neutron transport equation," in *Mathematical aspects of finite elements in partial differential equations*, 1974.
- [144] F. Q. Hu and H. Atkins, "Eigensolution analysis of the discontinuous Galerkin method with nonuniform grids: I. one space dimension," *Journal of Computa*tional Physics, vol. 182, no. 2, 2002.
- [145] M. Ainsworth, "Dispersive and dissipative behaviour of high order discontinuous Galerkin finite element methods," *Journal of Computational Physics*, vol. 198, no. 1, 2004.
- [146] F. Q. Hu, M. Hussaini, and P. Rasetarinera, "An analysis of the discontinuous Galerkin method for wave propagation problems," *Journal of Computational Physics*, vol. 151, no. 2, 1999.
- [147] F. Hu and H. Atkins, "Two-dimensional wave analysis of the discontinuous Galerkin method with non-uniform grids and boundary conditions," in 8th AIAA/CEAS Aeroacoustics Conference & Exhibit, 2002.
- [148] T. Toulorge, "Efficient Runge-Kutta discontinuous Galerkin methods applied to aeroacoustics," Ph.D. dissertation, Katholieke Universiteit Leuven, Feb. 2012.
- [149] H. Atkins, "Continued development of the discontinuous Galerkin method for computational aeroacoustic applications," in 3rd AIAA/CEAS Aeroacoustics Conference, 1997.
- [150] B.-T. Chu and L. S. Kovásznay, "Non-linear interactions in a viscous heat-conducting compressible gas," *Journal of Fluid Mechanics*, vol. 3, no. 5, 1958.
- [151] K. W. Thompson, "Time dependent boundary conditions for hyperbolic systems," *Journal of Computational Physics*, vol. 68, no. 1, 1987.
- [152] B. Engquist and A. Majda, "Absorbing boundary conditions for numerical simulation of waves," *Proceedings of the National Academy of Sciences*, vol. 74, no. 5, 1977.
- [153] B. Gustafsson, High Order Difference Methods for Time Dependent PDE. Berlin: Springer-Verlag, 2007, ch. 2.
- [154] S. Bilbao, B. Hamilton, J. Botts, and L. Savioja, "Finite volume time domain room acoustics simulation under general impedance boundary conditions," *IEEE/ACM Transactions on Audio, Speech and Language Processing (TASLP)*, vol. 24, no. 1, 2016.
- [155] D. Dragna, K. Attenborough, and P. Blanc-Benon, "On the inadvisability of using single parameter impedance models for representing the acoustical prop-

7 | BIBLIOGRAPHY 171

erties of ground surfaces," The Journal of the Acoustical Society of America, vol. 138, no. 4, 2015.

- [156] S. C. Reddy and L. N. Trefethen, "Stability of the method of lines," Numerische Mathematik, vol. 62, no. 1, 1992.
- [157] H. O. Kreiss and L. Wu, "On the stability definition of difference approximations for the initial boundary value problem," Applied Numerical Mathematics, vol. 12, no. 1-3, 1993.
- [158] C. Bogey and C. Bailly, "A family of low dispersive and low dissipative explicit schemes for flow and noise computations," *Journal of Computational Physics*, vol. 194, no. 1, 2004.
- [159] C. Geuzaine and J.-F. Remacle, "Gmsh: A 3-D finite element mesh generator with built-in pre- and post-processing facilities," *International Journal for Numerical Methods in Engineering*, vol. 79, no. 11, 2009.
- [160] X. Di and K. E. Gilbert, "An exact Laplace transform formulation for a point source above a ground surface," The Journal of the Acoustical Society of America, vol. 93, no. 2, 1993.
- [161] J. Saarelma, J. Botts, B. Hamilton, and L. Savioja, "Audibility of dispersion error in room acoustic finite-difference time-domain simulation as a function of simulation distance," The Journal of the Acoustical Society of America, vol. 139, no. 4, 2016.
- [162] O. Zaporozhets, V. Tokarev, and K. Attenborough, Aircraft noise assesment, prediction and control. Oxon: Spoon Press, 2011.
- [163] International Civil Aviation Organization, Guidance on the balanced approach to aircraft noise management, 2nd ed. 2008.
- [164] European Pariliament and Council of the European Union, "Regulation (EU) No 598/2014 on the establishment rules and procedures with regard to the introduction of noise-related operating restrictions at unioun airports within a balanced approach and repealing Directive 2002/30/EC," Official Journal of the European Union, 2014.
- [165] E. M. Salomons and K. B. Rasmussen, "Numerical computation of sound propagation over a noise screen based on an analytic approximation of the wind speed field," Applied Acoustics, vol. 60, 2000.
- [166] E. M. Salomons, "Reduction of the performance of a noise screen due to screeninduced wind-speed gradients. Numerical computations and wind-tunnel experiments," The Journal of the Acoustical Society of America, vol. 105, no. 4, 1999.
- [167] J. E. Rosenbaum, "Enhanced propagation modeling of directional aviation noise: A hybrid parabolic equation-fast field program method," Ph.D. dissertation, Pennsylvania State University, 2011.
- [168] C. Bosschaart, A. Eisses, and F. V. D. Eerden, "LF airport ground noise mitigation using scattering sections," *Euronoise 2012*, 2012.
- [169] T. V. Renterghem and D. Botteldooren, "Numerical simulation of the effect of trees on downwind noise barrier performance," Acta Acustica united with Acustica, vol. 89, 2003.

- [170] T. V. Renterghem, E. M. Salomons, and D. Botteldooren, "Efficient FDTD-PE model for sound propagation in situations with complex obstacles and wind profiles," Acta Acustica united with Acustica, vol. 91, 2005.
- [171] T. V. Renterghem and D. Botteldooren, "Numerical evaluation of tree canopy shape near noise barriers to improve downwind shielding," *Journal of the Acoustical Society of America*, vol. 2, 2008.
- [172] D. Heimann, "Three-dimensional linearised Euler model simulations of sound propagation in idealised urban situations with wind effects," Applied Acoustics, vol. 68, 2007.
- [173] T. Oshima, M. Imano, Y. Hiraguri, and Y. Kamoshida, "Linearized Euler simulations of sound propagation with wind effects over a reconstructed urban terrain using digital geographic information," *Applied Acoustics*, vol. 74, no. 12, 2013.
- [174] M. Hornikx, M. Dohmen, K. Conen, T. V. Hoo, and B. Blocken, "The wind effect on sound propagation over urban areas: Predictions for generic urban sections," *Building and Environment*, vol. 144, 2018.
- [175] K. Gerdes, "A review of infinite element methods for exterior helmholtz problems," *Journal of Computational Acoustics*, vol. 08, no. 01, 2000.
- [176] A. Pelat, S. Felix, and V. Pagneux, "A coupled modal-finite element method for the wave propagation modeling in irregular open waveguides," *The Journal* of the Acoustical Society of America, vol. 129, no. 3, 2011.
- [177] M. Molerón, S. Felix, V. Pagneux, and O. Richoux, "Sound propagation in periodic urban areas," *Journal of Applied Physics*, vol. 111, no. 11, 2012.
- [178] K. E. Piippo, "Noise in street canyons with asymmetrical cross sections," Ph.D. dissertation, Hong Kong Polytechnic University, 2017.
- [179] N. M. Papadakis and G. E. Stavroulakis, "Finite element method for the estimation of insertion loss of noise barriers: Comparison with various formulae (2d)," *Urban Science*, vol. 4, no. 4, 2020.
- [180] M. Hornikx, "Ten questions concerning computational urban acoustics," *Building and Environment*, vol. 106, 2016.
- [181] G. E. M. Karniadakis and S. Sherwin, Spectral/hp element methods fo rcomputational fluid dynamics. Oxford University Press, 2005.
- [182] H. Wang, I. Sihar, R. Pagán Muñoz, and M. Hornikx, "Room acoustics modelling in the time-domain with the nodal discontinuous Galerkin method," The Journal of the Acoustical Society of America, vol. 145, no. 4, 2019.
- [183] H. Wang and M. Hornikx, "Time-domain impedance boundary condition modeling with the discontinuous Galerkin method for room acoustics simulations," The Journal of the Acoustical Society of America, vol. 147, no. 4, 2020.
- [184] T. V. Renterghem, S. Taherzadeh, M. Hornikx, and K. Attenborough, "Meteorological effects on the noise reducing performance of a low parallel wall structure," *Applied Acoustics*, vol. 121, 2017.
- [185] H. G. Weller, G. Tabor, H. Jasak, and C. Fureby, "A tensorial approach to computational continuum mechanics using object-oriented techniques," *Com*puters in physics, vol. 12, no. 6, 1998.
- [186] E. Komen, A. Shams, L. Camilo, and B. Koren, "Quasi-DNS capabilities of OpenFOAM for different mesh types," en, Computers & Fluids, vol. 96, 2014.

7 BIBLIOGRAPHY 173

[187] B. E. Launder and D. B. Spalding, Lectures in mathematical models of turbulence. London; New York: Academic Press, 1972.

- [188] B. E. Launder and D. B. Spalding, "The numerical computation of turbulent flows," Computer methods in applied mechanics and engineering, vol. 3, no. 2, 1974.
- [189] S. Pope, Turbulent flows. Cambridge University Press, 2000.
- [190] B. Blocken, T. Stathopoulos, and J. Carmeliet, "CFD simulation of the atmospheric boundary layer: Wall function problems," *Atmospheric Environment*, vol. 41, no. 2, 2007.
- [191] J. Franke, A. Hellsten, H. Schlünzen, and B. Carissimo, "Best practice guideline for the CFD simulation of flows in the urban environment, COST Action 732," COST Office, Brussels, Tech. Rep., 2007.
- [192] R. Pagán Muñoz, "Numerical modeling for urban sound propagation: developments in wave-based and energy-based methods," Ph.D. dissertation, Technische Universiteit Eindhoven, 2019.
- [193] E. Buikema and M. Vercammen, "Gebulder op de grond," Geluid, no. 2, 2010.
- [194] M. Schiff, M. Hornikx, and J. Forssén, "Excess attenuation for sound propagation over an urban canyon," *Applied Acoustics*, vol. 71, no. 6, 2010.
- [195] C. Bosschaart and A. Eisses, "Berekening grondgeluid schilhoeve," TNO, Tech. Rep., 2016, p. 13.
- [196] J. Brunskog, "Energy based prediction models for building acoustics energy based prediction models for building acoustics," in *Proceedings of the joint Baltic-Nordic Acoustics Meeting*, 2012.
- [197] W. Soedel, Vibrations of shells and plates, 3rd ed. New York: Marcel Dekker, 2004.
- [198] S. Marburg and B. Nolte, Computational acoustics of noise propagation in fluids finite and boundary element methods. Springer, 2008.
- [199] J. Virieux, "P-SV wave propagation in heterogeneous media: velocity-stress finite-difference method," *Geophysics*, vol. 51, no. 4, 1986.
- [200] L. C. Wilcox, G. Stadler, C. Burstedde, and O. Ghattas, "A high-order discontinuous Galerkin method for wave propagation through coupled elastic-acoustic media," *Journal of Computational Physics*, vol. 229, no. 24, 2010.
- [201] A. Bermúdez, P.Gamallo, L. Hervella-Nieto, R. Rodríguez, and D. Santamarina, "Fluid-structure acoustic interaction," in S. Marburg, B. Nolte (eds), Computational Acoustics of Noise Propagation in Fluids Finite and Boundary Element Methods.
- [202] R. Pagán Muñoz and M. Hornikx, "Hybrid Fourier pseudospectral/discontinuous Galerkin time-domain method for wave propagation," *Journal of Computational Physics*, vol. 348, 2017.
- [203] H. Wang, I. Sihar, R. Pagán Muñoz, and M. Hornikx, "Room acoustics modelling in the time-domain with the nodal discontinuous Galerkin method," The Journal of the Acoustical Society of America, vol. 145, no. 4, 2019.
- [204] V. Etienne, E. Chaljub, J. Virieux, and N. Glinsky, "An hp-adaptive discontinuous Galerkin finite-element method for 3-D elastic wave modelling," Geophysical Journal International, vol. 183, no. 2, 2010.

- [205] ANSYS, Ansys fluent fluid simulation software, Apr. 3, 2022. [Online]. Available: https://www.ansys.com/.
- [206] S. H. Hashemi and M. Arsanjani, "Exact characteristic equations for some of classical boundary conditions of vibrating moderately thick rectangular plates," *International Journal of Solids and Structures*, vol. 42, 2005.
- [207] C. Y. Wang and C. M. Wang, Structural vibration. CRC Press, 2014.
- [208] S. Srinivas, C. Joga Rao, and A. Rao, "An exact analysis for vibration of simply-supported homogeneous and laminated thick rectangular plates," *Journal of Sound and Vibration*, vol. 12, no. 2, 1970.
- [209] D. Gorman, Free vibration analysis of rectangular plates. Elsevier, 1981.
- [210] N. J. Kessissoglou, "Power transmission in L-shaped plates including flexural and in-plane vibration," *The Journal of the Acoustical Society of America*, vol. 115, no. 3, 2004.
- [211] COMSOL AB, COMSOL Multiphysics ® version 5.4. Stockholm, Sweden, 2018. [Online]. Available: http://www.comsol.com.
- [212] C. Johansson, "Low-frequency impact sound insulation of a light weight wooden joist floor," *Applied Acoustics*, vol. 44, no. 2, 1995.
- [213] W. E. Blazier and R. B. DuPree, "Investigation of low-frequency footfall noise in wood-frame, multifamily building construction," The Journal of the Acoustical Society of America, vol. 96, no. 3, 1994.
- [214] R. Langley and K. Heron, "Elastic wave transmission through plate/beam junctions," *Journal of Sound and Vibration*, vol. 143, no. 2, 1990.
- [215] V. Zalizniak, Y. Tso, and L. Wood, "Waves transmission through plate and beam junctions," *International Journal of Mechanical Sciences*, vol. 41, no. 7, 1999.
- [216] X. Shi and D. Shi, "Free and forced vibration analysis of T-shaped plates with general elastic boundary supports," *Journal of Low Frequency Noise*, Vibration and Active Control, vol. 37, no. 2, 2018.
- [217] H. Chung and G. Emms, "Fourier series solutions to the vibration of rectangular lightweight floor/ceiling structures," *Acta Acustica united with Acustica*, vol. 94, no. 3, 2008.
- [218] J. Brunskog and H. Chung, "Non-diffuseness of vibration fields in ribbed plates," *The Journal of the Acoustical Society of America*, vol. 129, no. 3, 2011.
- [219] K. A. Dickow, J. Brunskog, and M. Ohlrich, "Modal density and modal distribution of bending wave vibration fields in ribbed plates," The Journal of the Acoustical Society of America, vol. 134, no. 4, 2013.
- [220] J. Brunskog and P. Hammer, "Prediction models of impact sound insulation on timber floor structures a literature survey," *Building Acoustics*, vol. 7, no. 2, 2000.
- [221] C. Fox and H. Chung, "Modeling low-frequency vibration in light-weight timber floor/ceiling systems," *The Journal of the Acoustical Society of America*, vol. 145, no. 2, 2019.
- [222] C. Hopkins, "Vibration transmission between coupled plates using finite element methods and statistical energy analysis. Part 1: Comparison of measured

7 | BIBLIOGRAPHY 175

and predicted data for masonry walls with and without apertures," *Applied Acoustics*, vol. 64, no. 10, 2003.

- [223] C. Hopkins, C. Crispin, J. Poblet-Puig, and C. Guigou-Carter, "Regression curves for vibration transmission across junctions of heavyweight walls and floors based on finite element methods and wave theory," *Applied Acoustics*, vol. 113, 2016.
- [224] J. Poblet-Puig and C. Guigou-Carter, "Using spectral finite elements for parametric analysis of the vibration reduction index of heavy junctions oriented to flanking transmissions and EN-12354 prediction method," Applied Acoustics, vol. 99, 2015.
- [225] I. Sihar and M. Hornikx, "Implementation of the nodal discontinuous Galerkin method for the plate vibration problem using linear elasticity equations," Acta Acustica united with Acustica, vol. 105, no. 4, 2019.
- [226] M. Dumbser and M. Käser, "An arbitrary high-order discontinuous Galerkin method for elastic waves on unstructured meshes - II. The three-dimensional isotropic case," *Geophysical Journal International*, vol. 167, no. 1, 2006.
- [227] K. Shin and J. Hammond, Fundamentals of signal processing for sound and vibration engineers. Wiley, 2008, p. 416.
- [228] J. Zhou, Y. Chui, M. Gong, and L. Hu, "Comparative study on measurement of elastic constants of wood-based panels using modal testing: Choice of boundary conditions and calculation methods," *Journal of Wood Science*, vol. 63, no. 5, 2017.
- [229] C. Simmons, K. Hagberg, and E. Backman, "Acoustical performance of apartment buildings resident's survey and field measurements"," AkuLite Report 2, SP Report 2011:58, Tech. Rep., 2011.
- [230] F. Ljunggren, C. Simmons, and K. Hagberg, "Correlation between sound insulation and occupants' perception proposal of alternative single number rating of impact sound," *Applied Acoustics*, vol. 85, 2014.
- [231] F. Ljunggren, C. Simmons, and R. Öqvist, "Correlation between sound insulation and occupants' perception proposal of alternative single number rating of impact sound, part ii," *Applied Acoustics*, vol. 123, 2017.
- [232] J. E. Cambridge, "An evaluation of various sound insulation software and their applications in the design of silent rooms," M.S. thesis, Chalmers University of Technology, 2006.
- [233] A. Neves e Sousa and B. Gibbs, "Parameters influencing low frequency impact sound transmission in dwellings," *Applied acoustics*, vol. 78, 2014.
- [234] H. Park, D. Yoon, and T. Cho, "Influence of plan configuration on low frequency vibroacoustic behaviour of floating floor with low natural frequency," Applied Acoustics, vol. 158, 2020.
- [235] F. J. Fahy, "Vibration of containing structures by sound in the contained fluid," *Journal of Sound and Vibration*, vol. 10, no. 3, 1969.
- [236] E. H. Dowell, G. Gorman, and D. Smith, "Acoustoelasticity: General theory, acoustic natural modes and forced response to sinusoidal excitation, including comparisons with experiment," *Journal of Sound and Vibration*, vol. 52, no. 4, 1977.

176 BIBLIOGRAPHY

[237] V. Bokil and U. S. Shirahatti, "A technique for the modal analysis of soundstructure interaction problems," *Journal of Sound and Vibration*, vol. 173, no. 1, 1994.

- [238] A. Neves e Sousa and B. Gibbs, "Low frequency impact sound transmission in dwellings through homogeneous concrete floors and floating floors," *Applied Acoustics*, vol. 72, no. 4, 2011.
- [239] J. Brunskog and P. Davidsson, "Sound transmission of structures. a finite element approach with simplified room description," Acta Acustica united with Acustica, vol. 90, no. 5, 2004.
- [240] N. Ferreira, "Vibroacoustics modelling using the finite difference time domain method: Incorporating porous materials and mechanically excited plates," Ph.D. dissertation, University of Liverpool, Mar. 2019.
- [241] I. Sihar, J. Yang, and M. Hornikx, "Numerical modelling of structural vibration with piece-wise constant material properties using the nodal discontinuous Galerkin method," in *Proceedings of Euronoise 2021*, Oct. 2021.
- [242] M. Käser and M. Dumbser, "A highly accurate discontinuous Galerkin method for complex interfaces between solids and moving fluids," *Geophysics*, vol. 73, no. 3, 2008.
- [243] K. Shukla, J. M. Carcione, J. S. Hesthaven, and E. L'heureux, "Waves at a fluid-solid interface: Explicit versus implicit formulation of boundary conditions using a discontinuous Galerkin method," The Journal of the Acoustical Society of America, vol. 147, no. 5, 2020.
- [244] Q. Zhan, Q. Ren, M. Zhuang, Q. Sun, and Q. H. Liu, "An exact riemann solver for wave propagation in arbitrary anisotropic elastic media with fluid coupling," Computer Methods in Applied Mechanics and Engineering, vol. 329, 2018.
- [245] A. Bermúdez, L. Hervella-Nieto, and R. Rodríguez, "Finite element computation of three-dimensional elastoacoustic vibrations," *Journal of Sound and Vibration*, vol. 219, no. 2, 1999.
- [246] J. M. Carcione, Wave Fields in Real Media Handbook of Geophysical Exploration: Seismic Exploration Wave Fields in Real, Third. Elsevier, 2015.
- [247] K. Attenborough, "Acoustical impedance models for outdoor ground surfaces," Journal of Sound and Vibration, vol. 99, no. 4, 1985.
- [248] C. Guan, H. Zhang, X. Wang, H. Miao, L. Zhou, and F. Liu, "Experimental and theoretical modal analysis of full-sized wood composite panels supported on four nodes," *Materials*, vol. 10, no. 6, 2017.
- [249] A. J. Pretlove, "Free vibrations of a rectangular panel backed by a closed rectangular cavity," *Journal of Sound and Vibration*, vol. 2, no. 3, 1965.
- [250] Z. Hu, L. Maxit, and L. Cheng, "Convergence criteria on the acoustic velocity continuity in a panel-cavity system," The Journal of the Acoustical Society of America, vol. 141, no. 3, 2017.
- [251] F. Fahy and P. Gardonio, Sound and structural vibration: radiation, transmission and response: second edition, 2nd ed. Academic Press, 2007.

1.1	is removed to see the building section	3
1.2	Deformation of the plate based on different plate theory adapted from Ref. [22]. (a) initial undeformed condition, (b) plate deformation based	
	on the classical plate theory (CPT), (c) plate deformation based on the	
	first-order shear deformation theory (FSDT)	4
1.3	Problem domains and boundary conditions for the sound and vibration in the built environment: (a) pure acoustic problem, (b) solid vibration	
	problem, (c) fluid-structure interaction problem.	6
1.4	Spatial distribution of absolute sound pressure at certain time over building canyons taken from an example case in Chapter 3	7
1.5	Spatial distribution of absolute sound pressure at certain time taken from impact sound radiation case in Chapter 6. Blue dot denotes the	_
	impact excitation position and grey cuboid denotes a concrete slab	7
2.1	Amplitude error and phase errors for the periodic propagation of a	20
2.2	single frequency plane wave.  Numerical reflection coefficient calculated with different polynomial	36
2.2	orders	38
2.3	Sound pressure level at receiver position in the configuration of the three-dimensional rigid cuboid room.	41
2.4	Graphical data of the room under investigation	43
2.5	Sound pressure level $L_p$ in the real room configuration for the experimental and the DG results	44
3.1	Top view of the area of interest	48
3.2	The top view of the simulated two-dimensional scenarios between the	
	noise source and the first row of residential houses. Two arrows repre-	51
3.4	sent the viewing angle of the computational cases	91
	representing (a) case 1: flat roof and (b) case 2: tilted roof. Dimensions	52
3.8	in meters	52 61
3.9	The horizontal wind velocity for Case 1b for $x = 1100 \mathrm{m}$ to $2127 \mathrm{m}$	61

	The horizontal wind velocity for Case 2a for $x=1100\mathrm{m}$ to $2127\mathrm{m}$ The horizontal wind velocity for Case 2b for $x=1100\mathrm{m}$ to $2127\mathrm{m}$	61 62
	·	0_
4.1	Illustration of the Ranking–Hugoniot jump conditions to construct the solution of the Riemann problem	82
4.2	Rectangular plate computational domain with thickness of $h = 0.12$	
	m. The excitation force (F) and receiver (R) locations are marked, and	
	the elements that are associated with the point force are highlighted	0.0
4.3	with red colour	86
4.0	force excitation location (F) and receiver (R1,R2,R3) locations are	
	marked by dots on the surface of the structure	90
4.4	Rectangular plate mobility with thickness of $h=0.12~\mathrm{m}$ and S-S-	
	S-S BCs. The red, black, dashed black, and blue lines represent the	
	mobility obtained by the nodal DG method, CPT, CPT with including	01
4.5	rotary inertia, and FSDT, respectively	91
1.0	S-S BCs. The red, black, dashed black, and blue lines represent the	
	mobility obtained by the nodal DG method, CPT, CPT with including	
	rotary inertia, and FSDT, respectively	91
4.6	Rectangular plate mobility with thickness of $h = 0.04$ m and S-S-	
	S-S BCs. The red, black, dashed black, and blue lines represent the mobility obtained by the nodal DG method, CPT, CPT with including	
	rotary inertia, and FSDT, respectively	92
4.7	Rectangular plate mobility with thickness of $h = 0.12$ m and S-S-S-C	02
	BCs. The red, black, and blue lines represent the mobility obtained	
	by the nodal DG method, CPT, and FSDT, respectively	94
4.8	Rectangular plate mobility with thickness of $h = 0.08$ m and S-S-S-C	
	BCs. The red, black, and blue lines represent the mobility obtained by the nodal DG method, CPT, and FSDT, respectively	94
4.9	Rectangular plate mobility with thickness of $h = 0.12$ m and S-S-S-C	94
	BCs. The red, black, and blue lines represent the mobility obtained	
	by the nodal DG method, CPT, and FSDT, respectively	95
4.10	Rectangular plate mobility with thickness of $h = 0.12$ m and S-S-S-F	
	BCs. The red, black, and blue lines represent the mobility obtained by the nodal DG method, CPT, and FSDT, respectively	97
4.11	Rectangular plate mobility with thickness of $h = 0.08$ m and S-S-S-F	91
	BCs. The red, black, and blue lines represent the mobility obtained	
	by the nodal DG method, CPT, and FSDT, respectively	97
4.12	Rectangular plate mobility with thickness of $h = 0.04$ m and S-S-S-F	
	BCs. The red, black, and blue lines represent the mobility obtained	00
112	by the nodal DG method, CPT, and FSDT, respectively Rectangular plate mobility with thickness of $h=0.12$ m and S-S-S-F	98
4.10	BCs at position R1 (solid lines) and R2 (dashed lines). The red and	
	blue lines represent the mobility obtained by the nodal DG method	
	and FSDT, respectively	100

4.14	Rectangular plate mobility with thickness of $h=0.12~\mathrm{m}$ and S-S-S-F	
	BCs at position R3 (solid lines) and R4 (dashed lines). The red and	
	blue lines represent the mobility obtained by the nodal DG method	1.01
4 1 5		101
4.15	L-shaped plate mobilities at position R1. The red, black, and blue	
	solid lines represent the mobility obtained by the nodal DG method, CPT, and FSDT, respectively. The red dashed line represent mobility	
	obtained by FEM	102
1 16	L-shaped plate mobilities at position R2. The red, black, and blue	102
4.10	solid lines represent the mobility obtained by the nodal DG method,	
	CPT, and FSDT, respectively. The red dashed line represent mobility	
	obtained by FEM	102
4 17	L-shaped plate mobilities at position R3. The red, black, and blue	102
1111	solid lines represent the mobility obtained by the nodal DG method,	
	CPT, and FSDT, respectively. The red dashed line represent mobility	
	obtained by FEM	103
5.1	The case of the T-shaped structure in which a different boundary con-	
	dition (fixed or free) is applied to the black coloured area. The red	
- 0	and blue dots indicate the excitation and receiver locations, respectively.	
5.2	The scaled LWF structure, all dimensions are in cm	113
5.3	Top view of the scaled LWF structure. The red dots represent the im-	
	pact source position and the blue dots represent the receiver positions of (a) the centre excitation configuration and (b) the corner excitation	
	configuration	11/
5.4	Experimental setup of the T-shaped structure for different configura-	114
0.1	tions. (a) The fixed BCs configuration, (b) The free BCs configuration.	118
5.5	Experimental setup for the scaled LWF structure. The structure was	
	elevated to have the free BCs	118
5.6	The mobilities at R2 position of the fixed BC configuration for different	
	element numbers	119
5.7	Mobilities of the T-shaped structure with the fixed BCs configuration	
	obtained by the nodal DG method and the experiment at the positions:	
	(a) R1, (b) R2, (c) R3, and (d) R4. (Thin lines represent nodal DG	
	results and thick lines represent experimental results)	121
5.8	Second mode shape of the T-shaped structure with fixed BCs configu-	
	ration obtained by (a) experiment (89 Hz) and (b) nodal DG method	100
<b>F</b> 0	(87 Hz)	122
5.9	Fourth mode shape of the T-shaped structure with fixed BCs configuration obtained by (a) experiment (270.4 Hz) and (b) nodal DG	
		122
5 10	The mobilities at R1 position of the free BC configuration for different	144
5.10	element numbers	123

5.11	tained by the nodal DG method and the experiment at the positions: (a) R1, (b) R2, (c) R3, and (d) R4. (Thin lines represent nodal DG	
5 19	results and thick lines represent experimental results) Second mode shape of the T-shaped structure with free BCs configura-	124
0.12	tion obtained by (a) experiment (199.7 Hz) and (b) nodal DG method (188 Hz).	125
5.13	Fourth mode shape of the T-shaped structure with free BCs configura- tion obtained by (a) experiment (406.6 Hz) and (b) nodal DG method	120
	(387 Hz)	125
5.14	Numerical solutions of the scaled LWF at position C1 for different element numbers with center excitation	126
5.15	Mobility of scaled LWF structure for the Centre excitation configuration at position (a) C1, (b) C2, (c) C3, and (d) C4. (Thin lines represent nodal DG results and thick lines represent experimental results)	127
5.16	Mobility of the scaled LWF structure at the receiver positions H1-H13 obtained with (a) the nodal DG method, and (b) the experiment	
5.17	Mobility of the scaled LWF structure based on the receiver position $V1-V6$ obtained with the (a) nodal DG method, and (b) experiment	130
5.18	Mobility of scaled LWF structure for the Corner excitation configura- tion at position V6. (Thin lines represent nodal DG results and thick lines represent experimental results)	
6.1	The jump conditions on the interface between solid and air	143
6.2	(a) The impact sound radiation case with the force and receiver positions, and (b) its mesh for the DG method computation	
6.3	(a) The sound transmission through a single concrete panel case, and (b) its mesh for the DG method computation	146
6.4	Sound transmission in rooms with flanking contribution, for case (a) via ceiling and (b) via ceiling and floor.	148
6.5	The normalised sound pressure for the impact sound radiation case at position (a) R1, (b) R2, and (c) R3. Black lines represent the nodal DG results, red dashed lines represent the modal expansion results, and the black dashed vertical lines represent the locations of the slab's	
6.6	natural frequencies based on FSDT	149
	by the FEM	151
6.7	One-third octave band sound pressure level difference between position (a) S1 and R1, (b) S2 and R2, and (c) S3 and R3. Black bars refer to the single panel with only direct transmission path, red bars refer to the panel with flanking transmission via the ceiling, and blue bars refer to the panel with flanking transmission via ceiling and floor	152

B.1	The geometry of the validation case with source (S) and receivers (R1
	& R2) positions. The arrows show the wind vectors at $x = 0$ 189
B.2	Normal-incidence sound absorption coefficients for the T3 configuration. 192
B.3	Comparison of the sound pressure level relative to the free-field at R1 and R2 between the nodal DG and the FEM solutions for (a) T1 Configuration, (b) T2 Configuration, (c) T3 Configuration, and (d) T4
	Configuration
C.1	Absorption coefficient for normal incidence of grass
C.2	Absorption coefficients for normal incidence of the tuned absorbers used in cases 'a' of the intervention area
C.3	Absorption coefficients for normal incidence of the tuned absorbers used in cases 'b' of the intervention area
E.1	Experiment setup for the extraction of Young's modulus of Joist 1 201
E.2	The positions of the accelerometers (blue dots) and impact source position (red dot) on Joist 1
E.3	The experimental results of the Joist 1. (a) Mobility at location $x = 1$ cm, (b) mode shape of frequency 109 Hz, (c) mode shape of frequency
	296 Hz, and (d) mode shape of frequency 556 Hz
F.1	Comparison between nodal DG method and FEM solutions at receiver
	R2 for the fixed BCs at surfaces $y = 0$ m

### List of Tables

$\frac{2.1}{2.2}$	$C_{CFL}$ number and time step $\Delta t$ for single reflection case ( $n$ =0.3 ii). Courant number $C_{CFL}$ and time step $\Delta t_{DG}$ for a rigid cuboid room	31
	(h=0.4  m)	40
3.1	Simulation configurations and reflection coefficients of the materials in	54
3.2	each case.	55 55
	Source and receiver positions for cases 0, 1a and 2a.	
3.3	Source and receiver positions for cases 'b' and case 0	56
3.4	The $k - \epsilon$ turbulence model constants	56
3.5	Main parameters used in the nodal DG simulation for noise intervention case	59
4.1	Numerical settings of the nodal DG method for the computation of	
	the rectangular plate configuration	86
4.2	Natural frequencies of the rectangular plate with thickness of $h=0.12$	
	m and S-S-S BCs for the frequency up to 1 kHz	92
4.3	Natural frequencies of the rectangular plate with thickness of $h = 0.08$	
	m and S-S-S BCs for the frequency up to 1 kHz	93
4.4	Natural frequencies of the rectangular plate with thickness of $h = 0.04$	
	m and S-S-S BCs for the frequency up to 1 kHz	93
4.5	Natural frequencies of the rectangular plate with thickness of $h = 0.12$	
	m and S-S-S-C BCs for the frequency up to 1 kHz	95
4.6	Natural frequencies of the rectangular plate with thickness of $h = 0.08$	
	m and S-S-S-C BCs for the frequency up to 1 kHz	96
4.7	Natural frequencies of the rectangular plate with thickness of $h = 0.04$	
	m and S-S-S-C BCs for the frequency up to 1 kHz	96
4.8	Natural frequencies of the rectangular plate with thickness of $h = 0.12$	
	m and S-S-S-F BCs for the frequency up to 1 kHz	98
4.9	Natural frequencies of the rectangular plate with thickness of $h = 0.08$	
	m and S-S-S-F BCs for the frequency up to 1 kHz	99
4.10	1 0 1	
	m and S-S-S-F BCs for the frequency up to 1 kHz	99

List of Tables 183

5.1	The mechanical properties of the constituting components of the T-	
	shaped structure	112
5.2	Mechanical properties of the individual components of the scaled LWF	
	structure.	113
5.3	The excitation and receiver positions of the centre excitation configu-	
٠.	ration on the scaled LWF case	114
5.4	Coordinates of the excitation and receiver positions for the corner exci-	
	tation configuration of the scaled LWF. All points are located between	
	joists 1 and 2	115
5.5	Coordinates of the receiver positions for the corner excitation configu-	
	ration on the scaled LWF. The receivers are located along the transver-	115
T C	sal direction of the joists.	115
5.6	Elements and time discretization used in the nodal DG simulation for	116
5.7	the T-shaped structure case	110
5.7	the scaled LWF case	117
5.8	Natural frequencies at the T-shaped structure obtained from the nodal	111
5.6	DG method and the experiment at position R2	120
5.9	Natural frequencies at the T-shaped structure obtained from the nodal	120
5.9	DG method and the experiment at position R1	123
5.10	Natural frequencies at the scaled LWF structure obtained from the	123
5.10	nodal DG method and experiment at position C1	126
5 11	List of natural frequencies of the scaled LWF structure based on the	120
0.11	corner excitation obtained by the nodal DG method and experiment	
	at position V6. The mode index in the x- and y- directions is defined	
	by the number of anti-nodes found at each resonant frequency	131
	,	
6.1	Locations of the source and receivers for the single panel transmission	
	case	148
6.2	Natural frequencies of the concrete slab obtained from FSDT. The	
	$m_1, m_2$ indicates the number of the anti-node in the x-, and y- direc-	
	tions. (see Appendix H)	150
6.3	Number of room modes with rigid BCs for each $1/3$ octave band	150
6.4	Number of the acoustic modes of the source and receiver rooms with	
	all room surfaces are assumed rigid	153
D 1	Main and the second in the sec	101
B.1	Main parameters used in the nodal DG simulation for validation case.	191
B.2	Parameters of the reflection coefficient functions representing the grass	191
B.3	impedance in T2 configuration	191
ம.ஏ	sorber in T3 configuration	192
	sorber in 10 comiguration	134
C.1	Parameters of the four-parameter model for the grassland surface	
	impedance	194

184 List of Tables

C.2	C.2 Coefficients of the rational reflection functions representing the resonant absorber rooftops in cases a (10 buildings) and cases b (14 build-	
	ings)	197
E.1	The list of eigenfrequency for Joist 1 obtained by FEM	203
E.2	The absolute difference of the natural frequency obtained by FEM compared to the experimental results for Joist 1.	203

#### Appendices

The following appendices are included in the next pages:

## A. Derivations of the total discrete acoustic energy of the semi-discrete system

In this appendix, it is proven that the total discrete acoustic energy is governed by Equation (2.22) as presented in Chapter 2.

#### B. Validation case for outdoor sound propagation applications

This appendix provides the validation of the nodal DG methodology with effective sound speed approach as employed in Chapter 3.

#### C. Impedance of ground surface and resonator absorber rooftops

In this appendix, the impedance of the ground surface and the resonator absorber rooftops as applied in Chapter 3 are presented.

#### D. Upwind numerical flux for linear elasticity equations

This appendix presents the upwind numerical flux that is employed by the nodal DG method to solve the linear elasticity equations in Chapters 4, 5, and 6.

#### E. Mechanical properties extraction of the wooden structure

This appendix presents the extraction of the mechanical properties of the wooden structures studied in Chapter 5.

#### F. Additional result on the T-shaped structure

This section provides an additional result of the T-shaped structure to support the findings in Chapter 5.

#### G. Upwind numerical flux for linear acoustic equations

This appendix presents the upwind numerical flux that is employed by nodal DG method to solve the linear acoustic equations in Chapter 6 for the vibroacoustic applications.

#### H. Solution of impact sound radiation case

This appendix presents the impact sound radiation solution based on the modal expansion method as employed in Chapter 6.

# $f{A}$ | Derivations of the total discrete acoustic energy of the semi-discrete system

In this appendix, it is proven that the total discrete acoustic energy is governed by Equation (2.22) as presented in Chapter 2. It can be seen that the local energy can be recovered from the product of the element mass matrix  $M^k$  and the nodal vectors  $u_h^k$  as follows:

$$(\boldsymbol{u}_h^k)^T \boldsymbol{M}^k \boldsymbol{u}_h^k = \int_{D^k} \sum_{i=1}^{N_p} u_h^k(\boldsymbol{x}_i^k, t) l_i^k(\boldsymbol{x}) \sum_{j=1}^{N_p} u_h^k(\boldsymbol{x}_j^k, t) l_j^k(\boldsymbol{x}) d\boldsymbol{x} = \|u_h^k\|_{D^k}^2.$$
(A.1)

Furthermore, it can be verified that:

$$(\boldsymbol{u}_{h}^{k})^{T}\boldsymbol{S}_{x}^{k}\boldsymbol{p}_{h}^{k} = \int_{D^{k}} \sum_{i=1}^{N_{p}} p_{h}^{k}(\boldsymbol{x}_{i}^{k}, t) l_{i}^{k}(\boldsymbol{x}) \sum_{j=1}^{N_{p}} u_{h}^{k}(\boldsymbol{x}_{j}^{k}, t) \frac{\partial l_{j}^{k}(\boldsymbol{x})}{\partial x} d\boldsymbol{x}$$

$$= \int_{D^{k}} p_{h}^{k}(\boldsymbol{x}, t) \frac{\partial u_{h}^{k}(\boldsymbol{x}, t)}{\partial x} d\boldsymbol{x} = \left(p_{h}^{k}, \frac{\partial u_{h}^{k}}{\partial x}\right)_{D^{k}}, \tag{A.2}$$

and

$$(\boldsymbol{u}_{h}^{k})^{T}\boldsymbol{M}^{kr}\boldsymbol{p}_{h}^{kr} = \int_{\partial D^{kr}} \sum_{i=1}^{N_{p}} u_{h}^{k}(\boldsymbol{x}_{i}^{k}, t) l_{i}^{k}(\boldsymbol{x}) \sum_{j=1}^{N_{fp}} p_{h}^{kr}(\boldsymbol{x}_{j}^{kr}, t) l_{j}^{kr}(\boldsymbol{x}) d\boldsymbol{x}$$

$$= \int_{\partial D^{kr}} \sum_{i=1}^{N_{fp}} u_{h}^{kr}(\boldsymbol{x}_{i}^{kr}, t) l_{i}^{k}(\boldsymbol{x}) \sum_{j=1}^{N_{fp}} p_{h}^{kr}(\boldsymbol{x}_{j}^{kr}, t) l_{j}^{kr}(\boldsymbol{x}) d\boldsymbol{x}$$

$$= \int_{\partial D^{kr}} u_{h}^{kr}(\boldsymbol{x}, t) p_{h}^{kr}(\boldsymbol{x}, t) d\boldsymbol{x} = (u_{h}^{kr}, p_{h}^{kr})_{\partial D^{kr}}. \tag{A.3}$$

Now, the total discrete acoustic energy  $E_h$  of the semi-discrete formulation Equation (2.13) can be calculated. By pre-multiplying Equation (2.13a) with  $\rho_0(\boldsymbol{u}_h^k)^T$ , pre-multiplying Equation (2.13b) with  $\rho_0(\boldsymbol{v}_h^k)^T$ , pre-multiplying Equation (2.13c) with

 $\rho_0(\boldsymbol{w}_h^k)^T$ , pre-multiplying Equation (2.13d) with  $\frac{1}{\rho_0 c_0^2}(\boldsymbol{p}_h^k)^T$  and sum them together, using the relations mentioned in Equations (A.1, A.2), yields:

$$\frac{d}{dt}E_{h}^{k} = 
-\sum_{r=1}^{f} \left( n_{x}^{kr} (u_{h}^{kr}, p_{h}^{kr})_{\partial D^{kr}} + n_{y}^{kr} (v_{h}^{kr}, p_{h}^{kr})_{\partial D^{kr}} + n_{z}^{kr} (w_{h}^{kr}, p_{h}^{kr})_{\partial D^{kr}} \right) \dots 
+ \rho_{0} (\boldsymbol{u}_{h}^{k})^{T} \sum_{r=1}^{f} M^{kr} \hat{\boldsymbol{F}}_{u}^{kr} + \rho_{0} (\boldsymbol{v}_{h}^{k})^{T} \sum_{r=1}^{f} M^{kr} \hat{\boldsymbol{F}}_{v}^{kr} + \rho_{0} (\boldsymbol{w}_{h}^{k})^{T} \sum_{r=1}^{f} M^{kr} \hat{\boldsymbol{F}}_{w}^{kr} 
+ \frac{1}{\rho_{0} c_{0}^{2}} (\boldsymbol{p}_{h}^{k})^{T} \sum_{r=1}^{f} M^{kr} \hat{\boldsymbol{F}}_{p}^{kr},$$
(A.4)

where the divergence theorem is used to obtain the surface integral term, that is:

$$(u_h^k, \frac{\partial p_h^k}{\partial x})_{D^k} + (v_h^k, \frac{\partial p_h^k}{\partial y})_{D^k} + (w_h^k, \frac{\partial p_h^k}{\partial z})_{D^k}$$

$$+ (p_h^k, \frac{\partial u_h^k}{\partial x})_{D^k} + (p_h^k, \frac{\partial v_h^k}{\partial y})_{D^k} + (p_h^k, \frac{\partial w_h^k}{\partial z})_{D^k}$$

$$= \sum_{r=1}^f \left( n_x^{kr} (u_h^{kr}, p_h^{kr})_{\partial D^{kr}} + n_y^{kr} (v_h^{kr}, p_h^{kr})_{\partial D^{kr}} + n_z^{kr} (w_h^{kr}, p_h^{kr})_{\partial D^{kr}} \right)$$

$$(A.5)$$

Substitute the numerical flux Equations (2.15) into Equation (A.4) and use Equation (A.3), after some simple algebraic manipulations, the semi-discrete acoustic energy balance on element yields:

$$\frac{d}{dt}E_h^k = \sum_{r=1}^f \mathcal{R}_h^{kr},\tag{A.6}$$

where

$$\mathcal{R}_{h}^{kr} = \left(p_{h}^{kr}, v_{hn}^{kr}\right)_{\partial D^{kr}} - \frac{1}{2} \left(\omega_{o}^{kr}, p_{h}^{kr} + \rho_{0}c_{0}v_{hn}^{kr}\right)_{\partial D^{kr}} + \frac{1}{2} \left(\omega_{i}^{ls}, p_{h}^{kr} - \rho_{0}c_{0}v_{hn}^{kr}\right)_{\partial D^{kr}} \tag{A.7}$$

is the discrete energy flux through the shared surface  $\partial D^{kr}$  or equivalently  $\partial D^{ls}$  between the neighboring elements  $D^k$  and  $D^l$  in the interior of the computation domain.  $\omega_0$  and  $\omega_i$  are the characteristic waves defined in Eq. (2.17). By using the condition that the outward normal vector of neighboring elements are opposite, the final form of energy contribution from the coupling across one shared interface reads

$$\mathcal{R}_{h}^{kr} + \mathcal{R}_{h}^{ls} = -\left(\frac{1}{2\rho_{0}c_{0}}\|[p_{h}^{kr}]\|_{\partial D^{kr}}^{2} + \frac{\rho_{0}c_{0}}{2}\|n_{x}^{kr}[u_{h}^{kr}] + n_{y}^{kr}[v_{h}^{kr}] + n_{z}^{kr}[w_{h}^{kr}]\|_{\partial D^{kr}}^{2}\right), (A.8)$$

which is non-positive. This ends the discussion for the interior elements. Now, for elements that have at least one surface lying on the real-valued impedance boundary, e.g., element  $D^m$  with surface  $\partial D^{mt} \in \partial \Omega_h$ , the numerical flux is calculated using

Eq. (2.18). After some algebraic operations, the energy flux through the reflective boundary surface becomes:

$$\mathcal{R}_{h}^{mt} = -\left(\frac{1 - R^{mt}}{2\rho_{0}c_{0}} \|p_{h}^{mt}\|_{\partial D^{mt}}^{2} + \frac{\rho_{0}c_{0}}{2}(1 + R^{mt}) \|v_{hn}^{mt}\|_{\partial D^{mt}}^{2}\right) \tag{A.9}$$

Finally, by summing the energy flux through all of the faces of the mesh, we get the total acoustic energy of the whole semi-discrete system as in Equation (2.22).

### 

This appendix provides the validation of the nodal DG methodology with the effective sound speed approach that is used in Chapter 3.

#### **B.1** Computational model

The validation case considers a sound propagation problem in a two-dimensional domain to validate the proposed nodal DG model with its impedance BCs. As shown in Figure B.1, a rectangular domain of size 150 m  $\times$  50 m is chosen where the atmospheric condition is present by a horizontal wind velocity with a logarithmic profile U(x,z) as given in Equation (3.1). This profile is invariant in x-direction with the friction velocity  $u^* = 0.888 \,\text{m/s}$ , the aerodynamic roughness length  $z_0 = 0.1 \,\text{m}$ , and the von Kármán constant  $\kappa = 0.41$ . These values are chosen to set the horizontal wind velocity at 10 meters height equals to 10 m/s.

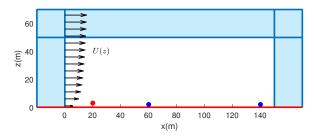


Figure B.1: The geometry of the validation case with source (S) and receivers (R1 & R2) positions. The arrows show the wind vectors at x = 0.

Two receivers are positioned at R1 = (60, 2) m and R2 = (140, 2) m, and the sound source is excited following Equation (3.5) at position S = (20, 3) m. To ensure an unbounded domain except the ground surface at z = 0 m, a perfectly matched layer (PML) is used to attenuate the reflection from z = 50 m, x = 0 m, and x = 150 m. The PML has a thickness of 20 m and denoted by the blue shaded area.

The validation case comprises four configurations representing different impedance BCs at the ground surface: T1, T2, T3, and T4. T1 represents a constant-valued surface impedance, T2 represents an impedance with monotonically increasing absorption in frequency, T3 represents a resonant absorber impedance, and T4 combines all the aforementioned configurations. Descriptions of these configurations are presented in the following subsections. For all validation configurations, the general parameters are summarised in Table B.1.

The validation is conducted by comparing the relative sound pressure levels  $\Delta L(f, \boldsymbol{x})$  at R1 and R2 obtained from the nodal DG simulation with the one obtained from an FEM simulation via the commercial software COMSOL Multiphysics 5.4 [211]. The sound pressure level relative to free-field is defined as:

$$\Delta L(f, \mathbf{x}_i) = L_p(f, \mathbf{x}_i) - L_{p,free}(f, \mathbf{x}_i), \tag{B.1}$$

where  $L_{p,free}$  is the free-field sound pressure level at location  $x_i$ , and f is the frequency. This quantity indicates the sound pressure level deviation from the free-field sound pressure level due to the presence of configuration, e.g. ground surface or screens.

The following settings in COMSOL Multiphysics 5.4 are used to compare the nodal DG solution with the FEM solution. The validation cases are modelled using the pressure acoustics module by solving the acoustic wave equation with the frequency-domain interface. In the model input, the sound speed is spatially defined following the effective sound speed of the validation cases. The ground impedance is defined as:

$$Z(\omega) = Z_0 \frac{(1 + R(\omega))}{(1 - R(\omega))},\tag{B.2}$$

where  $Z_0$  is the characteristic impedance of air. The reflection coefficients are given as the values presented in the following subsections. Moreover, the PML domain is used to attenuate the reflection from non-reflecting surfaces. The sound source is generated by a point monopole with a power equal to 1 watt. The FEM meshes are conditioned to have DPW  $\approx 10$  for each case. The validation case considers the following four cases of impedance boundary conditions.

#### Constant absorption (T1)

T1 configuration has a frequency-independent impedance on the reflecting plane (z = 0). This impedance is modelled with a constant reflection coefficient:

$$R(\omega) = R_{\infty},\tag{B.3}$$

with  $R_{\infty} = 0.8$ .

Parameter	Value
Medium density $\rho_0$ [kg/m <sup>3</sup> ]	1.2
Speed of sound $c_0$ [m/s]	344
Maximum frequency $f_{max}$ [Hz]	282
DG polynomial order $N$	6
Number of discrete mesh elements $K$	30k
Degrees of freedom per wavelength DPW	$\approx 10$
Gaussian source half-bandwidth $b$ [m]	0.5
Sound pressure recording duration $T$ [s]	1
Time step $\Delta t$ [s]	$8.7 \cdot 10^{-5}$

Table B.1: Main parameters used in the nodal DG simulation for validation case.

#### Monotonically increased absorption (T2)

The T2 configuration is chosen to simulate the impedance of a grass field. The reflecting surface of the T2 configuration presents an impedance with an absorption coefficient that is monotonically increasing over frequency. This impedance formulation follows the Attenborough's four parameters model presented in Appendix C.1. Equivalently, the T2 configuration has reflection coefficients that are monotonically reducing in frequency and can be defined as:

$$R(\omega) = \sum_{k=1}^{4} \frac{A_k}{\zeta_k + i\omega},\tag{B.4}$$

where the values of  $A_k$  and  $\zeta_k$  are given in Table B.2. These values are obtained by an optimisation function in MATLAB, where the average reflection coefficient error is less than 2.5% and the maximum error is less than 7.6%.

$\overline{k}$	$A_k$	$\zeta_k$
1	38944.5173103523	39999.8560346985
2	123.242859149582	1556.16553029109
3	-1690.27262893063	17138.6822577285
4	7.01360851666047	227.993345863625

Table B.2: Parameters of the reflection coefficient functions representing the grass impedance in T2 configuration.

#### Resonant absorber system (T3)

T3 configuration represents the impedance of a resonator absorber. This configuration is associated with the tuned absorbers for the rooftop surfaces on the noise mitigation scenarios. In this validation case, the absorption coefficients are tuned to have the absorption peak value of  $\alpha = 0.99$  at 25 Hz as shown in Figure B.2. This

resonant absorber can be modelled by the reflection function as:

$$R(\omega) = R_{\infty} + \frac{B_1 i \omega + C_1 \beta_1 + \alpha_1 B_1}{(\alpha_1 + i \omega)^2 + \beta_1^2},$$
(B.5)

with all the parameters presented in Table B.3.

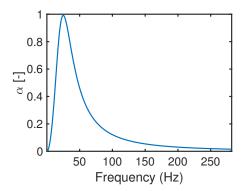


Figure B.2: Normal-incidence sound absorption coefficients for the T3 configuration.

Table B.3: Parameters of the reflection functions representing the resonant absorber in T3 configuration.

Parameter	Value
$R_{\infty}$	1
$B_1$	-200
$C_1$	196.1940185847559
$eta_1$	112.1338976524200
$\alpha_1$	110

#### Complex absorption (T4)

Finally, the T4 configuration combines the above BCs on the reflection plane, where constant absorption (T1) is imposed at x = [0, 50] m, the monotonically increased absorption (T2) for x = [50, 100] m, and the resonant absorber system (T3) at x = [100, 150] m. T4 configuration aims to mimic a real atmospheric sound propagation with various surface impedance boundary conditions.

#### B.2 Validation case result

In Figure B.3, the sound pressure levels relative to the free field under wind conditions are shown. The DG solutions display good agreement with the FEM solutions. There are small deviations between the two solutions, which might due to the different

implementation of the sound source excitation. The initial Gaussian pressure in the nodal DG method might lead to a slight different sound field compared to the point source in the FEM method under wind condition.

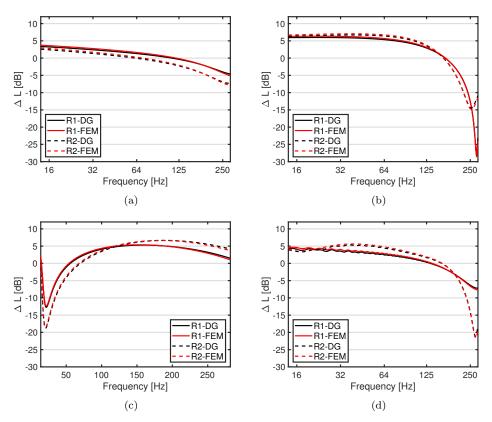


Figure B.3: Comparison of the sound pressure level relative to the free-field at R1 and R2 between the nodal DG and the FEM solutions for (a) T1 Configuration, (b) T2 Configuration, (c) T3 Configuration, and (d) T4 Configuration.

# $C \, | \, { m Impedance \, of \, ground \, surface \, and \, }$ resonator absorber rooftops

In this appendix, the impedance of ground surface and resonator absorber rooftops that employed in Chapter 3 are presented.

#### C.1 Ground surface impedance

In this section, the four-parameter model presented by Attenborough [247] is used to obtain the ground surface impedance as in Equation (C.1), with  $q^2 = \Omega^{-g}$ . The absorption coefficient is shown in Figure C.1 where the flow resistivity value is chosen for a winter condition [195]. The model's parameters are presented in Table C.1.

$$Z_{ground} = \left(\frac{4q^2}{3\Omega} + i\frac{s_f^2\sigma}{\rho\omega}\right)\frac{\omega}{kc},$$

$$k = \frac{\omega}{c}\sqrt{\gamma\Omega}\sqrt{\left(\frac{4}{3} - \frac{\gamma - 1}{\gamma}N_{pr}\right)\frac{q^2}{\Omega} + i\frac{s_f^2\sigma}{\rho\omega}}.$$
(C.1)

Table C.1: Parameters of the four-parameter model for the grassland surface impedance.

Parameter	Value
Flow resistivity $\sigma$ [Pa s m <sup>-2</sup> ]	$400 \cdot 10^3$
Grain shape factor $g$	0.5
Pore shape factor ratio $s_f$	0.75
Porosity $\Omega$	0.3
Prandtl number $N_{pr}$	0.7

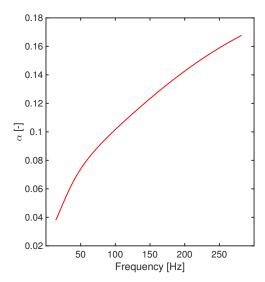


Figure C.1: Absorption coefficient for normal incidence of grass.

#### C.2 Parameters of the resonator absorber rooftops

In this section, the parameters of the resonator absorber rooftops used in the Chapter 3 are given. For cases 'a', 10 absorbers have been tuned at the frequencies of the 1/3 octave bands between 25 and 200 Hz and the absorption coefficients are presented in Figure C.2. For cases 'b', 14 absorbers have been tuned at the frequencies of the 1/3 octave bands between 16 and 315 Hz and the absorption coefficients are presented in Figure C.3. In both cases, legend indicates the building where the tuned absorber has been employed (Building 1 corresponds to the building closest to the sound source). The reflection function of each rooftop follows Equation (B.5) where all the buildings have coefficient of  $R_{\infty} = 1$ ,  $B_1 = -200$ , and  $\alpha_1 = 110$ .

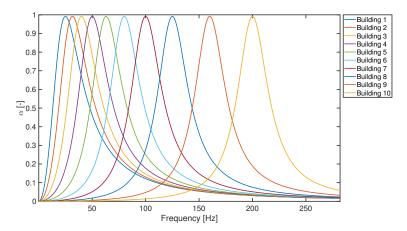


Figure C.2: Absorption coefficients for normal incidence of the tuned absorbers used in cases 'a' of the intervention area.

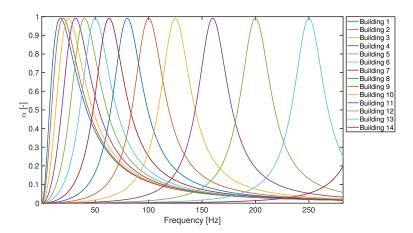


Figure C.3: Absorption coefficients for normal incidence of the tuned absorbers used in cases 'b' of the intervention area.

Table C.2: Coefficients of the rational reflection functions representing the resonant absorber rooftops in cases a (10 buildings) and cases b (14 buildings).

Case a	Case b	$C_1$	$\beta_1$
-	Buil.1	$1.938234687092393 \cdot 10^{3}$	11.350534662550537
-	Buil.2	$3.621004509404095 \cdot 10^{2}$	60.756621381895265
Buil.1	Buil.3	$1.961940185847559 \cdot 10^{2}$	$1.121338976524200 \cdot 10^{2}$
Buil.2	Buil.4	$1.337084399021496 \cdot 10^{2}$	$1.645371078751649 \cdot 10^{2}$
Buil.3	Buil.5	97.355170542539700	$2.259766982831900 \cdot 10^{2}$
Buil.4	Buil.6	74.760750862057500	$2.942720578153719 \cdot 10^{2}$
Buil.5	Buil.7	57.856717862926140	$3.802497067345282 \cdot 10^{2}$
Buil.6	Buil.8	44.854837006366400	$4.904710722029257 \cdot 10^{2}$
Buil.7	Buil.9	35.563330723912940	$6.186147234293526 \cdot 10^{2}$
Buil.8	Buil.10	28.290110483074190	$7.776569134702557 \cdot 10^2$
Buil.9	Buil.11	22.015995029420690	$9.992734814211524 \cdot 10^{2}$
Buil.10	Buil.12	17.574504787510350	$1.251813366350710 \cdot 10^{3}$
-	Buil.13	14.040103250726853	$1.566940043611222 \cdot 10^{3}$
-	Buil.14	11.132790690705793	$1.976144222164052 \cdot 10^{2}$

# 

This appendix presents the upwind numerical flux that is used for solving the linear elasticity equations using the nodal DG method in Chapters 4, 5, and 6. The methodology for deriving this numerical flux is based on the Rankine-Hugoniot jump conditions as given in Refs.[21], [200], [226]. This appendix provides the upwind numerical flux that can be used for the case where the interior and the adjacent media have different mechanical properties, as in Chapters 5, and 6. In Chapter 4, the whole problem domain has similar mechanical properties, which further simplify the current numerical flux. The upwind numerical flux can be written as:

$$egin{aligned} m{n}\cdotm{H}^* &= m{n}\cdotm{H} + \left[ egin{bmatrix} m{P}_{11} & m{P}_{12} & m{P}_{13} \ m{P}_{21} & m{P}_{22} & m{P}_{23} \ m{P}_{31} & m{P}_{32} & m{P}_{33} \end{bmatrix} - egin{bmatrix} m{S}_{11} & m{S}_{12} & m{S}_{13} \ m{S}_{21} & m{S}_{22} & m{S}_{23} \ m{S}_{31} & m{S}_{32} & m{S}_{33} \end{bmatrix} \end{bmatrix} m{q}_s 
brace, \end{aligned}$$

where  $[q_s] = q_{sh}^+ - q_{sh}^-$ . The components of the above matrix are given as follows:

$$m{P}_{11} = rac{-Z_p^+ \, c_p^-}{Z_p^- \left(Z_p^+ + Z_p^-
ight)} \left[ egin{array}{ccc} n_x^2 & n_x n_y & n_x n_z \ n_x n_y & n_y^2 & n_y n_z \ n_x n_z & n_y n_z & n_z^2 \end{array} 
ight],$$

$$\boldsymbol{P}_{21} = \frac{-Z_{p}^{+}}{Z_{p}^{+} + Z_{p}^{-}} \begin{bmatrix} n_{x} \left(\lambda^{-} + 2\mu^{-}n_{x}^{2}\right) & n_{y} \left(\lambda^{-} + 2\mu^{-}n_{x}^{2}\right) & n_{z} \left(\lambda^{-} + 2\mu^{-}n_{x}^{2}\right) \\ n_{x} \left(\lambda^{-} + 2\mu^{-}n_{y}^{2}\right) & n_{y} \left(\lambda^{-} + 2\mu^{-}n_{y}^{2}\right) & n_{z} \left(\lambda^{-} + 2\mu^{-}n_{y}^{2}\right) \\ n_{x} \left(\lambda^{-} + 2\mu^{-}n_{z}^{2}\right) & n_{y} \left(\lambda^{-} + 2\mu^{-}n_{y}^{2}\right) & n_{z} \left(\lambda^{-} + 2\mu^{-}n_{z}^{2}\right) \end{bmatrix},$$

$$\boldsymbol{P}_{31} = \frac{-2\mu^{-}Z_{p}^{+}}{Z_{p}^{+} + Z_{p}^{-}} \left[ \begin{array}{ccc} n_{x}^{2}n_{z} & n_{x}n_{y}n_{z} & n_{z}^{2}n_{x} \\ n_{x}n_{y}n_{z} & n_{y}^{2}n_{z} & n_{z}^{2}n_{y} \\ n_{x}^{2}n_{y} & n_{y}^{2}n_{x} & n_{x}n_{y}n_{z} \end{array} \right],$$

$$m{P}_{12} = rac{-c_p^-}{Z_p^- \left(Z_p^+ + Z_p^-
ight)} \left[ egin{array}{ccc} n_x^3 & n_y^2 n_x & n_z^2 n_x \ n_x^2 n_y & n_y^3 & n_z^2 n_y \ n_x^2 n_z & n_y^2 n_z & n_z^3 \end{array} 
ight],$$

$$\boldsymbol{P}_{22} = \frac{-1}{Z_p^+ + Z_p^-} \left[ \begin{array}{ccc} n_x^2 \left( \lambda^- + 2\mu^- n_x^2 \right) & n_y^2 \left( \lambda^- + 2\mu^- n_x^2 \right) & n_z^2 \left( \lambda^- + 2\mu^- n_x^2 \right) \\ n_x^2 \left( \lambda^- + 2\mu^- n_y^2 \right) & n_y^2 \left( \lambda^- + 2\mu^- n_y^2 \right) & n_z^2 \left( \lambda^- + 2\mu^- n_y^2 \right) \\ n_x^2 \left( \lambda^- + 2\mu^- n_z^2 \right) & n_y^2 \left( \lambda^- + 2\mu^- n_y^2 \right) & n_z^2 \left( \lambda^- + 2\mu^- n_z^2 \right) \end{array} \right],$$

$$\boldsymbol{P}_{32} = \frac{-2\mu^{-}}{Z_{p}^{+} + Z_{p}^{-}} \left[ \begin{array}{ccc} n_{x}^{3}n_{z} & n_{y}^{2}n_{x}n_{z} & n_{z}^{3}n_{x} \\ n_{x}^{2}n_{y}n_{z} & n_{y}^{3}n_{z} & n_{z}^{3}n_{y} \\ n_{x}^{3}n_{z} & n_{y}^{3}n_{x} & n_{z}^{2}n_{x}n_{y} \end{array} \right],$$

$$\boldsymbol{P}_{13} = \frac{-2c_p^-}{Z_p^- \left(Z_p^+ + Z_p^-\right)} \left[ \begin{array}{ccc} n_x^2 n_z & n_x n_y n_z & n_z^2 n_x \\ n_x n_y n_z & n_y^2 n_z & n_y^2 n_x \\ n_z^2 n_x & n_z^2 n_y & n_x n_y n_z \end{array} \right],$$

$$\boldsymbol{P}_{23} = \frac{-2}{Z_p^+ + Z_p^-} \left[ \begin{array}{ccc} n_x n_z \left( \lambda^- + 2 \mu^- n_x^2 \right) & n_y n_z \left( \lambda^- + 2 \mu^- n_x^2 \right) & n_x n_y \left( \lambda^- + 2 \mu^- n_x^2 \right) \\ n_y n_z \left( \lambda^- + 2 \mu^- n_y^2 \right) & n_x n_y \left( \lambda^- + 2 \mu^- n_y^2 \right) & n_x n_z \left( \lambda^- + 2 \mu^- n_y^2 \right) \\ n_x n_z \left( \lambda^- + 2 \mu^- n_z^2 \right) & n_y n_z \left( \lambda^- + 2 \mu^- n_y^2 \right) & n_x n_y \left( \lambda^- + 2 \mu^- n_z^2 \right) \end{array} \right],$$

$$\boldsymbol{P}_{33} = \frac{-4\mu^{-}}{Z_{p}^{+} + Z_{p}^{-}} \left[ \begin{array}{ccc} n_{x}^{2}n_{z}^{2} & n_{z}^{2}n_{x}n_{y} & n_{x}^{2}n_{y}n_{z} \\ n_{z}^{2}n_{x}n_{y} & n_{y}^{2}n_{z}^{2} & n_{y}^{2}n_{x}n_{z} \\ n_{x}^{2}n_{y}n_{z} & n_{y}^{2}n_{x}n_{z} & n_{x}^{2}n_{y}^{2} \end{array} \right],$$

$$m{S}_{11} = rac{-Z_s^+ c_s^-}{Z_s^+ + Z_s^-} \left[ egin{array}{ccc} n_x^2 - 1 & n_x n_y & n_x n_z \\ n_x n_y & n_y^2 - 1 & n_y n_z \\ n_x n_z & n_y n_z & n_z^2 - 1 \end{array} 
ight],$$

$$m{S}_{21} = rac{-2Z_s^+\mu^-}{Z_s^+ + Z_s^-} \left[ egin{array}{ccc} n_x \left(n_x^2 - 1
ight) & n_x^2 n_y & n_x^2 n_z \ n_y^2 n_x & n_y \left(n_y^2 - 1
ight) & n_y^2 n_z \ n_z^2 n_x & n_z^2 n_y & n_z \left(n_z^2 - 1
ight) \end{array} 
ight],$$

$$\boldsymbol{S}_{31} = \frac{-Z_{s}^{-}\mu^{-}}{Z_{s}^{+} + Z_{s}^{-}} \left[ \begin{array}{ccc} n_{z}\left(2n_{x}^{2} - 1\right) & 2n_{x}n_{y}n_{z} & n_{x}\left(2n_{z}^{2} - 1\right) \\ 2n_{x}n_{y}n_{z} & n_{z}\left(2n_{y}^{2} - 1\right) & n_{y}\left(2n_{z}^{2} - 1\right) \\ -n\left(2n_{x}^{2} - 1\right) & n_{x}\left(2n_{y}^{2} - 1\right) & 2n_{x}n_{y}n_{z} \end{array} \right],$$

$$m{S}_{12} = rac{-c_s^-}{Z_s^+ + Z_s^-} \left[ egin{array}{ccc} n_x \left( n_x^2 - 1 
ight) & n_y^2 n_x & n_z^2 n_x \ n_x^2 n_y & n_y \left( n_y^2 - 1 
ight) & n_z^2 n_y \ n_x^2 n_z & n_y^2 n_z & n_z \left( n_z^2 - 1 
ight) \end{array} 
ight],$$

$$oldsymbol{S}_{22} = rac{-2 \mu^-}{Z_s^+ + Z_s^-} \left[ egin{array}{ccc} n_x^2 \left(n_x^2 - 1
ight) & n_x^2 n_y^2 & n_x^2 n_z^2 \ n_x^2 n_y^2 & n_y^2 \left(n_y^2 - 1
ight) & n_y^2 n_z^2 \ n_x^2 n_z^2 & n_y^2 n_z^2 & n_z^2 \left(n_z^2 - 1
ight) \end{array} 
ight],$$

$$S_{32} = \frac{-\mu^{-}}{Z_{s}^{+} + Z_{s}^{-}} \left[ \begin{array}{ccc} n_{x}n_{z} \left(2n_{x}^{2} - 1\right) & 2n_{y}^{2}n_{x}n_{z} & n_{x}n_{z} \left(2n_{z}^{2} - 1\right) \\ 2n_{x}^{2}n_{y}n_{z} & n_{y}n_{z} \left(2n_{y}^{2} - 1\right) & n_{y}n_{z} \left(2n_{z}^{2} - 1\right) \\ n_{x}n_{y} \left(2n_{x}^{2} - 1\right) & n_{x}n_{y} \left(2n_{y}^{2} - 1\right) & 2n_{z}^{2}n_{x}n_{y} \end{array} \right],$$

$$\boldsymbol{S}_{13} = \frac{-c_s^{-}}{Z_s^{+} + Z_s^{-}} \left[ \begin{array}{ccc} n_z \left(2n_x^2 - 1\right) & 2n_x n_y n_z & n_y \left(2n_x^2 - 1\right) \\ 2n_x^2 n_y n_z & n_z \left(2n_y^2 - 1\right) & n_x \left(2n_y^2 - 1\right) \\ n_x \left(2n_z^2 - 1\right) & n_y \left(2n_z^2 - 1\right) & 2n_x n_z n_y \end{array} \right],$$

$$S_{23} = \frac{-2\mu^{-}}{Z_{s}^{+} + Z_{s}^{-}} \begin{bmatrix} n_{x}n_{z} \left(2n_{x}^{2} - 1\right) & 2n_{x}^{2}n_{y}n_{z} & n_{x}n_{y} \left(2n_{x}^{2} - 1\right) \\ 2n_{y}^{2}n_{x}n_{z} & n_{y}n_{z} \left(2n_{y}^{2} - 1\right) & n_{x}n_{y} \left(2n_{y}^{2} - 1\right) \\ n_{x}n_{z} \left(2n_{z}^{2} - 1\right) & n_{y}n_{z} \left(2n_{z}^{2} - 1\right) & 2n_{z}^{2}n_{x}n_{y} \end{bmatrix},$$

$$S_{33} = \frac{-\mu^{-}}{Z_{s}^{+} + Z_{s}^{-}} \begin{bmatrix} 4n_{x}^{2}n_{z}^{2} + n_{y}^{2} - 1 & n_{x}n_{z} \left(4n_{y}^{2} - 1\right) & n_{y}n_{z} \left(4n_{x}^{2} - 1\right) \\ n_{x}n_{y} \left(4n_{z}^{2} - 1\right) & 4n_{y}^{2}n_{z}^{2} + n_{x}^{2} - 1 & n_{x}n_{z} \left(4n_{y}^{2} - 1\right) \\ n_{y}n_{z} \left(4n_{x}^{2} - 1\right) & n_{x}n_{y} \left(4n_{z}^{2} - 1\right) & 4n_{x}^{2}n_{y}^{2} + n_{z}^{2} - 1 \end{bmatrix}.$$

Note that the P components represent the longitudinal wave contributions and the S components represent the shear wave contributions. There are two characteristic impedances. The first is the longitudinal wave impedance,  $Z_p = \rho c_p$ , and the second is the shear wave impedance,  $Z_s = \rho c_s$ .

# $E \, | \, { m Mechanical \; properties \; extraction \; of \; the \ \, wooden \; structure }$

This appendix presents the extraction of the mechanical properties of the structures used in Chapter 5. Prior to the numerical study, it is necessary to determine the mechanical properties of each component assembled into the T-shaped and the scaled LWF structures. Four independent mechanical properties, i.e., Young's modulus, Poisson's ratio, viscous damping, and density, should be available. For all components, Poisson's ratio is assumed to be 0.3 following Refs. [228], [248]. The density is calculated by dividing the component's mass by its volume. The viscous damping is chosen by trials to match the mobility magnitude of the nodal DG and the experimental results. For each structure, this value is a constant and given in Section 5.3. The constant viscous damping values is a limitation of the current work. More details on the solid viscoelastic model can be referred to [246].

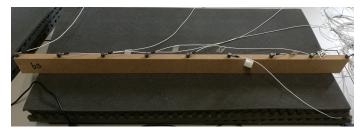


Figure E.1: Experiment setup for the extraction of Young's modulus of Joist 1.

The Young's modulus of each component is determined by extracting its natural frequencies and vibration mode shapes from the experiments. The experimental results are then compared to those obtained numerically using FEM with COMSOL Multiphysics for various elastic modulus values. In the COMSOL Multiphysics, each component is modelled using solid mechanics solver with a three-dimensional geometry. All components have free BCs as in the experiments. The eigenfrequency analysis is used to obtain the natural frequencies and the mode shapes. In the FEM simulation, the analysis is performed with the assumption that there is no damping mechanism in the structure. The density and Poisson's ratio are set as the values

mentioned above. The Young's modulus is then varied with a resolution of 0.01 GPa to obtain the minimum difference in natural frequencies from the experiments. An example of this approach for Joist 1 of the scaled LWF structure is as follows.

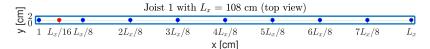


Figure E.2: The positions of the accelerometers (blue dots) and impact source position (red dot) on Joist 1.

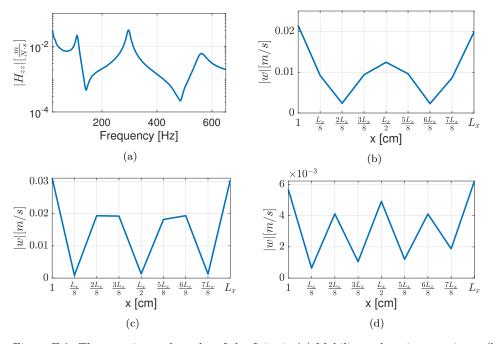


Figure E.3: The experimental results of the Joist 1. (a) Mobility at location x = 1 cm, (b) mode shape of frequency 109 Hz, (c) mode shape of frequency 296 Hz, and (d) mode shape of frequency 556 Hz.

Joist 1 was placed on a soft foam as shown in Figure E.1 to mimic free BCs. Nine accelerometers were distributed evenly along the joist axial direction (blue dots) to retrieve the mobility and the mode shapes (see Figure E.2). The impact excitation was given at the red dot position and was conducted three times to obtain the average mobility results. The average mobility curve of the joist at position x=1 cm is given in Figure E.3a. Three natural frequencies were obtained from this curve, i.e., 109 Hz, 296 Hz, and 556 Hz. The mode shapes of these natural frequencies are shown in Figures E.3b-E.3d. Afterwards, the eigenfrequencies with similar mode shapes

that obtained from the FEM simulations are listed in Table E.1. Their absolute differences ( $|\Delta f_n|$ ) were calculated and displayed in the Table E.2. The minimum differences over three natural frequencies were found for the Young's modulus equals to 1.89 GPa. In this case, the Young's modulus for Joist 1 was set as 1.89 GPa. This approach was conducted for all components of the structures.

		, 1				J			
Mode number	Natural frequency [Hz]								
	Young's modulus [GPa]								
	1.87	1.88	1.89	1.90	1.91	1.92			
1	108.9	109.2	109.4	109.7	110.0	110.3			
2	292.4	293.1	293.9	294.7	295.5	296.2			
3	553.3	554.7	556.2	557.7	559.2	560.6			

Table E.1: The list of eigenfrequency for Joist 1 obtained by FEM.

Table E.2: The absolute difference of the natural frequency obtained by FEM compared to the experimental results for Joist 1.

	$ \Delta f_n $ [Hz]								
Mode number	Young's modulus [GPa]								
	1.87	1.88	1.89	1.90	1.91	1.92			
1	0.1	0.2	0.4	0.7	1.0	1.3			
2	3.6	2.9	2.1	1.3	0.5	0.2			
3	2.7	1.3	0.2	1.7	3.1	4.6			

# $\mathbf{F} \mid \mathbf{A} \mathbf{d} \mathbf{d} \mathbf{i} \mathbf{t} \mathbf{i} \mathbf{o} \mathbf{n} \mathbf{t} \mathbf{h} \mathbf{e} \mathbf{T} \mathbf{-s} \mathbf{h} \mathbf{a} \mathbf{p} \mathbf{e} \mathbf{d} \mathbf{s} \mathbf{t} \mathbf{r} \mathbf{c} \mathbf{t} \mathbf{u} \mathbf{r} \mathbf{e}$

This section provides an additional result of the T-shaped structure in which all surfaces at y=0 m have fixed BCs as presented in Chapter 5. The nodal DG method solution is compared to the FEM solution at receiver R2 (refer to Section 5.6.1). Both methods use a similar number of elements as described in Section 5.4. Figure F.1 shows that the difference between the DG and FEM solutions at the highest natural frequency is at most 1 Hz, which is a closer agreement than for the BCs of Section 5.6.1. This confirms previous observations that the BCs discontinuity at y=0 m is the cause of the larger natural frequency difference between nodal DG and FEM solutions.

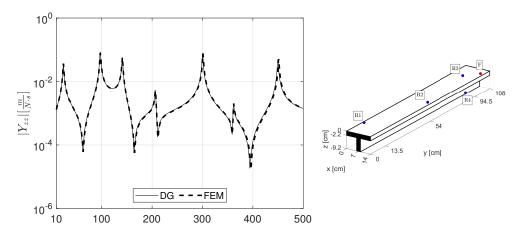


Figure F.1: Comparison between nodal DG method and FEM solutions at receiver R2 for the fixed BCs at surfaces y=0 m.

# $\begin{array}{c|c} G & \text{Upwind numerical flux for linear} \\ \text{acoustic equations} \end{array}$

In this appendix, the upwind numerical flux for acoustic wave propagation  $(n \cdot F^*)$  is presented. The methodology for obtaining this flux is based on the Rankine-Hugoniot jump condition, as shown in Chapter 4. More details on the derivation of this fluxes can be found in Ref.[21]. This numerical flux differs from the one obtained in Chapter 2 as it considers the media discontinuity, which is required to solve the vibroacoustic problems in Chapter 6. The upwind numerical flux can be written as:

where  $[q_a]=q_{ah}^--q_{ah}^+$  is the jump between interior and exterior acoustic variables. The interior bulk modulus is  $K_0^-=\rho_0^-(c_0^-)^2$ . The internal and external impedance are  $Z^-=\rho_0^-c_0^-$  and  $Z^+=\rho_0^+c_0^+$ , respectively.

# ${ m H}\,|\,{ m Impact}\,\,{ m sound}\,\,{ m radiation}\,\,{ m solution}$

In this appendix, the solution of the impact sound radiation based on modal expansion method is presented. This solution is used for calculating the impact sound radiation of a concrete slab in Chapter 6.

The modal expansion method is widely used to solve the coupling problem between sound in a cuboid cavity and a panel vibration. There are two approaches that are commonly used: the first approach uses modal functions to expand the velocity potential that satisfies the velocity continuity and pressure over the panel surface [60], [249]; the second technique uses the rigid-walled acoustic modes as the basis functions to expand the velocity potential [235]–[237].

The issue of the second approach is the velocity continuity over the panel that is not mathematically satisfied due to the use of the rigid-walled acoustic modes. However, the second approach is computationally more convenient. Hu et al. [250] have shown that both techniques were converged to the same solution as long as a sufficient number of modes were used in the second approach. In this appendix, the sound pressure under a slab is calculated based on Refs. [237], [251] following the second technique as a comparison for the nodal DG solution. The slab vibration is modelled by the first shear deformation theory (FSDT).

#### H.1 Sound field

Consider the room in Figure 6.2a as V enclosed by surface A, where  $A = A_R \cap A_C$ . The  $A_R$  and  $A_C$  are the surfaces with rigid walls and the concrete slab, respectively. The sound field in V satisfy the sound wave equation:

$$\begin{split} \nabla^2 \phi &= \frac{1}{c_0^2} \frac{\partial^2 \phi}{\partial t^2}, \\ \frac{\partial \phi}{\partial n} &= 0 \text{ on } A_R, \frac{\partial \phi}{\partial n} = \dot{w}^a \text{ on } A_C, \end{split} \tag{H.1}$$

where  $\phi$  is the velocity potential,  $c_0$  is the sound speed, and  $\dot{w}^a$  is the air particle velocity on  $A_C$ . The sound pressure inside V can be obtained as  $p = -\rho_0 \frac{\partial \phi}{\partial t}$ , with  $\rho_0$  is the air density. Solutions of the Equation (H.1) with only rigid BCs are  $\phi =$ 

 $\Phi_n \exp(i\hat{\omega}_n t)$  with  $n \in [0, 1, ...]$ .  $\Phi_n$  are the room mode functions that satisfy:

$$\nabla^2 \Phi_n = -\left(\frac{\hat{\omega}_n}{c_0}\right)^2 \Phi_n,$$

$$\frac{\partial \Phi_n}{\partial n} = 0,$$

$$\int_V \Phi_r \Phi_n \, dV = \begin{cases} = 0, \text{for, } r \neq n, \\ = \Lambda_n^A, \text{ for } r = n, \end{cases}$$
(H.2)

with  $\hat{\omega}_n$  are the natural angular frequencies of the room with rigid BCs. Having the room mode functions  $\Phi_n$ , Equation (H.1) can be transformed following the second Green's identity as [237]:

$$\int_{V} \frac{\Phi_{n}}{c_{0}^{2}} \left( \ddot{\phi} + \hat{\omega}_{n}^{2} \phi \right) dV = \int_{A_{F}} \Phi_{n} \dot{w}^{a} dS.$$
 (H.3)

To complete the interaction to the slab vibration on surface  $A_F$ , the air particle velocity  $(\dot{w}^a)$  should be equal to the velocity of the slab  $(\dot{w}^s)$  on surface  $A_C$ .

#### H.1.1 Structure vibration

Following the first shear deformation theory (FSDT) [22], the slab displacement  $(w^s)$  in Figure 6.2a follows:

$$I_0 \ddot{w}^s + L(w^s, \varphi^x, \varphi^y) = U - \rho_0 \dot{\phi}, \tag{H.4}$$

where L is a differential operator (see [207]), with  $\varphi^x$  and  $\varphi^y$  are the bending rotations with respect to the x- and y -directions, respectively.  $I_0 = \rho_c h$  with  $\rho_c$  and h are the slab's density and thickness, and U is the excitation force. The homogeneous solutions for Equation (H.4) can be written as  $w^s = \Xi_m \exp(i\omega_m t)$ , for  $m \in [1, 2, ...]$ . The slab mode functions  $\Xi_m$  satisfy:

$$L(\Xi_m, \Upsilon_m^x, \Upsilon_m^y) = I_0 \omega_m^2 \Xi_m, \tag{H.5}$$

with  $\omega_m$  are the angular natural frequencies of the slab.  $\Xi_m, \Upsilon_m^x$ , and  $\Upsilon_m^y$  are the mode functions for the displacement, and the two bending rotations. They are orthogonal functions, and their exact expressions for the simply-supported BCs can be found in Ref. [207].

### H.2 Modal interaction

To have the coupling conditions, the displacement, force excitation, and the velocity potential can be expanded using the slab and room mode functions as:

$$w^s = \sum_{m=1}^{\infty} w_m^s(t) \Xi_m(\boldsymbol{x}_{A_F}), \tag{H.6}$$

$$U = \sum_{m=1}^{\infty} U_m(t) \Xi_m(\boldsymbol{x}_{A_F}), \tag{H.7}$$

$$\phi = \sum_{n=0}^{\infty} \phi_n(t) \Phi_n(\mathbf{x}). \tag{H.8}$$

Afterwards, Equations (H.6) and (H.7) are substituted to Equation (H.4). Equation (H.4) then multiplied with  $\psi_q$  and integrated over the  $A_F$  to obtain:

$$\ddot{w}_m^s + \omega_m^2 w_m^s = \frac{U_m}{I_0} - \frac{\rho_0}{I_0 \Lambda_m^F} \sum_{n=0}^{\infty} L_{mn} \dot{\phi_n}, \tag{H.9}$$

$$\Lambda_m^F = \int_{A_F} \Xi_m^2(\boldsymbol{x}_{A_F}) \, \mathrm{dS}, \tag{H.10}$$

$$L_{mn} = \int_{A_F} \Xi_m(\boldsymbol{x}_{A_F}) \Phi_n(\boldsymbol{x}) \, \mathrm{dS}.$$

Equations (H.6) and (H.8) are substituted to Equation (H.3) to obtain:

$$\ddot{\phi}_n + \omega_n^2 \phi_n = \frac{c_0^2}{\Lambda_n^A} \sum_{m=1}^{\infty} L_{nm} \dot{w}_m^s,$$
 (H.11)

$$\Lambda_n^A = \int_V \Phi_n^2(\boldsymbol{x}) \, dV, \tag{H.12}$$

$$L_{nm} = \int_{A_F} \Phi_n(\boldsymbol{x}) \Xi_m(\boldsymbol{x}_{A_F}) \, dS.$$

 $L_{nm}$  is the coupling coefficient between structure vibration and sound field mode functions, notice that  $L_{mn} = L_{nm}^T$ . The mode functions are:

$$\begin{split} \Xi_m(\boldsymbol{x}_{A_F}) &= \sin\left(\frac{m_1\pi x}{L_x}\right) \sin\left(\frac{m_2\pi y}{L_y}\right), \\ \Phi_n(\boldsymbol{x}) &= \cos\left(\frac{n_1\pi x}{L_x}\right) \cos\left(\frac{n_2\pi y}{L_y}\right) \cos\left(\frac{n_3\pi z}{L_z}\right). \end{split}$$

with  $m_1, m_2 \in [1, 2, ...]$  represent the anti-nodes of the mode functions in x and y-directions of the slab, respectively.  $L_x, L_y, L_z$  are the length, width, and height of the room.  $n_1, n_2, n_3 \in [0, 1, ...]$  represents the number of nodes of mode functions in x, y and z-directions of the room, respectively. The integration in Equations (H.10)

and (H.12) are:

$$\Lambda_m^F = \frac{L_x L_y}{4},$$
 
$$\Lambda_n^A = \begin{cases} L_x L_y L_z & \text{if } n_1 = n_2 = n_3 = 0, \\ \frac{L_x L_y L_z}{2} & \text{if } n_i = n_j = 0, \& n_k > 0, \\ \frac{L_x L_y L_z}{4} & \text{if } n_i = 0, \& n_j, n_k > 0, \\ \frac{L_x L_y L_z}{4} & \text{if } n_i = 0, k = 0, \end{cases}$$

and the coupling coefficient can be obtained as:

$$L_{mp} = \frac{L_x L_y}{4\pi^2} \left[ \frac{1 - (-1)^{(n_1 - m_1)}}{(n_1 - m_1)} - \frac{1 - (-1)^{(n_1 + m_1)}}{(n_1 + m_1)} \right] \times \left[ \frac{1 - (-1)^{(n_2 - m_2)}}{(n_2 - m_2)} - \frac{1 - (-1)^{(n_2 + m_2)}}{(n_2 + m_2)} \right].$$

Remark that in case of  $(n_1 + m_1)$  or  $(n_2 + m_2)$  is even, the  $L_{nm} = 0$ . It means that there is no interaction between the slab and the room. Afterwards, assuming a steady-state condition at angular frequency  $\omega$ , Equations (H.9) and H.11 can be written as:

$$I_0(\omega_m^2 - \omega^2)w_m^s + \frac{i\omega\rho_0}{\Lambda_m^F} \sum_{n=0}^{\infty} L_{mn}\phi_n = U_m$$
(H.13)

$$(\hat{\omega}_n^2 - \omega^2)\phi_n - \frac{i\omega c_0^2}{\Lambda_n^A} \sum_{m=1}^{\infty} L_{nm} w_m^s = 0$$
 (H.14)

These equations, can be written in matrix form as follows:

$$\begin{bmatrix} \begin{array}{c|c} I^S & C^A \\ \hline C^S & I^A \end{array} \end{bmatrix} \begin{bmatrix} \begin{array}{c} W^S \\ \Phi^A \end{array} \end{bmatrix} = \begin{bmatrix} \begin{array}{c} U^S \\ 0 \end{array} \end{bmatrix},$$
 
$$W^S = \begin{bmatrix} w_1^s \\ w_2^s \\ \vdots \\ w_m^s \end{bmatrix}; \Phi^A = \begin{bmatrix} \phi_1 \\ \phi_2 \\ \vdots \\ \phi_n \end{bmatrix}; U^S = \begin{bmatrix} U_1 \\ U_2 \\ \vdots \\ U_p \end{bmatrix},$$
 
$$C^A = i\omega\rho_0 \begin{bmatrix} \frac{L_{11}^T}{\Lambda_1^F} & \frac{L_{12}^T}{\Lambda_2^F} & \cdots & \frac{L_{1n}^T}{\Lambda_1^F} \\ \frac{L_{21}^T}{\Lambda_2^F} & \frac{L_{22}^T}{\Lambda_2^F} & \cdots & \vdots \\ \vdots & \ddots & \ddots & \vdots \\ \frac{L_{m1}^T}{\Lambda_m^F} & \frac{L_{m2}^T}{\Lambda_m^F} & \cdots & \frac{L_{mn}^T}{\Lambda_m^F} \end{bmatrix},$$

$$\boldsymbol{C^{S}} = -i\omega c_{0}^{2} \begin{bmatrix} \frac{L_{11}}{\Lambda_{1}^{A}} & \frac{L_{12}}{\Lambda_{1}^{A}} & \cdots & \frac{L_{1m}}{\Lambda_{1}^{A}} \\ \frac{L_{21}}{\Lambda_{2}^{A}} & \frac{L_{22}}{\Lambda_{2}^{A}} & \ddots & \vdots \\ \frac{L_{n1}}{\Lambda_{n}^{A}} & \frac{L_{n2}}{\Lambda_{n}^{A}} & \cdots & \frac{L_{nm}}{\Lambda_{n}^{A}} \end{bmatrix},$$

$$\boldsymbol{I^{S}} = I_{0} \begin{bmatrix} (\omega_{1}^{2} - \omega^{2}) & 0 & \cdots & 0 \\ 0 & (\omega_{2}^{2} - \omega^{2}) & \ddots & \vdots \\ \vdots & \ddots & \ddots & 0 \\ 0 & \cdots & 0 & (\omega_{m}^{2} - \omega^{2}) \end{bmatrix},$$

$$\boldsymbol{I^{A}} = \begin{bmatrix} (\hat{\omega}_{1}^{2} - \omega^{2}) & 0 & \cdots & 0 \\ 0 & (\hat{\omega}_{2}^{2} - \omega^{2}) & \ddots & \vdots \\ \vdots & \ddots & \ddots & 0 \\ 0 & \cdots & 0 & (\hat{\omega}_{n}^{2} - \omega^{2}) \end{bmatrix}.$$

$$\boldsymbol{I^{A}} = \begin{bmatrix} (\hat{\omega}_{1}^{2} - \omega^{2}) & 0 & \cdots & 0 \\ 0 & (\hat{\omega}_{2}^{2} - \omega^{2}) & \ddots & \vdots \\ \vdots & \ddots & \ddots & 0 \\ 0 & \cdots & 0 & (\hat{\omega}_{n}^{2} - \omega^{2}) \end{bmatrix}.$$

Using this matrix-form, each modal coefficient in Equations (H.1)-(H.6) can be obtained using MATLAB to evaluate the sound pressure inside the room.

## Acknowledgements

"Can any one of you by worrying add a single hour to your life?"

Matthew 6:27

First and foremost, I give thanks to the Lord Jesus Christ, who helped me overcome various challenges I encountered and sustained me during this Ph.D. journey. This journey is long, and I find it to be a profoundly humbling experience. It has helped me to develop as a scholar and as an individual. In completing this journey, I am indebted to the people who have helped and accompanied me. I appreciate each of you. It would be too many to mention all the names here, but some people deserve special recognition.

I want to thank my supervisor, prof. Maarten Hornikx. Thank you for giving me the opportunity to work in your group back in 2015 and for guiding me through the completion of this Ph.D. project. Thank you for your time and patience in reading and improving each manuscript that I make; and for providing the critical and detailed input that I need. I greatly appreciate the support you have given me. You are a fine example of the modern academician, and I will continue to look up to you.

I also want to thank my second supervisor, dr. Jieun Yang. Thank you for helping me in the latter stages of my Ph.D. project. I am very grateful for all the insightful questions, suggestions, and support you gave during the completion of this dissertation. You have given me different perspectives while writing this dissertation, and they have been very helpful to me.

I also thank my supervisory committee members, prof. Carl Hopkins, prof. Steffen Marburg, prof. Akke Suiker, and prof. Ines Lopez. Thank you for taking the time to read my dissertation and provide positive feedback. I also want to thank the people who have inspired me to pursue higher education and taught me about acoustics, the late dr. Ardhana Putra, prof. Jeong Guon Ih, and prof. Benjamin Soenarko.

I would also like to thank my colleagues in the building acoustics group, with whom I shared numerous coffee breaks, lunches, research discussions in RPA, drinks at Zwarte Doos, workouts, and various activities together. Qin, Raúl, Wouter, Huiqing, Jieun, Sai, Chang, Fotis, Baltazar, Jikke, Ella, JinJack, Tanmayee, Matthias, Alessia, Remy, and Fanyu, thank you all. I also appreciate all the contributions from my co-authors, Raúl, Huiqing, and Gerson. Thanks for the efforts and the time invested in working

on our research. A massive thanks to Qin for the measurements we took together on the wooden floor and countless conversations on research and personal matters. I would also like to give special thanks to Raúl, who has been a mentor for me during his stay in Eindhoven. He is very supportive and always has a mature perspective during difficult phases of my study. Huge thanks to Wouter and Jieun, who welcomed me into their house during my final months in The Netherlands.

My gratitude to the Ministry of Finance of the Republic of Indonesia, through the Indonesia Endowment Fund for Education (LPDP), for their full financial support in conducting my Ph.D. research. I want to thank my colleagues in the Building Physics research group at Institut Teknologi Bandung, especially to dr. Iwan Prasetiyo, who supported me during my stay as a researcher over the last two years and encouraged me to finish my dissertation. I would also like to thank Arviandy, Mas Taufik, and Anggera, with whom I had discussed numerous topics outside of study, and Reyhan, who assisted me when I initially came to the Netherlands. I would also like to thank dr. Pranowo, who helped me to understand DG at the early stages of my research.

Outside of the university, me and my family were actively involved with the GKIN in Tillburg, where I built friendships and had fellowship. Saya mau berterima kasih kepada setiap orang di GKIN, terutama untuk Bang Togar dan Kak Susy, yang bantuannya sangat banyak untuk keluarga saya, Om Ronny dan Tante Yayang, Daniel Siregar, Anggera dan Kitty, Bhayu dan Erika, Gian, Stentty, Steffi, Pdt. Marla, Kak Nurpita, Om dan Tante Pereira, Kak Meri, Kak Mary, dan banyak lagi yang namanya tidak saya sebutkan. Terima kasih untuk kalian semua. Pada tahun akhir saya berada di Belanda, saya juga menemukan tempat untuk saya bertumbuh secara rohani di PkEdW, Wageningen. Saya ingin berterima kasih secara khusus untuk Mas Anto yang mengenalkan saya pada hidup yang kekal dan membangun saya secara rohani, dan juga untuk Hugo dan Febi yang menemani saat ber-PA bersama.

I also want to thank my family in Bekasi and Bandung. Untuk Mama, terima kasih untuk segala nasihat, dukungan, dan doa yang tidak hentinya buat saya. Tanpa Mama saya tidak akan sampai dimana saya sekarang. Saya juga mengingat almarhum Bapakku, terima kasih. Untuk kakaku Kando dan abangku Jimmy, terima kasih untuk bantuan dan supportnya selama ini. Untuk Amang dan Inang di Bandung, terima kasih untuk segala bantuan dan juga support untuk saya. Tanpa kalian, saya tidak akan bisa menyelesaikan disertasi ini. Saya juga mengingat semua ipar dan keponakan, terima kasih ada bersama dengan kami di dalam berbagai kesempatan.

Lastly, I want to thank my wife and my daughters, Dewi, Kana, and Nadine, to whom this dissertation is dedicated. Especially to my wife, thank you for your love, patience, encouragement, and willingness to walk through this journey with me. Your support all these years has been invaluable. I could not have done this without you. For my daughters, you are the main source of joy and happiness during this journey, I know it has been not easy with me this long in school. However, it is finished now. Thank you.

### Curriculum Vitae

Indra Sihar was born on 4 August 1984 in Pematang Siantar, North Sumatera, Indonesia. After finishing high school in 2002 at SMUN 1 Bekasi, West Java, he studied Engineering Physics at Institut Teknologi Bandung in Bandung, West Java, and graduated in 2007. In 2008, he came to South Korea for his master's study and earned an MSc degree in Mechanical Engineering from the Korea Advanced Institute of Science and Technology. From 2010 to 2012, he worked as a research engineer at LG Electronics in Seoul. From 2013 to 2015, he worked as an academic assistant at the Department of Engineering Physics in Institut Teknologi Bandung, Indonesia. In 2015, he started a PhD project at the Department of the Built Environment at the Eindhoven University of Technology, of which the results are presented in this dissertation. For this project, he received a scholarship from the Indonesia Endowment Fund for Education or LPDP under the Ministry of Finance of the Republic of Indonesia. Since 2020, he has been working as a researcher at the Building Physics research group in the Institut Teknologi Bandung.

**Bouwstenen** is een publicatiereeks van de Faculteit Bouwkunde, Technische Universiteit Eindhoven. Zij presenteert resultaten van onderzoek en andere activiteiten op het vakgebied der Bouwkunde, uitgevoerd in het kader van deze Faculteit.

**Bouwstenen** en andere proefschriften van de TU/e zijn online beschikbaar via: https://research.tue.nl/

## Reeds verschenen in de serie **Bouwstenen**

nr 1

Elan: A Computer Model for Building Energy Design: Theory and Validation

Martin H. de Wit H.H. Driessen R.M.M. van der Velden

nr 2

Kwaliteit, Keuzevrijheid en Kosten: Evaluatie van Experiment Klarendal, Arnhem

J. Smeets C. le Nobel M. Broos J. Frenken A. v.d. Sanden

nr3

Crooswijk:

Van 'Bijzonder' naar 'Gewoon'

Vincent Smit Kees Noort

nr 4

Staal in de Woningbouw

Edwin J.F. Delsing

nr 5

Mathematical Theory of Stressed Skin Action in Profiled Sheeting with Various Edge Conditions

Andre W.A.M.J. van den Bogaard

nr 6

Hoe Berekenbaar en Betrouwbaar is de Coëfficiënt k in x-ksigma en x-ks?

K.B. Lub A.I. Bosch

nr 7

Het Typologisch Gereedschap: Een Verkennende Studie Omtrent Typologie en Omtrent de Aanpak van Typologisch Onderzoek

J.H. Luiten

nr8

Informatievoorziening en Beheerprocessen

A. Nauta
Jos Smeets (red.)
Helga Fassbinder (projectleider)
Adrie Proveniers
J. v.d. Moosdijk

nr 9

Strukturering en Verwerking van Tijdgegevens voor de Uitvoering van Bouwwerken

ir. W.F. Schaefer P.A. Erkelens

nr 10

Stedebouw en de Vorming van een Speciale Wetenschap

K. Doevendans

nr 11

Informatica en Ondersteuning van Ruimtelijke Besluitvorming

G.G. van der Meulen

nr 12

Staal in de Woningbouw, Korrosie-Bescherming van de Begane Grondvloer Edwin J.F. Delsing

nr 13

Een Thermisch Model voor de Berekening van Staalplaatbetonvloeren onder Brandomstandigheden

A.F. Hamerlinck

R. Stolzenburg

nr 1/

De Wijkgedachte in Nederland: Gemeenschapsstreven in een Stedebouwkundige Context K. Doevendans

1r 15

Diaphragm Effect of Trapezoidally Profiled Steel Sheets: Experimental Research into the Influence of Force Application Andre W.A.M.J. van den Bogaard

nr 16

Versterken met Spuit-Ferrocement: Het Mechanische Gedrag van met Spuit-Ferrocement Versterkte Gewapend Betonbalken K.B. Lubir

M.C.G. van Wanroy

De Tractaten van Jean Nicolas Louis Durand

G. van Zeyl

nr 18

Wonen onder een Plat Dak: Drie Opstellen over Enkele Vooronderstellingen van de Stedebouw

K. Doevendans

nr 19

Supporting Decision Making Processes: A Graphical and Interactive Analysis of Multivariate Data

W. Adams

nr 20

Self-Help Building Productivity: A Method for Improving House Building by Low-Income Groups Applied to Kenya 1990-2000

P. A. Erkelens

nr 21

De Verdeling van Woningen: Een Kwestie van Onderhandelen

Vincent Smit

nr 22

Flexibiliteit en Kosten in het Ontwerpproces: Een Besluitvormingondersteunend Model M. Prins

nr 23

Spontane Nederzettingen Begeleid: Voorwaarden en Criteria in Sri Lanka

Po Hin Thung

nr 24

Fundamentals of the Design of Bamboo Structures

Oscar Arce-Villalobos

nr 25

Concepten van de Bouwkunde

M.F.Th. Bax (red.) H.M.G.J. Trum (red.)

nr 26

Meaning of the Site

Xiaodong Li

nr 27

Het Woonmilieu op Begrip Gebracht: Een Speurtocht naar de Betekenis van het Begrip 'Woonmilieu'

Jaap Ketelaar

nr 28

**Urban Environment in Developing Countries** 

editors: Peter A. Erkelens

George G. van der Meulen (red.)

nr 29

Stategische Plannen voor de Stad: Onderzoek en Planning in Drie Steden

prof.dr. H. Fassbinder (red.)

H. Rikhof (red.)

nr 30

Stedebouwkunde en Stadsbestuur

Piet Beekman

nr 31

De Architectuur van Djenné:

Een Onderzoek naar de Historische Stad

P.C.M. Maas

nr 32

**Conjoint Experiments and Retail Planning** 

Harmen Oppewal

nr 33

Strukturformen Indonesischer Bautechnik: Entwicklung Methodischer Grundlagen für eine 'Konstruktive Pattern Language' in Indonesien

Heinz Frick arch. SIA

nr 34

Styles of Architectural Designing: Empirical Research on Working Styles and Personality Dispositions

Anton P.M. van Bakel

nr 35

Conjoint Choice Models for Urban Tourism Planning and Marketing

Benedict Dellaert

nr 36

Stedelijke Planvorming als Co-Produktie

Helga Fassbinder (red.)

**Design Research in the Netherlands** 

editors: R.M. Oxman M.F.Th. Bax

M.F.Ih. Bax H.H. Achten

nr 38

**Communication in the Building Industry** 

Bauke de Vries

nr 39

Optimaal Dimensioneren van Gelaste Plaatliggers

J.B.W. Stark F. van Pelt L.F.M. van Gorp B.W.E.M. van Hove

nr 40

Huisvesting en Overwinning van Armoede

P.H. Thung

P. Beekman (red.)

nr 41

**Urban Habitat:** 

The Environment of Tomorrow

George G. van der Meulen

Peter A. Erkelens

nr 42

A Typology of Joints

Iohn C.M. Olie

nr 43

Modeling Constraints-Based Choices for Leisure Mobility Planning

Marcus P. Stemerding

nr 44

**Activity-Based Travel Demand Modeling** 

Dick Ettema

nr 45

Wind-Induced Pressure Fluctuations on Building Facades

Chris Geurts

nr 46

**Generic Representations** 

Henri Achten

nr 47

Johann Santini Aichel: Architectuur en Ambiguiteit

Dirk De Meyer

nr 48

**Concrete Behaviour in Multiaxial** 

Compression

Erik van Geel

nr 49

**Modelling Site Selection** 

Frank Witlox

nr 50

Ecolemma Model

Ferdinand Beetstra

nr 51

**Conjoint Approaches to Developing** 

**Activity-Based Models** 

Donggen Wang

nr 52

On the Effectiveness of Ventilation

Ad Roos

nr 53

Conjoint Modeling Approaches for Residential Group preferences

Eric Molin

nr 54

**Modelling Architectural Design** 

Information by Features

Jos van Leeuwen

nr 55

A Spatial Decision Support System for the Planning of Retail and Service Facilities

Theo Arentze

nr 56

**Integrated Lighting System Assistant** 

Ellie de Groot

nr 57

Ontwerpend Leren, Leren Ontwerpen

I.T. Boekholt

nr 58

Temporal Aspects of Theme Park Choice

**Behavior** 

Astrid Kemperman

1r 59

Ontwerp van een Geïndustrialiseerde

**Funderingswijze** 

Faas Moonen

Merlin: A Decision Support System for Outdoor Leisure Planning

Manon van Middelkoop

nr 61

The Aura of Modernity

Jos Bosman

nr 62

**Urban Form and Activity-Travel Patterns** 

Daniëlle Snellen

nr 63

Design Research in the Netherlands 2000

Henri Achten

nr 64

Computer Aided Dimensional Control in Building Construction

Rui Wu

nr 65

**Beyond Sustainable Building** 

editors: Peter A. Erkelens

Sander de Jonge August A.M. van Vliet co-editor: Ruth J.G. Verhagen

nr 66

Das Globalrecyclingfähige Haus

Hans Löfflad

nr 67

**Cool Schools for Hot Suburbs** 

René I. Dierkx

nr 68

A Bamboo Building Design Decision Support Tool

Fitri Mardjono

nr 69

**Driving Rain on Building Envelopes** 

Fabien van Mook

nr 70

**Heating Monumental Churches** 

Henk Schellen

nr 71

Van Woningverhuurder naar Aanbieder van Woongenot

Patrick Dogge

nr 72

**Moisture Transfer Properties of** 

**Coated Gypsum** 

**Emile Goossens** 

nr 73

**Plybamboo Wall-Panels for Housing** 

Guillermo E. González-Beltrán

nr 74

The Future Site-Proceedings

Ger Maas

Frans van Gassel

nr 75

Radon transport in

**Autoclaved Aerated Concrete** 

Michel van der Pal

nr 76

The Reliability and Validity of Interactive Virtual Reality Computer Experiments

Amy Tan

nr 77

Measuring Housing Preferences Using Virtual Reality and Belief Networks

Maciej A. Orzechowski

nr 78

Computational Representations of Words and Associations in Architectural Design

Nicole Segers

nr 70

Measuring and Predicting Adaptation in Multidimensional Activity-Travel Patterns

Chang-Hyeon Joh

nr 8o

**Strategic Briefing** 

Fayez Al Hassan

nr 81

**Well Being in Hospitals** 

Simona Di Cicco

nr 82

**Solares Bauen:** 

Implementierungs- und Umsetzungs-Aspekte in der Hochschulausbildung

in Österreich

Gerhard Schuster

Supporting Strategic Design of Workplace Environments with Case-Based Reasoning

Shauna Mallory-Hill

nr 84

ACCEL: A Tool for Supporting Concept Generation in the Early Design Phase

Maxim Ivashkov

nr 85

**Brick-Mortar Interaction in Masonry under Compression** 

Ad Vermeltfoort

nr 86

Zelfredzaam Wonen

Guus van Vliet

nr 87

Een Ensemble met Grootstedelijke Allure

Jos Bosman Hans Schippers

nr 88

On the Computation of Well-Structured Graphic Representations in Architectural Design

Henri Achten

nr 89

De Evolutie van een West-Afrikaanse Vernaculaire Architectuur

Wolf Schijns

nr 90

**ROMBO Tactiek** 

Christoph Maria Ravesloot

nr 91

External Coupling between Building Energy Simulation and Computational Fluid Dynamics

Ery Djunaedy

nr 92

Design Research in the Netherlands 2005

editors:

Henri Achten Kees Dorst

Pieter Jan Stappers Bauke de Vries

nr 93

Ein Modell zur Baulichen Transformation

Jalil H. Saber Zaimian

nr 94

**Human Lighting Demands:** 

**Healthy Lighting in an Office Environment** 

Myriam Aries

nr 95

A Spatial Decision Support System for the Provision and Monitoring of Urban

Greenspace

Claudia Pelizaro

nr 96

Leren Creëren

Adri Proveniers

nr 97

**Simlandscape** 

Rob de Waard

nr 98

**Design Team Communication** 

Ad den Otter

nr 99

Humaan-Ecologisch

**Georiënteerde Woningbouw** 

Juri Czabanowski

nr 100

Hambase

Martin de Wit

nr 101

Sound Transmission through Pipe Systems and into Building Structures

Susanne Bron-van der Jagt

nr 102

**Het Bouwkundig Contrapunt** 

Ian Francis Boelen

nr 103

A Framework for a Multi-Agent Planning Support System

Dick Saarloos

nr 104

**Bracing Steel Frames with Calcium** 

Silicate Element Walls

Bright Mweene Ng'andu

nr 105

Naar een Nieuwe Houtskeletbouw

F.N.G. De Medts

nr 106 and 107
Niet gepubliceerd

nr 108

Geborgenheid

T.E.L. van Pinxteren

nr 109

Modelling Strategic Behaviour in Anticipation of Congestion

Qi Han

nr 110

**Reflecties op het Woondomein** 

Fred Sanders

nr 111

On Assessment of Wind Comfort by Sand Erosion

Gábor Dezsö

nr 112

**Bench Heating in Monumental Churches** 

Dionne Limpens-Neilen

nr 113

**RE. Architecture** 

Ana Pereira Roders

nr 114

**Toward Applicable Green Architecture** 

Usama El Fiky

nr 115

Knowledge Representation under Inherent Uncertainty in a Multi-Agent System for Land Use Planning

Liying Ma

nr 116

Integrated Heat Air and Moisture Modeling and Simulation

Jos van Schijndel

nr 117

Concrete Behaviour in Multiaxial Compression

J.P.W. Bongers

nr 118

The Image of the Urban Landscape

Ana Moya Pellitero

nr 119

The Self-Organizing City in Vietnam

Stephanie Geertman

nr 120

A Multi-Agent Planning Support System for Assessing Externalities

of Urban Form Scenarios

Rachel Katoshevski-Cavari

nr 121

Den Schulbau Neu Denken, Fühlen und Wollen

Urs Christian Maurer-Dietrich

nr 122

**Peter Eisenman Theories and** 

**Practices** 

**Bernhard Kormoss** 

nr 123

**User Simulation of Space Utilisation** 

Vincent Tabak

nr 125

In Search of a Complex System Model

Oswald Devisch

nr 126

**Lighting at Work:** 

Environmental Study of Direct Effects of Lighting Level and Spectrum on Psycho-Physiological Variables

Grazyna Górnicka

nr 127

Flanking Sound Transmission through Lightweight Framed Double Leaf Walls

Stefan Schoenwald

nr 128

**Bounded Rationality and Spatio-Temporal Pedestrian Shopping Behavior** 

Wei Zhu

nr 129

**Travel Information:** 

**Impact on Activity Travel Pattern** 

Zhongwei Sun

nr 130

Co-Simulation for Performance Prediction of Innovative Integrated Mechanical Energy Systems in Buildings

Marija Trčka

nr 131

Niet gepubliceerd

Architectural Cue Model in Evacuation Simulation for Underground Space Design Chengyu Sun

nr 133

Uncertainty and Sensitivity Analysis in Building Performance Simulation for Decision Support and Design Optimization Christina Hopfe

nr 134

Facilitating Distributed Collaboration in the AEC/FM Sector Using Semantic Web Technologies

Jacob Beetz

nr 135

Circumferentially Adhesive Bonded Glass Panes for Bracing Steel Frame in Façades Edwin Huveners

nr 136

Influence of Temperature on Concrete Beams Strengthened in Flexure with CFRP

Ernst-Lucas Klamer

nr 137

Sturen op Klantwaarde

Jos Smeets

nr 139

Lateral Behavior of Steel Frames with Discretely Connected Precast Concrete Infill Panels

Paul Teewen

nr 140

Integral Design Method in the Context of Sustainable Building Design

Perica Savanović

nr 141

Household Activity-Travel Behavior: Implementation of Within-Household Interactions

Renni Anggraini

nr 142

Design Research in the Netherlands 2010 Henri Achten nr 143

Modelling Life Trajectories and Transport Mode Choice Using Bayesian Belief Networks

Marloes Verhoeven

nr 144

Assessing Construction Project Performance in Ghana

William Gvadu-Asiedu

nr 145

**Empowering Seniors through Domotic Homes** 

Masi Mohammadi

nr 146

An Integral Design Concept for Ecological Self-Compacting Concrete

Martin Hunger

nr 147

Governing Multi-Actor Decision Processes in Dutch Industrial Area Redevelopment Erik Blokhuis

nr 148

A Multifunctional Design Approach for Sustainable Concrete

Götz Hüsken

nr 149

**Quality Monitoring in Infrastructural Design-Build Projects** 

Ruben Favié

1r 150

Assessment Matrix for Conservation of Valuable Timber Structures

Michael Abels

nr 151

Co-simulation of Building Energy Simulation and Computational Fluid Dynamics for Whole-Building Heat, Air and Moisture Engineering

Mohammad Mirsadeghi

nr 152

External Coupling of Building Energy Simulation and Building Element Heat, Air and Moisture Simulation

Daniel Cóstola

Adaptive Decision Making In Multi-Stakeholder Retail Planning

Ingrid Janssen

nr 154

**Landscape Generator** 

Kymo Slager

nr 155

**Constraint Specification in Architecture** 

Remco Niemeijer

nr 156

A Need-Based Approach to Dynamic Activity Generation

Linda Nijland

nr 157

Modeling Office Firm Dynamics in an Agent-Based Micro Simulation Framework

Gustavo Garcia Manzato

nr 158

Lightweight Floor System for Vibration Comfort

Sander Zegers

nr 159

Aanpasbaarheid van de Draagstructuur

Roel Gijsbers

nr 160

'Village in the City' in Guangzhou, China

Yanliu Lin

nr 161

Climate Risk Assessment in Museums

Marco Martens

nr 162

**Social Activity-Travel Patterns** 

Pauline van den Berg

nr 163

**Sound Concentration Caused by** 

**Curved Surfaces** 

Martijn Vercammen

nr 164

Design of Environmentally Friendly Calcium Sulfate-Based Building Materials:

Towards an Improved Indoor Air Quality

Qingliang Yu

nr 165

Beyond Uniform Thermal Comfort on the Effects of Non-Uniformity and Individual Physiology

Lisje Schellen

nr 166

**Sustainable Residential Districts** 

Gaby Abdalla

nr 167

Towards a Performance Assessment Methodology using Computational Simulation for Air Distribution System

**Designs in Operating Rooms** 

Mônica do Amaral Melhado

nr 168

Strategic Decision Modeling in Brownfield Redevelopment

Brano Glumac

nr 169

Pamela: A Parking Analysis Model for Predicting Effects in Local Areas

Peter van der Waerden

nr 170

A Vision Driven Wayfinding Simulation-System Based on the Architectural Features Perceived in the Office Environment

Ounli Chen

nr 171

Measuring Mental Representations Underlying Activity-Travel Choices

Oliver Horeni

nr 172

Modelling the Effects of Social Networks on Activity and Travel Behaviour

Nicole Ronald

nr 173

Uncertainty Propagation and Sensitivity Analysis Techniques in Building Performance Simulation to Support Conceptual Building and System Design

Christian Struck

nr 174

Numerical Modeling of Micro-Scale Wind-Induced Pollutant Dispersion in the Built Environment

Pierre Gousseau

Modeling Recreation Choices over the Family Lifecycle

Anna Beatriz Grigolon

nr 176

Experimental and Numerical Analysis of Mixing Ventilation at Laminar, Transitional and Turbulent Slot Reynolds Numbers

Twan van Hooff

nr 177

Collaborative Design Support:
Workshops to Stimulate Interaction and
Knowledge Exchange Between Practitioners
Emile M.C.J. Quanjel

nr 178

**Future-Proof Platforms for Aging-in-Place**Michiel Brink

nr 179

Motivate:

A Context-Aware Mobile Application for Physical Activity Promotion

Yuzhong Lin

nr 180

Experience the City:
Analysis of Space-Time Behaviour and
Spatial Learning

Anastasia Moiseeva

nr 181

Unbonded Post-Tensioned Shear Walls of Calcium Silicate Element Masonry

Lex van der Meer

nr 182

Construction and Demolition Waste Recycling into Innovative Building Materials for Sustainable Construction in Tanzania Mwita M. Sabai

nr 183

**Durability of Concrete** with Emphasis on Chloride Migration Przemysław Spiesz

nr 184

Computational Modeling of Urban Wind Flow and Natural Ventilation Potential of Buildings

Rubina Ramponi

nr 185

A Distributed Dynamic Simulation Mechanism for Buildings Automation and Control Systems

Azzedine Yahiaoui

nr 186

Modeling Cognitive Learning of Urban Networks in Daily Activity-Travel Behavior Şehnaz Cenani Durmazoğlu

nr 187

Functionality and Adaptability of Design Solutions for Public Apartment Buildings in Ghana

Stephen Agyefi-Mensah

nr 188

A Construction Waste Generation Model for Developing Countries

Lilliana Abarca-Guerrero

nr 189

Synchronizing Networks: The Modeling of Supernetworks for Activity-Travel Behavior

Feixiong Liao

nr 190

Time and Money Allocation Decisions in Out-of-Home Leisure Activity Choices Gamze Zeynep Dane

nr 191

How to Measure Added Value of CRE and Building Design

Rianne Appel-Meulenbroek

nr 192

Secondary Materials in Cement-Based Products:

Treatment, Modeling and Environmental Interaction

Miruna Florea

nr 193

Concepts for the Robustness Improvement of Self-Compacting Concrete: Effects of Admixtures and Mixture Components on the Rheology and Early Hydration at Varying Temperatures Wolfram Schmidt

Modelling and Simulation of Virtual Natural Lighting Solutions in Buildings

Rizki A. Mangkuto

nr 195

Nano-Silica Production at Low Temperatures from the Dissolution of Olivine - Synthesis, Tailoring and Modelling

Alberto Lazaro Garcia

nr 196

Building Energy Simulation Based Assessment of Industrial Halls for Design Support

Bruno Lee

nr 197

Computational Performance Prediction of the Potential of Hybrid Adaptable Thermal Storage Concepts for Lightweight Low-Energy Houses

Pieter-Jan Hoes

nr 198

**Application of Nano-Silica in Concrete** George Quercia Bianchi

nr 199

Dynamics of Social Networks and Activity Travel Behaviour

Fariya Sharmeen

nr 200

**Building Structural Design Generation and Optimisation including Spatial Modification** Juan Manuel Davila Delgado

nr 201

Hydration and Thermal Decomposition of Cement/Calcium-Sulphate Based Materials

Ariën de Korte

nr 202

Republiek van Beelden: De Politieke Werkingen van het Ontwerp in Regionale Planvorming

Bart de Zwart

nr 203

Effects of Energy Price Increases on Individual Activity-Travel Repertoires and Energy Consumption

**Dujuan Yang** 

nr 204

Geometry and Ventilation: Evaluation of the Leeward Sawtooth Roof Potential in the Natural Ventilation of Buildings

Jorge Isaac Perén Montero

nr 205

Computational Modelling of Evaporative Cooling as a Climate Change Adaptation Measure at the Spatial Scale of Buildings and Streets

Hamid Montazeri

nr 206

Local Buckling of Aluminium Beams in Fire Conditions

Ronald van der Meulen

nr 207

Historic Urban Landscapes: Framing the Integration of Urban and Heritage Planning in Multilevel Governance Loes Veldpaus

nr 208

Sustainable Transformation of the Cities: Urban Design Pragmatics to Achieve a Sustainable City

Ernesto Antonio Zumelzu Scheel

nr 209

Development of Sustainable Protective Ultra-High Performance Fibre Reinforced Concrete (UHPFRC):

**Design, Assessment and Modeling** Rui Yu

nr 246

Uncertainty in Modeling Activity-Travel
Demand in Complex Uban Systems
Soora Rasouli

nr 211

Simulation-based Performance Assessment of Climate Adaptive Greenhouse Shells Chul-sung Lee

nr 212

Green Cities:

Modelling the Spatial Transformation of the Urban Environment using Renewable Energy Technologies

Saleh Mohammadi

A Bounded Rationality Model of Short and Long-Term Dynamics of Activity-Travel Behavior

Ifigeneia Psarra

nr 214

Effects of Pricing Strategies on Dynamic Repertoires of Activity-Travel Behaviour Elaheh Khademi

nr 215

Handstorm Principles for Creative and Collaborative Working

Frans van Gassel

nr 216

Light Conditions in Nursing Homes: Visual Comfort and Visual Functioning of Residents

Marianne M. Sinoo

nr 217

Woonsporen:

De Sociale en Ruimtelijke Biografie van een Stedelijk Bouwblok in de Amsterdamse Transvaalbuurt

Hüseyin Hüsnü Yegenoglu

nr 218

Studies on User Control in Ambient Intelligent Systems Berent Willem Meerbeek

nr 219

Daily Livings in a Smart Home: Users' Living Preference Modeling of Smart Homes

Erfaneh Allameh

nr 220

Smart Home Design: Spatial Preference Modeling of Smart Homes

Mohammadali Heidari Jozam

nr 221
Wonen:

Discoursen, Praktijken, Perspectieven

Jos Smeets

nr 222

Personal Control over Indoor Climate in

Impact on Comfort, Health and Productivity

Atze Christiaan Boerstra

nr 223

Personalized Route Finding in Multimodal Transportation Networks

Jianwe Zhang

nr 224

The Design of an Adaptive Healing Room for Stroke Patients

Flke Daemen

nr 225

Experimental and Numerical Analysis of Climate Change Induced Risks to Historic Buildings and Collections

Zara Huijbregts

nr 226

Wind Flow Modeling in Urban Areas Through Experimental and Numerical Techniques

Alessio Ricci

nr 227

Clever Climate Control for Culture: Energy Efficient Indoor Climate Control Strategies for Museums Respecting Collection Preservation and Thermal Comfort of Visitors

Rick Kramer

nr 228

Fatigue Life Estimation of Metal Structures Based on Damage Modeling

Sarmediran Silitonga

nr 229

A multi-agents and occupancy based strategy for energy management and process control on the room-level

Timilehin Moses Labeodan

nr 230

Environmental assessment of Building Integrated Photovoltaics:

Numerical and Experimental Carrying Capacity Based Approach

Michiel Ritzen

nr 231

Performance of Admixture and Secondary Minerals in Alkali Activated Concrete: Sustaining a Concrete Future

Arno Keulen

World Heritage Cities and Sustainable Urban Development:

Bridging Global and Local Levels in Monitoring the Sustainable Urban Development of World Heritage Cities

Paloma C. Guzman Molina

nr 233

Stage Acoustics and Sound Exposure in Performance and Rehearsal Spaces for Orchestras:

**Methods for Physical Measurements** 

Remy Wenmaekers

nr 234

Municipal Solid Waste Incineration (MSWI)
Bottom Ash:

From Waste to Value Characterization, Treatments and Application

Pei Tang

nr 235

Large Eddy Simulations Applied to Wind Loading and Pollutant Dispersion Mattia Ricci

nr 236

Alkali Activated Slag-Fly Ash Binders: Design, Modeling and Application

Xu Gao

nr 237

Sodium Carbonate Activated Slag: Reaction Analysis, Microstructural Modification & Engineering Application Bo Yuan

nr 238

**Shopping Behavior in Malls** Widiyani

nr 239

Smart Grid-Building Energy Interactions: Demand Side Power Flexibility in Office Buildings

Kennedy Otieno Aduda

nr 240

Modeling Taxis Dynamic Behavior in Uncertain Urban Environments

Zheng Zhong

nr 241

Gap-Theoretical Analyses of Residential Satisfaction and Intention to Move

Wen Jiang

nr 242

Travel Satisfaction and Subjective Well-Being: A Behavioral Modeling Perspective

Yanan Gao

nr 243

**Building Energy Modelling to Support** the Commissioning of Holistic Data Centre Operation

Vojtech Zavrel

nr 244

Regret-Based Travel Behavior Modeling: An Extended Framework

Sunghoon Jang

nr 245

Towards Robust Low-Energy Houses: A Computational Approach for Performance Robustness Assessment using Scenario Analysis

Rajesh Reddy Kotireddy

nr 246

Development of sustainable and functionalized inorganic binder-biofiber composites

Guillaume Doudart de la Grée

nr 247

A Multiscale Analysis of the Urban Heat Island Effect: From City Averaged Temperatures to the Energy Demand of Individual Buildings

Yasin Toparlar

nr 248

Design Method for Adaptive Daylight Systems for buildings covered by large (span) roofs

Florian Heinzelmann

nr 249

Hardening, high-temperature resistance and acid resistance of one-part geopolymers

Patrick Sturm

Effects of the built environment on dynamic repertoires of activity-travel behaviour

Aida Pontes de Aquino

nr 251

Modeling for auralization of urban environments: Incorporation of directivity in sound propagation and analysis of a framework for auralizing a car pass-by

Fotis Georgiou

nr 252

Wind Loads on Heliostats and Photovoltaic Trackers

Andreas Pfahl

nr 253

Approaches for computational performance optimization of innovative adaptive façade concepts

Roel Loonen

nr 254

Multi-scale FEM-DEM Model for Granular Materials: Micro-scale boundary conditions, Statics, and Dynamics

Jiadun Liu

nr 255

**Bending Moment - Shear Force Interaction** of Rolled I-Shaped Steel Sections

Rianne Willie Adriana Dekker

nr 256

Paralympic tandem cycling and handcycling: Computational and wind tunnel analysis of aerodynamic performance Paul Fionn Mannion

nr 257

Experimental characterization and numerical modelling of 3D printed concrete: Controlling structural behaviour in the fresh and hardened state

Robert Johannes Maria Wolfs

nr 258

Requirement checking in the building industry: Enabling modularized and extensible requirement checking systems based on semantic web technologies

Chi Zhang

nr 259

A Sustainable Industrial Site Redevelopment Planning Support System

**Tong Wang** 

nr 260

Efficient storage and retrieval of detailed building models: Multi-disciplinary and long-term use of geometric and semantic construction information

Thomas Ferdinand Krijnen

nr 261

The users' value of business center concepts for knowledge sharing and networking behavior within and between organizations Minou Weiis-Perrée

nr 262

Characterization and improvement of aerodynamic performance of vertical axis wind turbines using computational fluid dynamics (CFD)

Abdolrahim Rezaeiha

nr 263

In-situ characterization of the acoustic impedance of vegetated roofs

Chang Liu

nr 264

Occupancy-based lighting control: Developing an energy saving strategy that ensures office workers' comfort

Christel de Bakker

nr 26

Stakeholders-Oriented Spatial Decision Support System

Cahyono Susetyo

nr 266

Climate-induced damage in oak museum objects

Rianne Aleida Luimes

nr 267

Towards individual thermal comfort: Model predictive personalized control of heating systems

Katarina Katic

Modelling and Measuring Quality of Urban Life: Housing, Neighborhood, Transport and Job

Lida Aminian

nr 269

Optimization of an aquifer thermal energy storage system through integrated modelling of aquifer, HVAC systems and building Basar Bozkaya

nr 270

Numerical modeling for urban sound propagation: developments in wave-based and energy-based methods

Raúl Pagán Muñoz

nr 271

Lighting in multi-user office environments: improving employee wellbeing through personal control

Sanae van der Vleuten-Chraibi

nr 272

A strategy for fit-for-purpose occupant behavior modelling in building energy and comfort performance simulation

Isabella I. Gaetani dell'Aquila d'Aragona

nr 273

Een architectuurhistorische waardestelling van naoorlogse woonwijken in Nederland: Het voorbeeld van de Westelijke Tuinsteden in Amsterdam

Eleonore Henriette Marie Mens

nr 274

Job-Housing Co-Dependent Mobility Decisions in Life Trajectories

lia Guo

nr 275

A user-oriented focus to create healthcare facilities: decision making on strategic values

Emilia Rosalia Catharina Maria Huisman

nr 276

Dynamics of plane impinging jets at moderate Reynolds numbers – with applications to air curtains Adelya Khayrullina nr 277

Valorization of Municipal Solid Waste Incineration Bottom Ash - Chemical Nature, Leachability and Treatments of Hazardous Elements

Qadeer Alam

nr 278

Treatments and valorization of MSWI bottom ash - application in cement-based materials

Veronica Caprai

nr 279

Personal lighting conditions of office workers - input for intelligent systems to optimize subjective alertness

Juliëtte van Duijnhoven

nr 280

Social influence effects in tourism travel: air trip itinerary and destination choices
Xiaofeng Pan

nr 281

Advancing Post-War Housing: Integrating Heritage Impact, Environmental Impact, Hygrothermal Risk and Costs in Renovation Design Decisions

Lisanne Claartje Havinga

nr 282

Impact resistant ultra-high performance fibre reinforced concrete: materials, components and properties

Peipeng Li

nr 283

Demand-driven Science Parks: The Perceived Benefits and Trade-offs of Tenant Firms with regard to Science Park Attributes Wei Keat Benny Ng

nr 284

Raise the lantern; how light can help to maintain a healthy and safe hospital environment focusing on nurses

Maria Petronella Johanna Aarts

nr 285

Modelling Learning and Dynamic Route and Parking Choice Behaviour under Uncertainty

Elaine Cristina Schneider de Carvalho

Identifying indoor local microclimates for safekeeping of cultural heritage

Karin Kompatscher

nr 287

Probabilistic modeling of fatigue resistance for welded and riveted bridge details. Resistance models and estimation of uncertainty.

Davide Leonetti

nr 288

Performance of Layered UHPFRC under Static and Dynamic Loads: Effects of steel fibers, coarse aggregates and layered structures

Yangyueye Cao

nr 289

Photocatalytic abatement of the nitrogen oxide pollution: synthesis, application and long-term evaluation of titania-silica composites

Yuri Hendrix

nr 290

Assessing knowledge adoption in postdisaster reconstruction: Understanding the impact of hazard-resistant construction knowledge on reconstruction processes of self-recovering communities in Nepal and the Philippines

Eefje Hendriks

nr 291

Locating electric vehicle charging stations: A multi-agent based dynamic simulation Seheon Kim

nr 292

De invloed van Lean Management op de beheersing van het bouwproces

Wim van den Bouwhuijsen

nr 293

Neighborhood Environment and Physical Activity of Older Adults

**Zhengying Liu** 

nr 294

Practical and continuous luminance distribution measurements for lighting quality

Thijs Willem Kruisselbrink

nr 295

Auditory Distraction in Open-Plan Study Environments in Higher Education

Pieternella Elizabeth Braat-Eggen

nr 296

Exploring the effect of the sound environment on nurses' task performance: an applied approach focusing on prospective memory

likke Reinten

nr 297

Design and performance of water resistant cementitious materials— Mechanisms, evaluation and applications

Zhengyao Qu

nr 298

Design Optimization of Seasonal Thermal Energy Storage Integrated District Heating and Cooling System: A Modeling and Simulation Approach

Luyi Xu

nr 299

Land use and transport: Integrated approaches for planning and management Zhongqi Wang

nr 300

Multi-disciplinary optimization of building spatial designs: co-evolutionary design process simulations, evolutionary algorithms, hybrid approaches
Sionnie Boonstra

nr 301

Modeling the spatial and temporal relation between urban land use, temperature, and energy demand

Hung-Chu Chen

nr 302

Seismic retrofitting of masonry walls with flexible deep mounted CFRP strips

Ömer Serhat Türkmen

nr 303

Coupled Aerostructural Shape and Topology Optimization of Horizontal-Axis Wind Turbine Rotor Blades

Zhijun Wang

Valorization of Recycled Waste Glass and **Converter Steel Slag as Ingredients for Building Materials: Hydration and Carbona**tion Studies

Gang Liu

nr 305

Low-Carbon City Development based on **Land Use Planning** 

Gengzhe Wang

nr 306

Sustainable energy transition scenario analysis for buildings and neighborhoods -Data driven optimization

Shalika Saubhagya Wickramarachchi Walker

nr 307

In-between living and manufactured: an exploratory study on biobuilding components for building design Berrak Kirbas Akyurek

nr 308

**Development of alternative cementitious** binders and functionalized materials: design, performance and durability Anna Monika Kaja

nr 309

Development a morphological approach for interactive kinetic façade design: Improving multiple occupants' visual comfort

Seved Morteza Hosseini

nr 310

PV in urban context: modeling and simulation strategies for analyzing the performance of shaded PV systems

Ádám Bognár

nr 311

Life Trajectory, Household Car Ownership **Dynamics and Home Renewable Energy Equipment Adoption** 

Gaofeng Gu

nr 312

Impact of Street-Scale Built Environment on Walking/Cycling around Metro Stations Yanan Liu

Advances in Urban Traffic Network **Equilibrium Models and Algorithms** Dong Wang

nr 314

Development of an uncertainty analysis framework for model-based consequential life cycle assessment: application to activity-based modelling and life cycle assessment of multimodal mobility

Paul Martin Baustert

nr 315

Variable stiffness and damping structural joints for semi-active vibration control Qinyu Wang

nr 316

**Understanding Carsharing-Facilitating Neighborhood Preferences** Juan Wang

nr 317

Dynamic alignment of Corporate Real Estate to business strategies: An empirical analysis using historical data and in-depth modelling of decision making Howard Cooke

nr 318

Local People Matter: Towards participatory governance of cultural heritage in China Ji Li

nr 319

Walkability and Walkable Healthy Neighborhoods **Bojing Liao** 

nr 320

Light directionality in design of healthy offices: exploration of two methods Parisa Khademagha

nr 321

Room acoustic modeling with the timedomain discontinuous Galerkin method **Huiqing Wang** 

nr 322

Sustainable insulating lightweight materials for enhancing indoor building performance: miscanthus, aerogel and nano-silica Yuxuan Chen

Computational analysis of the impact of façade geometrical details on wind flow and pollutant dispersion

Xing Zheng

nr 324

Analysis of urban wind energy potential around high-rise buildings in close proximity using computational fluid dynamics
Yu-Hsuan lang

nr 325

A new approach to automated energy performance and fault detection and diagnosis of HVAC systems: Development of the 4S3F method

Arie Taal

nr 326

Innovative Admixtures for Modifying Viscosity and Volume Change of Cement Composites

Hossein Karimi

nr 327

Towards houses with low grid dependency: A simulation-based design optimization approach

Zahra Mohammadi

nr 328

Activation of demand flexibility for heating systems in buildings: Real-life demonstration of optimal control for power-to-heat and thermal energy storage

Christian Finck

nr 329

A computational framework for analysis and optimisation of automated solar shading systems

Samuel B. de Vries

nr 330

Challenges and potential solutions for cultural heritage adaptive reuse: a comparative study employing the Historic Urban Landscape approach

Nadia Pintossi

nr 331

**Shared control in office lighting systems** Tatiana Aleksandrovna Lashina

nr 332

Comfort in Urban Public Spaces

You Peng

nr 333

Numerical modelling of metal soap formation in historical oil paintings

Gerardus Johannes Anna Maria Eumelen

nr 334

A transdisciplinary decision-making approach to food-water-energy nexus: A guide towards sustainable development Maryam Ghodsvali The urban environment is increasingly exposed to excessive noise from environmental noise sources and neighbours. To address this problem, an acoustically high-quality built environment is needed to ensure health and comfort. In designing such an environment, the prediction of sound propagation and vibrations in buildings have a vital role. This research aims to develop an efficient yet detailed numerical model of sound propagation and vibration in building applications, especially in the low-frequency range. This research employs a wave-based method to solve these problems. The chosen wave-based method is the time-domain discontinuous Galerkin (DG) method due to its favourable features such as computational efficiency, high-order accuracy, geometric flexibility, and the potential for massive parallel computing.

This dissertation consists of three main parts. In the first part, the DG method is applied for sound propagation in air. The applications include room acoustics and outdoor sound propagation in the presence of wind flow. Examples include sound propagation in an experimental chamber and at an airport environment. In the second part, the DG method is developed for the structural vibrations of monolithic structures and structures with piece-wise constant properties. Examples include vibrations of rectangular plates, L- and T-shaped structures, and a scaled lightweight wooden floor. The third part expands the DG method to solve the sound and vibration interaction (vibroacoustic) problems. This part presents the impact sound radiation from a rectangular slab and sound transmissions of several walls as examples.

**DEPARTMENT OF THE BUILT ENVIRONMENT** 

